

THE UNIVERSITY OF CHICAGO

DISPROPORTIONATION OF IRON IN EARTH'S LOWER MANTLE

A DISSERTATION SUBMITTED TO
THE FACULTY OF THE DIVISION OF THE PHYSICAL SCIENCES
IN CANDIDACY FOR THE DEGREE OF
DOCTOR OF PHILOSOPHY

DEPARTMENT OF THE GEOPHYSICAL SCIENCES

BY

KELLIE ELIZABETH SWADBA

CHICAGO, ILLINOIS

DECEMBER 2023

TABLE OF CONTENTS

LIST OF FIGURES	iv
LIST OF TABLES	vii
ACKNOWLEDGEMENTS	viii
ABSTRACT	ix
1 MINERALOGY OF EARTH'S LOWER MANTLE	1
1.1 Composition of Earth's mantle	1
1.2 Bridgmanite in Earth's lower mantle	3
1.3 Bridgmanite and disproportionation	7
1.4 Implications of disproportionation	9
1.5 Factors that may affect disproportionation	11
1.6 Scope of this thesis	17
2 EXPERIMENTAL TECHNIQUES	20
2.1 Sample preparation	20
2.2 Pressure Generation	24
2.3 Laser Heating	26
2.4 X-ray Diffraction	28
2.5 Sample Recovery	29
2.6 SEM Analyses	32
2.7 TEM Analyses	34
2.8 STEM Analyses	36
3 THERMODYNAMIC MODELLING USING PERPLEX	38
3.1 Thermodynamic background	38
3.2 PerpleX overview	42
3.3 Stixrude and Lithgow-Bertelloni databases	46
3.4 Modification of thermodynamic input parameters to promote iron disproportionation ..	51
3.4.1 Addition of the fcc Fe and hcp Fe phases	52
3.4.2 Addition of the FeAlO ₃ phase	53
3.5 Demonstrations of disproportionation	60
4 DISPROPORTIONATION OF IRON IN ALMANDINE-PYROPE-GROSSULAR GARNET FROM 25 TO 65 GPA	67
4.1 Introduction	67
4.2 Materials and Methods	69

4.3	Results	72
4.3.1	XRD Results	72
4.3.2	SEM Results	75
4.4	Discussion	81
4.4.1	Phase Relations	81
4.4.2	PerpleX Predictions	83
4.4.3	Phase Compositions	87
4.4.4	Equation of State of Bridgmanite	89
4.5	Conclusions	91
5	DISPROPORTIONATION OF IRON IN PYROLITE FROM 24 TO 132 GPA	93
5.1	Introduction	93
5.2	Materials and Methods	96
5.3	Results	101
5.3.1	XRD Results	101
5.3.2	SEM Results	103
5.3.3	TEM Results	107
5.3.4	STEM Results	109
5.4	Discussion	115
5.4.1	Absence of identifiable davemaoite	115
5.4.2	Compression trends	117
5.4.3	Disproportionation of Fe throughout the lower mantle	121
5.4.4	STEM EDS observations	126
5.4.5	PerpleX modelling of disproportionation	128
5.4.6	Implications	131
5.5	Conclusion	133
6	CONCLUSIONS	135
APPENDIX A	SUPPLEMENTAL MATERIAL FOR CHAPTER 2	139
APPENDIX B	SUPPLEMENTAL MATERIAL FOR CHAPTER 3	150
APPENDIX C	SUPPLEMENTAL MATERIAL FOR CHAPTER 4	155
APPENDIX D	SUPPLEMENTAL MATERIAL FOR CHAPTER 5	158
REFERENCES	188

LIST OF FIGURES

Figure 1.1. Bridgmanite orthorhombic perovskite Pnma crystal structure.....	4
Figure 1.2. Measurements reproduced from Figure 1 Irifune et al. (2010).....	12
Figure 1.3. Fe ³⁺ content and partition coefficient changes across the lower mantle.....	14
Figure 2.1. Creation of glass samples.....	21
Figure 2.2. Mössbauer measurements of the pyrolite glass bead used in this study.....	22
Figure 2.3. Temperature history of a pyrolite sample heated at the synchrotron.....	27
Figure 2.4. Schematic representation of the interaction of the electron beam with sample.....	29
Figure 2.5. Demonstration of the sample recovery process.....	31
Figure 2.6. EDS measurements on sample K59.....	33
Figure 2.7. SEM EDS spectra collected over a metallic Fe grain in a garnet sample.....	34
Figure 3.1. Schematic representation of a Gibbs energy curve.....	40
Figure 3.2. Schematic representation of the construction of a phase diagram.....	43
Figure 3.3. Flow of running a calculation with PerpleX.....	46
Figure 3.4. Fe phase boundary.....	53
Figure 3.5. Modified solution model for bridgmanite.....	56
Figure 3.6. PerpleX predictions for the FeAlO ₃ phase.....	59
Figure 3.7. PerpleX predictions for the pyrope-almandine join.....	61
Figure 3.8. PerpleX predictions of an olivine + Al ₂ O ₃ composition.....	62
Figure 3.9. PerpleX predictions of the composition studied in Creasy et al. (2020).....	64
Figure 4.1. XRD patterns collected at 37 keV on a sample with an Ir foil (K8).....	73
Figure 4.2. XRD patterns collected at 37 keV on a sample with an Ir foil (K7).....	74
Figure 4.3. SEM results for sample K11.....	76
Figure 4.4. EDS maps and images collected on sample K11.....	78
Figure 4.5. Line scan across a metallic iron grain in sample K11.....	79
Figure 4.6. SEM images of sample K54. Top: SE image.....	80
Figure 4.7. PerpleX predictions for our garnet composition.....	84
Figure 4.8. PerpleX predictions for pure almandine.....	86
Figure 4.9. Lattice parameters of bridgmanite.....	90
Figure 5.1. Observations of disproportionated metallic Fe from previous studies.....	95
Figure 5.2. Mössbauer spectrum of pyrolite glass.....	97
Figure 5.3. Optical microscope image of the laser-heated spot.....	100
Figure 5.4. XRD results of K75 (pre-heat pressure 27 GPa) before and during heating.....	101
Figure 5.5. Quench patterns at high pressure.....	102
Figure 5.6. SEM images of sample recovered from 39 GPa and 2000 K (K59).....	103

Figure 5.7. EDS line scan collected at 7 kV across the laser-heated spot in sample K59.....	104
Figure 5.8. Images of all recovered samples	105
Figure 5.9. BSE images of samples K76 and K83	106
Figure 5.10. TEM images of recovered samples	107
Figure 5.11. High phase contrast TEM images of sample K60.....	108
Figure 5.12. STEM images of recovered samples.....	110
Figure 5.13. TEM and STEM image of a metallic Fe grain in sample K60.....	111
Figure 5.14. EDS elemental maps of sample K59 (39 GPa and 2015 K)	112
Figure 5.15. EDS elemental maps of sample K76 (72 GPa and 2260 K)	113
Figure 5.16. EDS line scan over a metallic Fe grain in sample K76 (72 GPa and 2260 K).....	114
Figure 5.17. Lattice parameters of bridgmanite.....	118
Figure 5.18. Lattice parameter ratios of bridgmanite	119
Figure 5.19. Volumes of bridgmanite left and ferropericlasite right	121
Figure 5.20. Example image analysis for sample K60	123
Figure 5.21. Volume percent and average radius of the metallic Fe grains	125
Figure 5.22. Updated observations of disproportionated metallic Fe.....	127
Figure 5.23. PerpleX predictions along the geotherm	129
Figure 5.24. Volume fraction of metallic Fe as a function of pressure along the geotherm	130
Figure 5.25. Schematic of Fe metal trends in the lower mantle.	133
Figure A.1. Lab and synchrotron Mössbauer results on glass beads.....	139
Figure A.2. Additional lab Mössbauer results on glass beads.....	139
Figure A.3. Example of a sample with C contamination.....	140
Figure A.4. Example of a pyrolite glass sample with C contamination.	141
Figure A.5. Example of a recovered powdered pyrolite sample	142
Figure A.6. Example of a recovered powdered peridotite sample	143
Figure A.7. Compressed garnet and pyrolite glass samples prior to laser heating.....	144
Figure A.8. Recovered sample in a gasket.	144
Figure A.9. Bending of a sample attached to a TEM post.....	145
Figure A.10. Example of Ga deposition.	145
Figure A.11. Example of a thinned sample viewed in the SEM.	146
Figure A.12. Example of an unevenly thinned sample.....	146
Figure A.13. Example of underfocusing in the TEM.	147
Figure A.14. Example of grain overlap.	147
Figure A.15. Examples of electron diffraction images.....	148
Figure A.16. Examples of visible contamination on samples	148
Figure A.17. EELS collection on a pyrolite glass sample.	149
Figure B.1. Sample problem definition file.	150

Figure B.2. Demonstration of removal of Landau transitions in stx21ver.dat database.	152
Figure B.3. Phase boundary generated by Komabayashi & Fei (2010) EOS in PerpleX.....	152
Figure B.4. Fits of fcc Fe and hcp Fe isotherms.....	153
Figure B.5. P-T plot of FeO bulk composition.....	154
Figure B.6. Fe ³⁺ prediction for the Shim et al. (2017) study.....	154
Figure C.1. XRD patterns collected at 42 keV on samples with no Ir foils.	155
Figure C.2. Example XRD pattern from the K11 thin section XRD map.....	156
Figure C.3. EDS maps collected in sample K54	156
Figure C.4. Line scan collected in K54	157
Figure D.1. Images of the pyrolite powder pellet and synthesized pyrolite glass bead.	163
Figure D.2. XRD patterns of decompressed samples.....	163
Figure D.3. mXRD pattern of K59 (recovered thin section).	164
Figure D.4. EDS map of sample K59 (as seen in Figure 5.6).	165
Figure D.5. SEM EDS line scan across sample K60.....	166
Figure D.6. TEM images of recovered samples at higher magnification than Figure 5.10.....	167
Figure D.7. TEM images for sample K59.	168
Figure D.8. TEM images for sample K60.	169
Figure D.9. TEM images for sample K67.	170
Figure D.10. TEM images for sample K76.	171
Figure D.11. TEM images for sample K84.	172
Figure D.12. TEM images for sample K86.	173
Figure D.13. STEM images and EDS maps for sample K59.	174
Figure D.14. STEM images and elemental EDS maps for sample K60.....	175
Figure D.15. Elemental EDS maps for sample K76.....	176
Figure D.16. STEM images and EDS line scans for sample K83.	177
Figure D.17. Elemental EDS maps for sample K83.....	178
Figure D.18. STEM images and EDS line scans for sample K84.	179
Figure D.19. Elemental EDS maps for sample K84.....	180
Figure D.20. STEM image and EDS line scans for sample K86.....	181
Figure D.21. Elemental EDS maps of sample K86.	182
Figure D.22. Example of image analysis on a “medium quality” image.	186
Figure D.23. Example of image analysis on a “low quality” image.....	187

LIST OF TABLES

Table 1.1. Major elements pyrolite compositions in weight percent and atomic percent.	2
Table 1.2. Pyrolite compositions in weight percent.....	2
Table 1.3. Pyrolite compositions in weight percent normalized to only the major elements.	2
Table 3.1. Parameters for EOS type 6 phases added in this work	54
Table 4.1. Sample details	70
Table 4.2. Average elemental quantities in atomic % for sample K11.....	77
Table 4.3. Third-order Birch-Murnaghan fit parameters for bridgmanite.....	89
Table 5.1. Composition of the starting material compared to Ringwood (1975)	96
Table 5.2. Experiment details	98
Table B.1. Thermodynamic parameters from the literature.....	151
Table C.1. WDS measurements on the natural almandine-pyrope-grossular garnet.....	155
Table D.1. Detailed review of SEM/TEM observations of disproportionated metallic Fe	158
Table D.2. SEM EDS measurements on recovered samples.	183
Table D.3. STEM EDS measurements on recovered samples.....	184
Table D.4. Lattice parameters and volumes for this study	185

ACKNOWLEDGEMENTS

I would like to thank my advisor, Andrew Campbell, for his guidance and support. I would also like to thank my committee members Fred Ciesla, Andrew Davis, and Dion Heinz. The microscopy work in this thesis would not have been possible without the support and patience of Gerard Olack at the University of Chicago and Fengyuan Shi at the University of Illinois at Chicago. The help of Catherine Macris from Indiana University – Purdue University Indianapolis was also indispensable for the creation of glass samples. I would also like to acknowledge the beamline staff at APS sector 13 ID-D for their support during X-ray diffraction experiments, as well as Barbara Lavina for her help with Mössbauer measurements. I would also like to acknowledge the students and postdocs I have had the pleasure to work with: Nigel Brauser, Anne Davis, Claire Zurkowski, Cara Vennari, and Emma Stoutenburg. And finally, thank you to my family for your unwavering support over the years.

ABSTRACT

The production of metallic Fe via the disproportionation of Fe^{2+} to Fe^0 and Fe^{3+} in the deep Earth has been a long debated topic with important implications for the geochemistry of the lower mantle. The presence of disproportionated metallic Fe can affect the siderophile element geochemistry of the lower mantle, notably through its impact on isotopic tracers such as Os, and on platinum group element distributions. Metallic iron could also serve as a likely host for volatile elements in the lower mantle, such as C, S, and H, impacting the mantle's carbon and hydrogen budgets. It is understood that bridgmanite is the dominant phase in the lower mantle, and it has been shown that the presence of Al promotes the partitioning of Fe^{3+} into the perovskite structure as an FeAlO_3 component, charge balanced by metallic iron. Frost et al. (2004) proposed that this disproportionation process occurs in the lower mantle, where the formation of aluminous perovskite implies the precipitation of approximately 1 wt% metallic Fe-rich alloy. However, literature data conflict on the pressure, temperature, and composition space in which this reaction occurs, and there has been little subsequent study to confirm this process at deeper lower mantle conditions.

This thesis focuses on the experimental detection and theoretical prediction of the iron disproportionation reaction across a range of lower mantle conditions. First, I describe modifications I made to the thermodynamic database of Stixrude & Lithgow-Bertelloni (2022), which contains thermodynamic parameters for the calculation of various lower mantle phase equations of state. I use the modified database to model high pressure and temperature phase equilibria with the PerpleX Gibbs energy minimization software (Connolly, 2009). I find that the disproportionation reaction can be successfully modeled with the updated database, and I identify

several results from the literature where the disproportionation reaction was incorrectly overlooked. Next, I explore the occurrence of the iron disproportionation reaction from 25 to 65 GPa in a natural almandine-pyrope-grossular garnet with *in-situ* X-ray diffraction in the laser-heated diamond anvil cell and with *ex-situ* scanning electron microscopy techniques. Examination of the samples recovered between 39-64 GPa by scanning electron microscopy analysis reveals the presence of nm-scale disproportionated iron metal grains as an additional product of this reaction that was not detectable in the X-ray diffraction patterns. I use volume compression data of the synthesized bridgmanite to estimate the FeAlO_3 content of the bridgmanite in this composition, which I confirm with PerpleX thermodynamic modeling. The PerpleX thermodynamic modeling also confirms the occurrence of the iron disproportionation reaction in this composition. Finally, I investigate the iron disproportionation reaction in a lower mantle pyrolite composition from 27 to 132 GPa along the geotherm with *in-situ* X-ray diffraction and *ex-situ* scanning electron and transmission electron microscopy techniques. I demonstrate that disproportionated metallic Fe can be detected in all assemblages recovered across the range of lower mantle conditions. Through TEM image analysis and PerpleX thermodynamic modeling, I determine that the amount of disproportionated metallic Fe decreases by a factor of ~ 5 from the top of the lower mantle to its base, dropping from ~ 0.6 vol% to 0.1 vol%. I explore the effect of this distribution of metallic Fe throughout the lower mantle on the stability of various C-bearing phases in the lower mantle.

1 MINERALOGY OF EARTH'S LOWER MANTLE

The lower mantle is volumetrically the largest portion of the Earth, accounting for approximately 55% of the Earth's volume and extending from 660 to 2,891 km. Pressures within the lower mantle range from 24 to 136 GPa, and temperatures range from approximately 1,850 to 2,800 K. To understand vital processes and features within the Earth, such as global mantle dynamics and the thermal structure of the Earth, we need a complete picture of the chemical composition and redox state of the lower mantle. Much is still unknown about this vast region, however. One open question concerns the potential for an iron disproportionation reaction to occur at lower mantle conditions (Frost et al., 2004). Such a reaction would stabilize small amounts of metallic iron as an accessory phase in the lower mantle, which could have implications for the behavior of siderophile and volatile elements in the lower mantle as well as the evolution of the mantle's redox state through time. Thus, further study of the disproportionation reaction, including its potential to occur across the range of lower mantle conditions, as well as the identification of the factors that control its occurrence, is critical to achieving an improved understanding of Earth's lower mantle.

1.1 Composition of Earth's mantle

The composition of Earth's mantle is often represented by the hypothetical pyrolite compositional model, introduced by Ringwood in a series of papers starting in 1962. Pyrolite represents the primitive mantle that, upon fractional melting, produces residual peridotite and basaltic magma. In a pyrolitic composition, Earth's mantle is dominated by O, Si, Mg, and Fe, which account for 94% of its elemental composition. A further 5% is accounted for by Ca and Al (Ringwood, 1975). Table 1.1 provides examples of pyrolitic compositions, and Table 1.2 provides

Oxide	Ringwood 1979	McDonough & Sun 1995	Palme & O'Neill 2014
MgO	38.10	37.80	36.77
Al ₂ O ₃	3.30	4.45	4.49
SiO ₂	45.10	45.00	45.40
CaO	3.10	3.55	3.65
FeO	8.00	8.05	8.10
Major element total	97.60	98.85	98.41
TiO ₂	0.20	0.20	0.21
Cr ₂ O ₃	0.40	0.38	0.37
NiO	0.20	0.25	0.24
MnO	0.15	0.14	0.14
Na ₂ O	0.40	0.36	0.35
K ₂ O	0.00	0.03	0.03

Table 1.1. Lower mantle compositions in weight percent.

Oxide	Ringwood 1979	McDonough & Sun 1995	Palme & O'Neill 2014
MgO	39.04	38.69	37.36
Al ₂ O ₃	3.38	3.38	4.56
SiO ₂	46.21	46.06	46.13
CaO	3.18	3.63	3.71
FeO	8.20	8.24	8.23

Table 1.2. Lower mantle compositions in weight percent normalized to only the major elements.

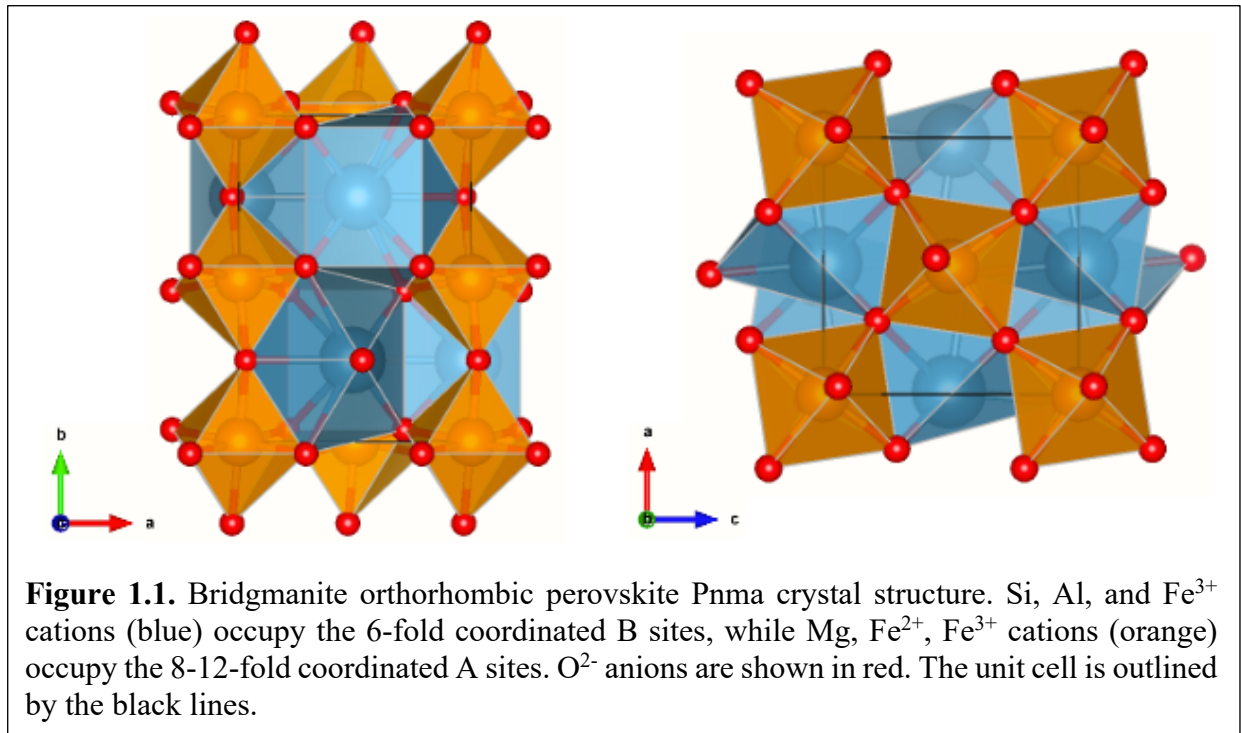
Element	Ringwood 1979 wt%	McDonough & Sun 1995 wt%	Palme & O'Neill 2014 wt%	Ringwood 1979 at%	McDonough & Sun 1995 at%	Palme and O'Neill 2014 at%
Mg	23.54	23.06	22.53	20.38	19.99	19.55
Al	1.79	2.38	2.41	1.40	1.86	1.89
Si	21.60	21.28	21.56	16.19	15.96	16.19
Ca	2.27	2.57	2.65	1.19	1.35	1.39
Fe	6.37	6.33	6.40	2.40	2.39	2.42
O	44.43	44.38	44.44	58.44	58.45	58.57

Table 1.3. Major elements lower mantle compositions in weight percent and atomic percent.

the same pyrolitic compositions normalized to only the major elements. Table 1.3 provides the normalized pyrolitic compositions in weight percent and atomic percent. In a pyrolitic composition, the lower mantle, and thus the Earth, is dominated by the bridgmanite phase, $(\text{Mg,Fe})(\text{Si,Al})\text{O}_3$ (Liu, 1976; Knittle and Jeanloz, 1987; O'Neill and Jeanloz, 1990). The remainder of the mantle is composed mainly of ferropericlase $((\text{Mg,Fe})\text{O})$ and davemaoite (CaSiO_3) (O'Neill 1990). The breakdown of these phases by volume is approximately 75%, 18%, and 7%, respectively (Wood, 2000; Lee et al., 2004; Irifune et al., 2010; Wang et al., 2015). The compositions of bridgmanite and ferropericlase will vary slightly throughout the lower mantle, due to the partitioning of Fe and Mg between the two phases. The variation is complicated by several factors that will be discussed more below. While bridgmanite, ferropericlase, and davemaoite account for the majority of the lower mantle, other minor accessory phases are also stable across the lower mantle regime. One such phase could be metallic Fe produced through a disproportionation reaction, whose presence and abundance is linked to bridgmanite. To explore the potential existence of a minor metallic iron phase throughout the lower mantle, the bridgmanite phase must first be well understood.

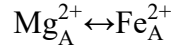
1.2 Bridgmanite in Earth's lower mantle

Bridgmanite is an important phase in the lower mantle not only because it is the most abundant phase but also because it acts as the primary host for Al in the lower mantle. Bridgmanite adopts the orthorhombic *Pnma* structure and has the general form ABO_3 , where A and B represent distinct crystallographic sites within the bridgmanite structure (Figure 1.1). The orthorhombic *Pnma* bridgmanite structure is distorted from the cubic perovskite structure by rotation and tilting of the octahedra, shortening eight of the cation-anion bonds and lengthening four of the bonds,

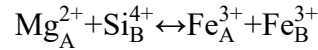


which reduces the coordination of the A-site cations from 12 to 8 (Horiuchi et al., 1987; Huang et al., 2021). The B-site cations are in 6-fold coordination with the oxygen anions, forming a network of corner-sharing octahedra. The bridgmanite structure can accommodate various cations in its A and B sites, but given that Mg and Si are the two most abundant elements in a pyrolitic mantle (behind O), the primary cation occupying the A site in bridgmanite is Mg²⁺, while the B site is primarily occupied by the smaller Si⁴⁺ cation, making the major component of bridgmanite MgSiO₃.

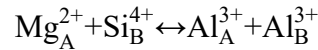
Beyond Mg and Si, bridgmanite can most notably accommodate Fe²⁺, Fe³⁺, and Al³⁺ in its structure. The role of iron in bridgmanite is complex because it can occupy different structural sites with different valence and spin states, which can affect partitioning, phase transition boundaries, and oxygen fugacity in the lower mantle. In the absence of Al, Fe can enter the A-site of the perovskite structure as Fe²⁺ through a simple substitution for Mg²⁺:



which creates an FeSiO₃ component (Kudoh et al., 1990; McCammon et al., 1992; Fei et al., 1994). At high f_{O_2} conditions, Fe can also enter bridgmanite as Fe³⁺, occupying both the A and B sites, through a coupled substitution:



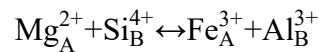
which creates the FeFeO₃ component (McCammon, 1997, 1998; Hummer and Fei, 2012). The ability of bridgmanite to accommodate Al (in the absence of Fe) has also been extensively studied and been found to have significant effects on important properties of bridgmanite (Irifune, 1994; Kesson et al., 1995). A pyrolite mantle should have approximately 3.3 wt% Al₂O₃ (Ringwood, 1979). In the upper mantle, Al is hosted in the spinel and garnet phases, but both of these phases break down from 23-24 GPa (Wood, 2000). Al can enter the bridgmanite structure above these pressures, however, through a coupled substitution:



which creates the AlAlO₃ component (Irifune, 1994). Bridgmanite can accommodate up to 25 mol% Al₂O₃ through pressures up to ~70 GPa and has even been shown to hold up to 30 mol% Al₂O₃ at 55 GPa (Liu, 1989; Kesson et al., 1995; Walter et al., 2004). It has further been shown that bridgmanite can accommodate increasing Al content with both increasing pressure and temperature, making it the major host of Al in the lower mantle (Irifune et al., 1996; Ito et al., 1998; Liu et al., 2021). Because Al enters the different sized A and B sites equally, it enhances the distortion of the orthorhombic structure, which is why higher pressures are required to allow more Al₂O₃ into bridgmanite. Additional substitution mechanisms for both Fe and Al can operate through the creation of O vacancies, but these mechanisms are not relevant at the high pressures

related to the majority of the lower mantle (Brodholt, 2000; Hummer and Fei, 2012; Huang et al., 2021).

A more comprehensive understanding of the behavior of bridgmanite must include both Al and Fe. It has been extensively shown that Al acts to stabilize Fe³⁺ in the perovskite structure, through a coupled substitution (McCammon, 1997; Richmond and Brodholt, 1998; Lauterbach et al., 2000; Vanpeteghem et al., 2006, Huang et al., 2021):

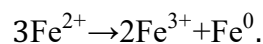


McCammon 1997 showed, for example, that a perovskite containing 3.3 mol% Al₂O₃ contained 50% of its iron as Fe³⁺. Calculations performed by Richmond and Brodholt (1998) showed that the substitution of Al into the B site, balanced by Fe³⁺ in the A site, is the most favorable mechanism for Fe and Al incorporation into the bridgmanite phase – more favorable than separate substitution of the individual species. It is likely that the similar ionic radii of Al³⁺ and Si⁴⁺ promote substitution of Al³⁺ in the B site, which stabilizes Fe³⁺ in the A site to maintain charge balance (Liu et al., 2020). Vanpeteghem et al. (2006) confirmed that in an Fe- and Al-bearing perovskite with more Fe than Al, there are little or no oxygen vacancies and less than 1 mol% of Fe on the B site. Further, it was shown that in addition to nearly all Fe occupying the A site, nearly all Al cations occupy the B site. Huang et al. (2021) similarly found that only a small amount of Fe³⁺ entered the B site in a bridgmanite composition with the concentration of Fe³⁺ exceeding Al, and only a small amount of Al entered the A site in a bridgmanite composition with the concentration of Al exceeding Fe³⁺. Huang et al. (2021) also find that FeAlO₃ substitution leads to increasing octahedral tilting to accommodate the smaller Fe³⁺ cation in the A site.

The concentration of Al also plays a role in the amount of Fe³⁺ incorporated into bridgmanite. Frost et al. (2004) found a nonlinear relationship between Al³⁺ concentration and Fe³⁺ concentration; higher Al³⁺ contents allow an increasing amount of Fe³⁺ to enter the perovskite structure. It has also been found that FeAlO₃ substitution is enhanced by increasing pressure (Nishio-Hamane et al., 2005). At 51 GPa and 2100 K, a synthesized perovskite with initial composition Mg₃Fe³⁺AlSi₃O₁₂ is found to have an FeAlO₃ component of ~25 mol%, while at 21 GPa, the same composition has 21 mol% FeAlO₃ and an additional 9 mol% Al₂O₃ (Nishio-Hamane et al., 2005). Observations from subsequent studies have expanded the range of FeAlO₃ incorporation in the perovskite structure. Liu et al. (2020) reported the maximum solubility of the FeAlO₃ component in bridgmanite at 27 GPa and 2000 K to be 67 mol%, which is well above the expected 9 mol% FeAlO₃ content of bridgmanite in a pyrolitic mantle. Finally, recent work (Ko et al., 2022) suggests that the incorporation of the FeAlO₃ component into bridgmanite may make Ca more soluble in bridgmanite.

1.3 Bridgmanite and disproportionation

Studies have also shown that Fe³⁺ concentrations in bridgmanite are independent of oxygen fugacity, indicating that observations of high Fe³⁺ content are related to crystal chemistry, not oxygen fugacity (Lauterbach et al., 2000; Frost et al., 2004). Lauterbach et al. (2000) performed multianvil experiments on synthetic aluminous orthopyroxene starting materials in Fe and Re capsules and found that perovskite Fe³⁺ content was not dependent upon the oxygen fugacity. They suggest that Fe³⁺ is produced in the reducing conditions of the Fe capsule through a disproportionation reaction:



Frost et al. (2004) extended the study of the Fe^{3+} -Al relationship to understand the role of Fe^{3+} and its potential to induce the precipitation of metallic Fe-rich alloy in the lower mantle. They note that the crystal-chemical constraints that make Fe^{2+} the dominant form of iron in the upper mantle may not hold for the transition zone and lower mantle, where mixtures of Fe^{3+} -rich minerals and metallic Fe can be stable, even if bulk oxygen contents are the same as in the upper mantle. To explore the relationship between Al and Fe^{3+} , Frost et al. (2004) synthesized perovskite from aluminous pyroxene materials mixed with metallic Fe in an Fe capsule and also from synthetic peridotite in graphite capsules. Their results demonstrate that the relationship between Al^{3+} and Fe^{3+} is independent of oxygen fugacity. Using their measured relationship and taking a lower mantle Al content of 0.105 Al per two-cation formula units, Frost et al. (2004) calculate that perovskite in the lower mantle must have an $\text{Fe}^{3+}/\Sigma\text{Fe}$ ratio of approximately 0.6, which is much larger than the whole-rock $\text{Fe}^{3+}/\Sigma\text{Fe}$ ratio of < 0.03 for the upper mantle. The large difference between these values for the upper mantle and lower mantle cannot be because of a compositional difference between the upper and lower mantle. This would be inconsistent with evidence for whole-mantle convection. Instead, the large $\text{Fe}^{3+}/\Sigma\text{Fe}$ ratio must be a result of Fe^{2+} from upper mantle phases being both oxidized and reduced under lower mantle conditions. Frost et al. (2004) determine that for a bulk silicate Earth composition, aluminous perovskite with a $\text{Fe}^{3+}/\Sigma\text{Fe}$ ratio similar to the upper mantle requires the precipitation of approximately 1 wt% metallic Fe-rich alloy. In the time since Frost et al (2004) introduced the proposed lower mantle disproportionation reaction, several researchers have either acknowledged or directly used the reaction to justify results in their work (Vanpeteghem et al., 2006; Zhang and Oganov, 2006; Smith et al., 2016; Xu et al., 2017; Shim et al., 2017; Kurnosov et al., 2017; Bindi et al., 2020; Piet et al., 2020). However,

SEM/TEM evidence from available lower mantle assemblages reported over the past thirty years does not demonstrate a clear trend in the occurrence of the disproportionation reaction across the range of lower mantle conditions (Irifune, 1994; Lauterbach et al., 2000; Frost et al., 2002; Frost et al., 2004; McCammon et al., 2004; Murakami et al., 2005; Irifune et al., 2010; Sinmyo et al., 2011; Sinmyo et al., 2013; Prescher et al., 2014; Piet et al., 2016; Creasy et al., 2020; Huang et al., 2021; Tsujino et al., 2023).

1.4 Implications of disproportionation

Occurrence of an iron disproportionation reaction has the potential to reveal important constraints on the mantle's modern redox state, as well as the evolution of the oxidation state through time. While we do not have access to the redox state of the lower mantle, the historical upper mantle fugacity (f_{O_2}) is well constrained by concentrations of Cr and V, as well as the V/Sc ratio of the oldest known rocks, which indicate that f_{O_2} has remained at approximately FMQ (i.e. relatively oxidized) over the past 3.5 Gyrs (Li and Lee, 2004). However, during core formation, the silicate portion of the Earth must have been exchanged with Fe-Ni-rich metal, creating a very reducing environment. Therefore, the mantle must have been oxidized by some process during the first billion years of Earth history (Frost and McCammon, 2008). It has been suggested that 'self-oxidation' of the mantle through the disproportionation reaction can help to explain the necessary increase in the mantle oxidation state (Galimov, 2005; Wood et al., 2006). This mechanism of self-oxidation through the disproportionation reaction has been termed the 'oxygen pump,' and its supposed absence in the formation of Mars can also help explain the reduced nature of the Martian mantle (Wood et al., 2006). Recently, Armstrong et al. (2019) also invoked the disproportionation reaction to speculate on the origins of the oxidation state of the mantle, as well as open issues such

as the partitioning of volatile elements into the core and overabundance of siderophile elements in the mantle. Determination of the bounds of the pressure-temperature-composition space in which the disproportionation reaction can occur is thus critically important for developing more complete models of mantle redox evolution, beginning with Earth's accretion and core segregation.

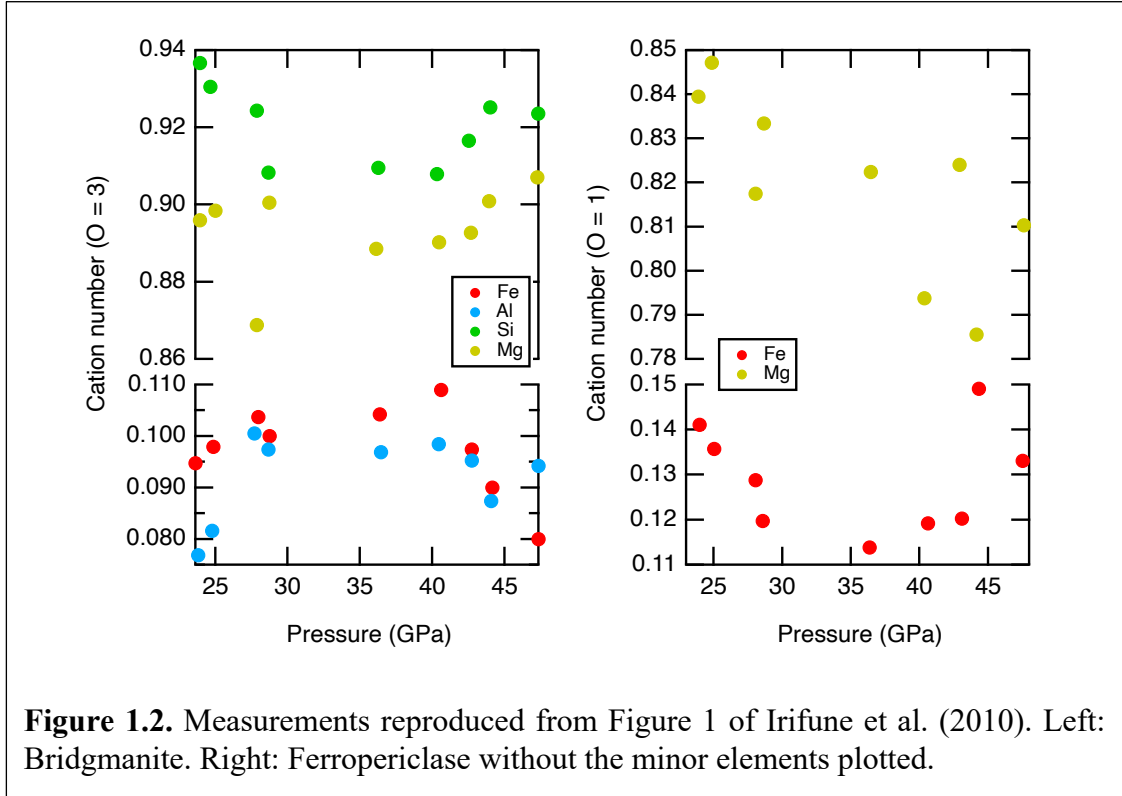
The operation of the disproportionation reaction in the modern mantle and the resultant production of metallic iron has significance beyond its potential role in mantle redox evolution. If metallic iron is present in the modern mantle (and in the historic mantle), it could act as a host for volatile (C, S, H) and siderophile (Ru, Rh, Pd, Os, Ir, Pt, Re, Os) elements. Smith and Kopylova (2014) suggest that metallic Fe should be a major host of mantle N and propose that retention of primordial mantle N in metallic Fe could explain the high N/³⁶Ar and low ¹⁵N/¹⁴N ratios of the mantle compared with the atmosphere. Earth's interior represents the largest reservoir of volatile elements, such as C, H, and S, on the planet. Constraining the conditions for storage and transport of these volatiles in the lower mantle is vital for better understanding whole-Earth volatile distribution and cycling. For example, at typical carbon concentrations of 20-250 ppm for sub-ridge mantle, C could combine with Fe-Ni alloy in the lower mantle and stabilize carbide phases like Fe₃C or Fe₇C₃, or dissolve in the metal phase, depending on the Fe/C ratio and P-T conditions (Rohrbach and Schmidt, 2011). In a C-rich subducted slab with a much greater level of C than ambient mantle, oxidized carbonatite melt could first consume metal to form carbides and then further oxidize the Fe and Ni in the carbide to leave a mantle domain that contains all iron as Fe²⁺ and Fe³⁺ in silicates and ferropicriase and all C as diamond. The boundaries of these C redox zones would be dependent upon the stability field of metallic Fe. At lower mantle conditions, S solubility in Fe is higher than in the upper mantle and transition zone, with more than 1 atomic

percent of S dissolving in solid Fe at 25 GPa near the eutectic temperature, indicating that the entire S budget of the mantle can be dissolved in Fe metal (Li et al., 2001). Studies have shown that H transported to the deep mantle via hydrated subducting slabs can be hosted in various high-pressure hydrous phases (Ohira et al., 2014; Hu, 2016). If metallic Fe is present throughout the lower mantle, it could react with H₂O released from these phases and stabilize Fe-Ni hydrides or other hydrous phases (e.g. FeOOH) (Terasaki et al., 2012; Piet et al., 2020).

It is vital to understand the distribution and behavior of siderophile elements throughout the mantle because of their ability to act as isotopic and geochemical tracers. For example, the Pt group elements (Os, Ir, Ru, Rh, Pt, and Pd) include two long-lived, geologically useful decay systems: ¹⁸⁷Re-¹⁸⁷Os and ¹⁹⁰Pt-¹⁸⁶Os (Day et al., 2016). Further, highly siderophile elements are used to inform on planetary accretion, differentiation, and core-mantle interaction. If metallic Fe is present throughout the lower mantle in present day as well as through Earth's history, the fractionation and distribution of these elements could be a result of not only partial melting but also metal-silicate partitioning.

1.5 Factors that may affect disproportionation

It is very evident that the existence of metallic iron in the lower mantle is closely tied to the bridgmanite phase, specifically the behavior of Fe in the bridgmanite phase. However, prediction of the composition of bridgmanite under lower mantle conditions is made very complex by the potential for Fe to be distributed among different combinations of valence states, crystallographic sites, and spin states. As a starting point, we can consider the composition of pyrolytic bridgmanite and ferropericlase measured by Irifune et al. (2010), reproduced in Figure

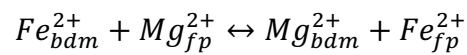


1.2. If we use the results of their electron microprobe analyses between 30 and 40 GPa and assign components based on stoichiometry, the bridgmanite composition is 88.8 mol% MgSiO_3 , 8.6 mol% FeAlO_3 , 2 mol% FeSiO_3 , and 0.6 mol% AlAlO_3 . The ferropericlasite composition is 82 mol% MgO and 12 mol% FeO , with the remainder composed of minor substitutions of Ni, Al, Si, Cr, and Na.

As a transition metal, Fe has partially filled $3d$ electronic orbitals that give rise to a series of possible energy configurations that depend on its atomic environment. Thus, Fe can be in the high-spin (HS) or low-spin (LS) state, and the transition between these states can be affected by pressure, temperature, and composition (Badro, 2014). Spin transitions have been detected in both ferropericlasite and bridgmanite (Figure 1.3). In ferropericlasite, there is a transition from HS to LS between approximately 50 to 90 GPa at mantle temperatures, or 1,100 to 1,900 km (Badro, 2014).

The spin transitions in bridgmanite have been a topic of study, both experimental and theoretical, for decades and are still not completely resolved. It is fairly well established that Fe^{2+} in the A-site undergoes a transition from HS to LS at 120 GPa (Badro, 2014). It is thought that Fe^{3+} in the B-site transitions from HS to LS in the range 30 to 70 GPa (this range is still up for debate), or approximately 1,000 to 1,500 km depth (Catalli et al., 2010). The ionic size of Fe^{3+} becomes smaller with the spin transition, Further, Fe^{3+} in the A-site should always be in the HS state, but it is thought that when the B-site Fe^{3+} transitions to LS at ~ 70 GPa, A-site Fe^{3+} will migrate toward the B-site, and therefore the LS state (Fujino et al., 2012; Zhu et al., 2020). Fujino et al. (2012) thus expect bridgmanite below ~ 50 GPa to have the $^{\text{HS}}\text{Fe}^{3+}\text{AlO}_3$ component, while higher pressure bridgmanites have the $\text{Al}^{\text{LS}}\text{Fe}^{3+}\text{O}_3$ component. Spin transitions in bridgmanite, as well as review of the techniques used to measure them (e.g. Mössbauer spectroscopy) are still being studied and clarified (Dorfman et al., 2020).

Predictions are further complicated when one takes into account the ability for Fe to partition between bridgmanite and ferropericlase in the lower mantle. Partitioning of Fe between ferropericlase and bridgmanite is dependent upon pressure, temperature, spin state, and Al_2O_3 content. The partitioning can be defined by an Fe-Mg exchange reaction:



The resulting apparent exchange constant/coefficient, which describes the total iron (Fe^{2+} and Fe^{3+}) partitioning between the bridgmanite and ferropericlase, can be written as:

$$K_{app} = \frac{X_{bdm}^{Fe} X_{fp}^{Mg}}{X_{bdm}^{Mg} X_{fp}^{Fe}}$$

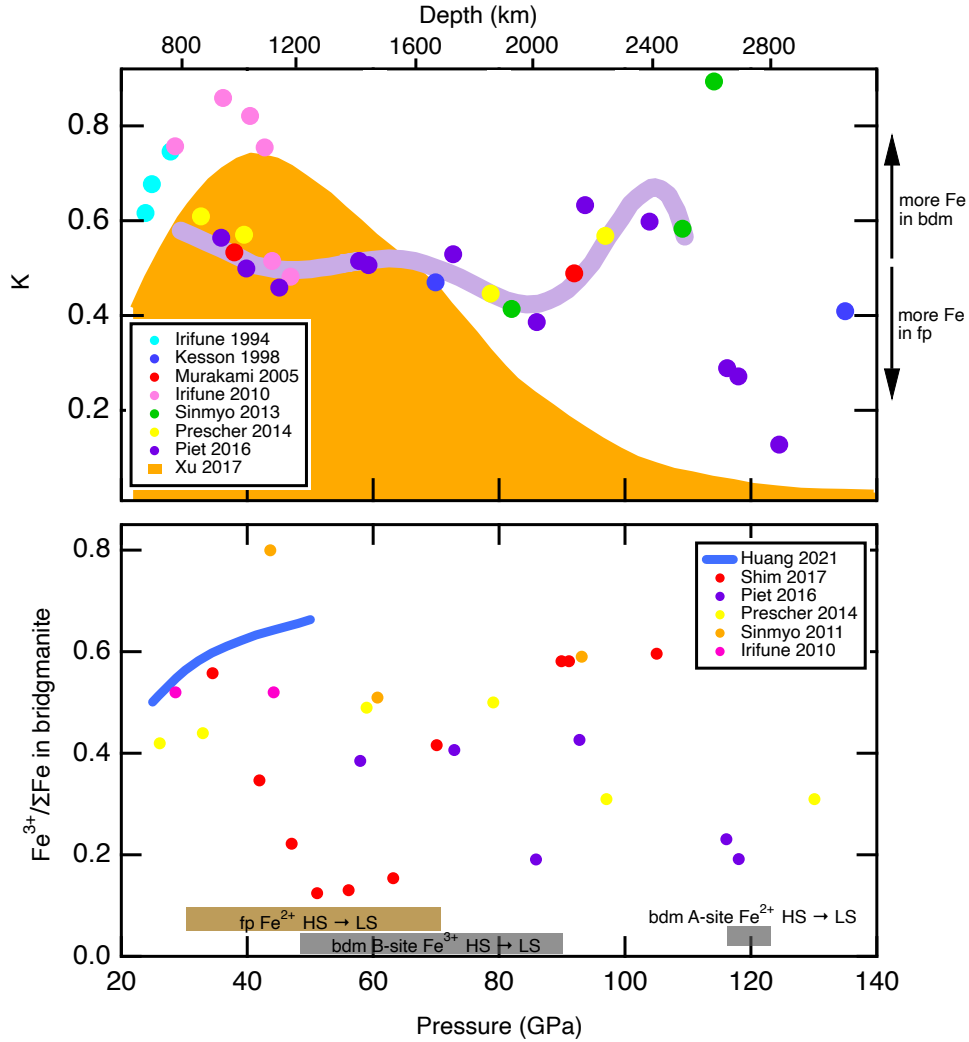


Figure 1.3. Fe^{3+} content and partition coefficient changes across the lower mantle. Top: Partition coefficient predictions from Xu et al. (2017) are based upon calculations. Plotted points are from experimental results from Irifune et al. (1994), Kesson et al. (1998), Murakami et al. (2005), Irifune et al. (2010), Sinmyo & Hirose (2013), Prescher et al. (2014), and Piet et al. (2014). The Piet trendline is a linear least-squares regression. Bottom: Huang et al. (2021) predictions are based on calculations. Plotted points are experimental results from Irifune et al. (2010), Sinmyo et al. (2011), Prescher et al. (2014), Shim et al. (2017) and Piet et al. (2016). Bars along the bottom indicate the general regions of predicted iron spin transitions.

where X_{bdm}^{Fe} represents the mole fraction of Fe in bridmanite. High values of K_{app} indicate Fe-rich silicates, and low values indicate Fe-rich ferroperricline. An important point here is that only Al content seems to control partitioning, not the relative Fe, Mg, Si, or Ca concentrations in the rock

(Piet et al., 2016). In Al-free systems (with Fe as Fe²⁺) containing bridgmanite in equilibrium with ferropericlase, Fe primarily partitions into ferropericlase (Mao et al., 1997; Frost and Langenhorst, 2002; Dorfman et al., 2021). Studies on Al-bearing systems have shown how difficult it is to understand the interdependence of valence state, crystallographic site, spin state, and the resultant partitioning between phases, especially when considering different compositions, pressures, and temperatures.

I will highlight several recent studies here that offer differing predictions for the depth dependence of Fe³⁺ content in bridgmanite and the partition coefficient. First, Piet et al. studied Al-bearing olivine and Ca-free pyrolite and claim that up to pressures of 70 GPa, the partition coefficient remains relatively constant, in agreement with studies on other Al-bearing phases (Fig. 3) (Piet et al., 2016). The decrease in the partition coefficient at 70 GPa is attributed to the onset of the Fe²⁺ spin transition in ferropericlase, where ferropericlase is expected to become Fe-rich and corresponds to a similar drop in Fe³⁺ in bridgmanite, which implies an increase in Fe²⁺ content. Piet et al. (2016) thus predict an Fe-depleted bridgmanite from approximately 70 to 100 GPa (1,500 to 2,200 km) and an Fe-rich bridgmanite at pressures greater than 100 GPa. Notably, no metallic Fe was reported in this study. Shim et al. (2017) studied bridgmanite synthesized from Fe²⁺-rich starting material and Fe metal powder (Shim et al., 2017). They found that the Fe³⁺ content of bridgmanite drops from ~60% around 40 GPa to 13 to 22% at 47 to 63 GPa, differing from the drop seen in Piet et al. (2016) (Fig. 3). This difference is attributed to the different composition studied by Piet et al. (2016), while the decrease seen in both is emphasized. Shim et al. (2017) suggest the decrease of Fe³⁺ in bridgmanite around 50 GPa is due to the energetic favorability of the AlAlO₃ substitution over FeAlO₃ as pressures approach 50 GPa and a potential change in the

spin state of Fe^{2+} in the A site. At pressures above 70 GPa when B-site Fe^{3+} transitions from HS to LS, the $(^{\text{HS}}\text{Fe}^{3+}, \text{Al})\text{-VI} (^{\text{LS}}\text{Fe}^{3+}, \text{Al})$ configuration is stabilized, resulting in an increase in Fe^{3+} content in bridgmanite. Shim et al. (2017) thus expect lower ferric iron bridgmanite (overall depleted in Fe) from 1,100 to 1,700 km depths (50 to 70 GPa), whereas bridgmanite in the regions above and below contain greater than 50% of iron in the ferric state (overall enriched in Fe). Finally, Xu et al. (2017) made partitioning predictions based upon an integrated *ab initio* thermodynamic model. They predict that in a pyrolitic assemblage, the partition coefficient increases from 20 to 40 GPa and then gradually decreases from 40 to 120 GPa. The peak at ~40 GPa is attributed in part to the increasing incorporation of Al into bridgmanite driving HS Fe^{2+} and Fe^{3+} into the A-site of the perovskite, but mostly to the Fe^{2+} spin transition in ferropericlasite. Because of the spin transition, Fe prefers to enter ferropericlasite, and the Fe in lower mantle thus increasingly enters ferropericlasite over bridgmanite. Xu et al. (2017) thus predict that metallic Fe production will also decrease with depth, reducing it to less than 1% of the Fe toward the deeper lower mantle (Fig. 4). The results of Xu et al. (2017) should be treated with some skepticism, however, because of their reliance on an *ab initio* model, not experimental results.

Finally, the above discussion considers only the effects of Fe and Al substitution into bridgmanite, but Ko et al. (2022) suggest that Ca can also enter the bridgmanite structure to such an extent that davemaoite may disappear at certain points in the lower mantle. They suggest that the changes in substitution mechanisms and spin states of Fe in bridgmanite may be related to the Ca solubility increase in bridgmanite, but further investigation is required to understand this relationship.

A final consideration to take into account when exploring the disproportionation reaction across the range of the lower mantle is the fact that bridgmanite undergoes a phase transition in the deepest part of the lower mantle. At the base of the lower mantle, bridgmanite is expected to transform to the post-perovskite phase (Murakami et al., 2004). The pressure at which the transition occurs could be around 120 GPa but has been found to be dependent upon the Fe and Al content of the bridgmanite, with increasing Fe and Al content requiring a higher pressure to achieve the transition to post-perovskite (Shieh et al., 2011; Dorfman et al., 2012). Zhang and Oganov (2006) predicted that despite Al-Al and Fe^{3+} - Fe^{3+} substitutions becoming more favorable in post-perovskite, the disproportionation reaction can still occur in the lowermost mantle. However, experimental studies have shown that post-perovskite coexisting with ferropericlase at lowermost mantle pressures is Fe-poor and reportedly not coexistent with metallic Fe (Murakami et al., 2005; Sinmyo et al., 2006, 2011).

1.6 Scope of this thesis

Given the demonstrated significance of a metallic iron phase in the lower mantle and the conspicuous lack of consistent evidence for this phase, I will use this thesis to explore the occurrence of the disproportionation reaction across the range of lower mantle pressures and temperatures. To accomplish this goal, I have combined both experimental and theoretical approaches. Experiments are centered on FIB recovery and SEM, TEM and STEM analyses of samples prepared in a laser-heated diamond anvil cell (LHDAC). These results have been supplemented with X-ray diffraction (XRD) measurements. Theoretical work is centered on the use of the Gibbs energy minimization software PerpleX (Connolly, 2009).

In Chapter 2, I describe the experimental techniques that I explored and utilized for the creation of lower mantle phase assemblages and the detection of disproportionated metallic Fe.

In Chapter 3, I describe modifications I made to the thermodynamic database of Stixrude & Lithgow-Bertelloni (2022), which contains thermodynamic parameters for the calculation of various lower mantle phase equations of state. I use the modified database to model high pressure and temperature phase equilibria with the PerpleX Gibbs energy minimization software (Connolly, 2009). I find that the disproportionation reaction can be successfully modeled with the updated database, and I identify several results from the literature where the disproportionation reaction was incorrectly overlooked.

In Chapter 4, I explore the occurrence of the iron disproportionation reaction from 25 to 65 GPa in a natural almandine-pyrope-grossular garnet with *in-situ* XRD in the LHDAC and with *ex-situ* scanning electron microscopy techniques. Upon heating the natural almandine-pyrope-grossular garnet up to 3000 K up to 65 GPa, the formation of a phase assemblage consisting of bridgmanite, stishovite, and davemaoite was confirmed by XRD, but because of the low abundance of Fe metal and small grain size, XRD was determined not to be effective to detect the disproportionation reaction. Examination of the samples recovered between 39-64 GPa by scanning electron microscopy analysis revealed the presence of nm-scale disproportionated iron metal grains as an additional product of this reaction that was not detectable in the XRD patterns. Volume compression data of bridgmanite synthesized in the experiments were fit to the Birch-Murnaghan equation of state and compared to similar compositions. Bridgmanite was found to decompress to the LiNbO_3 -type structure, indicating a high FeAlO_3 content, in accordance with the occurrence of a disproportionation reaction. Finally, we use the PerpleX software with

modified input files to theoretically predict the occurrence of iron disproportionation in our experimental composition as well as a pure almandine composition.

In Chapter 5, I explore the occurrence of the iron disproportionation reaction from 26 to 132 GPa in a pyrolite glass with *in-situ* XRD in the LHDAC along the geotherm and with *ex-situ* SEM, TEM, and STEM techniques. The XRD experiments confirmed the transformation of the pyrolite glass to the lower mantle phase assemblage of bridgmanite, ferropericlase, and davemaoite, though davemaoite could not be conclusively identified in all patterns. Lattice parameters and volumes were determined for the lower mantle bridgmanite phase and compared against similar bridgmanite compositions. Several samples recovered from 39 to 132 GPa were examined with SEM, TEM, and STEM techniques, and all were found to contain disproportionated metallic Fe. We use image analysis on the TEM images to estimate the volume fraction of disproportionated metallic Fe produced across lower mantle conditions, and we find a trend of decreasing disproportionated metallic Fe with increasing pressure from the top to the base of the lower mantle. Finally, we use the PerpleX software with modified input files to theoretically predict the occurrence of iron disproportionation across the lower mantle and find that the predicted trend matches well with our experimental results. We explore the implications of a decreasing volume of disproportionated metallic Fe on the distribution of C in the lower mantle.

2 EXPERIMENTAL TECHNIQUES

Experimentally investigating the occurrence of the iron disproportionation reaction across lower mantle pressure and temperature conditions requires a suite of techniques. We describe the methods that yielded the best results below, which include scanning electron microscopy (SEM), transmission electron microscopy (TEM), and scanning transmission electron microscopy (STEM) analyses in addition to X-ray diffraction (XRD).

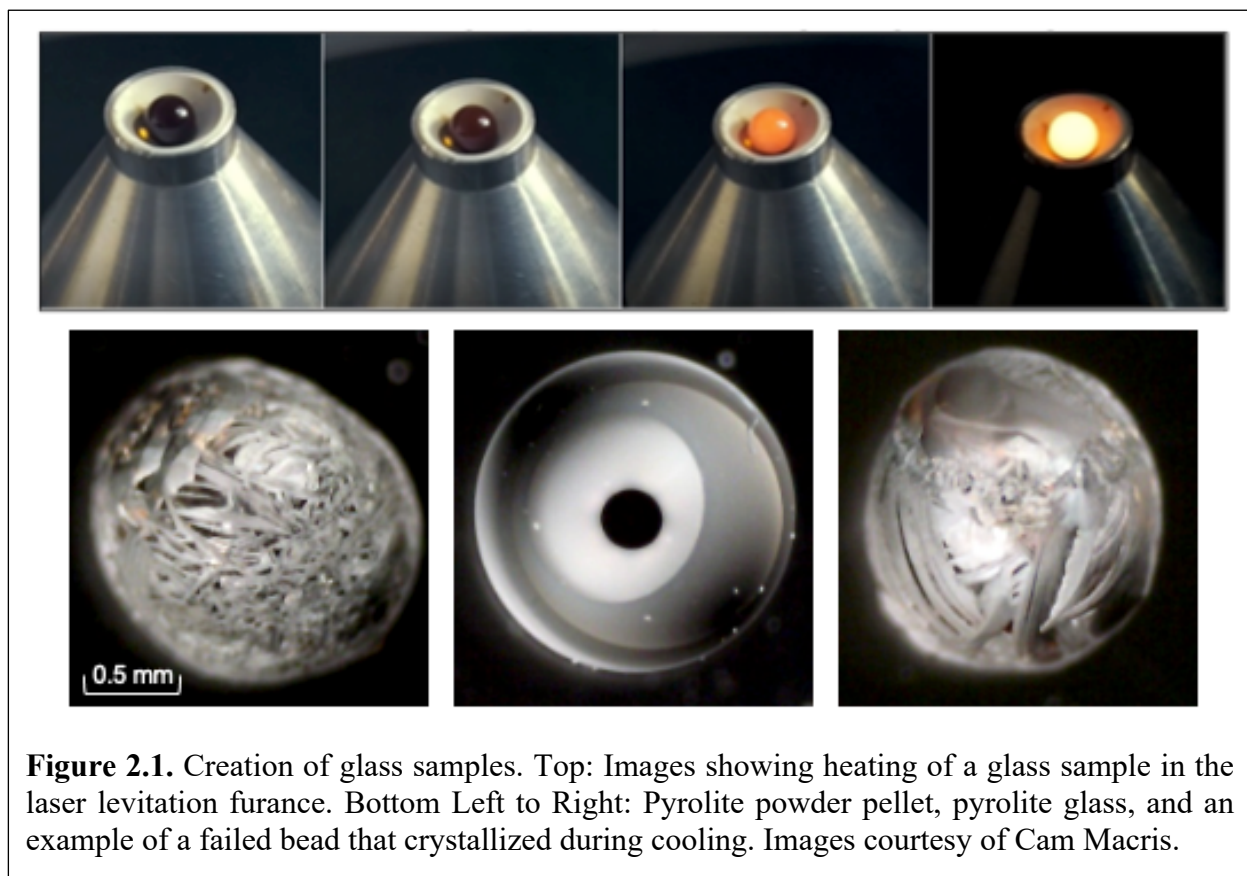
2.1 Sample preparation

Because the iron disproportionation reaction in the lower mantle is understood to be driven by the incorporation of the $\text{Fe}^{3+}\text{AlO}_3$ component into bridgmanite, it is essential to study materials that contain both Fe and Al and to ensure that these starting materials have Fe primarily in its ferrous (Fe^{2+}) state. As an initial demonstration of iron disproportionation, we first selected a natural garnet with a majority almandine-pyrope-grossular composition for study. Almandine has the composition $\text{Fe}_3\text{Al}_2\text{Si}_3\text{O}_{12}$, pyrope has the composition $\text{Mg}_3\text{Al}_2\text{Si}_3\text{O}_{12}$, and grossular has the composition $\text{Ca}_3\text{Al}_2\text{Si}_3\text{O}_{12}$. The specific composition of the natural garnet was determined by wavelength-dispersive X-ray spectroscopy (WDS) at the University of Maryland to be $\text{Alm}_{52}\text{Pyr}_{34}\text{Grs}_{11}\text{Sps}_2\text{And}_1$. This composition was selected because of its high Fe and Al content, which should promote the iron disproportionation reaction. The $\text{Fe}^{3+}/\Sigma\text{Fe}$ ratio of the starting material was determined to be 0.016 based on stoichiometry of the WDS analyses.

For the pyrolite study, high-purity oxide powders of MgO , SiO_2 , Al_2O_3 , and CaSiO_3 were dehydrated in a furnace at 1000 °C for 24 hrs. FeO powder was not dehydrated in the furnace because we did not wish to oxidize the iron. The dehydrated powders and FeO were individually ground in an agate mortar and pestle and then mixed together to produce a pyrolite composition

following the major element proportions of Ringwood (1975). Ethanol was not used during the mortar and pestling process because we have suspicions that it may introduce organics into the mixture when it evaporates during the mixing process, as discussed below.

A pyrolite glass was created for these studies because we determined that using a pyrolite powder would not be sufficient for the study of subsolidus phase equilibria, as discussed below. A portion of the pyrolite powder mixture was pressed into a pellet and fused at 2000 °C for 10 s in an aerodynamic levitation laser furnace at Indiana University – Purdue University Indianapolis using Ar carrier gas. In an aerodynamic levitation furnace, the powdered pellet is floated in a vertical gas stream as a CO₂ laser heats the sample (Figure 2.1). Gas mixing allows for control of the atmosphere in the chamber, loosely managing the oxygen fugacity of the sample. Ar gas was



applied in the synthesis of the bead used in this study to keep Fe in its ferrous state, but several other beads were also synthesized using O₂ glass. Levitating the pellet allows for containerless melting at high temperatures, which avoids problems related to the chemical interaction between the sample and container walls (Pack et al., 2010). Because the sample has no contact with any surroundings in the laser levitation furnace, there are no heterogeneous nucleation sites, so the apparatus can be used for the preparation of glasses from substances that otherwise crystallize during cooling. Additionally, the laser levitation furnace is able to achieve very high cooling rates which allows for the vitrification of fragile melts such as pyrolite.

To confirm the oxidation state of Fe in the glass bead, Mössbauer spectroscopy was performed in the offline laboratory of Sector 3 at the Advanced Photon Source (APS), Argonne National Laboratory on a chip of the starting glass material (Figure 2.2). Because the sample was not enriched in Fe⁵⁷ and the thickness is not uniform, the measurement is noisy, but we are able to conclude that the Fe³⁺/ΣFe content is <10% (with an estimate of ~7.3%). The same glass chip was

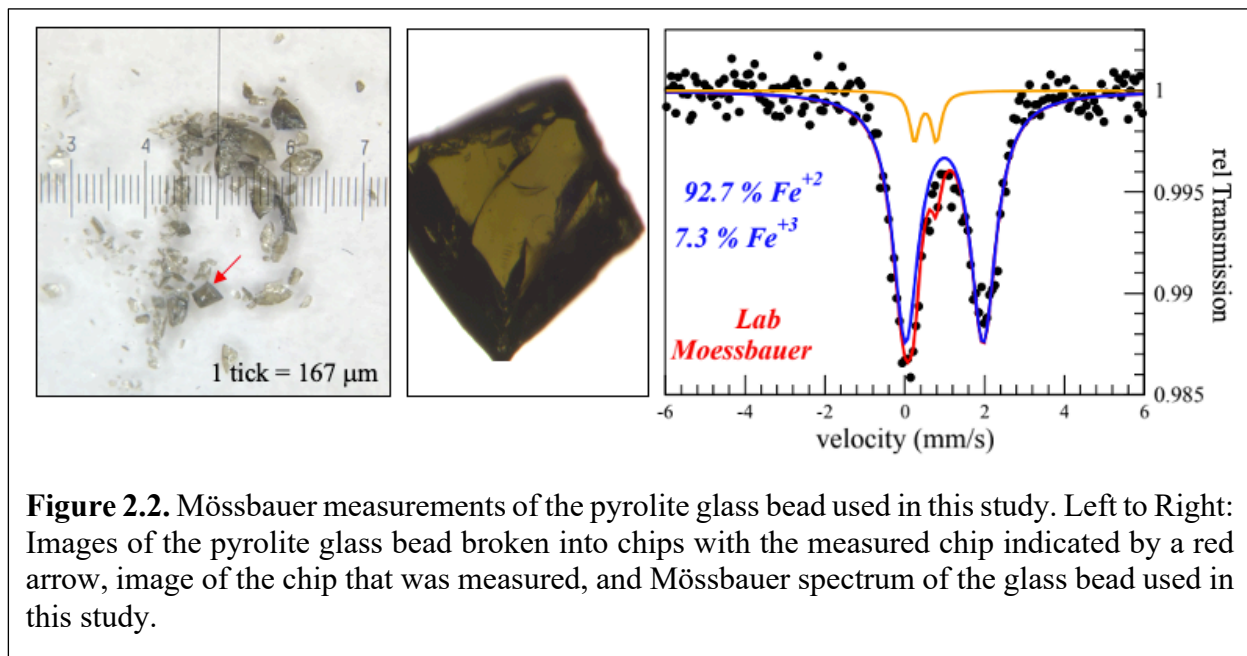


Figure 2.2. Mössbauer measurements of the pyrolite glass bead used in this study. Left to Right: Images of the pyrolite glass bead broken into chips with the measured chip indicated by a red arrow, image of the chip that was measured, and Mössbauer spectrum of the glass bead used in this study.

also measured using synchrotron Mössbauer spectroscopy at Sector 3, along with a bead produced under O₂ gas. These results are discussed in Figures A.1-A.2.

As noted above, we found that use of ethanol during sample preparation may introduce contaminants into the sample material, as evidenced by several recovery experiments we performed in which we observed large regions of C adjacent to Fe metal (Figure A.3). We found that similar observations have been made anecdotally by researchers on the Mineralogical Society of America listserv, where people have shared that some organics are difficult to remove from a sample once added; one researcher found that acetone persisted on powders that were oven-dried. Blanchard et al. (2022) note that C is a prominent contaminant in the laboratory due to the use of ethanol and acetone, as well as ambient contamination. Despite heating at temperatures up to 1400 °C, their glass samples that were created using powders mixed in acetone yielded experimental results containing ¹²C even though they created the samples using only ¹³C. Thus, we avoid use of ethanol in all sample preparation as a precaution against C contamination. Despite these precautions, several recovered samples were still found to have C contamination (Figure A.4), and these were not used in any analyses or presented in this work.

Several initial experiments were performed using the pyrolite powder mixture. These experiments revealed the limitations of using powdered samples for studies of phase equilibria at subsolidus conditions. The recovered samples demonstrated that the powder grain size was too large (several grains larger than 2-3 μm) to produce equilibrium reactions (Figure A.5). Similar grain sizes and lack of equilibrium is seen in the powder pyrolite results of Sinmyo et al. (2013), though the authors do not address this. Additionally, while efforts were made to thoroughly mix the sample, slight variations in oxide grain distribution are inevitable. Because of this, laser heating

of these samples was challenging due to the uneven absorption of the laser beam by the FeO grains and absorption by the FeO grains located adjacent to the diamond culets, which acted as a heat sink, requiring continued increases in laser power to maintain the desired temperature. Several initial experiments were also performed on a natural peridotite that was powdered in an agate mortar and pestle in addition to being ball-milled. These experiments also emphasized the limitations of using powdered samples, as the recovered samples have some grains of starting material that are larger than 5 μm (Figure A.6). Finally, several initial experiments were performed using natural basaltic glass, but these could not be successfully laser-heated and are not discussed further. Ono et al. (2005) had a similar experience with basaltic glass, noting unstable heating temperatures that fluctuated by several hundred degrees Celsius despite constant laser power.

2.2 Pressure Generation

To achieve the high pressure conditions of the lower mantle, we use symmetric diamond anvil cells (DACs). Symmetric diamond anvil cells with 100, 150, 250 or 300 μm diameter culets were used to achieve pressures up to 135 GPa. For all experiments presented in this work, the sample material was broken into small fragments for loading into the DAC. Garnet samples were loaded either with an Ir foil to act as an internal pressure calibrant and laser absorber or with no foil, while pyrolite glass samples were loaded with Ar gas or with no pressure medium. The Ar was loaded cryogenically in the Laboratory for Mineral Physics at the University of Chicago. Pyrolite samples were generally loaded with no pressure medium because this made them better suited for the FIB recovery process described below. Non-hydrostatic strain in the sample is expected to be eliminated during recrystallization at the high temperatures achieved during laser heating. Lee et al. (2004) documented that in their pyrolitic experiments performed with and

without an Ar pressure medium, there was no correlation between the presence or absence of the Ar medium and the observed scatter in measured volumes of phases present (Figure 2 of that paper). Similarly, Ono et al. (2005) found no obvious differences in phase relations and cell parameters between pyrolitic experiments with and without a pressure medium. Samples were loaded in 35-100 μm diameter holes drilled through pre-indented Re, W, or Ni gaskets. Ni gaskets were pre-indented to 18-20 GPa, while Re and W gaskets were pre-indented to 28-30 GPa. Re and W gaskets were used for synchrotron X-ray diffraction (XRD) experiments. Ni gaskets were used for lab experiments below 50 GPa, while W gaskets were used for lab experiments above 50 GPa to maintain sample thickness at higher pressures. Generally, sample chambers were 35 μm in diameter for samples that were intended for FIB recovery, as we found that this made identification of the laser-heated spot easier (discussed more below). The samples were dried at 100 °C for 30-60 minutes after loading but prior to closing the cell to remove any moisture from the sample.

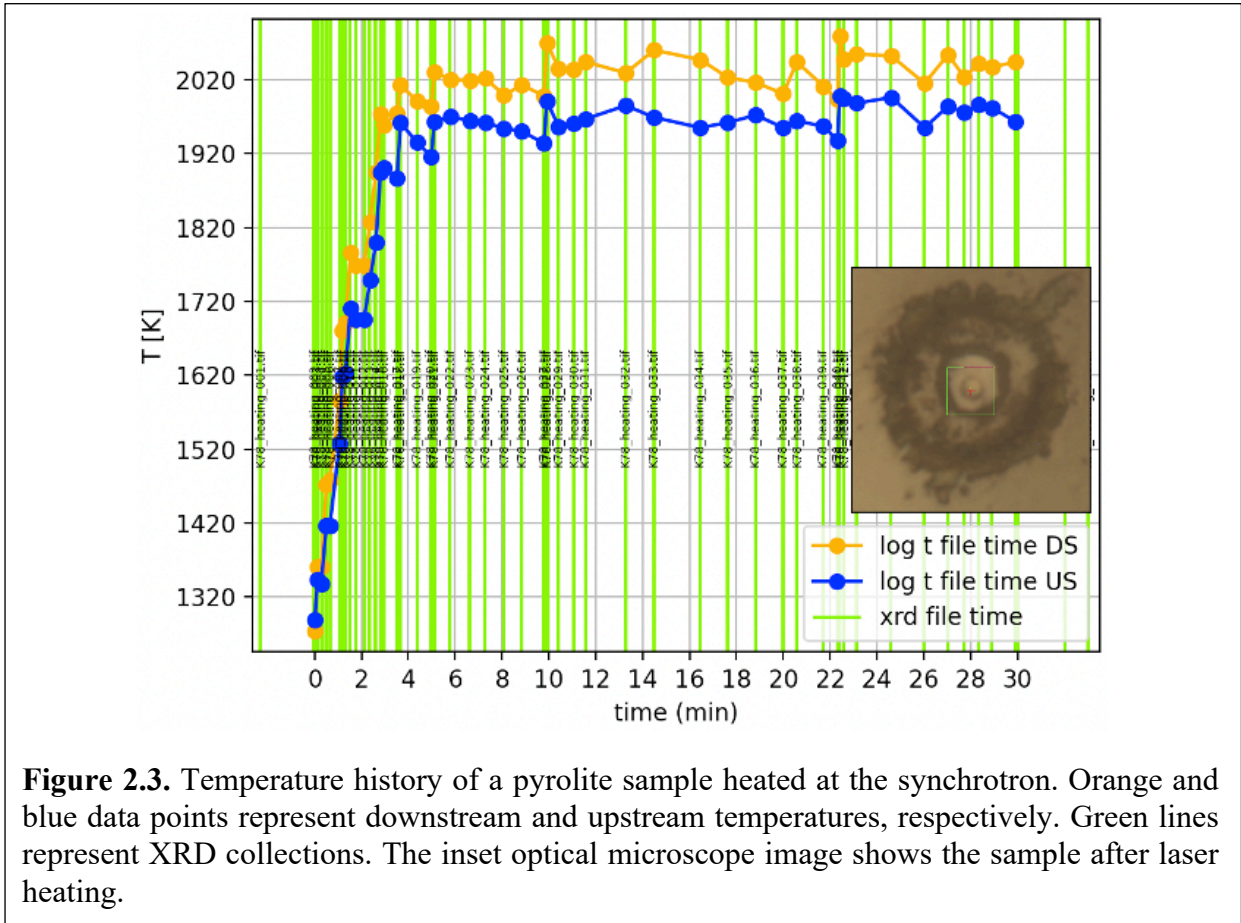
Pressures in synchrotron XRD experiments were determined using the Ir equation of state (Cerenius & Dubrovinsky, 2000), the Ar equation of state (Ross et al., 1986), or Raman spectroscopy on the diamond anvil culets before and after laser-heating (Akahama & Kawamura, 2004). Pressures in lab experiments were determined only using Raman spectroscopy on the diamond anvil culets. Pressure uncertainties for Raman measurements are determined based upon the minimum and maximum possible values chosen for the inflection point of the diamond Raman peak. Upon compression and prior to laser-heating, each sample was visually inspected using an optical microscope to ensure that no contaminants had entered the sample material. As both the natural garnet and pyrolite glass become optically transparent upon compression above \sim 5-10 GPa,

any amount of contaminant became very noticeable, and samples would be re-loaded if contaminants were observed. Figure A.7 shows examples of compressed samples.

2.3 Laser Heating

Single- and double-sided laser heating of the high pressure samples was carried out either at the GSECARS beamline 13-ID-D (APS, Argonne National Laboratory) (Prakapenka et al., 2008) or in the Laboratory for Mineral Physics at the University of Chicago (Campbell, 2008). The synchrotron laser is a 1064 nm fiber laser shaped to a ~ 10 μm radius flat top, and temperatures were measured on both sides of the sample using spectroradiometry and fitting to a gray body approximation (Heinz & Jeanloz, 1987). The lab laser is a 1064 nm fiber laser focused to a ~ 20 μm diameter, and temperatures were measured on both sides of the sample by multispectral imaging radiometry (Campbell, 2008). Initial experiments were performed using double-sided laser heating, but we found that because of the optically transparent nature of the samples, single-sided laser heating yielded the same results and avoided any complications associated with alignment of the laser beams required for double-sided heating. For pyrolite glass experiments, the thickness of the sample and size of the laser-heated spot clearly decreases with increasing pressure, from a spot diameter of ~ 11 μm at 27 GPa to a diameter of ~ 3.5 μm at 132 GPa. The shrinking spot size is due to the decreased thickness of the samples at higher pressures, which allows the heat to diffuse into the diamond culets more efficiently.

During each laser heating experiment, temperature was gradually increased to the desired subsolidus target temperature. The transition to bridgmanite in Fe-rich silicates is accompanied by a color change from transparent to dark brown (Kesson et al., 1995; O'Neill & Jeanloz, 1994). In the garnet samples, the transformation from garnet to a bridgmanite assemblage was accompanied



by a sudden increase in laser coupling, observed as a flash accompanied by a sudden spike in temperature. Similar heating experiences are detailed in Dorfman et al. (2012). Laser power was adjusted during these intervals to attempt to maintain stable temperatures. The pyrolite glass samples loaded without a pressure coupled well with the laser, and steady heating was achieved with only minor adjustments to laser power (Figure 2.3). We found that the pyrolite glass samples loaded with Ar underwent very sluggish phase transformations. We attribute this to the fact that thin chips of glass were loaded in experiments with the Ar pressure medium to ensure that the sample did not fracture when the cell was closed, and we suggest that the thinness of the samples contributed to the difficulties with heating. Ono et al. (2005) also found that pyrolitic glass loaded

in a pressure transmitting medium was difficult to heat due to lack of laser absorbance by the sample. Samples were held at the maximum temperature for anywhere in the range of 2 minutes to 1 hour. All garnet samples were quenched from high temperatures, with the exception of one sample (K11), which was slowly cooled. All pyrolite glass samples were quenched directly from high temperatures.

2.4 X-ray Diffraction

X-ray diffraction was used in this work to detect the phase assemblages created at high pressure and temperature conditions. Two types of XRD were used in this work. First, several samples were studied during and after laser heating with synchrotron XRD at the GSECARS beamline 13-ID-D (APS, Argonne National Laboratory) (Figure 2.3). Diffraction patterns were collected using a CdTe 1M Pilatus detector. The position and orientation of the detector were calibrated using a LaB₆ NIST standard. The X-ray energy was tuned to either 37 keV (corresponding to a wavelength of 0.3344 Å) or 42 keV (0.2952 Å) and focused to full width, half max dimensions of 2 μm x 3 μm. 1064 nm fiber lasers were shaped to ~10 μm radius flat tops and aligned with the X-ray beam using the X-ray induced fluorescence of the sample.

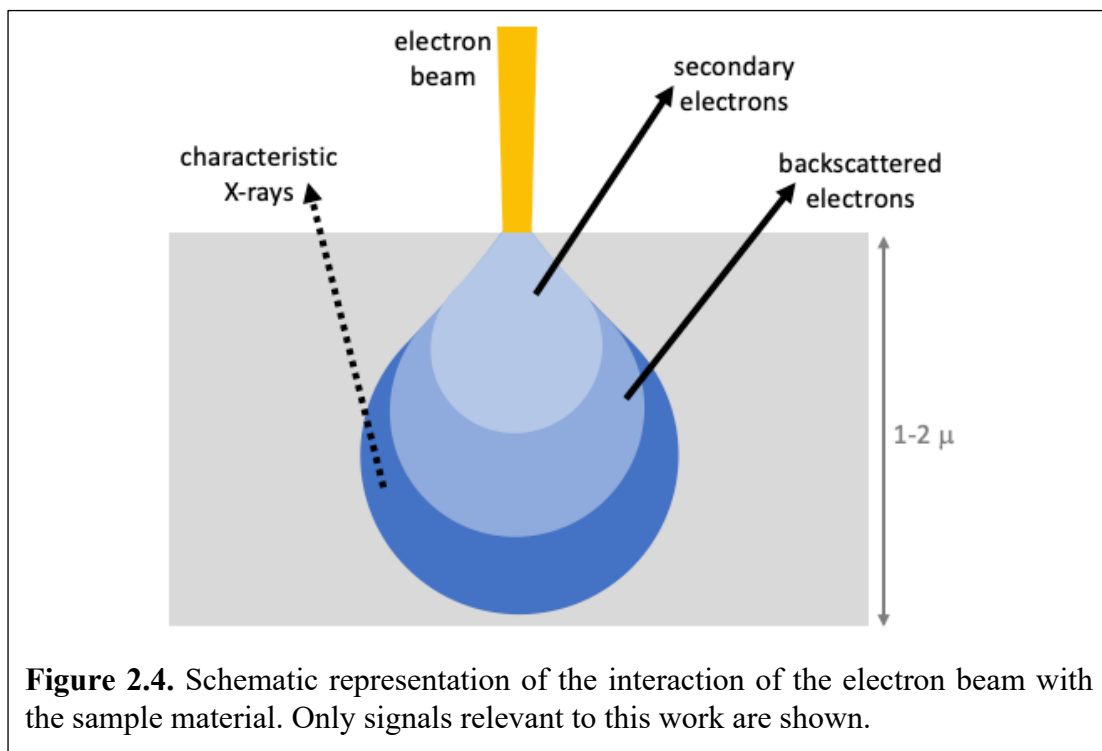
Second, several recovered samples were studied using micro-XRD (mXRD) at beamline 34-ID-E (APS, Argonne National Laboratory). Diffraction patterns were collected using an amorphous silicon Perkin Elmer detector. The position and orientation of the detector were calibrated using a CeO₂ standard. The X-ray energy was tuned to 22 keV (0.5636 Å) and focused to full width, half max dimensions of 250 nm x 250 nm. We utilized mXRD in an attempt to measure the disproportionated metallic Fe grains in recovered samples, expecting that the small beam size would decrease the bridgmanite to metallic Fe signal, but we found that the tails of the

X-ray beam interacted too strongly with the Cu TEM (transmission electron microscope) grid that the samples were mounted on, which blocked large portions of the mXRD pattern. Several mXRD patterns are used in this study, but the majority yielded minimal results.

For all XRD measurements, diffraction images were integrated to produce 1-D diffraction patterns using the Dioptas software (Prescher & Prakapenka, 2015). Diffraction patterns were collected before, during, and after laser heating at high pressures. Samples were also decompressed to 0 GPa for collection of ambient pressure diffraction patterns.

2.5 Sample Recovery

Several garnet and pyrolite samples were recovered from high pressure and temperature conditions for *ex-situ* analysis of the phase assemblage formed inside the laser-heated spot. Samples were decompressed from high pressures over ~30 minutes, and the gasket (containing the



sample) was removed from the DAC and placed on carbon tape on an aluminum SEM pin stub (Figure A.8). Samples were coated with a thin (<10 nm) layer of gold or carbon to provide a conductive surface for imaging with an electron beam. We used the Tescan Lyra3 field-emission scanning electron microscope (SEM) with a focused ion beam (FIB) in the Department of the Geophysical Sciences at the University of Chicago to cut into the samples and prepare thin sections for further analysis. The SEM/FIB is equipped with an Oxford OmniProbe-400 micromanipulator and an Oxford OmniGIS gas-injection system, set up for carbon or platinum deposition. With the SEM/FIB, we are able to capture images with secondary electrons and backscattered electrons generated by the electron beam (we refer to these as SE and BSE images, respectively), as well as secondary electrons generated by the focused ion beam (we refer to these as FIB images) (Figure 2.4). Imaging using secondary electrons yields information about the surface topography of a sample, as secondary electrons have low energies on the order of 50 eV and thus short mean free paths, so only the secondary electrons near the surface of the sample escape. Imaging using backscattered electrons yields information about distribution of elements in a sample, as backscattered electrons have higher energies due to elastic scattering and can emerge from deeper locations within the sample. The backscattered electron intensity is strongly related to the atomic number of the material, and thus heavier elements appear brightest in BSE images. We are also able to mill into the sample and deposit Pt with the FIB.

Because samples were heated at subsolidus conditions, the laser-heated spot was generally not apparent on the surface of the sample in the SE image prior to cutting (Figure 2.5). By using a combination of the post-heating optical microscope image and the SE/FIB images for a sample, we were able to generally identify the location of the laser-heated spot prior to cutting. A layer of

Pt was deposited across the center of the laser-heated spot to protect the top surface of the sample during subsequent milling. Often the exact center of the laser-heated spot was not exactly identifiable, and Pt could not be deposited until the sample was thinned. A 30 kV Ga⁺ beam operating at 1-5 nA was used to mill away material from either side of the center of the laser-heated spot until a section ~2 μm thick remained. The combination of gasket material and/or high

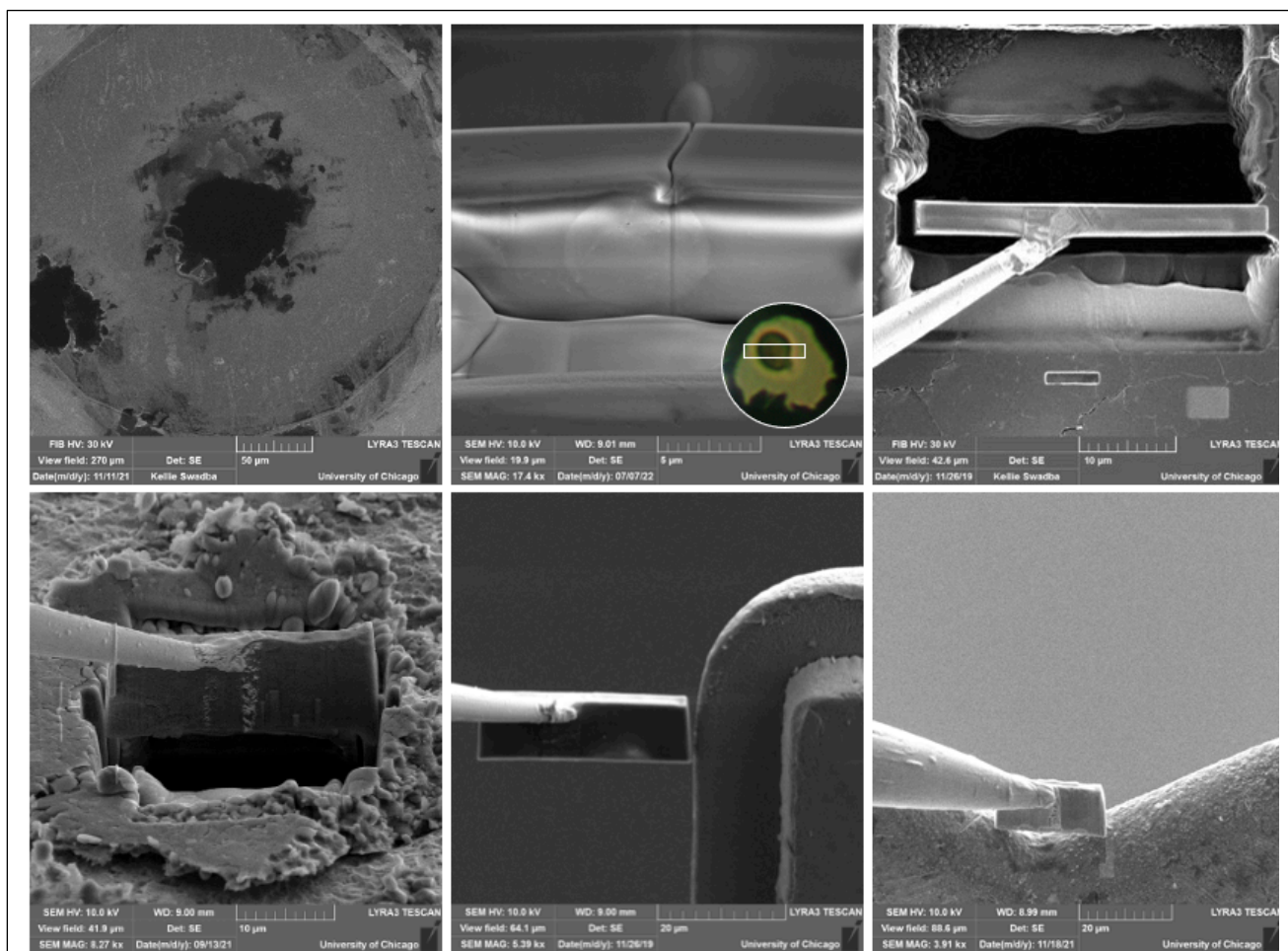


Figure 2.5. Demonstration of the sample recovery process. Top Left to Bottom Right: FIB image of the sample, SE image of a portion of the laser-heated spot during trenching (the inset shows the location of the thinned section in the optical microscope image), FIB image of the needle attached to the thinned section, SE image of the thinned section being pulled out of the gasket, SE image of the thin section being attached to the TEM grid post, and SE image of the thin section being attached to the TEM grid v-shaped location.

pressures generally made the samples $<10\ \mu\text{m}$ thick along the axis of compression. As a result, we were able to cut through the entire thickness of the sample during trenching. To lift the section out of the gasket, we cut one end of the section free from the rest of the sample and then attached the OmniProbe needle to the top of the section with a strip of Pt. To capture the entire laser-heated spot, we generally pulled sections that were $\sim 15\ \mu\text{m}$ across (though the size of the laser-heated spot decreased with increasing pressure). We then cut the other end of the section free and lifted the needle and sample out of the gasket and attached it to either a post or in the v-shaped location of a copper TEM grid using Pt. We found that attaching samples to the post of the TEM grid did not provide enough support during further thinning for TEM samples, so samples were attached in the v-shaped location whenever possible (Figure A.9). Once attached to the TEM grid, Sections were further thinned to $\sim 1\ \mu\text{m}$ and polished using lower operating currents (50-500 pA). It should be noted that certain phases become amorphous under a strong electron beam. It is well established in the literature that bridgmanite becomes amorphous under a strong electron beam (Nzogang et al., 2018), so we expect the milling process and subsequent SEM, TEM, and STEM analyses to amorphize the bridgmanite in the samples. Additionally, use of the Ga^+ ion beam to mill the sample can leave behind some Ga on the sample. Samples were “cleaned” at a voltage of 5 kV and current of 29 pA to remove Ga deposits, but some samples were found to still have some regions of Ga deposition (Figure A.10).

2.6 SEM Analyses

For all recovered samples at this point, BSE images were collected at acceleration voltages of 5-10 kV. For most recovered samples, chemical analyses were also obtained with the same range of acceleration voltages using energy dispersive X-ray spectroscopy (EDS) on the same

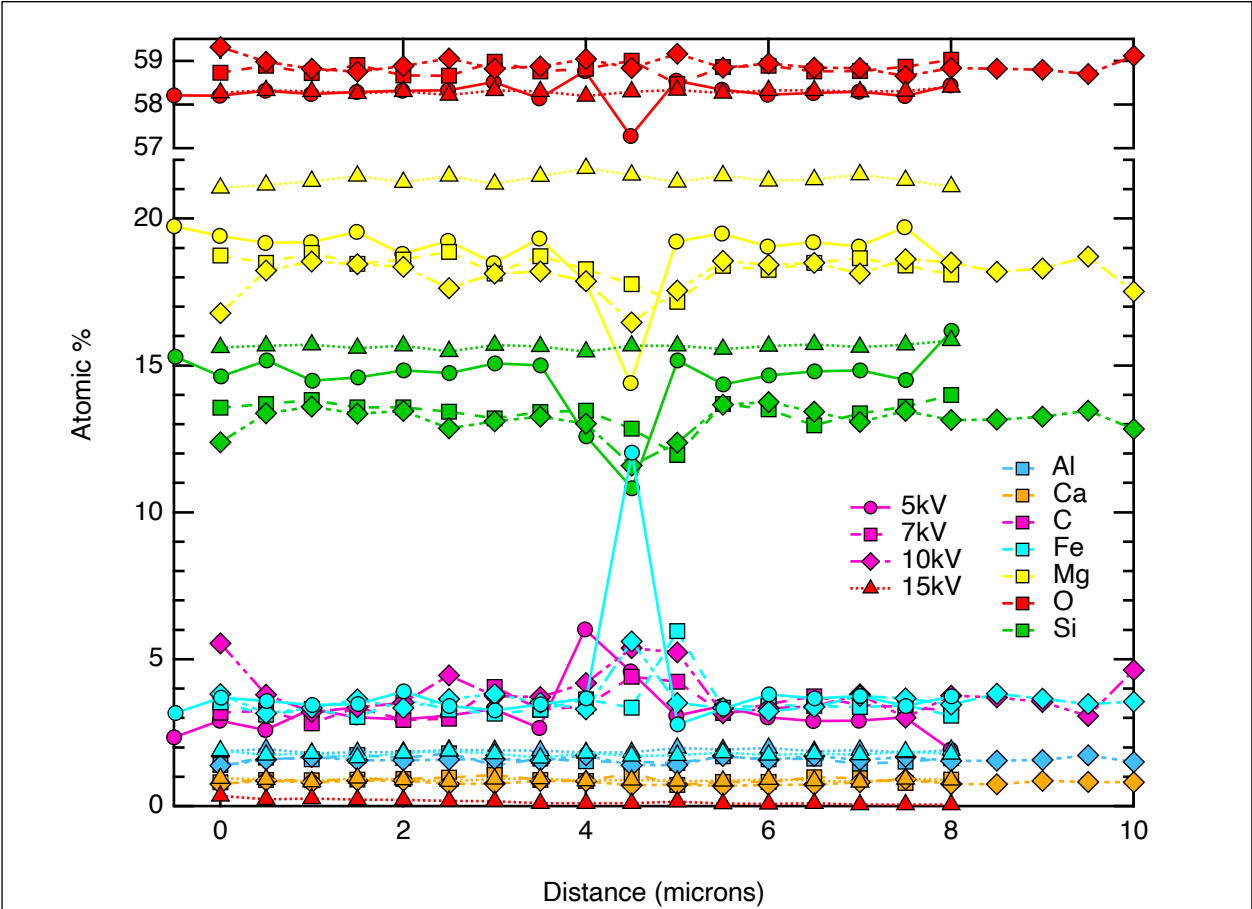


Figure 2.6. EDS measurements on sample K59 (corresponding to Figure 5.5). Measurements collected with different accelerating voltages generally give similar results. Measurements collected at 5 kV could not detect Al or Ca.

Tescan instrument, and compositions were obtained using Oxford Instruments Aztec software. Spatial resolution of the measurements was $\sim 1 \mu\text{m}$. Spatial resolution depends on the sample material and the size of the electron beam spot as well as the beam intensity and energy. The calculated electron beam spot size is $<10 \text{ nm}$, but in practice the resolution is controlled by the interaction volume (Figure 2.4). Lower beam energies yield higher resolution but are less capable of picking out heavier elements, so there is a tradeoff between resolution and which elements are capable of being measured. We were able to perform EDS measurements using beam energies

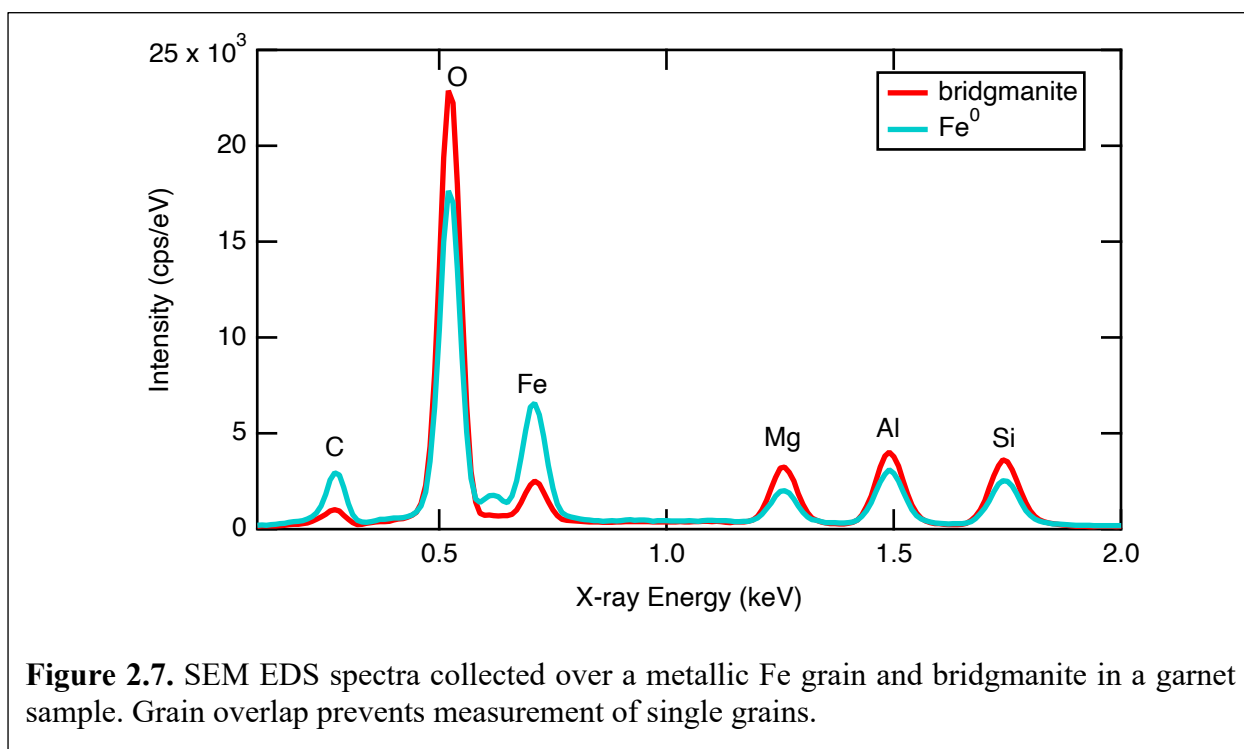


Figure 2.7. SEM EDS spectra collected over a metallic Fe grain and bridgmanite in a garnet sample. Grain overlap prevents measurement of single grains.

ranging from 5-15 kV and found that generally measurements performed at 7 kV or 10 kV yielded the best resolution while being capable of reliably detecting all of the relevant elements (Figure 2.6). In both the garnet and pyrolite glass studies, the grains in the high pressure phase assemblages were generally too small to be measured with SEM EDS without substantial overlap from surrounding grains (Figure 2.7).

2.7 TEM Analyses

Several pyrolite glass samples were further thinned after SEM BSE imaging and EDS analysis for TEM and STEM imaging and analysis. A TEM has a much higher accelerating voltage than an SEM, which corresponds to smaller electron wavelengths and improved resolution. Samples must be extremely thin (<100 nm) for electrons to pass through to the camera and detectors at the base of the TEM column. To ensure that appropriate thicknesses were achieved,

we used the bright field (BF) and dark field (DF) TEM detectors available in the Tescan SEM at the University of Chicago. Samples were thinned until grains could be observed in BF or DF mode at 10 kV (Figure A.11). Due to variations in the sample material and deposition of the Pt layer on the top of the section, samples were sometimes unevenly thinned (Figure A.12), so regions of uniform thickness were specifically identified for imaging and analysis.

We used the JEOL JEM-3010 TEM at the University of Illinois at Chicago, which has a LaB₆ electron source with a 300 kV electron beam. Images were collected with a Gatan Orius SC200 CCD camera using Digital Micrograph software. The electron beam is passed through a column that contains a series of electromagnetic lenses and apertures to focus the beam on the sample, minimize distortions, and magnify the resulting image onto the viewing screen or detectors. In a bright field TEM image, the unscattered (transmitted) electron beam is selected with an aperture and the scattered electrons are blocked. Thus, the areas of the sample that can absorb or scatter electrons (i.e. have high electron density) will appear darker, and the areas that transmit electrons (i.e. have low electron density) will appear brighter. Smaller apertures increase the contrast in bright field images. The TEM images are collected in two modes – one set using no objective aperture (for atomic resolution imaging) and one set using a 60 μm objective aperture (for enhanced phase contrast imaging). In this work, we use the TEM images of the pyrolite samples to estimate the fraction of metallic Fe present in the high pressure and temperature phase assemblages, relying on high quality images to identify the metallic Fe grains. To ensure the acquisition of high quality images, as much as possible, we chose to image regions of uniform thickness and discarded out of focus images such as the one shown in Figure A.13. Additionally,

though samples are extremely thin (<100 nm), we found that there still was grain overlap in the images because of the small size of the grains (Figure A.14).

The JEOL JEM-3010 TEM was also equipped with a set of selected area diffraction apertures, which can be used to produce electron diffraction patterns. We collected several patterns from three pyrolite glass samples using apertures that select 100, 200, 500, and 1000 nm² areas (Figure A.15). Because of grain overlap and uncertainties in calibration, these patterns could not be conclusively used to identify metallic Fe in the phase assemblages, though certain diffraction spots could be tentatively attributed to FeO, which was likely metallic Fe oxidized during the recovery or microscopy process. Due to the uncertainties, these results are not included in this work.

2.8 STEM Analyses

For STEM work, we use the JEOL JEM-ARM200CF Aberration corrected cold field emission STEM at the University of Illinois at Chicago, operated at 200 kV. The microscope is equipped with high- and low-angle annular dark-field (HAADF and LAADF) and BF detectors, and images are collected with a Gatan CCD camera. The microscope is also equipped with an Oxford X-max 100TLE windowless SDD X-ray detector capable of atomic resolution EDS mapping. When using the STEM, contamination from hydrocarbon buildup can occur, so it was necessary to periodically treat the sample with a plasma cleaning. Figure A.16 shows the extent of contamination seen after EDS measurements were performed on a sample. For each sample that was analyzed with the STEM, we acquired HAADF and LAADF images in addition to EDS measurements. Resolution depends on the thickness of the sample as well as the electron probe size, and measurements in this work were performed with probes ranging from ~0.078-0.1 nm.

EDS maps and line scans were collected for ~5-30 minutes. Because grains in the high pressure and temperature phase assemblages were so small (average ~20 nm), STEM EDS measurements still reveal overlap between grains being measured and the surrounding matrix.

The JEOL JEM-ARM200CF STEM was also equipped with a Gatan Quantum ER Model 965 GIF, which allows electron energy loss spectroscopy (EELS) to be performed. EELS yields information about the oxidation state of elements within a sample. We performed EELS measurements on two pyrolite glass samples but did not pursue extended analysis of the results or application of the technique to all samples because it yielded similar information to what had already been acquired with EDS mapping, and sample thickness made spectra interpretation difficult (Figure A.17).

3 THERMODYNAMIC MODELLING USING PERPLEX

PerpleX is a collection of Fortran77 programs for calculating phase diagrams, manipulating thermodynamic data, and modeling equilibrium phase fractionation and reactive transport (Connolly, 2009). In this work, we used PerpleX to produce predictions of the occurrence of iron disproportionation across the entire range of pressure and temperature conditions in Earth's lower mantle. In this chapter, I will provide a brief overview of essential thermodynamic principles, a description of the PerpleX software, a review of the Stixrude & Lithgow-Bertelloni thermodynamic databases, a description of how I modified thermodynamic input parameters to allow for iron disproportionation, and a demonstration of how my modifications affect results from previous studies.

3.1 Thermodynamic background

When studying high pressure and temperature phase assemblages, it is useful to produce thermodynamically derived predictions of equilibrium phase assemblages to supplement experimental results. A thermodynamic equilibrium phase assemblage calculation can indicate the relative amount and composition of every phase in a stable equilibrium system. At a fixed pressure and temperature in a system, the most stable phase assemblage will be that which minimizes the Gibbs energy of the system ($dG_{system} = 0$). Gibbs energy is a function of pressure, temperature, and composition, where composition is defined as the number of moles of the various components that are present: $G_j(P, T, n_1, n_2, \dots, n_c)$, where j represents the phase and n represents the number of moles of component $1, 2, \dots, c$. A system is always defined with the minimum number of components that can fully describe all phases present.

The Gibbs energy of a c -component system is equal to the sum of all of the Gibbs energies of the constituent phases:

$$G_{system}(P, T, n_1, n_2, \dots, n_c) = \sum_j^p G_j(P, T, n_1, n_2, \dots, n_c) \quad (3.1)$$

where there are phases from $j = 1$ to p . The Gibbs energy of a phase j can be written as:

$$G_j(P, T, n_1, n_2, \dots, n_c) = \sum_i^c n_i^j \mu_i^j(P, T, n_1, n_2, \dots, n_c) \quad (3.2)$$

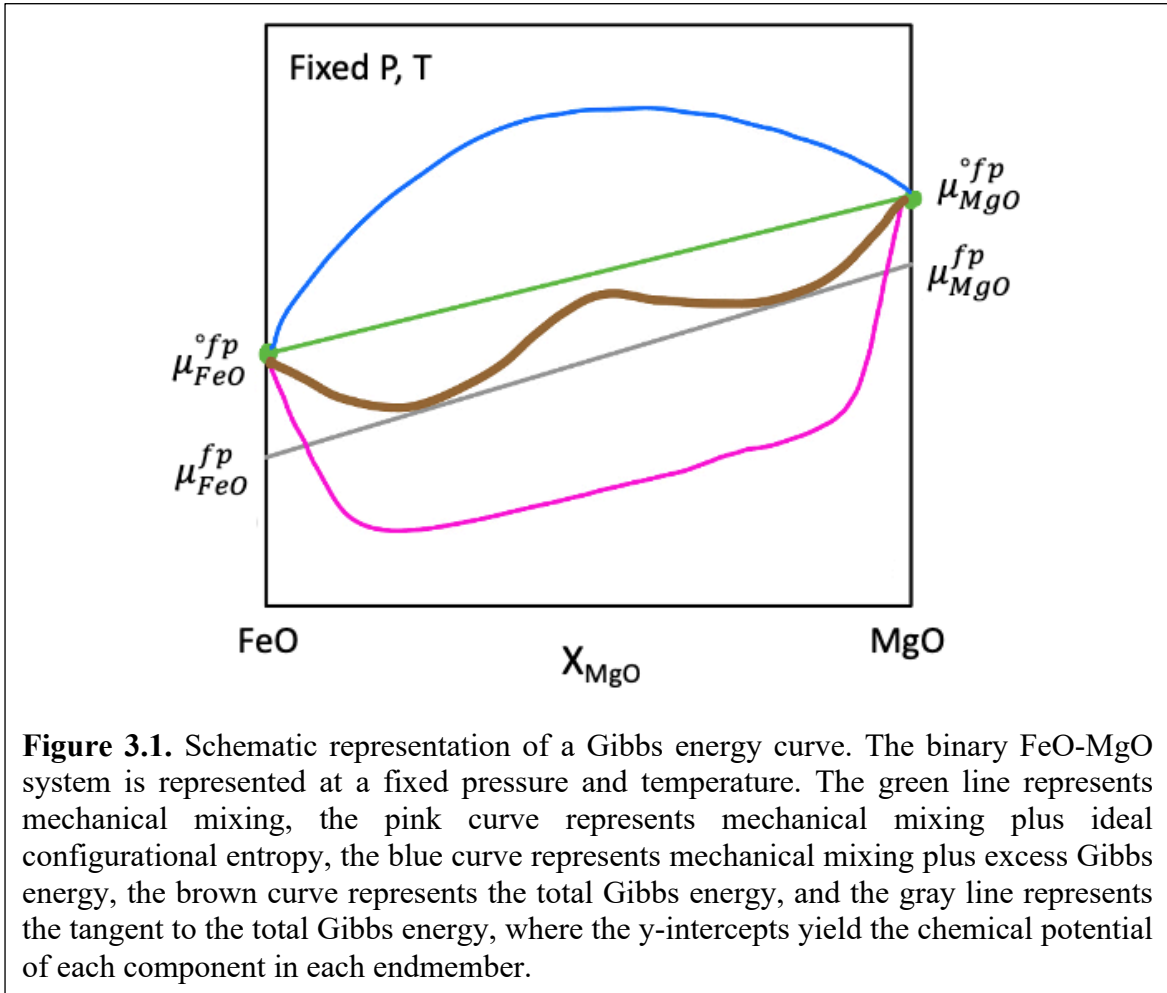
where μ_i represents the chemical potential of component i in phase j and has a dependence on P , T , and molar amounts of each component. At equilibrium, the chemical potential of component i is equal across all phases: $\mu_{c1}^{p1} = \mu_{c1}^{p2} = \dots = \mu_{c1}^p$. With an equation for each phase G_j and relationship between chemical potentials, a phase diagram can be produced by solving for the chemical potential of each component.

Generally, it is easier to work with the molar Gibbs energy $\bar{G} = \sum_i^c X_i^j \mu_i^j$, where $X_i^j = \frac{n_i^j}{\sum_i^c n_i^j}$, which is the mole fraction of component i in phase j (the number of moles of component i in phase j divided by the total number of components in phase j). This allows the constraint $\sum_i^c X_i^j = 1$, which says that the sum of all mole fractions of all components in phase j is equal to unity. In the whole system, the total number of moles of component i should equal the sum of the moles of component i in each phase: $N_i = \sum_j^p (\sum_i^c n_i^j) X_i^j$. Using the molar Gibbs energy, we can write:

$$\bar{G}_j(P, T, X_1, X_2, \dots, X_c) = \sum_i^c X_i^j \mu_i^j(P, T, X_1, X_2, \dots, X_c) \quad (3.3)$$

For example, in a 2-component system where ferropericlase is stable, defined by the components FeO and MgO, the Gibbs energy of ferropericlase would be written as:

$$\bar{G}^{fp}(P, T, X_{FeO}, X_{MgO}) = X_{FeO}^{fp} \mu_{FeO}^{fp} + X_{MgO}^{fp} \mu_{MgO}^{fp} \quad (3.4)$$



where X_{FeO}^{fp} and μ_{FeO}^{fp} represent the mole fraction of FeO in the ferropicriase and the chemical potential of FeO in the ferropicriase, respectively. Figure 3.1 shows a schematic representation of the $\bar{G}^{fp}(P, T, X_{FeO}, X_{MgO})$ curve for this 2-component system at a fixed pressure and temperature.

For phases that form solid solutions, the Gibbs energy can be broken into three components: The contribution of mechanical mixing of pure endmember species, the contribution of energy from configurational entropy of mixing (for an ideal solution), and the contribution from excess Gibbs energy. This can be written as:

$$\bar{G}_j = \bar{G}^{mech} + \bar{G}^{config} + \bar{G}^{excess} \quad (3.5)$$

The mechanical mixing term is defined as:

$$\bar{G}^{mech} = \sum_i^c X_i^j \mu_i^{\circ j} \quad (3.6)$$

where $\mu_i^{\circ j}(P, T)$ represents the chemical potential of component i in phase j in its pure form. In Figure 3.1, this energy of mechanical mixing is represented by the green line drawn between $\mu_{FeO}^{\circ fp}$ and $\mu_{MgO}^{\circ fp}$. In a solution, however, there is more than just mechanical mixing – crystallographic sites can have different cations occupying them. In an ideal solution, the microscopic interactions between each pair of chemical species are the same, so we need only consider the configurational entropy of mixing (not the enthalpy of mixing). This leads to the molar Gibbs energy of mixing in an ideal solution:

$$\bar{G}^{config} = RT \sum_i^c X_i^j \ln X_i^j \quad (3.7)$$

Generally, a component exhibits nearly ideal behavior at very high mole fractions. In a non-ideal (regular) solution, there is a non-zero enthalpy of mixing because different cations interact differently in the crystallographic sites of the mineral, which affects the energetics of the system and thus the ability of components to react in the system. The excess molar Gibbs energy can have different forms depending on the solution model being used (e.g. symmetric, asymmetric). Margules interaction parameters are used in symmetric and asymmetric solution models to “correct” for the excess energy related to non-ideal interactions of different atoms in a crystalline lattice.

The ability of components to react in the system is encompassed by a parameter called the activity. The activity can be thought of as the effective amount of a component in a phase, while

the chemical potential is the reactive energy that the component has. Chemical potential and activity are related by this expression:

$$\mu_i^j(P, T, X_1, X_2, \dots, X_c) = \mu_i^{\circ j}(P, T) + RT \ln a_i^j(X_1, X_2, \dots, X_c) \quad (3.8)$$

where R is the gas constant, and $a_i^j(n_1, n_2, \dots, n_c)$ is the activity of component i in phase j . As written, a_i^j is independent of pressure and temperature, which allows non-ideal enthalpy of solution but neglects the contribution of non-ideality to other physical properties like volume or entropy. This is the way Stixrude & Lithgow-Bertelloni (2011) treat the activity. With this definition of activity, the molar Gibbs energy can be written as:

$$\bar{G}_j(P, T, X_1, X_2, \dots, X_c) = \sum_i^c X_i^j \mu_i^{\circ j}(P, T) + RT \sum_i^c X_i^j \ln a_i^j(X_1, X_2, \dots, X_c) \quad (3.9)$$

Returning to the example of ferropicrlase, in the FeO-MgO system the Gibbs energy of ferropicrlase would be written as:

$$\begin{aligned} \bar{G}^{config}(P, T, X_{FeO}, X_{MgO}) = & X_{FeO}^{fp} \left(\mu_{FeO}^{\circ fp}(P, T) + RT \ln a_{FeO}^{fp}(X_{FeO}, X_{MgO}) \right) + \\ & X_{MgO}^{fp} \left(\mu_{MgO}^{\circ fp}(P, T) + RT \ln a_{MgO}^{fp}(X_{FeO}, X_{MgO}) \right) \end{aligned} \quad (3.10)$$

With the appropriate thermodynamic data and solution models, one can construct continuous functions for the Gibbs energy of all possible phases. A phase equilibrium calculation must be able to use these Gibbs energy functions to identify the p phases of matter that minimize the Gibbs energy of the system.

3.2 PerpleX overview

Phase diagrams can be produced with phase equilibrium calculators (e.g. THERMOCALC) or minimization programs (e.g. PerpleX). With a phase equilibrium calculator, the phase assemblage must be specified before the calculation, and through the calculation, the compositions

of the phases are computed. In the minimization process, the user specifies a pressure, temperature, and composition for a system, and the set of possible phases is calculated, with the assemblage yielding the minimum energy selected. For example, if the bulk composition of a system is FeO (two components), the Gibbs Phase Rule mandates that there must be less than or equal to two phases present at the specified pressure and temperature (two degrees of freedom). Possible phase combinations would include FeO (wüstite), $\text{Fe}_2\text{O}_3+\text{Fe}$ (hematite and iron metal), or $\text{Fe}_3\text{O}_4+\text{Fe}$ (magnetite and iron metal). The Gibbs energy minimization process would consider each of these possibilities and choose the one that minimizes the Gibbs energy of the system. To generate a phase diagram, this Gibbs energy minimization is repeated across a cartesian grid (axes can be

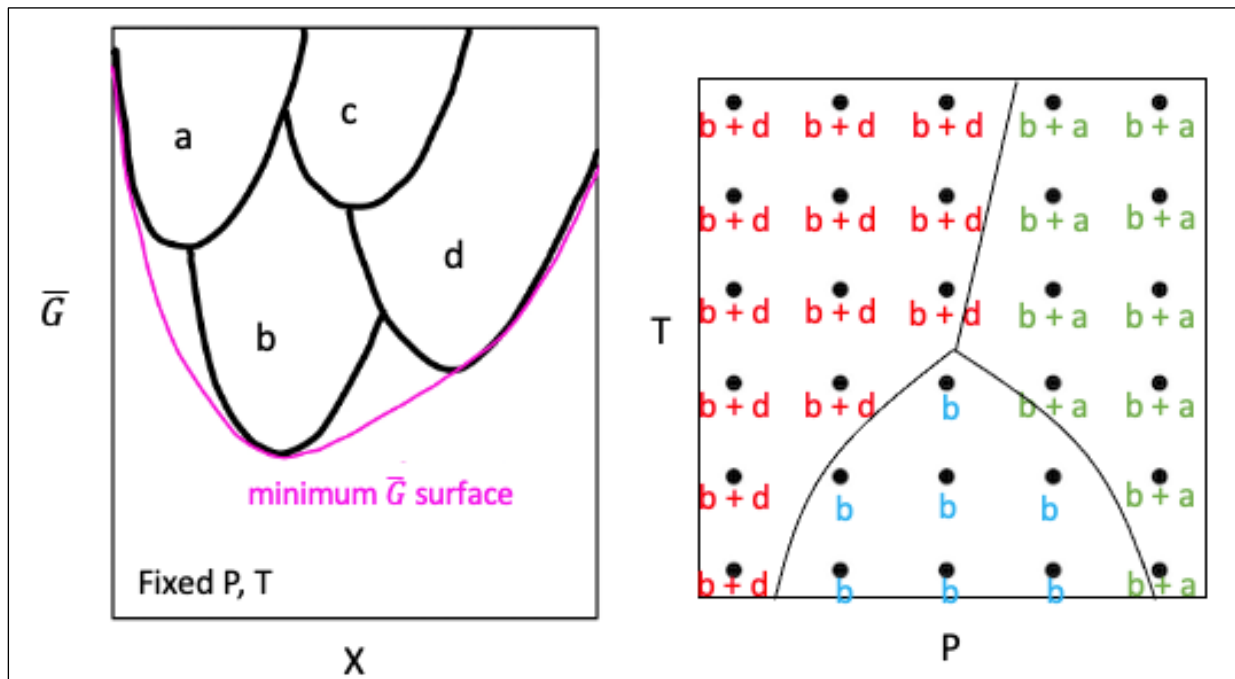


Figure 3.2. Schematic representation of the construction of a phase diagram. Left: Determination of the minimum Gibbs energy surface of a binary system at a given pressure and temperature. Right: Mapping of stable phases as determined by Gibbs energy minimization onto grid in P-T space. Iterative refinement would generate the phase boundaries draw in black.

composition, pressure, temperature), and the grid is refined iteratively to better constrain the position of reactions, as schematically illustrated in Figure 3.2.

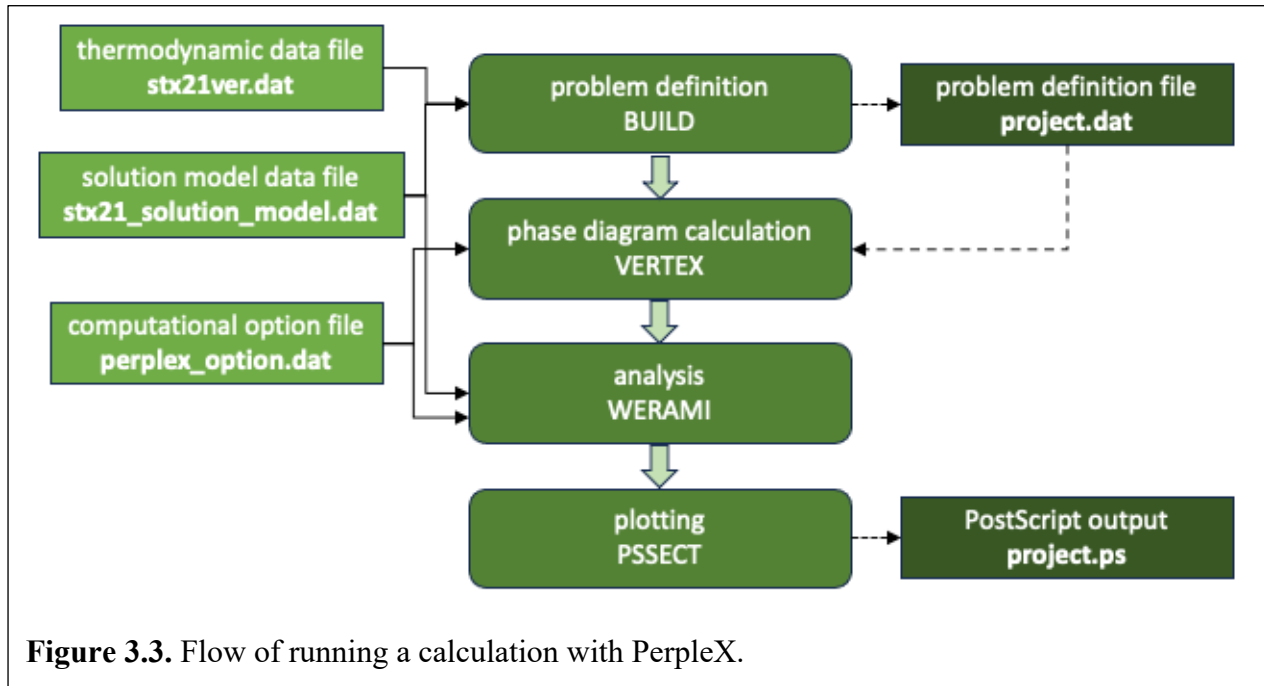
Finding the minimum Gibbs energy surface of a system is a very challenging mathematical problem but can be presented schematically in a simple binary system at a specified pressure and temperature as in Figure 3.2, where four phases are represented by their Gibbs energy curves. Different programs employ varying strategies for finding the minimum Gibbs energy surface for a specific composition. PerpleX overcomes the challenges involved in evaluating and keeping track of all of the changes that occur on the minimum Gibbs energy surface of a system as a function of pressure and temperature by using a simple linear algorithm to evaluate thermodynamic surfaces (Connolly, 2009). PerpleX approximates the continuous Gibbs energy-composition surface of solutions by a series of arbitrarily defined pseudocompounds that discretize the possible composition of the solution. This strategy allows the calculation to be efficient and virtually independent of the number of phases considered in the calculation. The calculation of the minimum Gibbs energy configuration proceeds in two phases: an exploratory phase and an auto-refinement phase. In the exploratory phase, the program identifies stable and nearly stable compositions (refinement points) through linear programming. In the auto-refine phase, the program resamples the composition space, subdividing the composition space around the refinement points to optimize the resolution (Figure 3.2). These two steps are repeated until the target resolution is achieved.

It should be noted that the PerpleX software is actively updated and different versions of the software exist. The calculation steps described above are relevant to all versions of the software before 6.9.0, while in versions 6.9.1 onwards, the refinement strategy is changed. The re-sampling

of the composition space is performed with quadratic programming that optimizes the composition of each refinement point relative to the current linear programming solution. This change in refinement strategy in versions 6.9.1 onwards overcomes difficulties caused by complex solution models and high-dimensional composition spaces. However, the change can cause problems when compositions include zeroed components, especially when zeroed components have solution behavior in one or more phases. In this case, the compositional derivatives used in the quadratic programming technique may point the refinement in a direction that violates the zero component restraint, so the optimal composition is difficult to find. Because we use relatively simple compositions and solution models in this work, we use version 6.8.9 of PerpleX for this work.

The work flow for running a calculation with PerpleX is described below and represented schematically in Figure 3.3.

1. Run the *build* executable, which will set up the data file (.dat file) for the minimization program. An annotated sample problem definition file is included in Figure B.1. The *build* executable requires the following user input to define the problem:
 - a. Axes of the diagram (P, T, X).
 - b. Thermodynamic database and solution phase database to be used. For this work, we use the Stixrude & Lithgow-Bertelloni (2022) database and associated solution models with slight modifications (discussed below).
 - c. PerpleX option file (*perplex_option.dat*), which contains controls for features such as the exploratory and refinement grid sizes.
2. Run the *vertex* executable, which performs the Gibbs energy minimization procedure.
3. Run *pssect* to plot the phase diagram. The output is a PostScript file.



4. Run *werami* to extract information from the phase diagram. For example, we can extract the mole fraction of each phase present or the composition of a solution phase.

We chose to use the PerpleX software in this work over the Hefesto software because of its thorough documentation and demonstrated compatibility with the Stixrude & Lithow-Bertelloni (2011 and 2022) databases. With a database of thermodynamic data and solution models for relevant mineral phases such as that of Stixrude & Lithgow-Bertelloni, (2011 and 2022), PerpleX can construct functions of Gibbs energy.

3.3 Stixrude and Lithgow-Bertelloni databases

In order to model the mineralogy of Earth’s lower mantle, we need a thermodynamic database that includes mineral phases relevant to the pressure and temperature conditions of the lower mantle. The thermodynamic database provided by Stixrude & Lithgow-Bertelloni in 2011 and updated in 2022 is the most complete and widely used database for mantle-relevant

calculations. With their 2011 and 2022 papers, Stixrude & Lithgow-Bertelloni aimed to “construct an equilibrium thermodynamic theory capable of self-consistent computation of phase equilibria and physical properties of mantle assemblages, including those most important for understanding dynamic processes and geophysical observations” (Stixrude & Lithgow-Bertelloni, 2011).

In PerpleX, the thermodynamic database file contains basic data for chemically pure entities, which are real stoichiometric phases or endmember compositions of a solution phase. A thermodynamic database file includes the standard variables used in the calculation (P , T , μ) and the components that will be used to define the phases. Components are typically (including in Stixrude & Lithgow-Bertelloni, 2011, 2022) given as oxides (e.g. MgO , FeO , Al_2O_3). The rest of the file is composed of the phases that are part of the database. Phases are defined by the type of equation of state (EOS) that has been provided to describe the phase, and the chemical equation of the phase is written out in terms of the database components. PerpleX allows a range of different EOS formulations to be used in its calculations, each designated with a unique EOS number in the data file. The EOS for Stixrude & Lithgow-Bertelloni (2011, 2022) is designated as type 6, and is a Mie-Grüneisen form built from a third-order Birch-Murnaghan equation of state and Debye thermal term, which will be detailed below.

From above, we have two definitions of the molar Gibbs energy of a phase j where the molar Gibbs energy of phase j is defined in terms of component mole fractions and chemical potentials (Equation 3.3) and mechanical mixing, configuration, and excess terms (Equation 3.5). Following these definitions, Stixrude & Lithgow-Bertelloni (2005) assume a form of the chemical potential for each phase that includes a term due to the pure end member species, a term due to the

configurational entropy in an ideal solution, and a term due to excess contribution from non-ideal behavior.

For the term of the chemical potential due to the pure endmember species, Stixrude & Lithgow-Bertelloni (2005) use the Legendre transformation of Gibbs energy:

$$G(P, T) = F(V, T) + P(V, T)V \quad (3.11)$$

where $F(V, T)$ is the Helmholtz energy. The Helmholtz energy is divided into a “cold” part $F_c(V, T)$ and a thermal part $F_{th}(V, T)$:

$$F(V, T) = F_0 + F_c(V, T_0) + F_{th}(V, T) - F_{th}(V, T_0) \quad (3.12)$$

The cold part is represented with the third-order Birch-Murnaghan equation of state:

$$F_c(V, T_0) = 9K_0V_0 \left[\frac{1}{2}f^2 + \frac{1}{3}a_1f^3 \right] \quad (3.13)$$

where K_0 is the bulk modulus and

$$f = \frac{1}{2} \left[\left(\frac{V_0}{V} \right)^{2/3} - 1 \right] \quad (3.14)$$

$$a_1 = \frac{3}{2} [K'_0 - 4] \quad (3.15)$$

and K'_0 is the derivative of the bulk modulus.

The thermal part is represented with the Mie-Grüneisen formulation of the Debye model:

$$F_{th}(V, T) = 9nRT \left(\frac{T}{\theta} \right)^3 \int_0^{\frac{\theta}{T}} \ln(1 - e^{-t}) t^2 dt \quad (3.16)$$

$$\theta = \theta_0 \left(1 + a_1f + \frac{1}{2}a_2f^2 \right) \quad (3.17)$$

$$a_1 = 6\gamma_0 \quad (3.18)$$

$$a_2 = -12\gamma_0 + 36\gamma_0^2 - 18q_0\gamma_0 \quad (3.19)$$

$$\gamma = \frac{1}{2} \frac{\theta_0^2}{\theta^2} (2f + 1) [a_1 + a_2f] \quad (3.20)$$

where n is the number of atoms per formula unit, θ is the Debye temperature and γ is the Grüneisen parameter. The relationship between γ and γ_0 is hidden within Equation 3.20 within the a_1 and a_2 terms. These form of the Debye temperature differs from the expression commonly used in other literature, which appears as:

$$\theta = \theta_0 e^{\left(\frac{\gamma_0 - \gamma}{q}\right)} \quad (3.21)$$

However, both parameterizations follow the form

$$q = \frac{d \ln \gamma}{d \ln V} \quad (3.22)$$

which can be rearranged to

$$\gamma = \gamma_0 \left(\frac{V}{V_0}\right)^q \quad (3.23)$$

The PerpleX software is able to use the Helmholtz energy to calculate the Gibbs energy of pure endmember phases.

The second term in the Stixrude & Lithgow-Bertelloni chemical potential formulation is the contribution to the Gibbs energy from configurational entropy in an ideal solution. The configurational entropy is dependent upon the number of mixing sites and the number of atoms of different components on the different sites. To clarify the terms, we can consider ferropericlase, which has the formula (Mg,Fe)O. Ferropericlase has one mixing site that can host both Mg and Fe.

The third term in the Stixrude & Lithgow-Bertelloni chemical potential formulation is the contribution to the Gibbs energy from excess (or non-ideal) behavior in the solution. This term follows the asymmetric van Laar formulation, where pairs of phases that have solid solution (e.g. phases α and β) have an interaction parameter $W_{\alpha\beta}$, which is then size-weighted with the

interacting phases' van Laar size parameter d_α . The excess contribution reduces to a symmetric regular solution model when all the size parameters d_α are equal.

Phases in the Stixrude & Lithgow-Bertelloni (2022) thermodynamic data file (named `stx21ver.dat` in the PerpleX repository) must have values for the following parameters: Helmholtz energy at the reference condition (F_0), number of atoms per formula unit (n), initial volume (V_0), isothermal bulk modulus (K_0), pressure derivative of the isothermal bulk modulus (K'_0), Debye temperature (θ), Grüneisen parameter (γ), and Mie-Grüneisen exponent (q) (as termed in the PerpleX database). At 0 GPa, the Gibbs energy is equal to the Helmholtz energy because $F = G - PV$, so the value entered for the Helmholtz energy at the reference condition (F_0) is equivalent to the Gibbs energy at the reference condition (G_0). Gibbs energies are computed relative to an arbitrary reference condition, and in thermodynamic databases, there are two conventions that are generally followed: HSC and SUPCRT. The Stixrude & Lithgow-Bertelloni (2022) database follows the SUPCRT convention, in which G_0 is the Gibbs energy of formation from the elements at the reference condition $G_f(T_r, P_r)$. In the Stixrude database, the reference condition is ambient pressure and temperature: 1 bar and 298 K. The Stixrude & Lithgow-Bertelloni (2022) thermodynamic data file must be used along with the Stixrude & Lithgow-Bertelloni (2022) solution model data file (`stx21_solution_model.dat`). Phases that have solid solution (e.g. bridgmanite, ferropericlase, corundum, etc.) require the following information in the solution model data file: the model type (`stx21_solution_model.dat` uses type 2: Margules model with symmetric mixing), the number of endmembers, the names of the endmembers, the relevant interaction parameters, the number of mixing sites, the number of species (cations) that can coexist in each mixing site, and the atomic site fraction for each cation for each mixing site.

The Stixrude & Lithgow-Bertelloni (2011) database was the first to provide the most comprehensive database for mantle phase relations. The database was updated in 2022 with a new global inversion of all parameters based on newer results from experiment and first principles theory (Stixrude & Lithgow-Bertelloni, 2022). Both the 2011 and 2022 databases contain three endmembers of bridgmanite (MgSiO_3 , FeSiO_3 , and Al_2O_3) along with the accompanying solution model information. The 2022 update resulted in slight adjustments to most of the thermodynamic parameters in the thermodynamic database for each of these endmembers (Table B.1). In addition, the 2022 update resulted in a change to the interaction parameter between MgSiO_3 - Al_2O_3 ($W_{\text{perov-aperov}}$) from 116 to 35 and the addition of an interaction parameter between MgSiO_3 - FeSiO_3 ($W_{\text{perov-fperov}} = -11.4$). Additionally, in the 2011 version, the Al_2O_3 endmember had a van Laar size of 0.39, while the other two endmembers had van Laar sizes of 1. In the 2022 version, all van Laar sizes are 1. Finally, the 2022 update introduces Landau (magnetic disordering) transitions for all phases containing Fe. The transition type is indicated by a flag in the thermodynamic data file that is only recognized in versions of PerpleX beyond 6.9.1, but we have confirmed that the problem types explored in this work are best studied with versions prior to 6.9.0. Therefore, in this work, we neglect the Landau transitions that have been introduced in the Stixrude & Lithgow-Bertelloni (2022) database. We confirm that this does not cause any meaningful differences in phase stability (Figure B.2).

3.4 Modification of thermodynamic input parameters to promote iron disproportionation

To use PerpleX to model the iron disproportionation reaction in Earth’s lower mantle, we made certain modifications to the Stixrude & Lithgow-Bertelloni (2022) thermodynamic database

and solution models. As demonstrated in Chapter 1, the iron disproportionation reaction in the lower mantle is driven by the incorporation of the FeAlO_3 component into the bridgmanite phase. The Stixrude & Lithgow-Bertelloni (2022) database does not contain the FeAlO_3 endmember of bridgmanite, fcc Fe, or hcp Fe, however. Therefore, in order to model the disproportionation reaction, we needed to add these phases to the thermodynamic database.

3.4.1 Addition of the fcc Fe and hcp Fe phases

Both fcc Fe and hcp Fe are necessary phases to add to the thermodynamic database to model the iron disproportionation reaction across the entire pressure and temperature range of the lower mantle. We note that PerpleX has specific EOS types and accompanying data for the Komabayashi and Fei (2010) fcc Fe and hcp Fe phases, but we did not use these, as the hcp Fe phase is taken directly from Dewaele et al. (2006) and has dummy values for thermal expansivity and the Grüneisen parameter, which creates an incorrect phase boundary between fcc Fe and hcp Fe (Figure B.3). To add each Fe phase, we fit a selected equation of state to the Stixrude & Lithgow-Bertelloni (2005) EOS type 6 formulation (Mie-Grüneisen type with Birch-Murnaghan cold compression and a Debye thermal term). For fcc Fe, we used the equation of state of Tsujino et al. (2013). We generated four isotherms (800 K, 1500 K, 2000 K, 2800 K) from the Tsujino et al. (2013) equation of state and then fit these isotherms to the Stixrude & Lithgow-Bertelloni (2005) formulation, fixing $q = 1$ and $\theta = 340 \text{ K}$. For hcp Fe, we used the equation of state of Dewaele et al. (2006). We generated four isotherms (300 K, 1000 K, 2000 K, 3000 K) from the Dewaele et al. (2006) equation of state and then fit these isotherms to the Stixrude & Lithgow-Bertelloni (2005) formulation, fixing $q = 1$ and $\theta = 417 \text{ K}$. For both fcc Fe and hcp Fe, the

resulting values for the remaining parameters are listed in Table 3.1. Plots of the isotherms and residuals are provided in Figure B.4, along with the uncertainties associated with the fitting.

To determine the Gibbs energy values at the reference state for fcc Fe and hcp Fe, we used the fact that Gibbs energies are relative values, which means that a Gibbs energy value by

itself has no significance. Therefore, when adding or editing phases in the thermodynamic database, the Gibbs free energy values can be modified to achieve phase relations that are expected based on previous studies and experiments. For the fcc and hcp Fe phase relations, we used the phase boundary of Komabayashi et al. (2009). We set the fcc Fe $G_0 = 0 \text{ J/mol}$ and adjusted the hcp Fe G_0 until the phase boundary best matches the boundary of Komabayashi et al. (2009). The results are plotted in Figure 3.4.

3.4.2 Addition of the FeAlO_3 phase

While FeAlO_3 is an endmember of bridgmanite, FeAlO_3 has not been well studied experimentally at high pressure and temperature conditions. There are no studies that experimentally confirm that pure FeAlO_3 adopts the bridgmanite structure at high pressures and

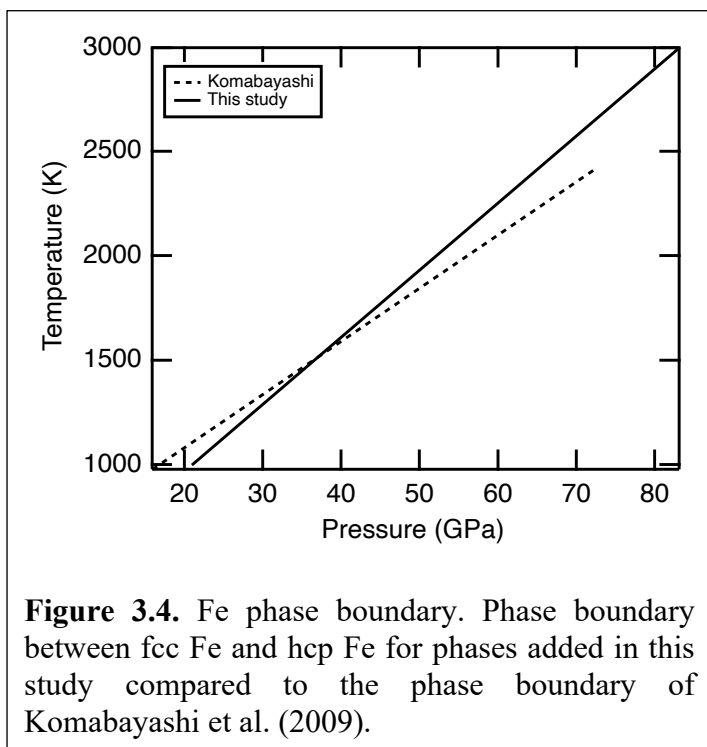


Figure 3.4. Fe phase boundary. Phase boundary between fcc Fe and hcp Fe for phases added in this study compared to the phase boundary of Komabayashi et al. (2009).

temperatures and no measurements of the thermodynamic and elastic parameters of FeAlO₃. We exclude the experimental study of Nagai et al. (2005) because it suggests that FeAlO₃ adopts the Rh₂O₃(II) phase but provides inconclusive evidence. As a result, there are not readily available experimentally derived thermodynamic parameters for the FeAlO₃ phase. However, Caracas (2010) performed static first-principles calculations on high pressure low-spin, high-spin ferromagnetic, and high-spin antiferromagnetic AlFeO₃ and FeAlO₃. These calculations yielded the initial volume ($V_0 = 2.761 \text{ J/bar}$), isothermal bulk modulus ($K_0 = 211 \text{ GPa}$), and pressure derivative of the isothermal bulk modulus ($K'_0 = 3.73$) for the most stable form, which was determined to be antiferromagnetic FeAlO₃ (labeled pv-AFM12 in the paper). Myhill (2018) then used a parameterization of solution models in terms of the Helmholtz energy, which includes the energetic contribution from elastic deformation of the endmember lattices, to model the pressure

PerpleX symbol	Parameter	fe_fcc Fe	fe_hcp Fe	hem Fe ₂ O ₃	faperov FeAlO ₃
G0	Helmholtz energy $F_0 = G_0 \left[\frac{\text{J}}{\text{mol}}\right]$	0	-150	-743740.7	-1180500
S0	Negative number of atoms pfu	-1	-1	-5	-5
V0	Negative volume $V_0 \left[\frac{\text{J}}{\text{bar}}\right]$	-6.859	-0.6710	-3.0274	-2.768
c1	Isothermal bulk modulus $K_0 [\text{bar}]$	1685000	1761000	1996000	2070000
c2	Pressure derivative of isothermal bulk modulus K'_0	4.724	4.890	4	3.73
c3	Debye temperature $\theta [K]$	340*	417*	551.6762	858.26509
c4	Grüneisen thermal parameter γ	2.650	2.485	1.897022	1.54222
c5	Mie-Grüneisen exponent q	1*	1*	1*	0.84088

Table 3.1. Parameters for EOS type 6 phases added in this work. A * indicates a value fixed during fitting or assigned (in the case of hematite). See text for discussion of the sources of parameters.

dependence of K_0 as a function of pressure for MgSiO_3 and FeAlO_3 bridgmanite. They make small thermal adjustments to the values derived from Caracas (2010) to produce $V_0 = 2.768 \text{ J/bar}$, $K_0 = 207 \text{ GPa}$, and $K'_0 = 3.73$. We used these values for the FeAlO_3 phase that we added to the Stixrude & Lithgow-Bertelloni (2022) database (Table 3.1). As no values exist for the Debye temperature (θ), Grüneisen parameter (γ), and Mie-Grüneisen exponent (q), we adopted the Debye temperature from the Stixrude & Lithgow-Bertelloni (2022) AlAlO_3 endmember ($\theta = 858.26509 \text{ K}$). The Grüneisen parameter and Mie-Grüneisen exponent are the same across all of the bridgmanite endmembers in the Stixrude & Lithgow-Bertelloni (2022) database, so we adopted these values ($\gamma = 1.54222$, $q = 0.84088$).

Adding the FeAlO_3 phase to the Stixrude & Lithgow-Bertelloni (2022) thermodynamic database also required its addition as an endmember in the bridgmanite solution model (named the Pv solution in the database). The bridgmanite solution model is a 2-site entropy model, meaning that mixing can occur on 2 sites: the 8- or 12-fold A site (which can host Mg, Fe^{2+} , Fe^{3+} , or Al) and the 6-fold B site (which can host Si or Al). In the PerpleX solution model file, when multiple species can exist on the same site, the site fraction of a species must be defined in terms of the mole fractions of the endmembers. The modified solution model is presented in Figure 3.5. To add the FeAlO_3 endmember, we modified the solution model file to indicate that 4 species can mix on site A by adding an Fe^{3+} atomic site fraction for the FeAlO_3 component. The line $z(\text{fe3}) = 1 \text{ faperov}$ indicates that one of the species for the site with 4 possible species (called the M site in the file) is the species in the A site of the faperov endmember (Fe^{3+}). We also added an additional Al atomic site fraction on the B site to indicate that both the AlAlO_3 and FeAlO_3 endmembers have Al on the

```

begin_model
| perovskite solution
Pv
2 | model type: Margules, macroscopic
4 | 4 endmembers
aperov perov fperov faperov
0 0 0 0
0. 1. 0.1 0
0. 1. 0.1 0
0. 1. 0.1 0

begin_excess_function
W(perov fperov) -11.4d3
W(perov aperov) 35d3
end_excess_function

2 2 site entropy model
4 1. 4 species on M site multiplicity = 1.
z(mg) = 1 perov
z(fe2) = 1 fperov
z(fe3) = 1 faperov
2 1. 2 species on T site multiplicity = 1.
z(al) = 1 aperov + 1 faperov

end_of_model

```

Figure 3.5. Modified solution model for bridgmanite.

B site. The line $z(al) = 1\ aperov + 1\ faperov$ indicates that one of the species for the site with 2 possible species (called the T site in the file) is the species in the B site of both the aperov and faperov endmembers (Al). Additionally, in the Stixrude & Lithgow-Bertelloni (2022) database, all phases in the bridgmanite solution have a van Laar size parameter of $d_\alpha = 1$, which PerpleX assumes as the default, so this information does not need to be added to the solution model. Finally, we did not add an excess function for $MgSiO_3$ - $FeAlO_3$ because our method for determining the reference Gibbs energy (G_0) captures the non-ideal behavior of the $FeAlO_3$ endmember.

To determine the reference value for the Gibbs energy, we used the phase relations established along the $MgSiO_3$ - $FeAlO_3$ join by Liu et al. (2020). In Liu et al. (2020), six compositions along the $MgSiO_3$ - $FeAlO_3$ join were studied at 27 GPa and 2000 K using a multi-anvil apparatus combined with *in situ* synchrotron X-ray diffraction measurements and BSE imaging of recovered samples. EDS measurements from the recovered samples provide data on

the quantities of the endmember components in bridgmanite across the join (Figure 3.6). Notably, the FeAlO_3 component saturates in bridgmanite at 65 mol% for the composition containing 25% MgSiO_3 and 75% FeAlO_3 (labeled $\text{En}_{25}\text{FA}_{75}$). We adjusted the G_0 value of the FeAlO_3 phase in the thermodynamic database until we achieved the behavior observed by Liu et al. (2020) in the PerpleX phase diagrams.

Prior to testing the FeAlO_3 phase, however, we needed to add the hematite phase to the thermodynamic database in order to fully model the MgSiO_3 - FeAlO_3 join at 27 GPa and 2000 K. This is because hematite is present in the $\text{En}_{25}\text{FA}_{75}$ (25% MgSiO_3 and 75% FeAlO_3) and FA_{100} phase assemblages in the Liu et al. (2020) study. While the Stixrude & Lithgow-Bertelloni (2022) database does not contain the hematite phase, the Holland & Powell (1998) database contains hematite. In PerpleX, the thermodynamic database file for Holland & Powell (1998) is the *hp02ver.dat* file, as it also include data for the Ghiorso et al. (2002) pMELTS model. The Holland & Powell (1998) database uses a different equation of state formulation than Stixrude & Lithgow-Bertelloni (2022), however. In this equation of state formulation, values exist for the following parameters: Gibbs energy at the reference condition (G_0), entropy at the reference condition (S_0), initial volume (V_0), isothermal bulk modulus (K_0), and pressure derivative of the isothermal bulk modulus (K'_0). The database does not provide a Debye temperature (θ), Grüneisen thermal parameter (γ), or Mie-Grüneisen exponent (q), which are necessary for EOS type 6, which is used in the Stixrude & Lithgow-Bertelloni (2022) database. However, the Holland & Powell (2011) formulation does include parameters for the Einstein temperature (θ_E), coefficient of thermal expansion (α), and coefficients for the calculation of the heat capacity at constant pressure C_P . We used the fact that the Debye temperature is related to the Einstein temperature by:

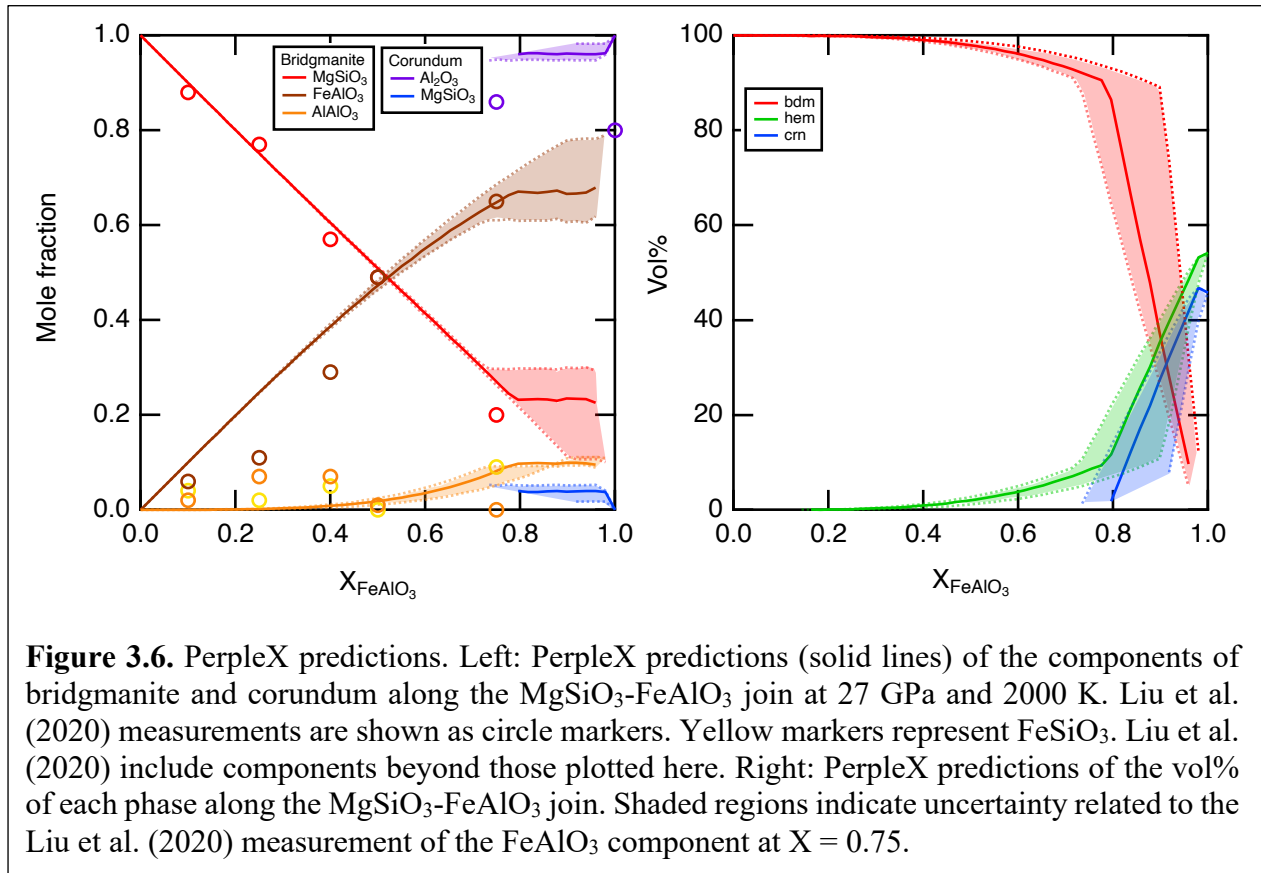
$$\theta_E \sim \theta_D \left(\frac{\pi}{6} \right)^{1/3} \quad (3.24)$$

to calculate the Debye temperature for hematite. This expression relating Debye temperature and Einstein temperature was provided by Bob Myhill via the PerpleX discussion group (Myhill, 2018). We also used the relationship between the Grüneisen parameter and heat capacity at constant pressure to calculate the Grüneisen parameter for hematite:

$$\gamma = \frac{V_0 K_T}{C_P - V_0 \alpha^2 K_T T} \quad (3.25)$$

By setting Mie-Grüneisen exponent to $q = 1$, we had all of the parameters necessary to define hematite as a type 6 EOS in the thermodynamic database (Table 3.1). We confirmed that the hematite phase behaves as expected by plotting the bulk composition FeO. We expect the wustite (FeO) phase to be stable at high pressures and temperatures, not a mixture of hematite and metallic Fe. Figure B.5 confirms this to be the case. We also confirmed that casting the hematite phase as an EOS type 6 produces higher quality results than directly placing the hematite EOS type 2 (Holland & Powell (1998) formulation) into the Stixrude & Lithgow-Bertelloni database (Figure B.5).

With an appropriate hematite phase in the thermodynamic database along with the FeAlO₃ phase, we determined that for the FeAlO₃ component to saturate at 65 mol% in the bridgmanite solid solution at $X_{\text{FeAlO}_3}=0.75$ at 27 GPa and 2000 K, the FeAlO₃ phase must have $G_0 = -1180500 \text{ J/mol}$ (Figure 3.6). Liu et al. (2020) report an uncertainty of ± 4 mol% of the FeAlO₃ measurement, which corresponds to a minimum $G_0 = -1177500 \text{ J/mol}$ and a maximum $G_0 = -1185600 \text{ J/mol}$. We used this range of FeAlO₃ content to generate uncertainties in our predictions. With this value for G_0 , the experimental results of Liu et al. (2020) are well replicated,

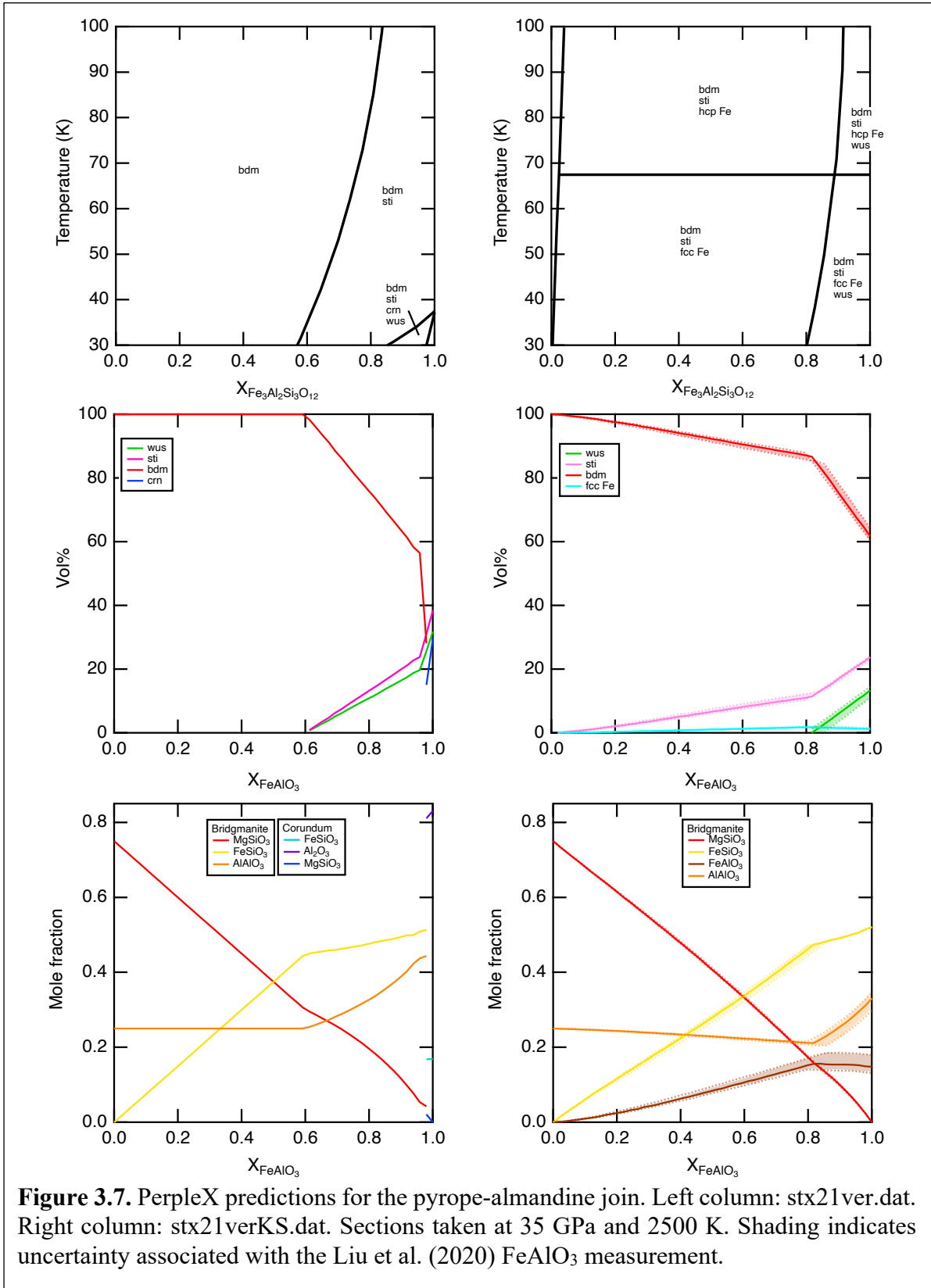


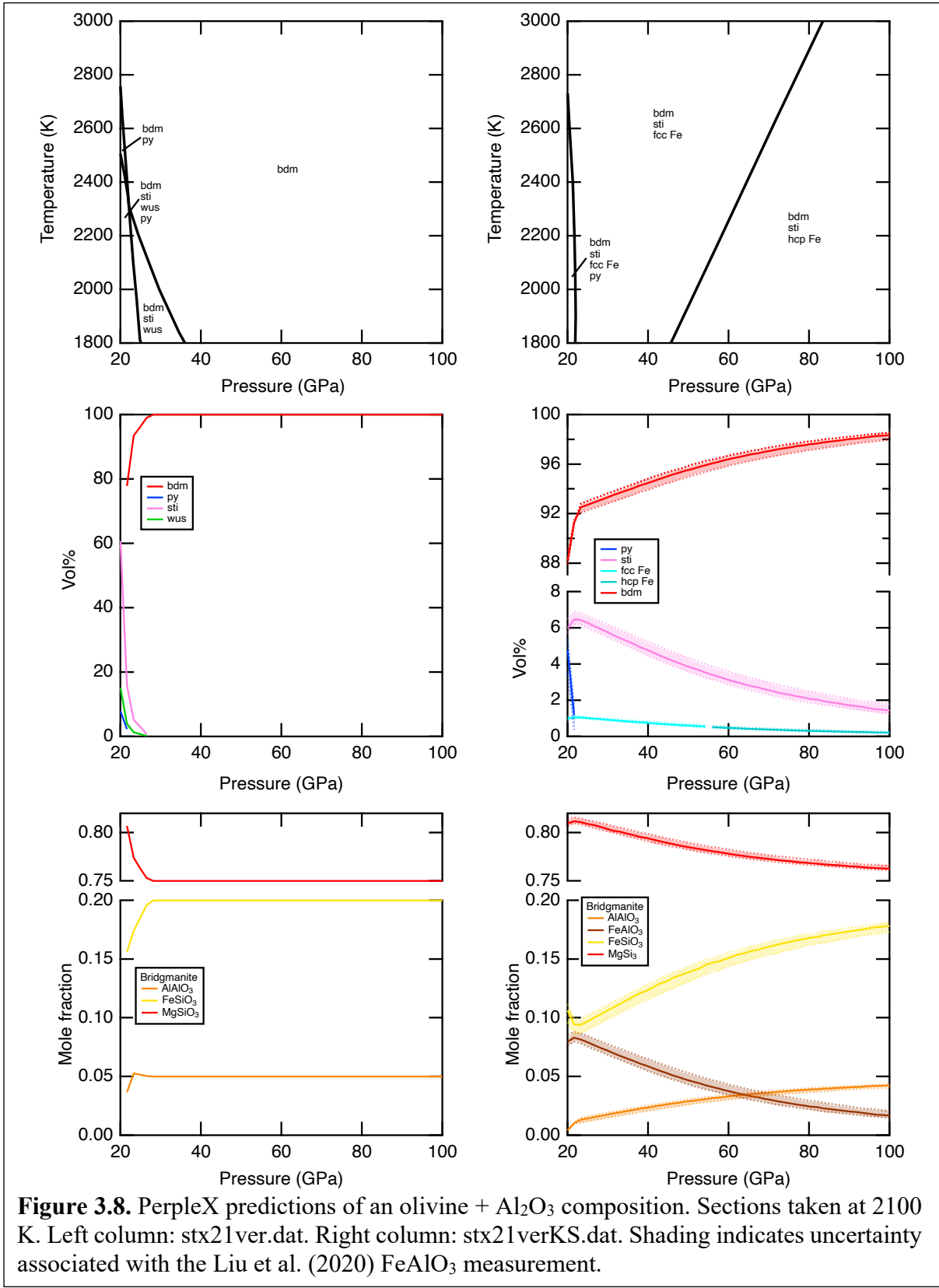
with the MgSiO_3 component decreasing across the join while the FeAlO_3 component increases and bridgmanite disappearing at the pure FeAlO_3 endmember. Liu et al. (2020) measure small quantities of the FeSiO_3 and AlAlO_3 components of bridgmanite across the join, but these show no distinct trends. The PerpleX calculation does not predict any amount of the FeSiO_3 component, and the AlAlO_3 component remains around 0 mol% and reaches a maximum of 10 mol%. In the PerpleX calculation, hematite is stable across much of the join, but it exists in very low quantities (<10 mol%). This is in contrast to the results from Liu et al. (2020), where hematite only appears in trace amounts along the join starting at $\text{En}_{25}\text{FA}_{75}$. Both Liu et al. (2020) and the PerpleX model predict a 50/50 mixture of corundum and hematite at the FeAlO_3 end of the join.

3.5 Demonstrations of disproportionation

In this section we provide demonstrations of the changes in phase diagrams resulting from the new additions to the thermodynamic database. Plotting the pyrope-almandine ($\text{Mg}_3\text{Al}_2\text{Si}_3\text{O}_{12}$ - $\text{Fe}_3\text{Al}_2\text{Si}_3\text{O}_{12}$) join at 2500 K from 20 GPa to 100 GPa using the Stixrude & Lithgow-Bertelloni (2022) database versus our modified database reveals the impact of the FeAlO_3 and metallic Fe additions (Figure 3.7). With the modified database, we predict the occurrence of iron disproportionation across the pyrope-almandine join due to the incorporation of the FeAlO_3 component in bridgmanite. The amount of disproportionated metallic Fe increases as the proportion of almandine increases until wustite enters the phase assemblage at Alm_{80} . Our prediction of the coexistence of bridgmanite, stishovite, and metallic Fe in the phase assemblage across much of the pyrope-almandine join partially explains the results of Dorfman et al. (2012), who detected bridgmanite and oxides at high pressures across the join (Fig. 4 in their paper). At 35 GPa, Dorfman et al. (2012) suggest that at the pyrope endmember, a single phase bridgmanite will be stable, and with the increasing proportion of almandine, a mixture of bridgmanite and oxides will be stable. At the highest almandine proportions, they detect a mixture of an unknown phase and oxides. Our model likewise predicts a single phase bridgmanite at the pyrope endmember, and as the almandine proportion increases, the addition of stishovite but also metallic Fe. The almandine endmember produces a mixture of bridgmanite, stishovite, wustite, and metallic Fe. The bridgmanite has the following component breakdown: 52% FeSiO_3 , 33% AlAlO_3 , and 15% FeAlO_3 .

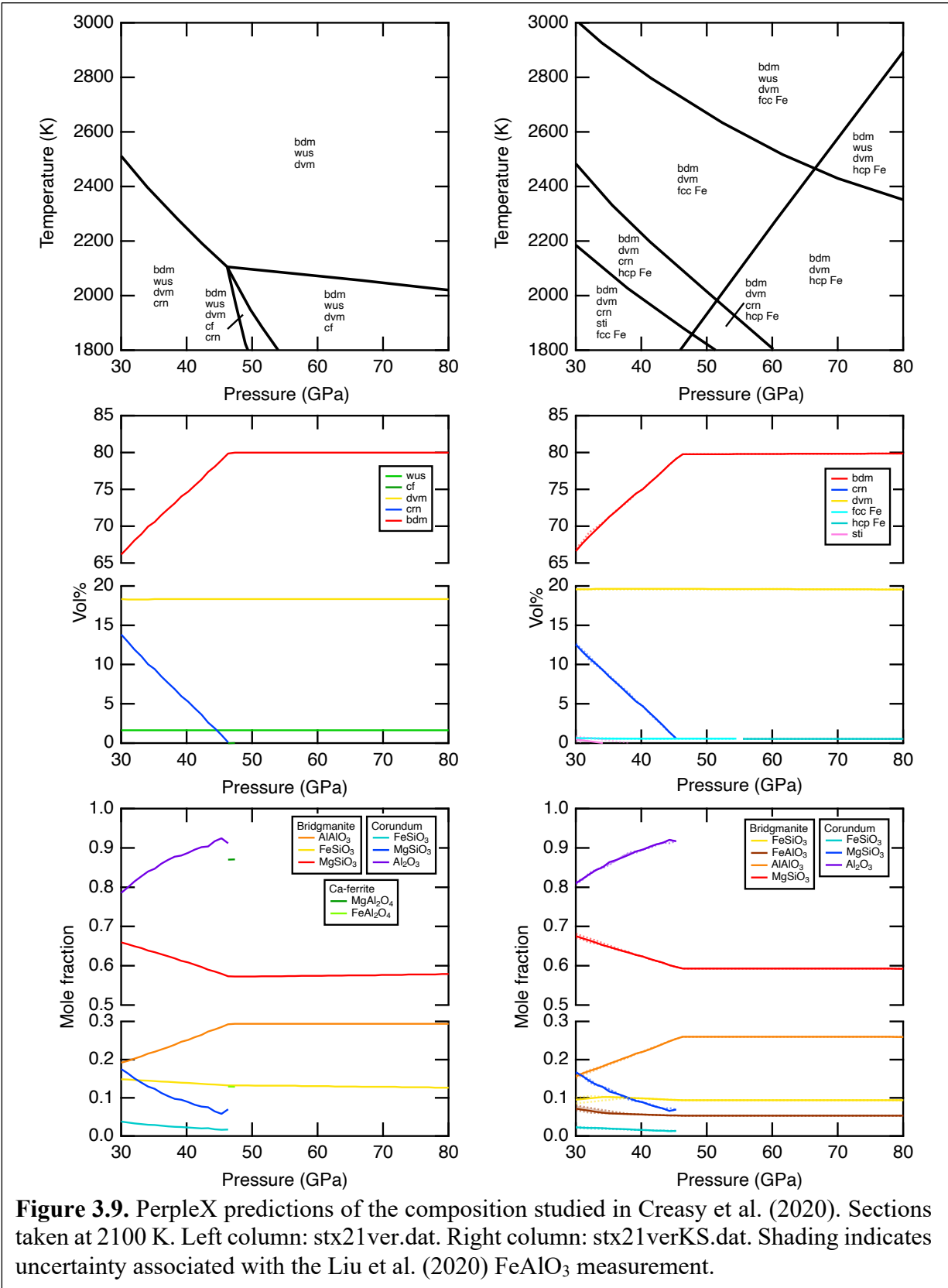
We can also test our PerpleX model against aluminous olivine compositions, such as the composition studied in Shim et al. (2017) (28.8 wt% MgO , 53.6 wt% SiO_2 , 12.8 wt% FeO , and





4.8 wt% Al₂O₃). Shim et al. (2017) studied this composition from 30 GPa to 100 GPa at high temperatures using synchrotron XRD, as well as at ambient conditions after recovery using EDS. They also used SMS at high pressures after temperature quench as well as at ambient conditions. The starting material had $\frac{Fe^{3+}}{\Sigma Fe} = 10\%$ (glass starting material) or $\frac{Fe^{3+}}{\Sigma Fe} = 0\%$ (non-glass starting material). They found that all of the samples contained bridgmanite (and metallic Fe, which was added to the starting material), and samples below 40 GPa contained small amounts of silica. When modeling this composition using the Stixrude & Lithgow-Bertelloni (2022) database, we find that bridgmanite is stable over much of the high pressure and temperature space (Figure 3.8). When we use our updated database, however, we find that while bridgmanite is the main stable phase, minor amounts of stishovite and metallic Fe should also be stable at high pressures and temperatures. This result can explain why Shim et al. (2017) (and other studies including Lauterbach et al. (2000)) find minor amounts of stishovite in Fe-,Al-bearing bridgmanite synthesis experiments. It is possible that in the study of Shim et al. (2017), stishovite existed beyond 40 GPa but was below detectable limits. Disproportionation would not have been recognized by Shim et al. (2017) because of the pre-loaded metallic Fe that was added to the samples. We note that the $\frac{Fe^{3+}}{\Sigma Fe}$ behavior of bridgmanite in the study of Shim et al. (2017) is not replicated by our model (Figure B.6). This may be attributed to the suggested role of low-spin Fe³⁺ in the B site of the bridgmanite structure, which is not accounted for in the database.

Finally, we can test our PerpleX model against the results of Creasy et al. (2020), who studied a reduced Al-rich pyroxenite sample based on the MIX1G Pyroxenite Model. The bulk composition is 27.1 mol% MgO, 41.6 mol% SiO₂, 13.1 mol% Al₂O₃, 10.2 mol% CaO, and 7.97



mol% FeO. Creasy et al. (2020) studied this composition from 40 GPa to 70 GPa at high temperatures between 2000 K and 2300 K using synchrotron XRD, as well as ambient conditions after recovery using EPMA measurements. In the XRD patterns, the authors clearly identify bridgmanite, davemaoite, and stishovite (or the CaCl_2 structure for pressures greater than 65 GPa). A Ca-ferrite structured phase ($(\text{Mg,Fe})\text{Al}_2\text{O}_4$), alumina, and metallic Fe may be present in the XRD patterns as well, but are not identified conclusively. The authors use Monte Carlo modeling to estimate the approximate amounts of each phase present in the phase assemblage. They predict bridgmanite with 93% MgSiO_3 , 3% FeSiO_3 , and 4% FeAlO_3 . The relative abundances of the bridgmanite components are primarily constrained from the unit-cell volume at room conditions taken from the literature. The phase assemblage breakdown is as follows: 50 mol% bridgmanite, 18.2 mol% davemaoite, 12.1 mol% Ca-ferrite, 10.4 mol% Al_2O_3 , 9 mol% stishovite, and 0.17 mol% metallic Fe. The authors state that metallic Fe formation cannot exceed 0.7 mol% because of limitations on how much Fe^{3+} can form within the sample based on Monte Carlo modeling. When modeling the composition using the Stixrude & Lithgow-Bertelloni (2022) database from 30 GPa to 80 GPa and 1800 K to 3000 K, we find that bridgmanite and davemaoite are stable across the entire P-T space, but stishovite is only present at lower pressures and temperatures (Figure 3.9). This is actually somewhat in alignment with the results of Creasy et al. (2020) because they find SiO_2 in the CaCl_2 structure above 65 GPa, and a separate phase for CaCl_2 -type SiO_2 does not exist in the Stixrude & Lithgow-Bertelloni (2022) database. We do not predict any stability of the Ca-ferrite phase, however, while Creasy et al. (2020) suggest that the Ca-ferrite phase is required for charge balance. Discrepancies between our results may arise from the constraints imposed during the Monte Carlo modelling by Creasy et al. (2020), as well as the fact that in the

PerpleX model, MgSiO_3 and FeSiO_3 are allowed to dissolve into corundum. At 2100 K and 40 GPa, we predict ~2.1 mol% metallic Fe, 75.4 mol% bridgmanite, 17.8 mol% davemaoite, and 4.6 mol% corundum (with solid solution). The bridgmanite has 62% MgSiO_3 , 22% AlAlO_3 , 10% FeSiO_3 , and 6% FeAlO_3 . We note that Creasy et al. (2020) did measure Fe^{3+} in the starting material ($\frac{\text{Fe}^{3+}}{\Sigma \text{Fe}} = 0.11$), which would account for part of the mismatch between our disproportionated Fe metal prediction and their value. Additionally, in the Monte Carlo model, they set the condition that metallic Fe could only vary between 0 mol% to 1 mol%. Overall, however, the results obtained with the updated thermodynamic database in PerpleX outperform the results obtained using the unmodified Stixrude & Lithgow-Bertelloni (2022) database.

4 DISPROPORTIONATION OF IRON IN ALMANDINE-PYROPE-GROSSULAR GARNET FROM 25 TO 65 GPa

This chapter is based on Swadba, K. E., Davis, A. H., Zurkowski, C. C., Chariton, S., Prakapenka, V. B., and Campbell, A.J. (2023). Disproportionation of iron in almandine-pyropes-grossular garnet from 25 to 65 GPa. *Geochemistry, Geophysics, Geosystems*. 24, e2023GC011081.

4.1 Introduction

It is well established that bridgmanite is likely the most abundant mineral in the lower mantle and adopts the perovskite *Pnma* structure (Knittle & Jeanloz, 1987; Liu, 1976; O'Neill & Jeanloz, 1990). Bridgmanite ((Mg,Fe)(Si,Al)O₃) can accommodate several different cation substitutions into its perovskite structure (ABO₃). Specifically, it has been extensively shown that the trivalent cations Fe³⁺ and Al³⁺ can be incorporated through a charge-coupled substitution, with Al³⁺ entering the B site and stabilizing Fe³⁺ in the A site (Frost & Langenhorst, 2002; Lauterbach et al., 2000; Liu et al., 2020; McCammon, 1997; Richmond & Brodholt, 1998; Vanpeteghem et al., 2006). Because Al has a chemical preference for the bridgmanite structure, when Al is present along with Fe in the phase assemblage, the disproportionation reaction will be promoted. In an Fe²⁺-rich starting composition, incorporation of an FeAlO₃ component into bridgmanite can occur through the disproportionation of Fe according to the following reaction: $3\text{Fe}^{2+} \rightarrow 2\text{Fe}^{3+} + \text{Fe}^0$. Although this reaction produces a small volume of metallic iron, it has been suggested that this disproportionation reaction plays a critical role in the geochemistry of the lower mantle (Frost et al., 2004). Studies have also suggested that the disproportionation reaction may proceed to different degrees as a function of depth (Shim et al., 2017, Tsujino et al., 2023). The occurrence of this reaction and creation of small amounts of metallic Fe can have significant implications for

the siderophile element geochemistry of the lower mantle, notably through its impact on isotopic tracers such as Os and on platinum group element distributions. Metallic Fe could also serve as a likely host for volatile elements in the lower mantle, such as C, S, and H, which are known to easily alloy with iron at relevant pressures and temperatures. The presence of metallic iron in the lower mantle presents a reservoir to store these elements and would notably impact the distribution of volatile elements in the Earth's deep interior.

It has been shown that garnets along the pyrope-almandine join form bridgmanite assemblages at high pressure and temperature conditions (Dorfman et al., 2012; Irifune et al., 1996; Kesson et al., 1995). Because pyrope-almandine garnets have both ferrous Fe and Al, the Fe disproportionation reaction is likely to occur during the formation of bridgmanite, resulting in the incorporation of the FeAlO_3 component in bridgmanite and the production of accompanying metallic Fe. However, there has been no consistent identification of Fe disproportionation occurring in pyrope-almandine garnet samples in existing experimental studies. Kesson et al. (1995) performed transmission electron microscopy (TEM) analyses on garnet samples recovered from high pressure and temperature conditions in the diamond anvil cell (DAC), and noted the existence of “blebs and runnels of an Fe-rich phase” at grain boundaries, accompanied by minor amounts of stishovite, but they did not identify disproportionated metallic Fe. Similarly, Dorfman et al. (2012) found no evidence of Fe disproportionation in garnet samples analyzed with synchrotron X-ray diffraction.

In this work, we investigate the disproportionation of Fe in a natural almandine-pyrope-grossular garnet to 65 GPa and 3500 K with *in situ* X-ray diffraction (XRD) in the laser-heated

diamond anvil cell and *ex situ* scanning electron microscopy (SEM) analysis on recovered samples. The results will inform our understanding of Fe disproportionation reactions in the Earth's mantle.

4.2 Materials and Methods

A natural almandine-pyrope-grossular garnet was selected for this study. The composition was determined by wavelength-dispersive X-ray spectroscopy (WDS) at the University of Maryland to be $\text{Alm}_{52}\text{Pyr}_{34}\text{Grs}_{11}\text{Sps}_2\text{And}_1$. Measurements are given in Table C.1. The $\text{Fe}^{3+}/\Sigma\text{Fe}$ ratio of the starting material was determined to be 0.016 based on stoichiometry of the WDS analyses. This garnet was selected for its high Fe^{2+} and Al content, which should increase the amount of Fe disproportionation that will occur. For all experiments, the natural garnet was broken into small fragments, which were loaded either with an Ir foil to act as an internal pressure calibrant and laser absorber, or with no foil. Samples were loaded in 50-100 μm -sized holes drilled through pre-indented Re or Ni gaskets. Symmetric diamond anvil cells with 250-300 μm culets were used to achieve pressures up to 65 GPa. Pressures were determined using the Ir equation of state (Cerenius & Dubrovinsky, 2000), or Raman spectroscopy on the diamond anvil culets before and after laser-heating (Akahama & Kawamura, 2004). Pressures at high temperatures were calculated with the approximation of a 1% increase in pre-heat pressure per 250 K increase, after Fischer et al. (2015) and Chidester et al. (2017). Table 4.1 gives a list of experimental conditions and analysis details.

XRD was performed at the GSECARS beamline 13-ID-D (APS, Argonne National Laboratory). Diffraction patterns were collected using a CdTe 1M Pilatus detector. The position and orientation of the detector was calibrated using a LaB_6 NIST standard. The X-ray energy was tuned to either 37 keV (0.3344 Å) or 42 keV (0.2952 Å) and focused to full width, half max

Sample	Foil	Pre-heat P (GPa)	Post-heat P (GPa)	Est. P at high T (GPa)	T history	Heating time	Analysis method	High P,T phases detected
K7_1	Ir	25	21	26.8	Flash then held ~2100 K	14 min	XRD	Sti
K8	Ir	28	27	30.3	Max 2380 K	5 min	XRD	Bdm, Sti
	-	-	5	-	Decompressed sample K8	-	XRD	Bdm, Sti
K7_2	Ir	39	35	43.7	Flash to 3000 K then held ~2000 K	20 min	XRD	Bdm, Sti, Dvm
K44_2	none	39	37	41.8	Heated on pre-heated (melted) spot; held ~2100 K	30 min	XRD + SEM	Bdm, Sti, Dvm, Fe ⁰
K44_1	none	47	39	52.1	Unknown max T; melted	15 min	XRD + SEM	Bdm, Sti, Dvm, Fe ⁰
K52_1	none	48	44	51.8	Flash to 2280 K then held ~2100 K	20 min	XRD	Bdm, Sti, Dvm
K47	none	51	51	54.5	Flash to unknown T then held ~2000 K	4 min	XRD	Bdm, Sti, Dvm
K11	none	52	No record	57.6	Melted and slowly cooled	4min	XRD + SEM	Bdm, Sti, Dm, Crn, Fe ⁰
K52_2	none	54	55	60.0	Flash to 3100 K then held ~2300 K	30 min	XRD	Bdm, Sti, Dvm
K7_3	Ir	53	55	58.7	No flash; gradual increase to ~3000 K	8 min	XRD	Bdm
K54	none	64	59	68.9	No flash; held ~2200 K	30 min	XRD + SEM	Bdm, Sti, Dvm, Crn, Fe ⁰

Table 4.1. Sample details. Pressure was recorded either form Ir foil or Diamond Raman spectroscopy. Bdm = bridgmanite, Sti = stishovite, Dvm = davemaoite, Crn= corundum, Fe⁰ = metallic Fe. Sample K8 was decompressed to 5 GPa and measured at 300 K with no laser heating.

dimensions of 2 μm x 3 μm . Double-sided laser-heating of the samples was carried out with *in-situ* XRD measurements (Prakapenka et al., 2008). 1064 nm fiber lasers were shaped to ~ 10 μm radius flat tops and aligned with the X-ray beam. Temperatures were measured on both sides using spectroradiometry and fitting to a gray body approximation (Heinz & Jeanloz, 1987). Diffraction images were integrated to produce 1-D diffraction patterns using the Dioptas software (Prescher & Prakapenka, 2015).

One sample (K11) was heated with a 1064 nm fiber laser at the University of Chicago. In this experiment, the laser spot size was approximately 20 μm and temperatures were measured on both sides by multispectral imaging radiometry (Campbell, 2008). XRD was performed at GSECARS on a recovered thin section from this sample.

The transition to bridgmanite in Fe-rich silicates is accompanied by a color change from transparent to dark brown (Kesson et al., 1995; O'Neill & Jeanloz, 1994). In most samples, transformation from garnet to a bridgmanite assemblage was accompanied by a sudden increase in laser coupling, observed as a flash accompanied by a sudden spike in temperature. Similar heating experiences are detailed in Dorfman et al. (2012). Laser power was adjusted during these intervals to attempt to maintain stable temperatures. All samples were quenched from high temperatures, with the exception of K11, which was slowly cooled.

Several samples were recovered from high pressure and temperature conditions and prepared for SEM analysis using the focused ion beam (FIB) in the Tescan Lyra3 field-emission SEM in the Department of the Geophysical Sciences at the University of Chicago. The instrument is equipped with SE and BSE detectors, along with an Oxford OmniProbe 400 micromanipulator and Oxford OmniGIS gas injection system capable of C or Pt deposition and two Oxford XM-Max

80 mm² SDD X-ray detectors. A 30 kV Ga⁺ beam operating at 1-5 nA was used to mill a section from the center of the laser-heated spot, and sections measuring approximately 15x10x2 μm were lifted out and attached to a copper TEM grid. Sections were further thinned to ~1 μm using lower operating currents (50-500 pA). Backscattered electron (BSE) images were collected at an acceleration voltage of 5-10 kV. Chemical analyses were obtained with the same range of acceleration voltages using energy dispersive X-ray spectroscopy (EDS) on the same Tescan instrument, and compositions were obtained using Oxford Instruments Aztec software. Spatial resolution of the measurements was ~1 μm.

4.3 Results

4.3.1 XRD Results

The synchrotron XRD experiments were used to establish what phases are detectable at high pressures and temperatures in almandine-pyrope-grossular garnet using *in-situ* techniques. Sample pressures range from 5 to 55 GPa in these experiments. To allow for comparison of high pressure and ambient pressure diffraction patterns, sample K8 was compressed to 28 GPa, heated for 10 minutes up to 2300 K, quenched, and then decompressed to 5 GPa (Fig. 4.1). The high pressure and temperature diffraction pattern shows bridgmanite and stishovite in addition to untransformed garnet, and the decompressed pattern shows the same phases. Neither pattern had evidence for fcc, hcp, or bcc iron. Garnet persists in these patterns because the X-ray beam passes through a thin layer of unheated sample material adjacent to the diamonds. Dorfman et al. (2012) also notes that peaks corresponding to untransformed garnet persist in several samples at high pressures even after heating at 2000 K for 30 or more minutes. They attribute this to the sluggish transformation from metastable crystalline garnet to perovskite. In this pattern and all other

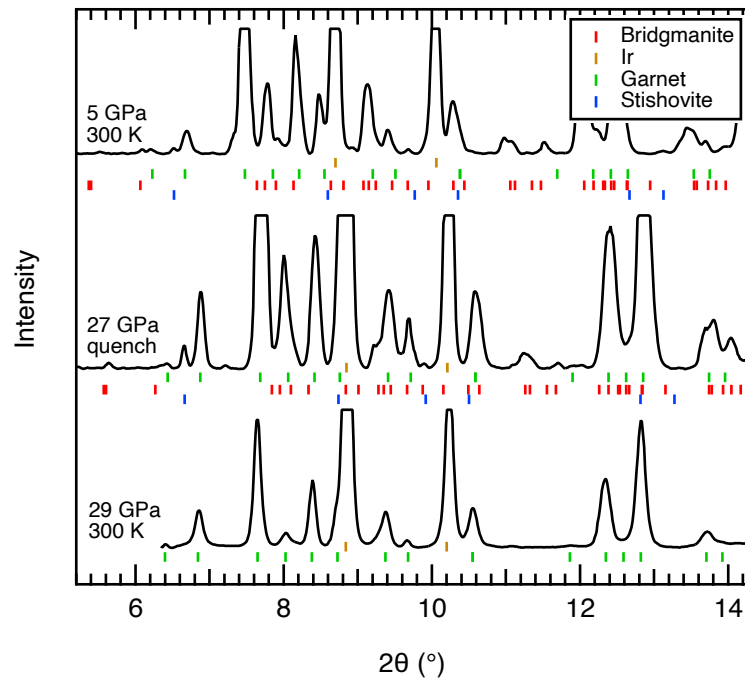


Figure 4.1. XRD patterns collected at 37 keV on a sample with an Ir foil (K8). From bottom to top, patterns correspond to unheated garnet at 29 GPa, the quench pattern, and a decompressed 5 GPa pattern. The tops of the most intense peaks have been truncated.

patterns, stishovite can be identified through the strong 110 peak. Generally, the 020, 112, 200 triplet is diagnostic for the bridgmanite phase, and the low-angle 002, 110, and 111 peaks can be used to identify bridgmanite if there is a high level of peak overlap at higher angles.

To further explore the detectable phase assemblage at higher pressures, another sample loaded with Ir foil was heated at three different pressures (K7_1, K7_2, K7_3) (Figure 4.2). At 21 GPa, the pattern quenched from 2100 K contains only stishovite and untransformed garnet. At 35 GPa, the pattern quenched from 2000 K contains stishovite, bridgmanite, davemaoite, and untransformed garnet. The pattern quenched from 3000 K at 55 GPa contains bridgmanite and untransformed garnet. Several additional samples were prepared without Ir foil and heated with *in-situ* XRD monitoring to assess any differences in heating progression and resultant phases if Ir

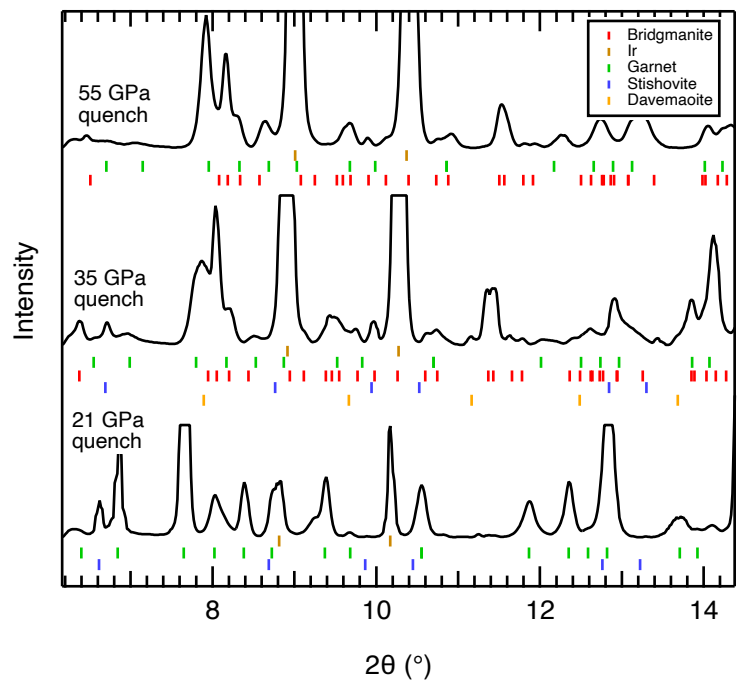


Figure 4.2. XRD patterns collected at 37 keV on a sample with an Ir foil (K7_1, K7_2, K7_3). Quench patterns at 21, 35, and 55 GPa.

is not present. Quenched XRD patterns for samples with no Ir foil were collected at 42 keV and are shown in Figure C.1. These patterns, ranging from quench pressures of 37 to 59 GPa, show evidence of stishovite, bridgmanite, davemaoite, and untransformed garnet. The davemaoite is identified primarily through the 200 and 211 peaks, and the lattice parameters appear to be slightly larger than would be expected for pure CaSiO_3 . Shim et al. (2000) note that the 200 lines of CaSiO_3 perovskite yield larger unit cell parameters than other lines as a result of non-hydrostatic stresses in the sample. The composition of the davemaoite will be discussed further below. Corundum or ilmenite structured $(\text{Al,Fe})_2\text{O}_3$ cannot be uniquely identified in each pattern because of peak overlap, but it may exist in the heated samples. Ferropericlase similarly cannot be uniquely identified in each pattern because of peak overlap but may exist in the heated samples. Synchrotron XRD measurements were also performed on a thin section of sample K11, which was

recovered and thinned using the FIB to a thickness of 1 μm . While the patterns are dominated by the Cu grid and Pt coating deposited during the FIB recovery process, we can also identify untransformed garnet, stishovite, the LiNbO_3 -type structure, and FeO (Figure C.2).

4.3.2 SEM Results

SEM analyses were conducted on several recovered samples to determine what phases could be detected using *ex situ* techniques (Table 4.1); two examples are presented here. Sample K11 was compressed to 52 GPa, melted (maximum temperature ~ 3300 K), and cooled slowly to allow growth of large observable crystals. The BSE image of the recovered section clearly reveals textures related to the temperature gradient that was generated during the heating and cooling of the sample (Figure 4.3). One can identify the boundary separating the untransformed starting material from the rest of the sample (red dashed line in Figure 4.3). Outside of this boundary, temperatures were not high enough to promote any transformation of the garnet, while immediately inside of the boundary, temperatures were high enough to promote sub-solidus phase transitions but not high enough for melting to occur. Grains in this region reach a maximum of ~ 100 nm in size. Further inward, textural changes reveal the solidus (orange dashed line in Figure 4.3), beyond which melt coexisted with solid phases. The outermost portion of this region is dominated by micron-sized Al-rich grains, followed by micron-sized grains of stishovite embedded in a bridgmanite matrix. The matrix is scattered with 100 nm-sized grains of metallic Fe, indicating that the disproportionation reaction did occur. We provide details below on how a metallic Fe grain is identified. The 100-nm sized grains are identified as metallic Fe based upon the standard BSE albedo that we find for the metallic Fe grains. It is improbable that the Fe metal was produced through only reduction because we find Fe in the silicate and only see a small

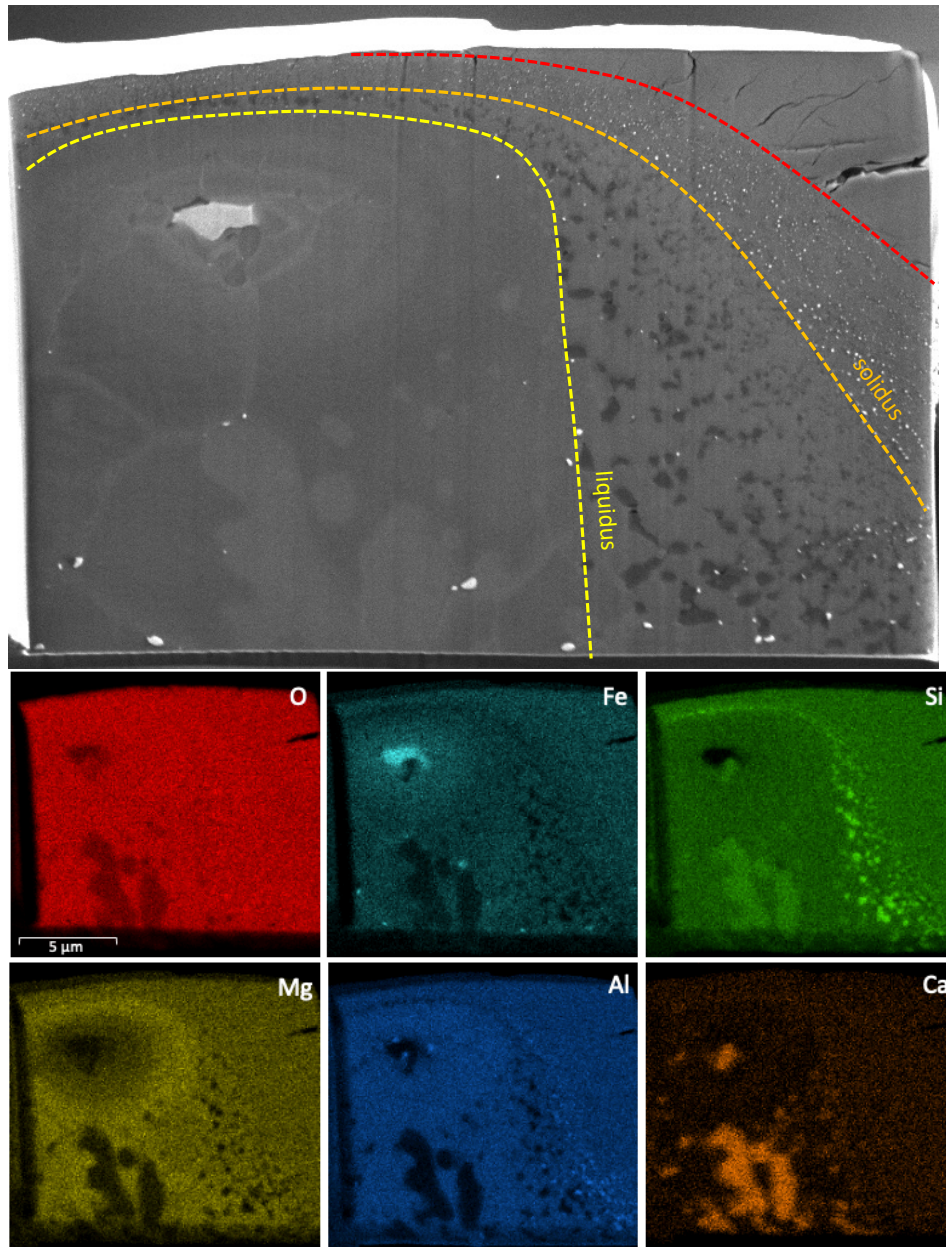


Figure 4.3. SEM results for sample K11. Top: BSE image collected at 5 kV of a section recovered from 52 GPa that was melted (3300 K) and slowly cooled (K11). Red, orange, and yellow lines indicate edge of laser-heated spot, solidus, and liquidus, respectively. The dashed box indicates the region of interest mapped in Fig. 4. Bottom: EDS maps collected at 7 kV (Si, Al, Mg) and 10 kV (Ca).

amount of Fe metal on the scale expected for disproportionation rather than reduction from an

external reactant. Inward from the solidus, we identify the liquidus, beyond which the sample texture is characterized by the gradual cooling history of the liquidus melt composition. Several large grains of davemaoite grew from the melt, along with small grains of metallic Fe. As cooling progressed, the melt became enriched in Fe and depleted in Mg, as seen in the EDS maps.

Table 4.2 shows averages of EDS measurements collected at 5 kV on the largest selected grains in K11. Because of small grain sizes and potential beam overlap, these measurements may not represent the true composition of the phases present. A composition for bridgmanite is not provided, as these grains were too small to measure. The subsolidus region should contain the same phases present in larger sizes between the solidus and liquidus: bridgmanite, metallic Fe,

Phase	O	Mg	Al	Si	Ca	Fe
Stishovite (<i>n</i> = 3)	61.9 (0.5)	2.67 (0.05)	4.54 (0.08)	24.9 (0.1)	1.5 (0.6)	4.5 (0.2)
Davemaoite (<i>n</i> = 4)	59.0 (0.3)	1.63 (0.15)	2.00 (0.14)	18.5 (0.4)	15.0 (0.6)	3.91 (0.16)
Garnet (<i>n</i> = 1)	57.32	5.17	9.94	14.38	2.57	10.62
Center (<i>n</i> = 3)	48.6 (0.4)	0.75 (0.06)	1.53 (0.02)	0.4 (0.3)	0.05 (0.09)	48.7 (0.8)
Subsolidus (<i>n</i> = 8)	57.2 (1.0)	5.2 (0.3)	10.2 (0.3)	14.8 (0.5)	2.0 (0.4)	10.6 (1.4)
Fe grain (<i>n</i> = 1)	48.45	5.25	9.88	10.45	0.68	25.28

Table 4.2. Average elemental quantities in atomic % for different phases and regions collected at 5 kV on sample K11. The number of point analyses used for measurement is given by *n* in parentheses. Standard deviations are given in parentheses below atomic % values. Instrumental uncertainty is typically 5% relative accuracy (Chidester et al., 2017). Measurements on small grains include overlap with adjacent grains. Center refers to the brightest region (melt) at the center of the laser-heated spot. Subsolidus refers to measurements taken over the subsolidus region between the orange and red lines in Figure 4.3.

davemaoite, stishovite, and Al-rich phase. An EDS map of a region between the solidus and liquidus shows grains smaller than 250 nm in diameter (Figure 4.4). The Mg and Fe maps reveal the background bridgmanite matrix, while the Si map highlights the stishovite grains, and the Al map highlights the Al-rich grains. Hotspots in the Fe map reveal the metallic iron grains. The Ca map reveals an even distribution of davemaoite. Because the disproportionated metallic Fe grains are so small, EDS spectra pick up signal from the grain as well as the surrounding material. Point measurements taken in a line across such grains, however, show a spike in Fe content at the

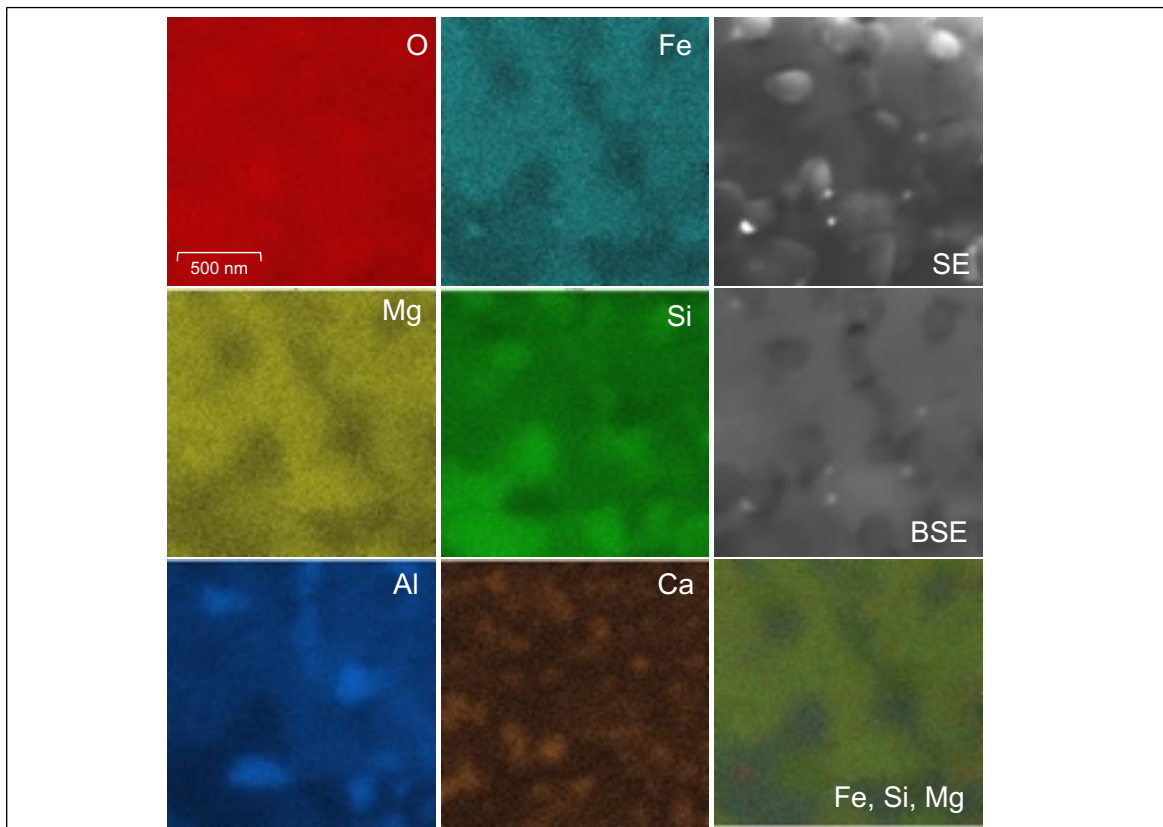
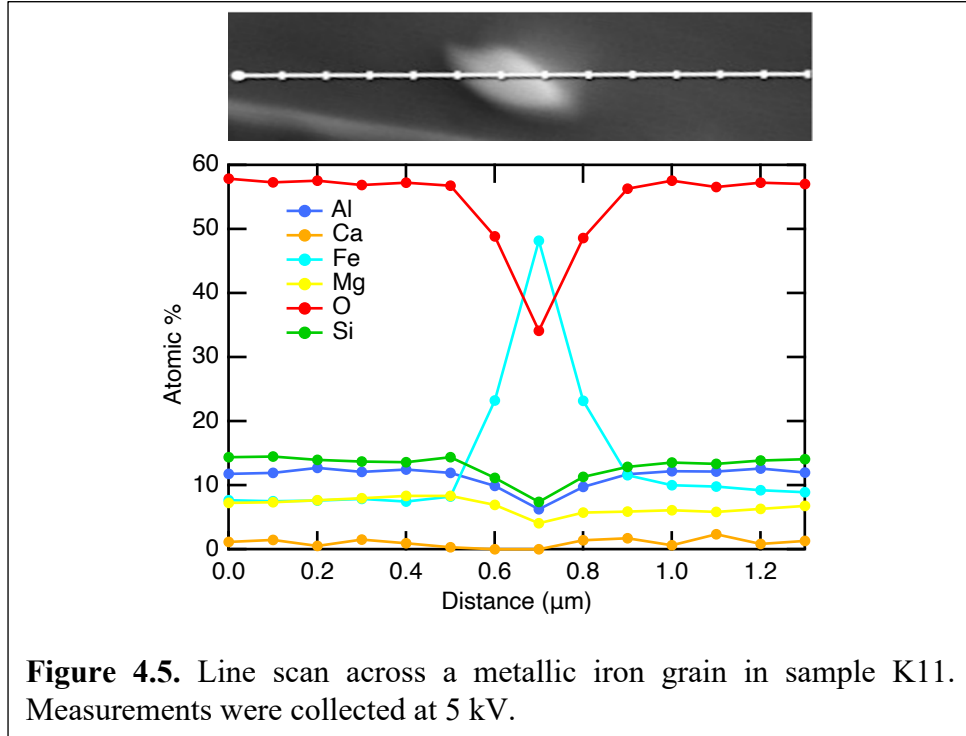


Figure 4.4. EDS maps and images collected on sample K11. Maps were collected at 5 kV as well as SE and BSE images of the region of interest (shown on larger image in Figure 4.3). A layered map including the Fe, Si, and Mg measurements is shown in the bottom right (Fe=red, Si=blue, Mg=green). Blue arrows indicate the largest metallic iron grain in the region.



expense of all other elements, including O, indicating that these grains are likely metallic Fe (Figure 4.5). Disproportionation is evident in both the subsolidus and partially melted regions of this garnet at 52 GPa, as revealed in this recovered section with BSE imaging.

To establish the occurrence of Fe disproportionation at higher pressure, we also performed recovery, imaging, and EDS mapping on sample K54, which was compressed to 64 GPa, heated at ~2200 K for 30 minutes with *in-situ* XRD collection, and quenched. Both the SE and BSE images of the recovered section reveal the new assemblage created within the laser-heated spot and the untransformed garnet outside of the hot region (Figure 4.6). Similar to the previous thin section, there is a subsolidus region adjacent to the untransformed garnet defined by nm-sized grains. Further inwards toward the center of the spot, we can observe a ring of Al enrichment and a ring of Si enrichment, similar to what was seen in the previous sample. EDS maps of the laser-heated region (Figure C.3) and point analyses along a line through the laser-heated spot (Figure

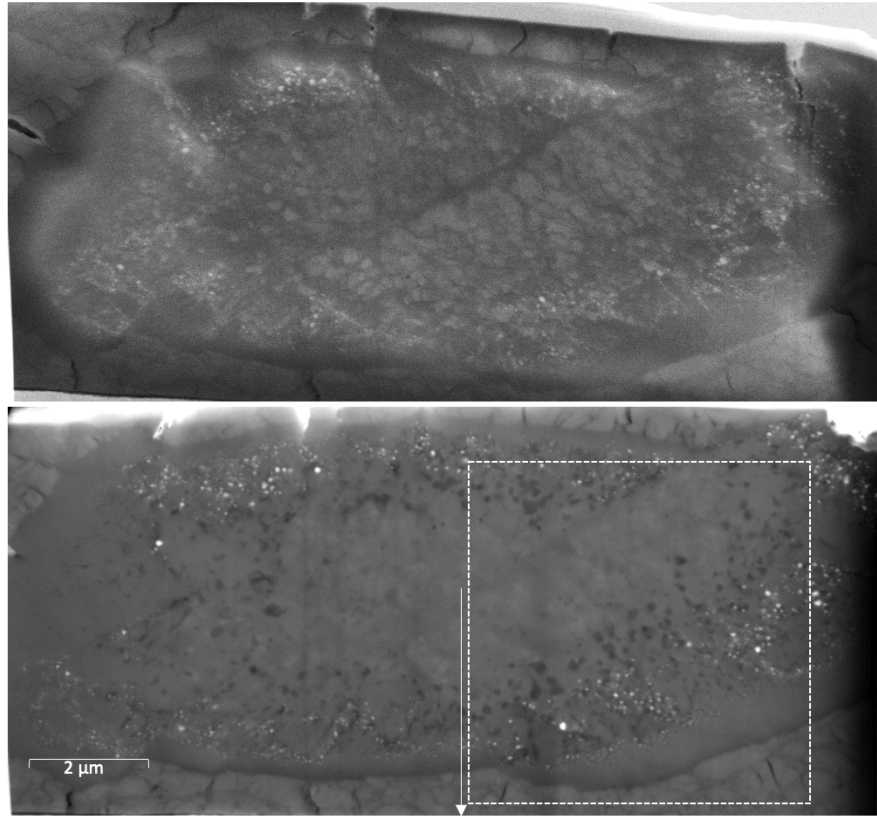


Figure 4.6. SEM images of sample K54. Top: SE image. Bottom: BSE image of a section recovered from 64 GPa that was heated at ~2200 K for 30 minutes. The small white dots in the BSE image are metallic iron and are abundant around the edges of the laser-heated spot. White dotted box and arrow show map region and line scan of Fig. S3 and Fig. S4, respectively.

C.4) show that the center of the heated region is depleted in Si and slightly enriched in Al. EDS spectra reconstructed from the EDS maps show that the region with a mixture of bright and dark grains has the same bulk composition as the garnet starting material. The bright grains in this ring are identified as disproportionated metallic Fe, similar to those seen in the previous section, while the dark grains are identified as stishovite. Overall, textures seen in the 64 GPa section (Figure 4.6) are similar to those seen in the 52 GPa section (Figure 4.3).

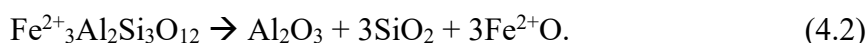
4.4 Discussion

4.4.1 Phase Relations

No metallic Fe was detectable in any of the XRD patterns from 5-64 GPa, but metallic Fe was clearly found in each of the recovered sections between 39 and 64 GPa. These findings demonstrate the possibility for Fe disproportionation to go undetected in samples that are only probed with XRD techniques. The size of the disproportionated Fe grains, as well as the presence of accompanying bridgmanite with its myriad and overlapping peaks, prevent the metallic Fe phase from being identified in XRD patterns. The presence of metallic Fe in the recovered sections, however, demonstrates that the Fe disproportionation reaction has occurred, indicating that Fe³⁺ was created alongside the metallic Fe according to the following reaction:



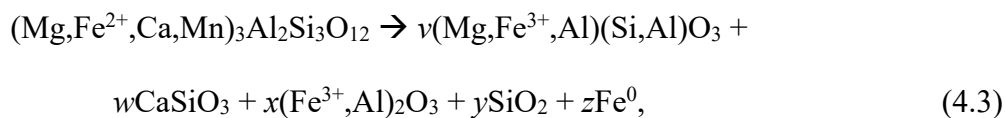
This reaction is simplified here to the decomposition of pure endmember almandine only, neglecting the pyrope, grossular, and spessartine components of the studied composition. In this reaction, Fe³⁺ enters the A site of the bridgmanite phase, shown as an FeAlO₃ component. Stishovite is also created along with metallic Fe. While the XRD results confirm the creation of only bridgmanite and stishovite, the SEM results reveal all three phases present in reaction 4.1. At lower pressure and temperature conditions where bridgmanite is not stable, almandine will decompose according to the following reaction:



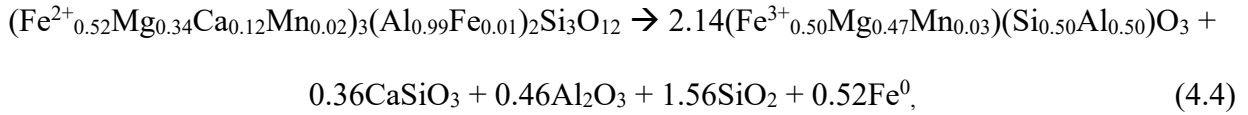
This decomposition reaction has been observed in experiments on pure almandine (Akaogi et al., 1998; Conrad et al., 1996; Dorfman et al., 2012). The results of reaction 4.2 can be seen in K7_1, which had a starting pressure of 25 GPa and showed only stishovite without bridgmanite in the XRD pattern (Figure 4.2). The untransformed garnet and Ir peaks likely obscured the wüstite and

corundum peaks in this pattern. This sample was not recovered and imaged with the SEM, so we do not have conclusive proof of the existence or absence of metallic Fe, but the absence of bridgmanite suggests that reaction 4.1 did not occur at 25 GPa in this garnet composition.

While our XRD results can confirm the presence of stishovite and bridgmanite in accordance with reaction 4.1, we note that corundum (or an ilmenite-structured Al-rich phase) cannot be ruled out as a phase present in the patterns, as the peaks could be obscured by the other phases present, and we do detect Al-rich grains in the recovered thin sections in areas of partial melt (see Figure 4.3, Figure 4.4, Figure C.3). Liu et al. (2017) demonstrated that for a pyrope composition, bridgmanite and corundum can coexist at 42 GPa and 2000 K, with Al entering the bridgmanite phase and Mg entering the corundum phase. When Fe is present, we can also expect Fe³⁺ to be incorporated into the corundum phase. The incorporation of Fe³⁺ into the Al phase in addition to its incorporation into bridgmanite further serves to drive the disproportionation reaction. Additionally, we note that ferropericlasite ((Mg,Fe)O) cannot be ruled out as a phase present in the patterns in addition to the metallic Fe. Both reaction 4.1 and reaction 4.2 could thus take place at the same time to produce both FeO and Fe metal as reaction products. Because we do not find conclusive evidence for the existence of FeO in the SEM results, in the following discussion, we will neglect the potential production of FeO. Finally, the coexistence of davemaoite with the above phases is expected from the grossular and andradite components of our starting material. An Al- and Fe-rich phase can be created in conjunction with bridgmanite, davemaoite, stishovite, and metallic Fe through the following general reaction:



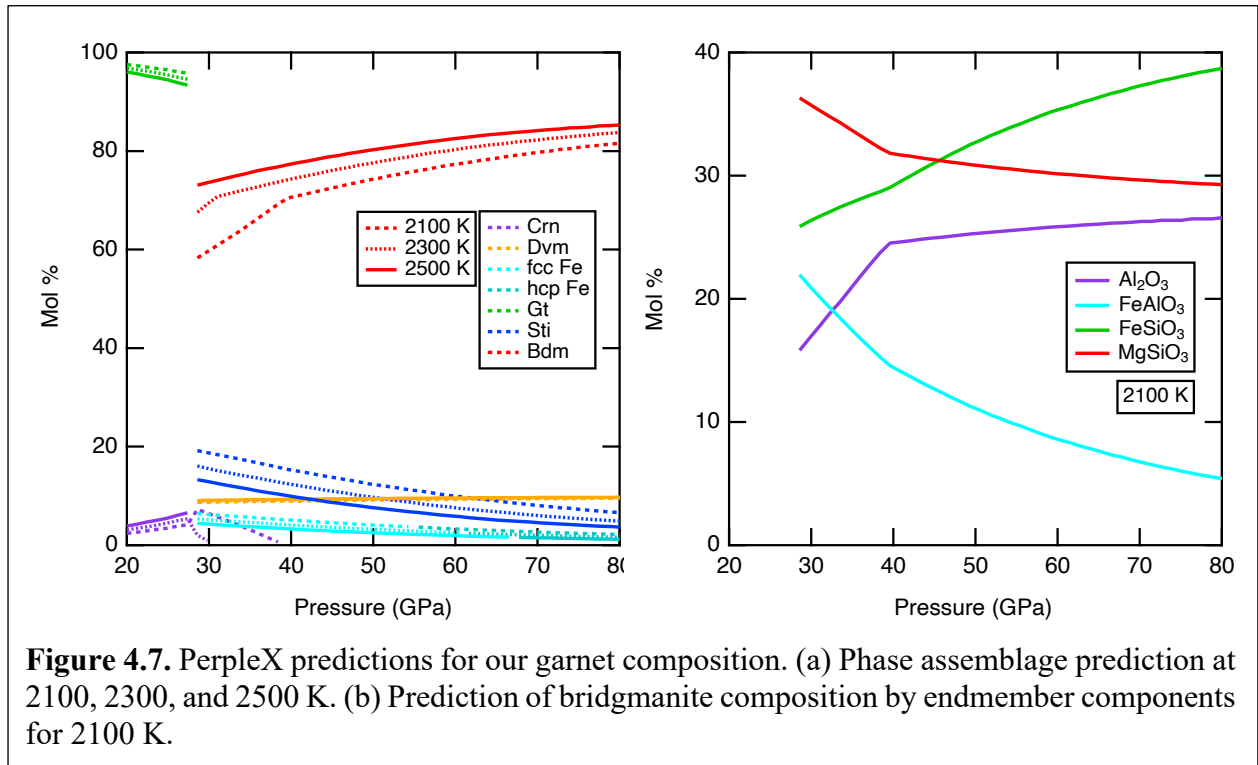
where v , w , x , y , and z represent coefficients that vary according to how the components will partition between phases. The reaction corresponding to the composition in this study ($\text{Alm}_{52}\text{Pyr}_{34}\text{Grs}_{11}\text{SpS}_2\text{And}_1$) is as follows:



with the following assumptions: all Fe^{2+} is disproportionated, all FeAlO_3 component enters bridgmanite (not corundum), all Al_2O_3 component enters corundum (not bridgmanite), and davemaoite is endmember CaSiO_3 . In the samples in this study, the occurrence of a ring of stishovite grains closer to the center of the laser heated spot surrounded by a ring of Al-rich grains can be explained by the existence of a temperature gradient in this partial melt region. While the temperature gradient indicates nonequilibrium across the entire laser-heated spot, we assume local equilibrium at each point along the temperature gradient. This will be further explored in the discussion section below.

4.4.2 *PerpleX Predictions*

The PerpleX thermodynamic calculation package (Connolly, 2005) can be used with the thermodynamic database provided by Stixrude & Lithgow-Bertelloni (2022) to predict the phase assemblage at our experimental conditions for our specific composition, and the results match well with our observations from the XRD and SEM results. Figure 4.7 shows the PerpleX phase assemblage predictions at 2100, 2300, and 2500 K from 20 to 80 GPa. In the lower mantle pressure region, we predict the occurrence of garnet, bridgmanite, stishovite, davemaoite, corundum, and fcc/hcp Fe, and the presence of each of these phases is confirmed in our XRD and SEM results. Based on the PerpleX prediction, one expects to see ~3 mol% metallic Fe, which aligns with our

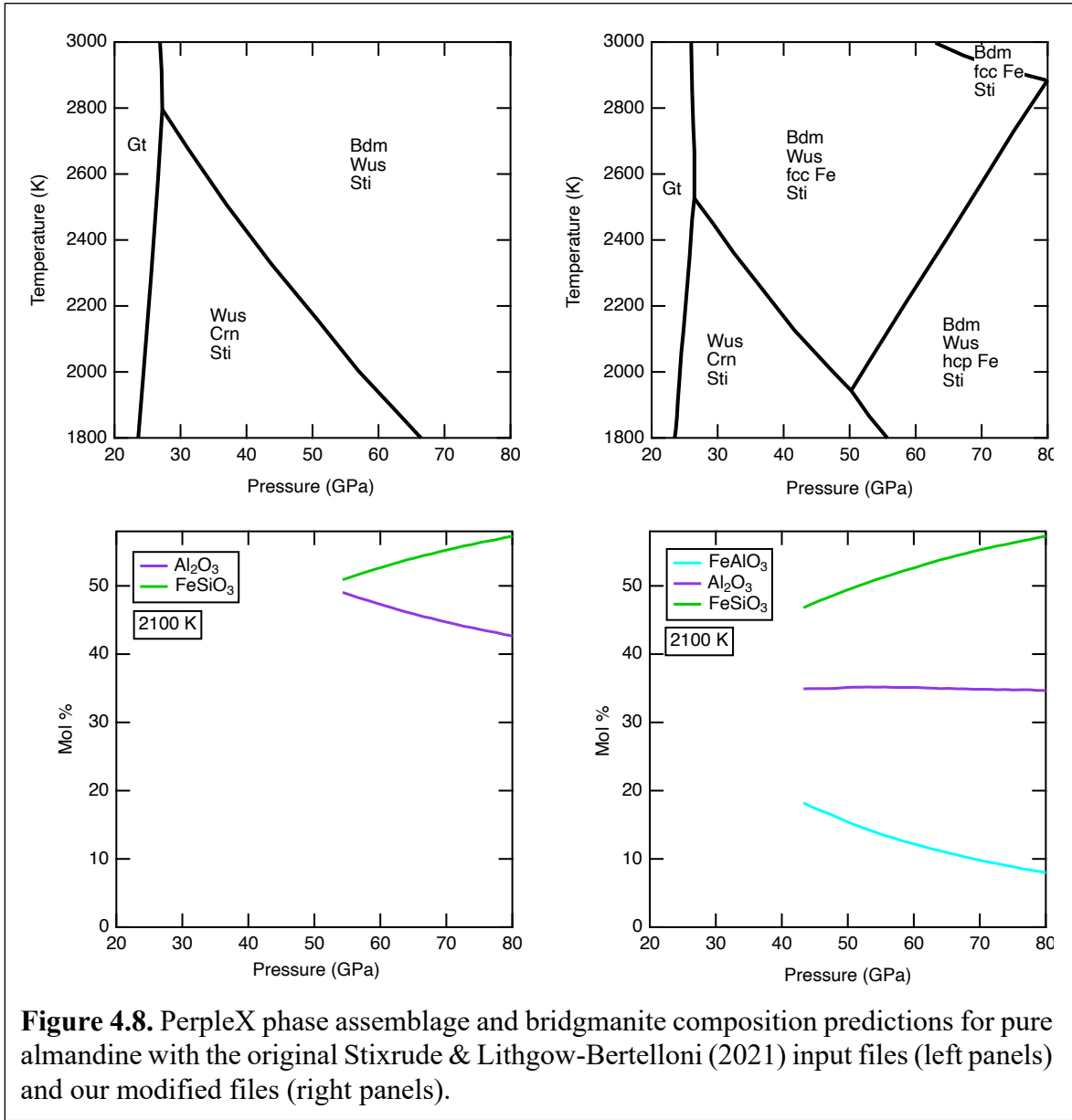


SEM images (Figures 4.3 and 4.6). Because the starting material has such high Fe^{2+} and Al contents, the amount of disproportionated metallic Fe is larger than that expected from a pyrolytic composition representing the lower mantle, which has been predicted to be ~1 wt% (Frost et al., 2004). With increasing temperature, Al_2O_3 increasingly enters bridgmanite, resulting in the disappearance of corundum at lower pressures as temperature increases. The occurrence of corundum in rings in our SEM samples can thus be confirmed as a consequence of the temperature gradient within the laser heated spot, as suggested above. The amount of stishovite present decreases with increasing temperature, but does not vanish.

Our XRD results confirming the transformation of majority almandine-pyrope-grossular garnet into bridgmanite and stishovite are also in alignment with previous work. Dorfman et al. (2012) noted that for their Alm38 composition, heating at 38 GPa produced a mixture of

bridgmanite and oxides, and with increasing pressure, the ratio of bridgmanite to oxides increased, leading bridgmanite to be the dominant phase by 45 GPa. Additionally, all compositions showed stishovite diffraction peaks on decompression and heating between 59-71 GPa. It is possible that the presence of stishovite indicates that disproportionation occurred following reaction 4.1. However, in an Alm54 sample compressed to 74 GPa and then decompressed to 23 GPa and reheated for 10 min at 1100 K, they observed a reversion to only the garnet phase, which they take to indicate that a high- pressure single phase bridgmanite existed with no major compositional gradients. They also suggest that the recovery of garnet with no other detectable phases suggests that the synthesis of bridgmanite was not accompanied by significant oxidation of Fe^{2+} to ferric iron because this would have made it more difficult to re-synthesize a single phase garnet composition. Our SEM results on a sample recovered from 64 GPa show a multiphase assemblage inside the laser heated spot rather than a single bridgmanite phase with the same composition as the starting material. It can be observed, however, that in the subsolidus rim at the edge of the spot, bright metallic Fe grains are visible closest to the partial melt region and must also exist throughout the subsolidus rim in sizes too small to be seen. The PerpleX results for our composition also likewise suggest that bridgmanite will not exist as a single phase at high pressures and temperatures for our composition.

For further context, we also calculated phase proportions and bridgmanite component proportions for pure almandine using our modified input files as well as the original Stixrude & Lithgow-Bertelloni (2022) data (Figure 4.8). We demonstrate that the inclusion of hcp and fcc iron in addition to the FeAlO_3 endmember of bridgmanite results in a notably different P-T phase space and bridgmanite composition. At 2100 K, the FeAlO_3 component is predicted to reach a maximum



of 18 mol% at 43 GPa. Dorfman et al. (2020) found that an almandine with an initial $\text{Fe}^{3+}/\Sigma\text{Fe}$ of 18% created a bridgmanite with 12% $\text{Fe}^{3+}/\Sigma\text{Fe}$ at 99 GPa, which, if correct, indicates that the Fe was somehow reduced. No accompanying phases were detected in the XRD patterns. The observation of a single bridgmanite phase does not align with our PerpleX predictions, but the quantity of Fe^{3+} roughly aligns with our prediction of FeAlO_3 content.

4.4.3 Phase Compositions

In the experiments of Kesson et al. (1995) on Alm50-Py50, Si-poor, Al-rich bridgmanite was found to coexist with stishovite at 50 GPa, and the same assemblage was observed at 60 GPa in addition to Fe in “hot spots.” In the present study, all of the samples but one exhibited the bridgmanite phase coexisting with stishovite, which is consistent with the observations of Dorfman et al. (2012) and Kesson et al. (1995) even though the composition in this study is more complex than the almandine-pyrope-grossular compositions studied by either; specifically the garnet in this study contains Ca and small amounts of Mn (Table S1). The presence of Ca stabilizes davemaoite, as seen in the XRD and SEM results as well as the PerpleX results, which may influence the composition and stability of bridgmanite. It has been shown that from 40-110 GPa above 2300 K, davemaoite will dissolve into bridgmanite in a pyrolitic composition, but we observe davemaoite in all but one of our samples above 39 GPa, regardless of temperature, likely due to the high Ca content of our starting material (Ko et al., 2022). The composition of the davemaoite in this study as given in Table 4.2 indicates that there may be minor amounts of Mg, Fe, and Al in the phase. Studies have shown a solubility of Mg into davemaoite between 5 and 10 mol% at 55 GPa and 2000 K (Armstrong et al., 2012). Fujino et al. (2004) demonstrated that the addition of Fe increases the solubility of MgSiO_3 in Ca-rich cubic perovskite coexisting with bridgmanite, with a (Mg,Fe) solubility of nearly 0.34 cations per formula unit at 78 GPa. It has also been shown that Al_2O_3 partitions preferentially into bridgmanite coexisting with davemaoite (Ricolleau et al., 2008). Given the shape of the davemaoite grain and thickness of the sample, however, it is also possible that the measurement encompasses small amounts of other phases as well. As noted earlier, the

measured lattice parameters for the davemaioite in this study are larger than would be expected. We conclude that the overestimate could be a result of nonhydrostatic stress conditions.

While we were unable to make EDS measurements on the bridgmanite in this study because of small grain size, we are able to put some constraints on its composition. In XRD measurements on a recovered thin section, we detected the LiNbO_3 structure, which corresponds to decompressed bridgmanite. Dorfman et al. (2012) also decompressed an Alm54 sample directly from 84 GPa to ambient pressure, and some of its diffraction peaks are consistent with a LiNbO_3 -type rhombohedral structure as previously reported for pyrope-almandine compositions (Funamori et al., 1997; Kesson et al., 1995). Alm100 synthesized at 90 GPa and decompressed to 5 GPa retained the orthorhombic structure but had LiNbO_3 peaks at ambient pressure. Liu et al. (2020) determined that bridgmanite with more than 33 mol% FeAlO_3 transforms into the LiNbO_3 -type phase upon decompression. We identified several diffraction peaks corresponding to the LiNbO_3 structure in the XRD patterns collected on the recovered K11 thin section (Figure C.2), indicating that the FeAlO_3 content of the high pressure bridgmanite was greater than 33 mol%. The LiNbO_3 in our sample has lattice parameters of $a = 4.863 \text{ \AA}$ and $c = 12.749 \text{ \AA}$, resulting in a molar volume of $26.207 \text{ cm}^3/\text{mol}$. Using the linear fit for LiNbO_3 volumes along the MgSiO_3 - FeAlO_3 join from Liu et al. (2020), we estimate that the bridgmanite in this sample contains 32 mol% FeAlO_3 , which is within 1% of the 33 mol% bound referenced above. This estimate falls within the range where Liu et al. (2020) saw bridgmanite at 0 GPa rather than LiNbO_3 , but it is likely that the LiNbO_3 in our study has additional components besides just FeAlO_3 , such as AlAlO_3 , which would act to decrease the volume. PerpleX calculations suggest that our garnet composition should create a bridgmanite with majority MgSiO_3 and FeAlO_3 components (Figure 4.7). At the conditions of K11

(52 GPa) in the subsolidus region, one expects ~41 mol% MgSiO₃, 39 mol% FeAlO₃, 14 mol% AlAlO₃, and 6 mol% FeSiO₃.

4.4.4 Equation of State of Bridgmanite

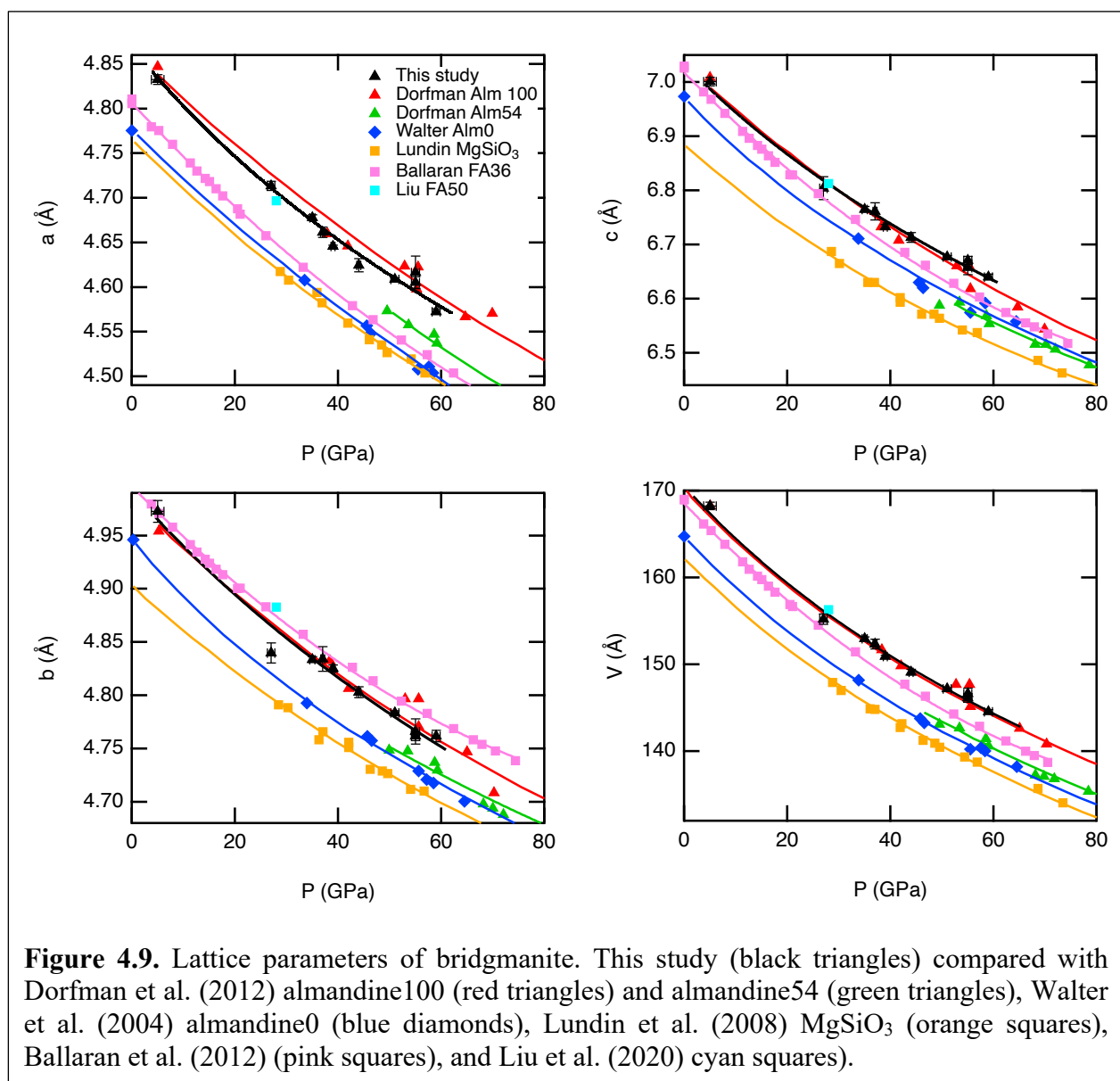
Previous studies have documented the effects of Fe³⁺ and Al substitutions into the bridgmanite structure and shown that the FeAlO₃ component increases the molar volume of bridgmanite (Huang et al., 2021; Liu et al., 2020; Vanpeteghem et al., 2006). To investigate this in the present study, bridgmanite lattice parameters and volumes (Figure 4.9) were obtained as a function of pressure for samples where more than three bridgmanite peaks could be distinctively identified upon quench after laser heating. Unit cell volumes were calculated from bridgmanite lattice parameters and fit to a second-order Birch-Murnaghan equation of state. Fitted parameters are listed in Table 4.3. These are compared to the results of Dorfman et al (2012), which include Alm100 and Alm54 (Alm₅₄Py₄₃Grs₃Sps₁), as well as Alm0 (pure pyrope, which forms (Mg_{0.75}Al_{0.25})(Si_{0.75}Al_{0.25})O₃ bridgmanite) from Walter et al. (2004), MgSiO₃ from Lundin et al. (2008), (Mg_{0.64}Fe_{0.36})(Si_{0.64}Al_{0.36})O₃ from Boffa Ballaran et al. (2012), and (Mg_{0.5}Fe_{0.5})(Si_{0.5}Al_{0.5})O₃ from Liu et al. (2020). While the almandine component of our sample is most similar to Alm54, slight differences in the proportions of components of our sample (Alm₅₂Py₃₄Gr₁₁Sp₂And₁) versus the Alm54 sample may cause the higher lattice parameter values

Composition	V ₀ (Å)	K ₀ (GPa)	K' ₀
Alm ₅₂ Py ₃₄ Grs ₁₁ Sps ₂ And ₁	170.5	257.6	4 ^a
Alm ₅₄ Py ₄₃ Grs ₃ Sps ₁ ^b	165.6	261	4 ^a
Alm100 ^b	170.6	252	4 ^a
Alm0 ^c	164.85	253.4	4 ^a

^a Parameter fixed during fit.
^b Dorfman et al. (2012).
^c Walter et al. (2004).

Table 4.3. Third-order Birch-Murnaghan fit parameters for bridgmanite.

seen in our samples, which overlap with Alm100 (Dorfman et al., 2012). Differences in lattice parameters can be attributed to inclusion of the AlAlO_3 component as well as small amounts of Ca into the bridgmanite structure (Huang et al., 2021; Ko et al., 2022). Huang et al. (2021) suggest that an increasing amount of the FeAlO_3 component in bridgmanite should result in the c lattice parameter increasing the most and the b lattice parameter increasing more than the a lattice



parameter, which is reflected in our results as well as those of other studies plotted in Figure 4.9, including Alm100, confirming the PerpleX results. Because our samples were not loaded in a pressure medium (other than five samples with Ir foil) and were not mixed with gold or platinum (like the samples of Dorfman et al. (2012) and Walter et al. (2004)), this may also affect the stress state, pressure reading, and bridgmanite composition.

4.5 Conclusions

Fe metal was positively identified in an $\text{Alm}_{52}\text{Py}_{34}\text{Gr}_{11}\text{Sp}_2\text{And}_1$ composition from 39-64 GPa using SEM analyses, and from 28 GPa upwards, bridgmanite is detected with XRD, which suggests that Fe metal was formed at these conditions as well through a disproportionation reaction. Thus, at lower mantle conditions (28-65 GPa), Fe metal is a stable part of the phase assemblage, having been produced by disproportionation of Fe, as has been observed in other mafic compositions. The lower mantle will not have the same quantity of disproportionated metallic Fe as was observed in this study, but the results nonetheless provide compelling experimental evidence across a significant range of lower mantle-relevant conditions that the incorporation of an FeAlO_3 component into bridgmanite will promote the disproportionation reaction. The PerpleX results also suggest that the amount of the FeAlO_3 component in bridgmanite decreases at higher pressures, which corresponds to a decrease in the amount of disproportionated metallic Fe with increasing pressure. The FeAlO_3 component may affect the elastic properties of bridgmanite, and the metallic Fe can alloy with siderophile and volatile elements in the lower mantle, affecting their distribution.

The phase assemblage in this study also consists of bridgmanite, stishovite, corundum, and davemaoite, as determined by X-ray diffraction, and is consistent with prior work (Dorfman et al.,

2012; Kesson et al., 1995). However, because of the low abundance of Fe metal and small grain size, XRD was not sufficient to detect the disproportionation reaction, and examination of the recovered product by FIB/SEM was required. The bridgmanite was found to decompress to the LiNbO_3 -type structure, indicating a high FeAlO_3 content, which was confirmed with PerpleX predictions.

5 DISPROPORTIONATION OF IRON IN PYROLITE FROM 24 TO 132 GPA

5.1 Introduction

It has been proposed that metallic iron exists as an accessory phase in the lower mantle, as a result of the disproportionation of Fe^{2+} to Fe^{3+} and Fe^0 (Frost et al., 2004). This has significant implications for the siderophile element geochemistry of the lower mantle, notably through its impact on isotopic tracers such as Os, and on platinum group element distributions. Metallic iron could also serve as a likely host for some volatile elements in the lower mantle, such as C, S, and H, impacting the mantle's carbon, sulfur, and hydrogen budgets. It is understood that bridgmanite is the dominant phase in the lower mantle, and it has been shown that the presence of Al promotes the partitioning of Fe^{3+} into the perovskite structure as an FeAlO_3 component, charge balanced by metallic iron. Frost et al. (2004) proposed that this disproportionation process occurs in the lower mantle, where the formation of aluminous perovskite implies the precipitation of approximately 1 wt% metallic Fe-rich alloy. In the time since Frost et al (2004). introduced the proposed lower mantle disproportionation reaction, several researchers have either acknowledged or directly used the reaction to justify results in their work (examples include Galimov, 2005; Vanpeteghem et al., 2006; Zhang and Oganov, 2006; Ryabchikov & Kaminsky, 2014; Smith et al., 2016; Andrault et al., 2017; Xu et al., 2017; Shim et al., 2017; Kurnosov et al., 2017; Bindi et al., 2020; Piet et al., 2020). Evidence for disproportionated metallic Fe coexisting with aluminous bridgmanite has also been found in a shock vein of the Suizhou meteorite (Bindi et al., 2020). However, literature data conflict on the pressure, temperature, and composition space in which this reaction occurs across the lower mantle, and there has been little subsequent study to confirm this process at deeper lower mantle conditions.

We will briefly review the existing literature on pyrolite and lower mantle-relevant compositions. X-ray diffraction (XRD) studies on pyrolite and lower mantle-relevant compositions have primarily been used to confirm the existence of the major phases present in the lower mantle assemblage and/or track the volume evolution of the major phases with increasing pressure. XRD studies confirm the presence of bridgmanite, ferropericlase, and davemaoite from 25 GPa to 113 GPa, but no XRD studies identify the occurrence of the iron disproportionation reaction at lower mantle conditions (Lee et al., 2004; Murakami et al., 2005; Ono et al., 2005; Fiquet et al., 2010; Irifune et al., 2010; Sinmyo et al., 2011; Prescher et al., 2014; Tateno et al., 2014).

Scanning electron microscopy (SEM) studies on pyrolite and lower mantle-relevant compositions yield inconsistent observations of iron disproportionation (Irifune, 1994; Lauterbach et al., 2000; Frost et al., 2002; Frost et al., 2004; McCammon et al., 2004; Murakami et al., 2005; Irifune et al., 2010; Sinmyo et al., 2011; Sinmyo et al., 2013; Prescher et al., 2014; Piet et al., 2016; Andrault et al., 2017; Creasy et al., 2020; Lobanov et al., 2020; Huang et al., 2021; Ko et al., 2022; Tsujino et al., 2023). Figure 5.1 shows all of the documented observations of disproportionated metallic Fe in SEM/TEM studies across the pressure-temperature range of the lower mantle, as well as results in which metallic Fe was not observed. Table D.1 provides details on these studies. Comparisons between the various studies shown in Figure 5.1 are complicated by the different starting compositions and experimental techniques used. The studies include both multianvil and diamond anvil cell (DAC) techniques with SEM and TEM imaging. Studies performed in a multianvil apparatus may have samples exposed to oxidizing agents, as recognized by Irifune et al. (2010) (supplemental information). Compositions include pyrolite, peridotite, and pyrolite-like

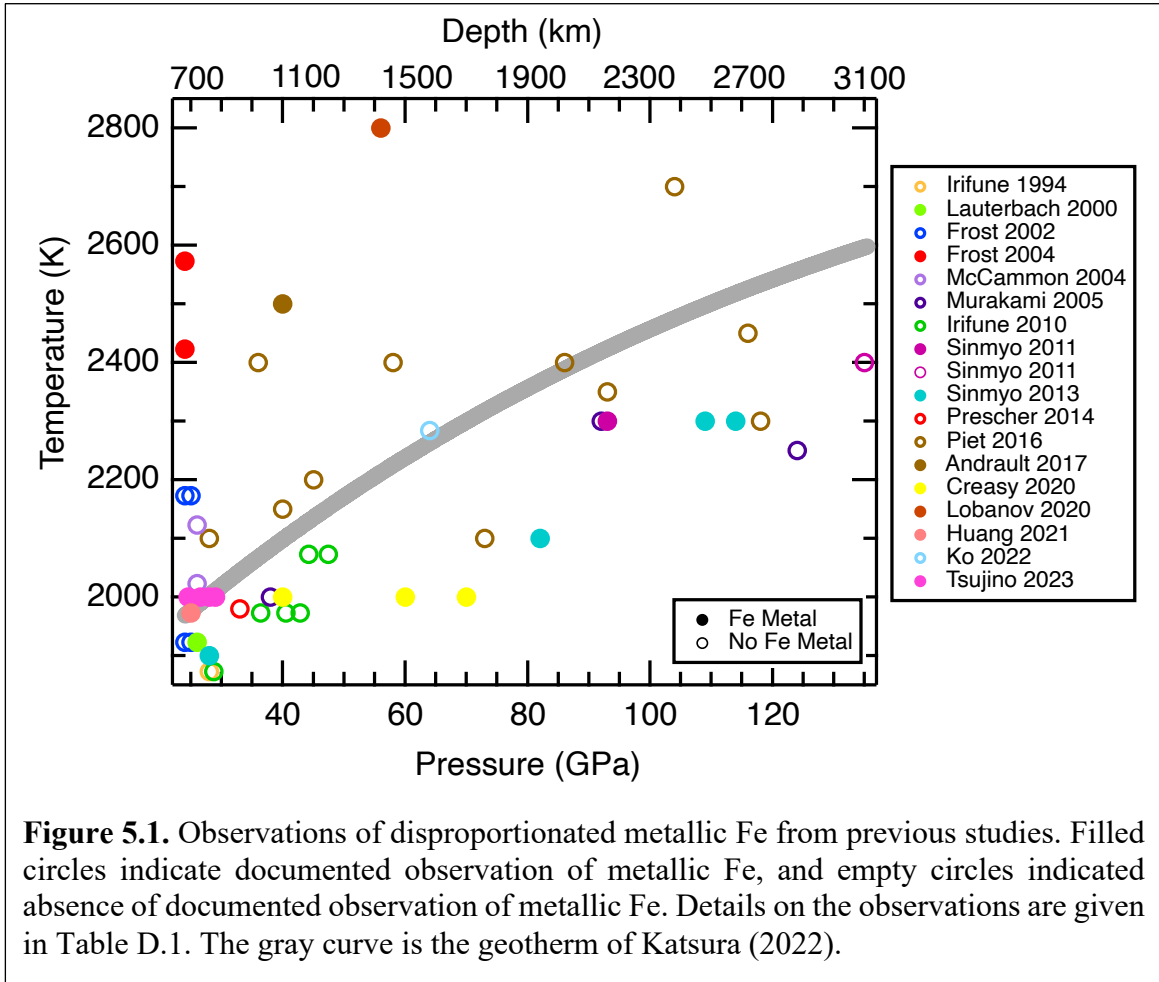


Figure 5.1. Observations of disproportionated metallic Fe from previous studies. Filled circles indicate documented observation of metallic Fe, and empty circles indicated absence of documented observation of metallic Fe. Details on the observations are given in Table D.1. The gray curve is the geotherm of Katsura (2022).

mixtures such as Al-rich pyroxenes. Additionally, none of these studies were designed specifically to detect or identify disproportionated metallic Fe, so any metallic Fe could have been overlooked or not documented if seen.

To provide some clarity on this issue, we have performed laser-heated diamond anvil cell experiments on pyrolite glass at lower mantle conditions. We use XRD, SEM, and TEM techniques to analyze these samples, in which we find evidence for the disproportionation of iron at deep mantle conditions. We supplement these experimental results with thermodynamic phase equilibrium modelling using the PerpleX Gibbs energy minimization software (Connolly, 2009).

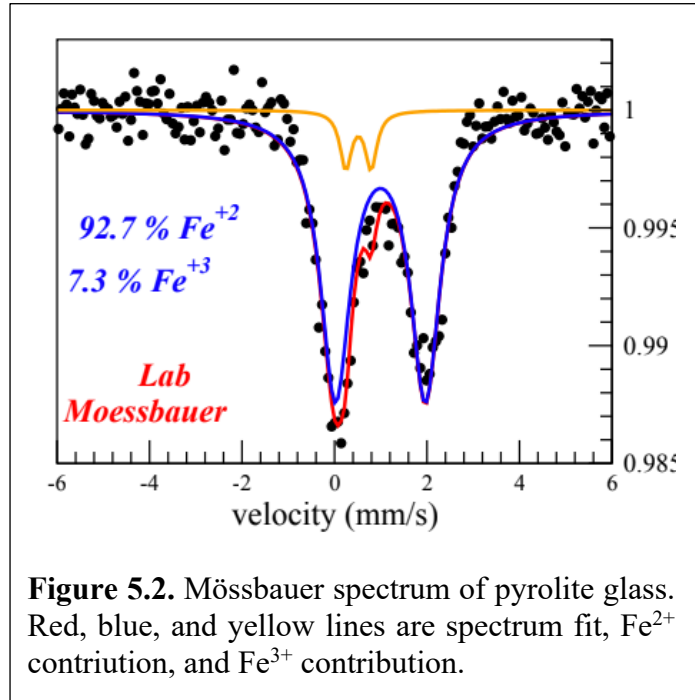
5.2 Materials and Methods

We synthesized a powder sample of pyrolite from a mixture of high-purity oxide powders. MgO, SiO₂, Al₂O₃, and CaSiO₃ were dehydrated in a furnace at 1000 °C for 24 hrs. These powders and FeO powder were each individually ground in a mortar and pestle without ethanol and then mixed together to produce a pyrolite composition following the major element proportions of Ringwood (1975). The FeO powder was not dehydrated in the furnace because we did not want the iron to oxidize. Ethanol was not used in the mortar and pestle process to avoid contamination of the powders with organics. The composition of the powder is given in Table 5.1. A portion of the powder mixture (7.26 mg) was pressed into a pellet and fused at 2000 °C for 10 s in an aerodynamic levitation laser furnace at Indiana University – Purdue University Indianapolis using Ar carrier gas, creating a glass bead of 1.64 mm diameter (Figure D.1). Having the majority of Fe in the sample in the Fe²⁺ oxidation state is essential for the study of disproportionation. Mössbauer spectroscopy was performed at the offline laboratory of Sector 3 at the Advanced Photon Source on a chip of the starting glass material and indicates $\frac{Fe^{3+}}{\Sigma Fe} = 7.3\%$ (Figure 5.2).

Oxide	Ringwood 1975 wt%	This study powder	This study glass wt%	Element	Ringwood 1975 at%	This study at%	Ringwood 1975 wt%	This study wt%
MgO	38.56	40.00	39.76	Mg	20.11	21.12	23.25	23.98
SiO₂	45.65	44.90	44.17	Si	15.98	15.78	21.34	20.65
Al₂O₃	4.66	4.08	5.76	Al	1.92	2.41	2.47	3.05
CaO	3.14	2.99	2.91	Ca	1.18	1.11	2.24	2.08
FeO	8.00	8.02	10.24	Fe	2.34	2.81	6.22	7.96
				O	58.47	56.77	44.49	42.28

Table 5.1. Composition of the starting material compared to Ringwood (1975). O values are determined assuming all of the oxides are stoichiometric. This study wt% glass values are calculated from the non-O wt% element values.

For all experiments, the pyrolite glass bead was broken into small fragments, which were loaded in 50-100 μm -sized holes drilled through pre-indented Ni or W gaskets. Ni gaskets were used for samples below 55 GPa, while W gaskets were used for samples above 55 GPa. With the exception of 3 samples loaded with Ar, the samples were not loaded with any



pressure medium. We are not concerned with non-hydrostaticity of the samples because phase assemblages are crystallized during laser heating, which reduces non-hydrostatic stresses. Lee et al. (2004) also documented that there was no correlation between presence or absence of an Ar medium and observed scatter in measured volumes of phases present in experiments performed on a pyrolitic sample with and without Ar loading (Figure 2 of that paper). Similarly, Ono et al. (2005) found no obvious differences in phase relations and cell parameters between samples with and without Ar or NaCl. Symmetric diamond anvil cells with 100-300 μm culets were used to achieve pressures up to 132 GPa. Pressures were determined using Raman spectroscopy on the diamond anvil culets before and after laser-heating (Akahama & Kawamura, 2004). Pressures at high temperatures were calculated with the approximation of a 1% increase in pre-heat pressure per 250 K increase, after Fischer et al. (2015) and Chidester et al. (2017). Table 5.2 gives a list of experimental conditions and analysis details.

Sample	Pressure medium	Pre-heat P (GPa)	Post-heat P (GPa)	Est. P at high T (GPa)	T (K)	Heating time	Analysis method
K75	None	27.0 ±0.4	24.5	29.2	2000 ±50	30 min	XRD, SEM
K78	None	35.0 ±0.4	35.9	37.8	2000 ±50	30 min	XRD
K59	None	39.2 ±0.4	n.c.	42.4	2015 ±90	24 min	mXRD, SEM, TEM, STEM
K60	None	38.8 ±0.4	36.6	41.7	1875 ±15	1 hr	SEM, TEM, STEM
K67	None	55.3 ±0.8	n.c.	59.6	1965 ±90	10 min	SEM, TEM
K74	None	54.0 ±1	52.0	58.6	2150 ±50	35 min	XRD
K79	Ar	59 ±1	62	64.3	2700 ±200	12 min	XRD
K76	None	71.9 ±0.9	70.0	78.4	2260 ±50	30 min	XRD, SEM, TEM, STEM
K83	None	94.2 ±1.0	n.c.	103.8	2560 ±100	5 min	SEM, STEM
K80	Ar	92 ±3	99.8	100.1	2200 ±200	8 min	XRD
K84	None	110.0 ±1.0	107.7	120.6	2400 ±100	11 min	SEM, TEM, STEM
K85	None	127.4 ±1.2	124.8	140.3	2540 ±150	6 min	SEM
K81	Ar	131.5 ±1.1	135.0	147.3	3000 ±200	15 min	XRD
K86	None	132.9 ±1.1	129.0	147.3	2700 ±200	11 min	SEM, TEM STEM

Table 5.2. Experiment details. Pressure was determined by diamond Raman. Pressure uncertainties are from error associated with locating the diamond Raman edge. Temperatures are average of upstream and downstream measurements over the entire heating time. Temperature uncertainties are from the standard deviation of the upstream and downstream averages. n.c.: not collected.

XRD was performed at the GSECARS beamline 13-ID-D (APS, Argonne National Laboratory). Diffraction patterns were collected using a CdTe 1M Pilatus detector. The position and orientation of the detector was calibrated using a LaB₆ NIST standard. The X-ray energy was tuned to either 37 keV (0.3344 Å) or 42 keV (0.2952 Å) and focused to full width, half max dimensions of 2 μm x 3 μm. Double-sided laser-heating (or single-sided laser-heating) of the

samples was carried out with *in-situ* XRD measurements (Prakapenka et al., 2008). 1064 nm fiber lasers were shaped to ~ 10 μm radius flat tops and aligned with the X-ray beam. Temperatures were measured on both sides using spectroradiometry and fitting to a gray body approximation (Heinz & Jeanloz, 1987). Diffraction images were integrated to produce 1-D diffraction patterns using the Dioptas software (Prescher & Prakapenka, 2015). A recovered thin section of sample K59 was measured with micro-XRD at beamline 34-ID-E (APS, Argonne National Laboratory).

Samples that were not analyzed with XRD techniques were laser heated with a 1064 nm fiber laser at the University of Chicago. In these experiments, the laser spot size was approximately 20 μm and temperatures were measured on both sides by multispectral imaging radiometry (Campbell, 2008). All non Ar-loaded samples exhibited stable subsolidus heating for temperatures ranging from 1800 K to 2700 K. The transition to bridgmanite in Fe-rich silicates is accompanied by a color change from transparent to dark brown (Kesson et al., 1995; O'Neill & Jeanloz, 1994). The transformed phase assemblage is easily identifiable when using an optical microscope, as demonstrated in Figure 5.3. All samples were quenched from high temperature.

Samples were recovered from high pressure and temperature conditions and prepared for SEM analysis using the focused ion beam (FIB) in the Tescan Lyra3 field-emission SEM in the Department of the Geophysical Sciences at the University of Chicago. A 30 kV Ga^+ beam operating at 1-5 nA was used to mill a section from the center of the laser-heated spot, and sections measuring approximately $15 \times 10 \times 2$ μm were lifted out and attached to a copper TEM grid. Sections were further thinned to ~ 1 μm using lower operating currents (50-500 pA). Backscattered electron (BSE) images were collected at an acceleration voltage of 5-10 kV. Chemical analyses were

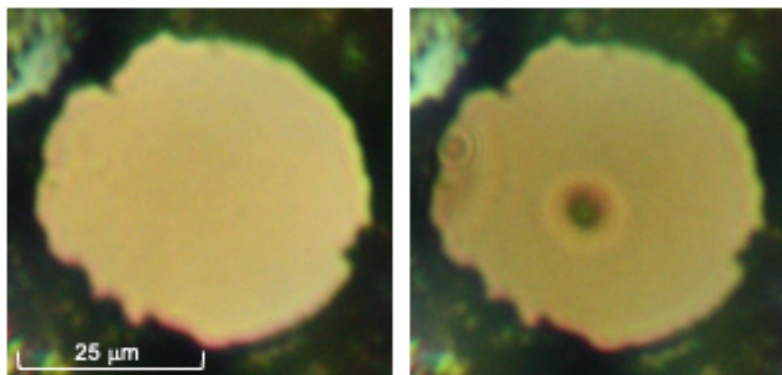


Figure 5.3. Optical microscope image of the laser-heated spot. Left: Compressed and unheated pyrolite glass. Right: Heated pyrolite glass (still compressed). Laser-heated spot (new phase assemblage) is clearly visible in the center of the chamber.

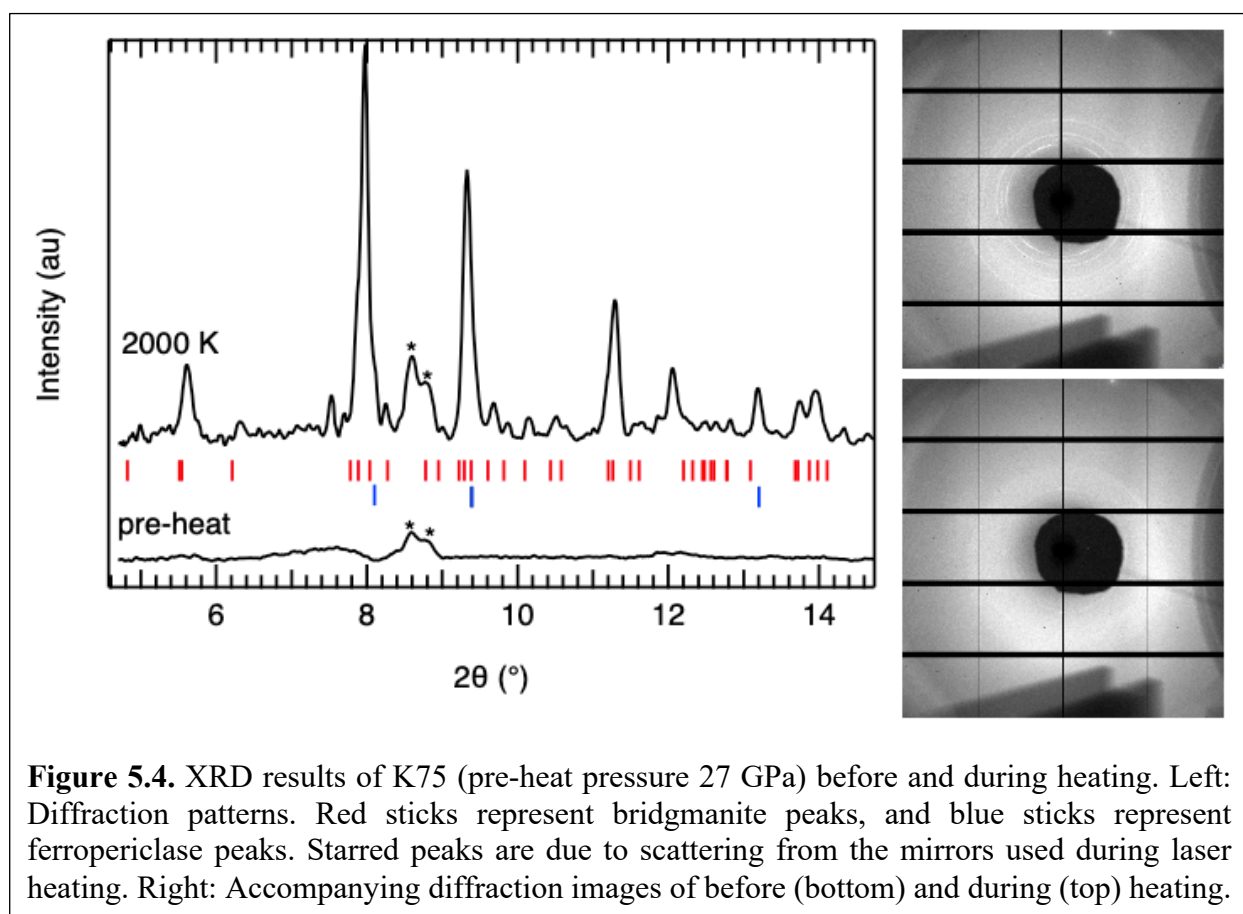
obtained with the same range of acceleration voltages using energy dispersive X-ray spectroscopy (EDS) on the same Tescan instrument, and compositions were obtained using Oxford Instruments Aztec software. Spatial resolution of the measurements was $\sim 1 \mu\text{m}$.

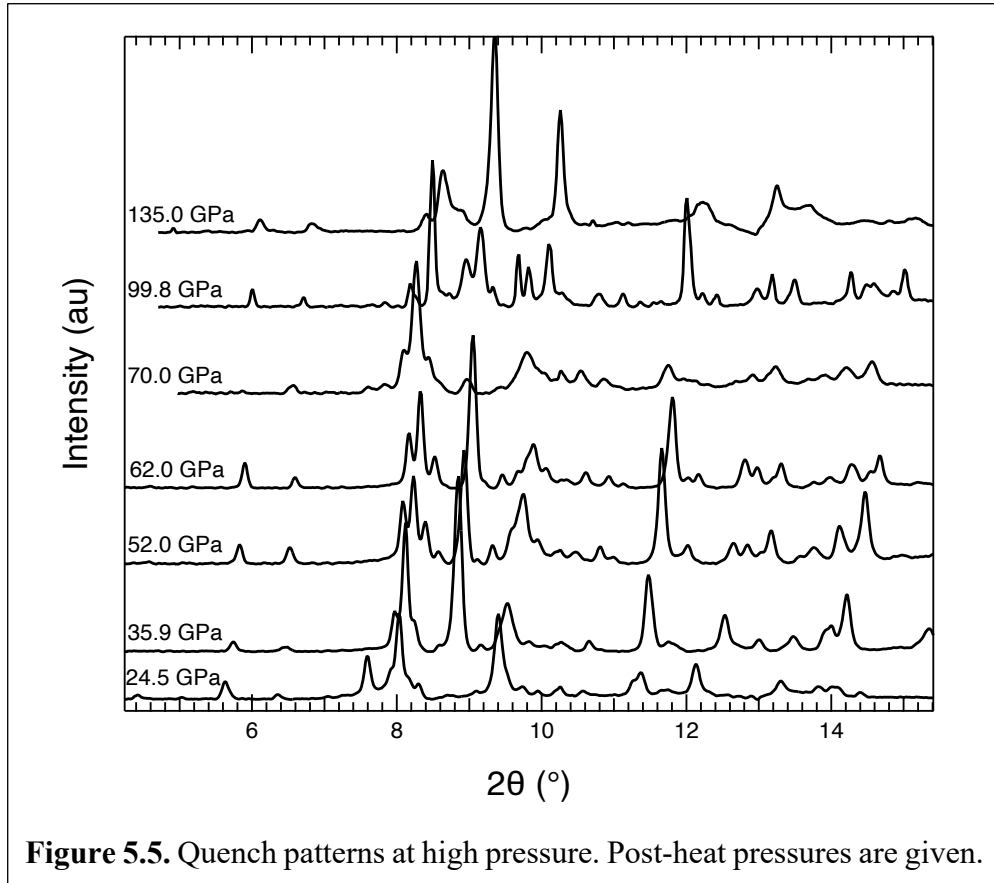
Several samples were further thinned using the FIB to $< 100 \text{ nm}$ for TEM and/or STEM imaging and analysis. We use the JEOL JEM-3010 TEM at the University of Illinois at Chicago, which has a LaB_6 electron source with a 300 kV electron beam. Images are collected with a Gatan Orius SC200 CCD camera using Digital Micrograph software. For scanning TEM work, we use the JEOL JEM-ARM200CF Aberration corrected cold field emission STEM at the University of Illinois at Chicago, operated at 200 kV. The microscope is equipped with HAADF, LAADF, and BF detectors, and images are collected with a Gatan CCD camera. The microscope is also equipped with an Oxford X-max 100TLE windowless SDD X-ray detector capable of atomic resolution EDS mapping.

5.3 Results

5.3.1 XRD Results

The synchrotron XRD experiments were used to confirm that our pyrolite glass produces the expected phase assemblage detected in other *in-situ* XRD experiments (bridgmanite, ferropericlasite, and davemaoite) and explore the compressional behavior of bridgmanite. Sample pressures range from 27 GPa to 131.5 GPa in these experiments. In each synchrotron XRD experiment, we observe the formation of bridgmanite and ferropericlasite at high pressure and temperature conditions that roughly follow the geotherm (Figure 5.4). Davemaoite is likely also part of the phase assemblage, but because of peak overlap and its low abundance, unique peaks



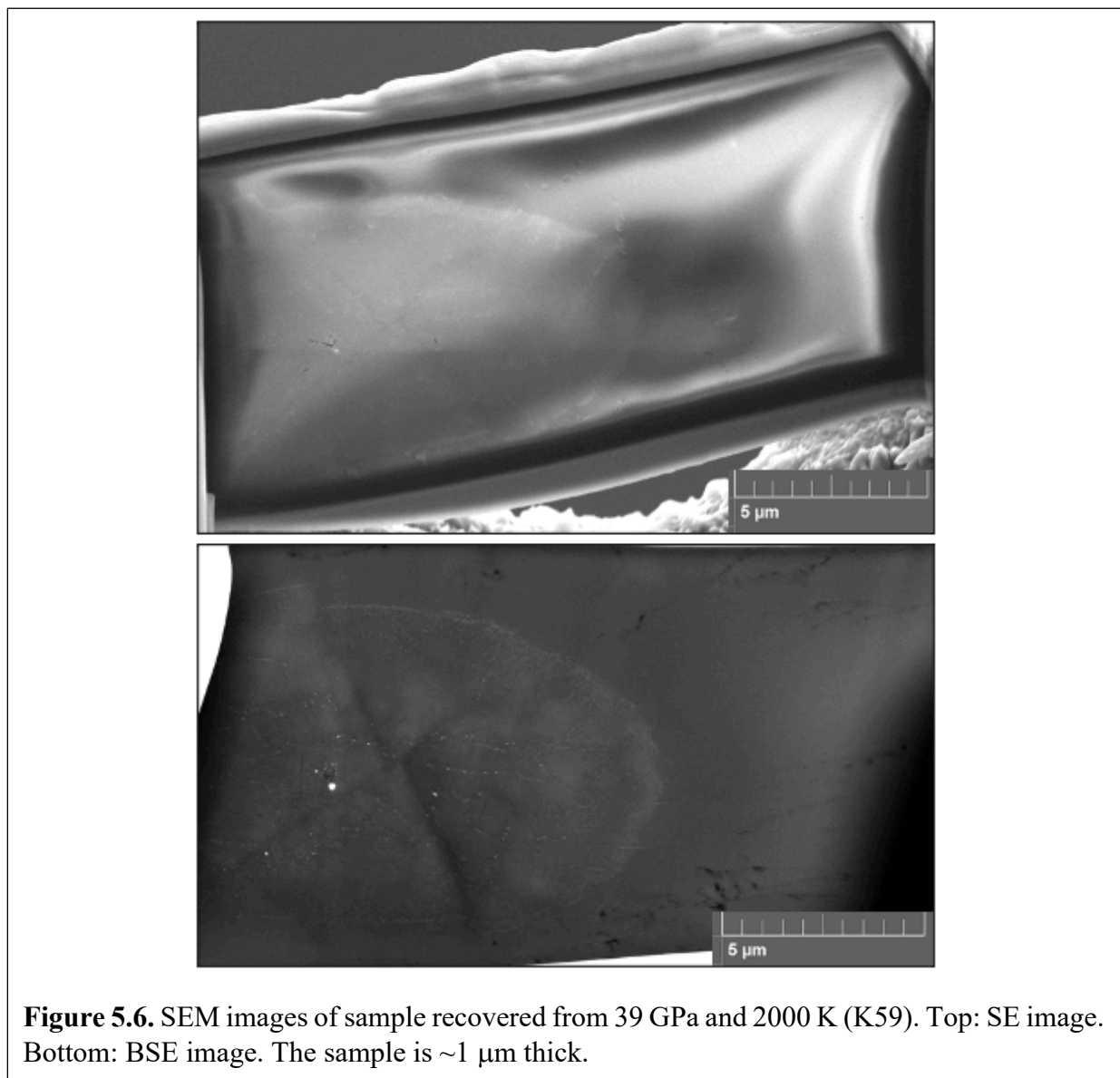


cannot be identified in most patterns. The strongest evidence for davemaoite is found in experiments K80 and K81, which both likely experienced melting temperatures that allowed larger davemaoite grains to grow. These samples experienced melting because the glass was slow to transform to the lower mantle phase assemblage at temperatures along the geotherm (likely due to the Ar-loading and thinness of the sample), which led us to drastically increase temperature until the expected phase changes occurred. Ono et al. (2005) noted a similar difficulty in raising the temperature of the sample when using pressure transmitting media. The phase assemblage is not observed to change during heating, even for samples heated for up to 30 minutes. The created phase assemblage is very fine-grained, as evidenced by the fine rings seen in the diffraction

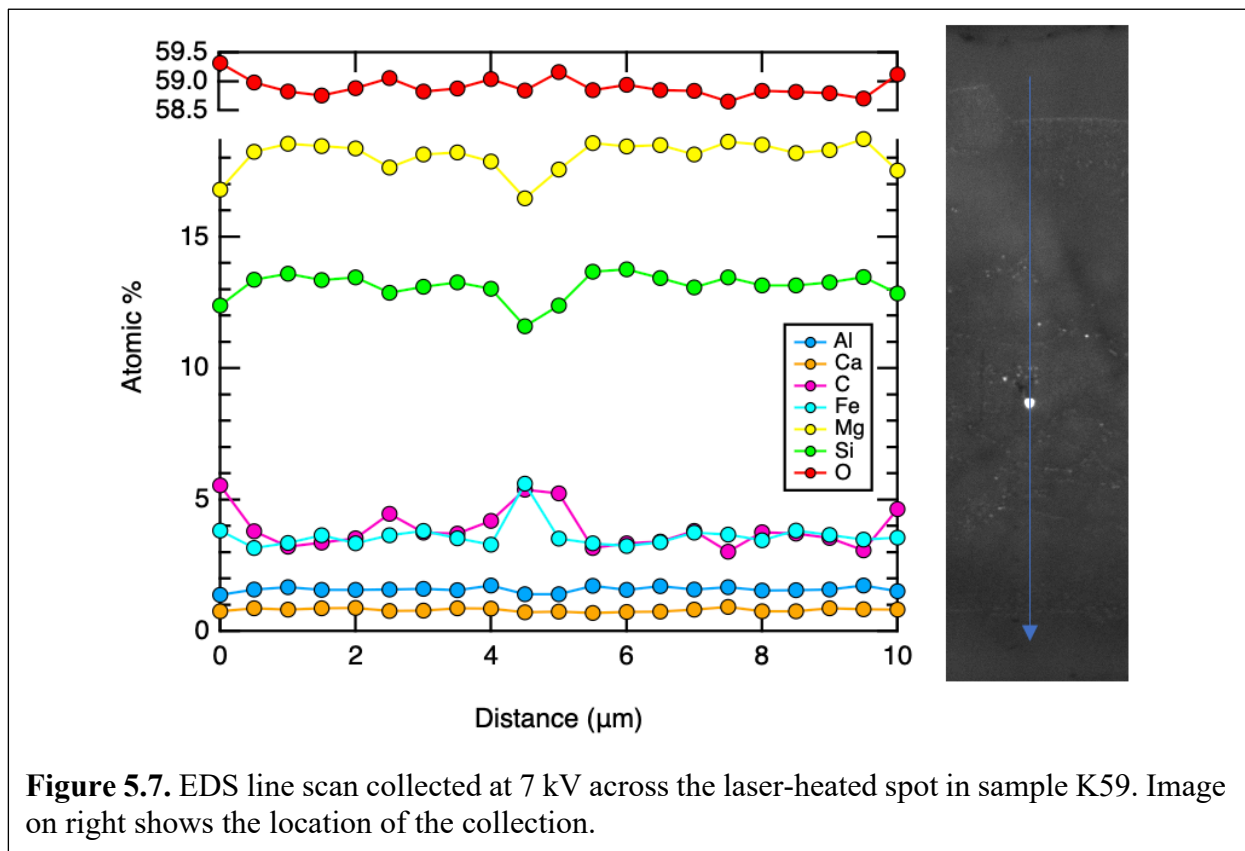
images. XRD patterns were also collected upon quench at high pressures (Figure 5.5), as well as upon decompression to ambient pressure (Figure D.2 and Figure D.3).

5.3.2 SEM Results

SEM, TEM and STEM analyses were conducted on samples recovered from 27 GPa to 132 GPa. In all samples, both secondary electron (SE) and backscattered electron (BSE) images reveal the laser-heated spot, which contains the transformed lower mantle phase assemblage (Figure 5.6).



The SE image reveals the textural difference between the untransformed glass and the transformed phase assemblage inside the laser-heated spot. As seen in Figure 5.6, the untransformed glass is homogeneous, and the laser-heated portion of the sample is very fine-grained, with grain sizes on the scale of 10's to 100's of nm. The BSE image reveals bright grains dispersed throughout the laser-heated spot. In BSE images, albedo is proportional to mean atomic number. These grains can be shown to be metallic Fe, as demonstrated below. Because the grain sizes are so small, SEM EDS measurements show little variation across the laser-heated spot (Figure 5.7 and Figure D.4). A line scan across sample K59 collected at 7 kV reveals that across the laser-heated spot, the bulk composition remains constant. A slight spike in Fe content (and drop in Mg and Si) is seen over the largest Fe grain in the center of the laser-heated spot. Carbon is measured in low levels (<5



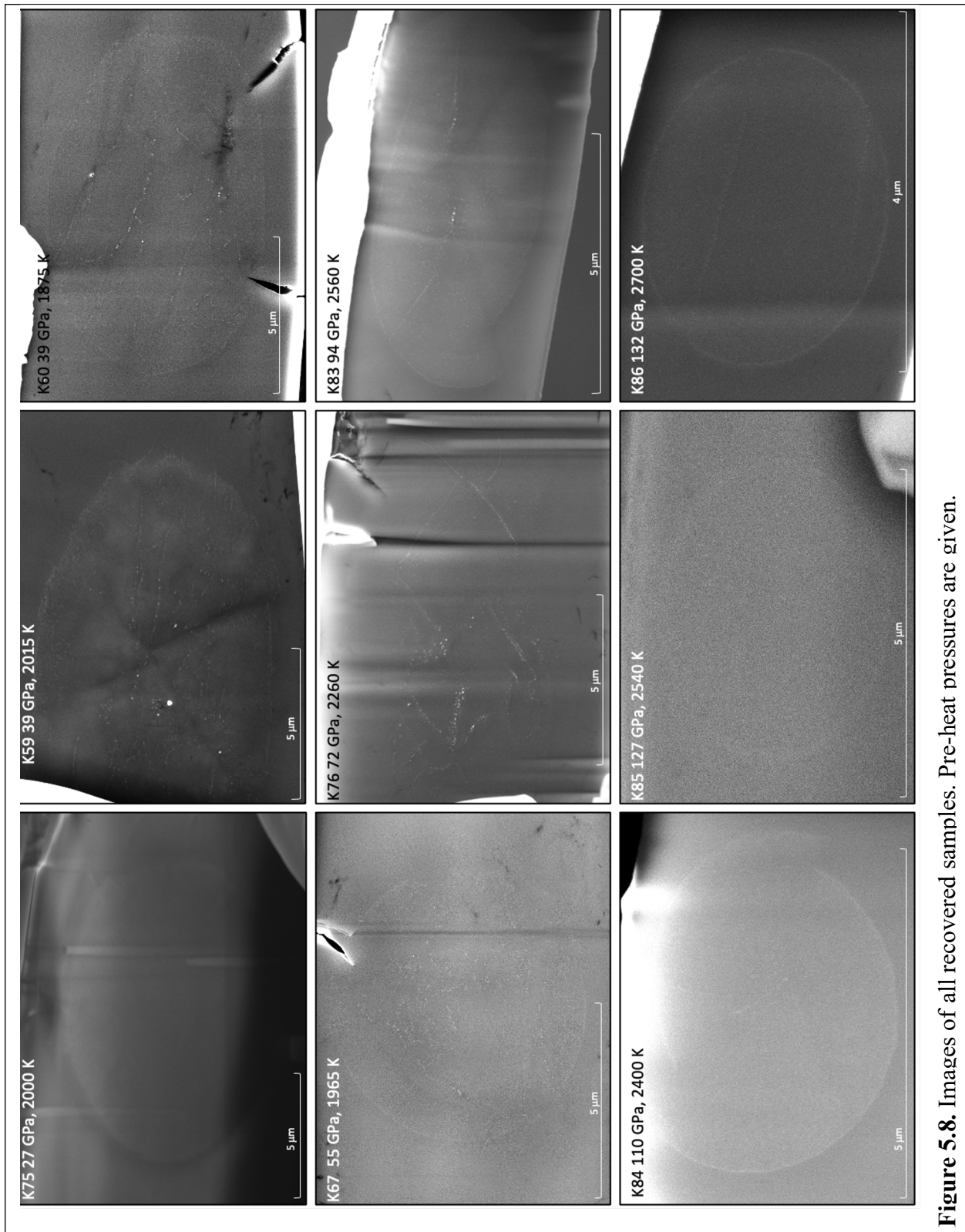
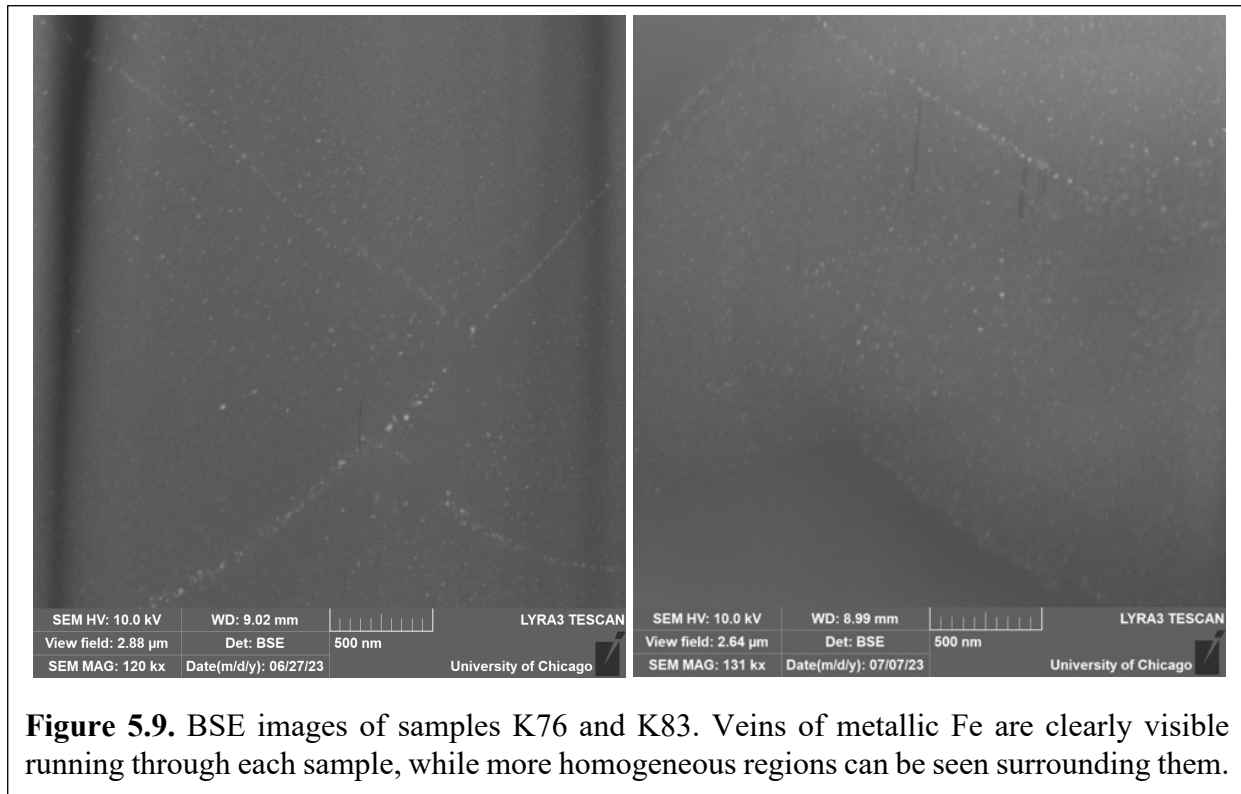


Figure 5.8. Images of all recovered samples. Pre-heat pressures are given.



at%) across the sample due to general environmental and instrumental contamination. Figure D.5 provides a line scan across sample K60, which also demonstrates that the bulk composition of the sample does not change across the laser-heated spot and outside of the laser-heated spot, indicating no evidence for Soret diffusion despite heating for 1 hour. BSE images for all recovered samples are shown in Figure 5.8. All images show an elliptical cross section of the laser-heated spot, in which a fine-grained phase assemblage is present. The thickness of the sample (in the direction of compression) and size of the laser-heated spot clearly decreases with increasing pressure, from a transformed spot diameter of $\sim 11 \mu\text{m}$ at 27 GPa to a diameter of $\sim 3.5 \mu\text{m}$ at 132 GPa. The shrinking spot size is due to the decreased thickness of the samples at higher pressures, which allows the heat to diffuse into the diamond culets more efficiently. In several samples, networks or veins of bright metallic Fe grains can be seen within the laser-heated spot. We posit that these veins

represent cracks in the glass, which promoted faster diffusion of Fe during transformation and thus larger grain size. Metallic Fe is seen in regions with homogenous grain distributions outside of these veins, and these observations of metallic Fe are used to identify the occurrence of the disproportionation reaction (Figure 5.9).

5.3.3 TEM Results

Because the grains of the high pressure assemblage are so small (<100 nm), it is necessary to use TEM techniques to more precisely image and analyze the assemblage. Six of the recovered samples were further thinned to <100 nm and imaged with the TEM at UIC. Use of the TEM allows for the acquisition of higher resolution images, as seen in Figure 5.10. In TEM images heavier elements appear as darker grains. Thus, the metallic Fe grains appear as the darkest grains

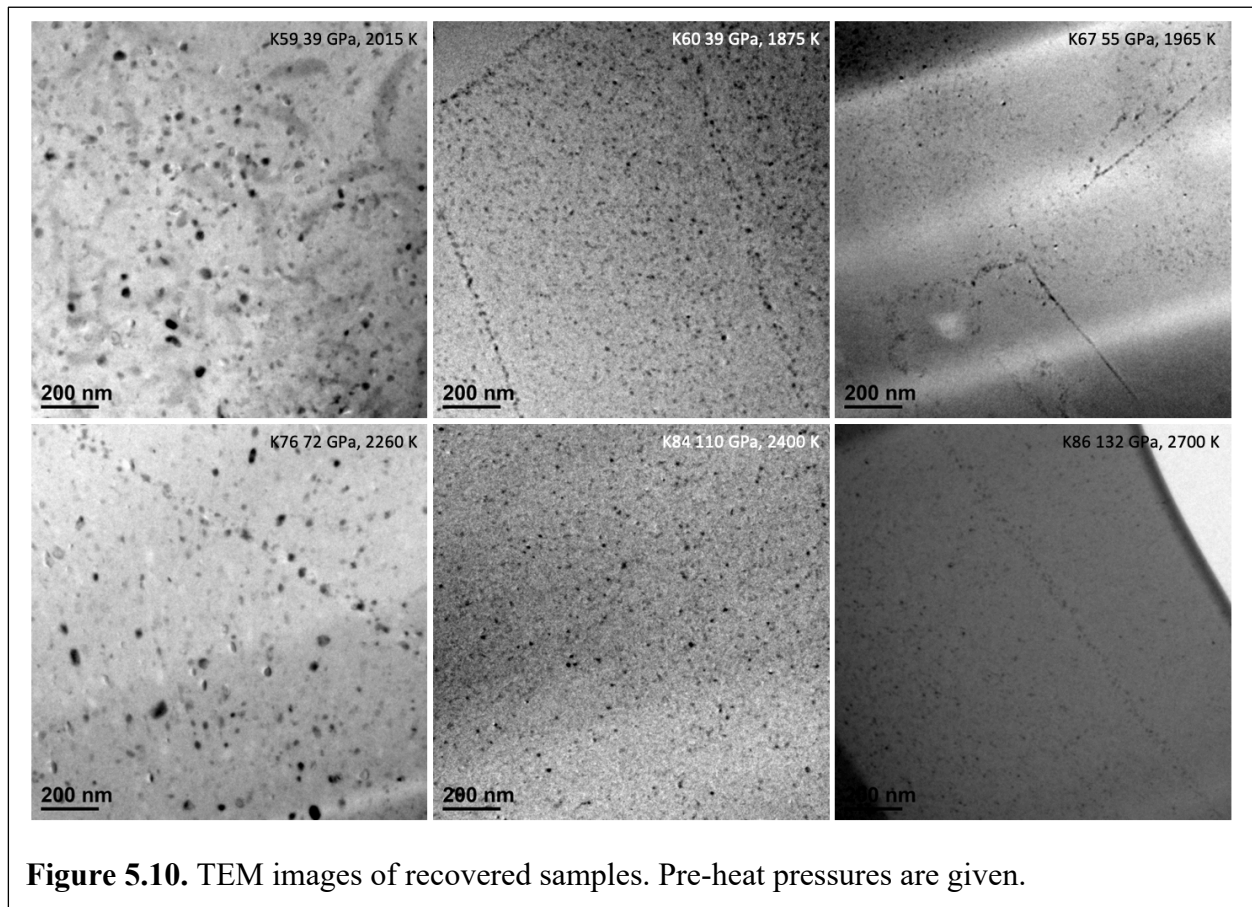
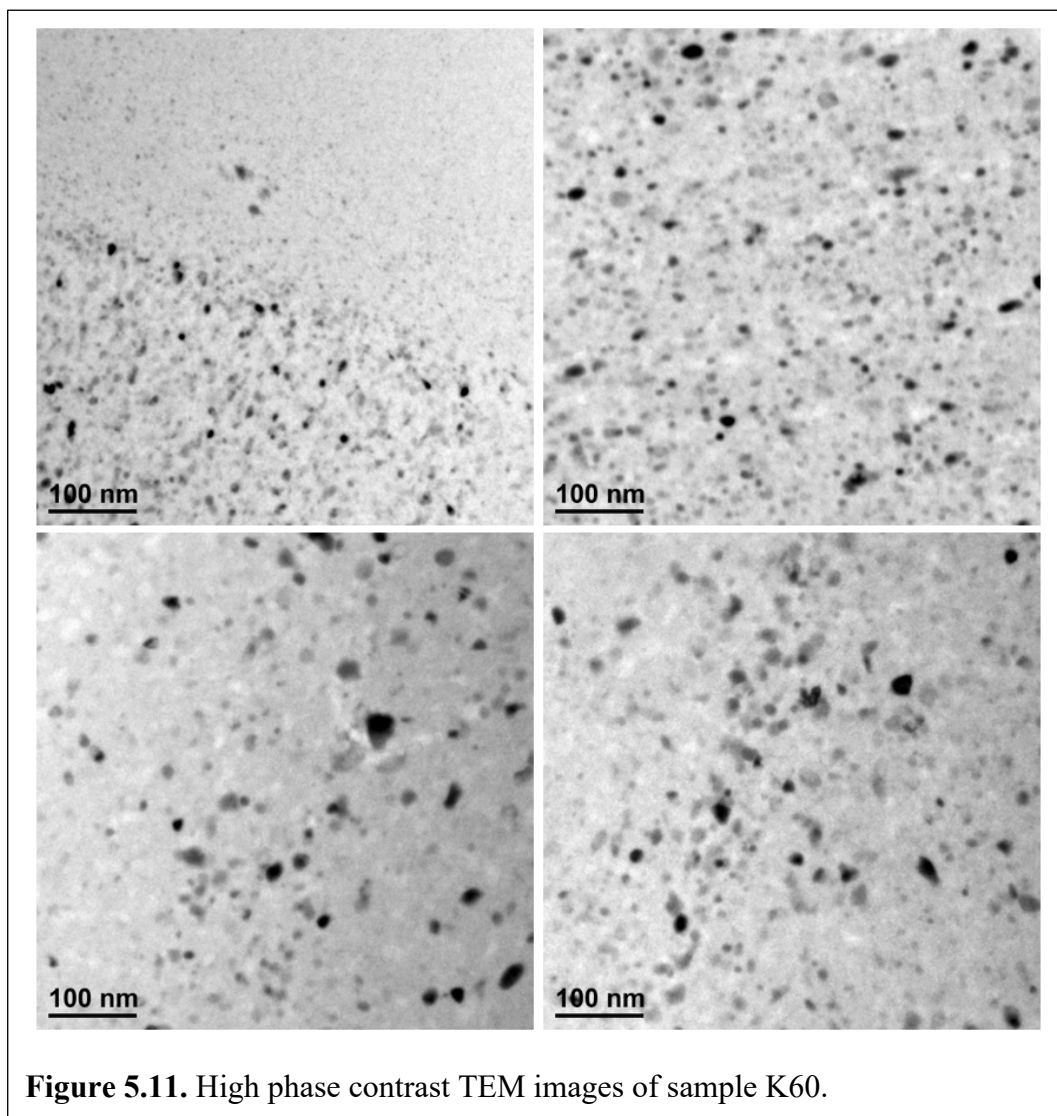


Figure 5.10. TEM images of recovered samples. Pre-heat pressures are given.

in these images. The TEM images are collected in two modes – one set using no objective aperture (for atomic resolution imaging) and one set using a 60 μm objective aperture (for enhanced phase contrast imaging). As seen in Figure 5.10, metallic Fe grains are seen in each sample recovered from pressures ranging from 39 GPa to 132 GPa. Variations in image quality are likely due to different thicknesses of the thin sections. Grainier images (K60 and K84) were likely samples that were not thinned as well as the others. Streaks in images are due to irregular thinning within a thin section. Images were selected that were collected at the same magnification and had some portion



of a homogeneous distribution of phases for best comparison between samples (though the selection for sample K67 was limited). Figure D.6 provides another set of TEM images at higher magnification, while Figures D.7-D.12 provide additional TEM images of each sample. Figure 5.11 shows examples of high-phase contrast images for sample K60. These images show the decrease in grain size towards the edge of the laser-heated spot and lack of any grains in the untransformed glass outside of the laser-heated region. Dark metallic Fe grains are observed to range in size from ~50 nm to <10 nm. There are clearly regions that contain a homogenous distribution of grains. Without EDS analysis, we can qualitatively identify three phases in the assemblage based on the contrast of the grains. In TEM bright field images such as these, the higher electron density phases appear darker. We can assign the observed grains in the following way: the darkest grains are metallic Fe, the medium gray grains are ferropericlase or partial grains of metallic Fe, and the light gray matrix is bridgmanite. It has been demonstrated in the literature (Nzogang et al., 2018) that bridgmanite becomes amorphous under the electron beam, so its lighter color can be explained by both its composition and amorphization. White regions may be thin regions of the matrix, or davemaoite grains that have amorphized upon decompression and additionally experienced beam damage.

5.3.4 *STEM Results*

Several samples were also imaged and analyzed using the STEM at UIC. With the STEM, we were able to acquire HAADF and LAADF images, as well as EDS analyses. In the STEM images, heavier elements appear brighter. The STEM images reveal the same distribution of metallic Fe grains as seen in the TEM images (Figure 5.12). We note that sample K67 was not analyzed with the STEM, while sample K83 was analyzed with the STEM and not the TEM. Figure

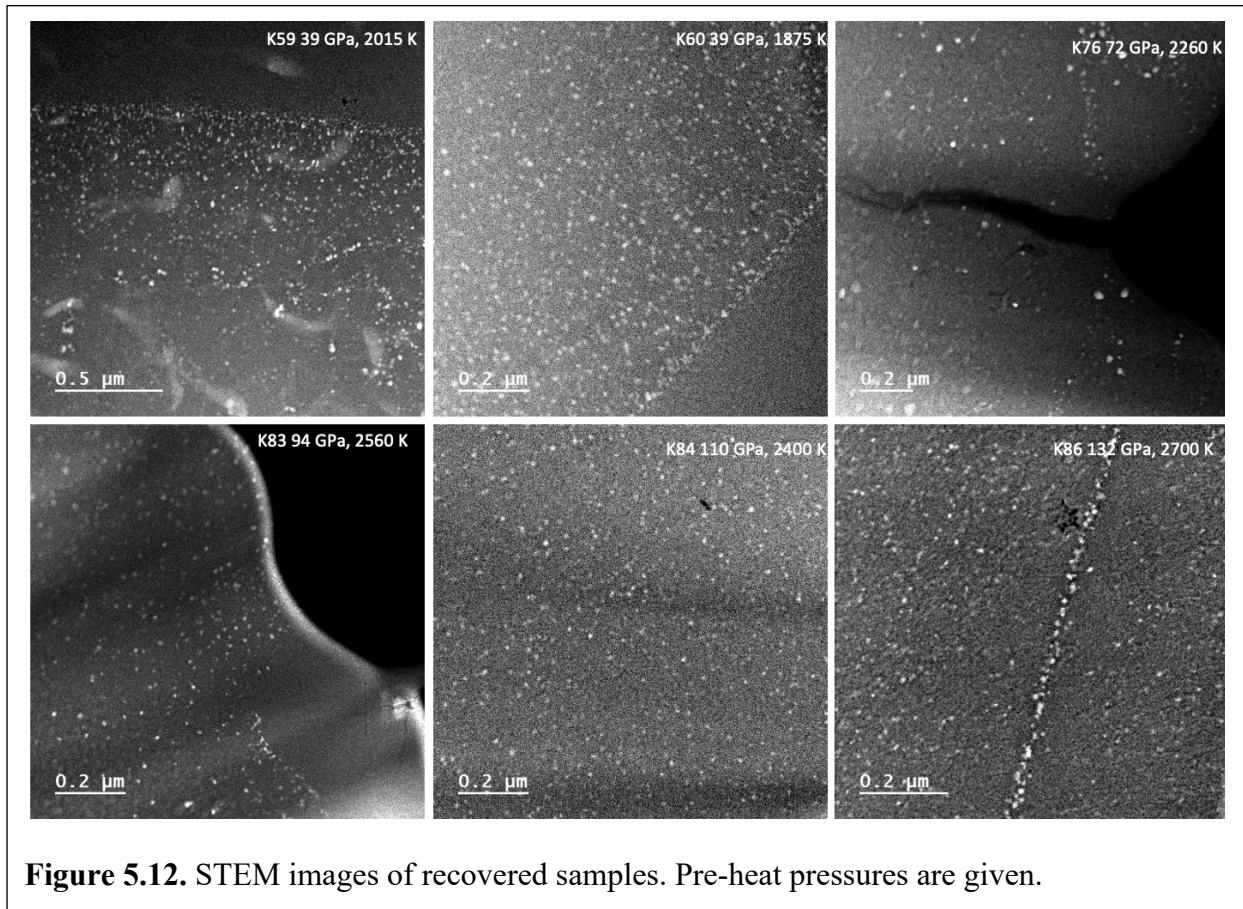
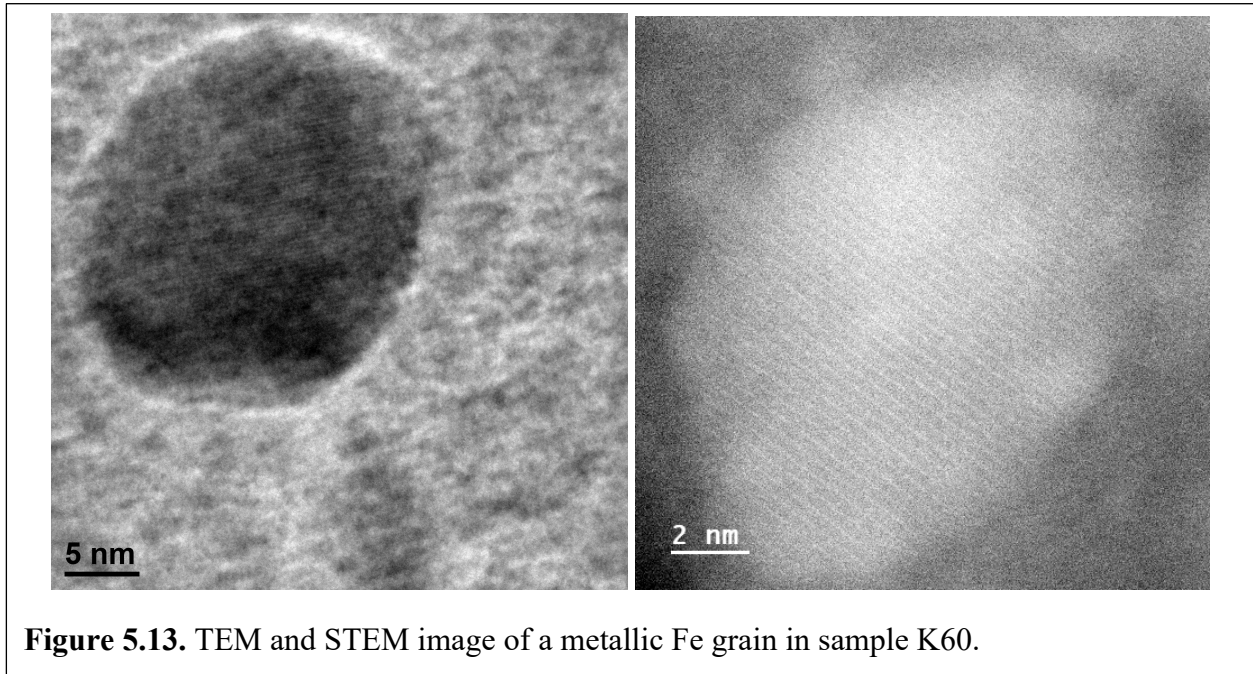
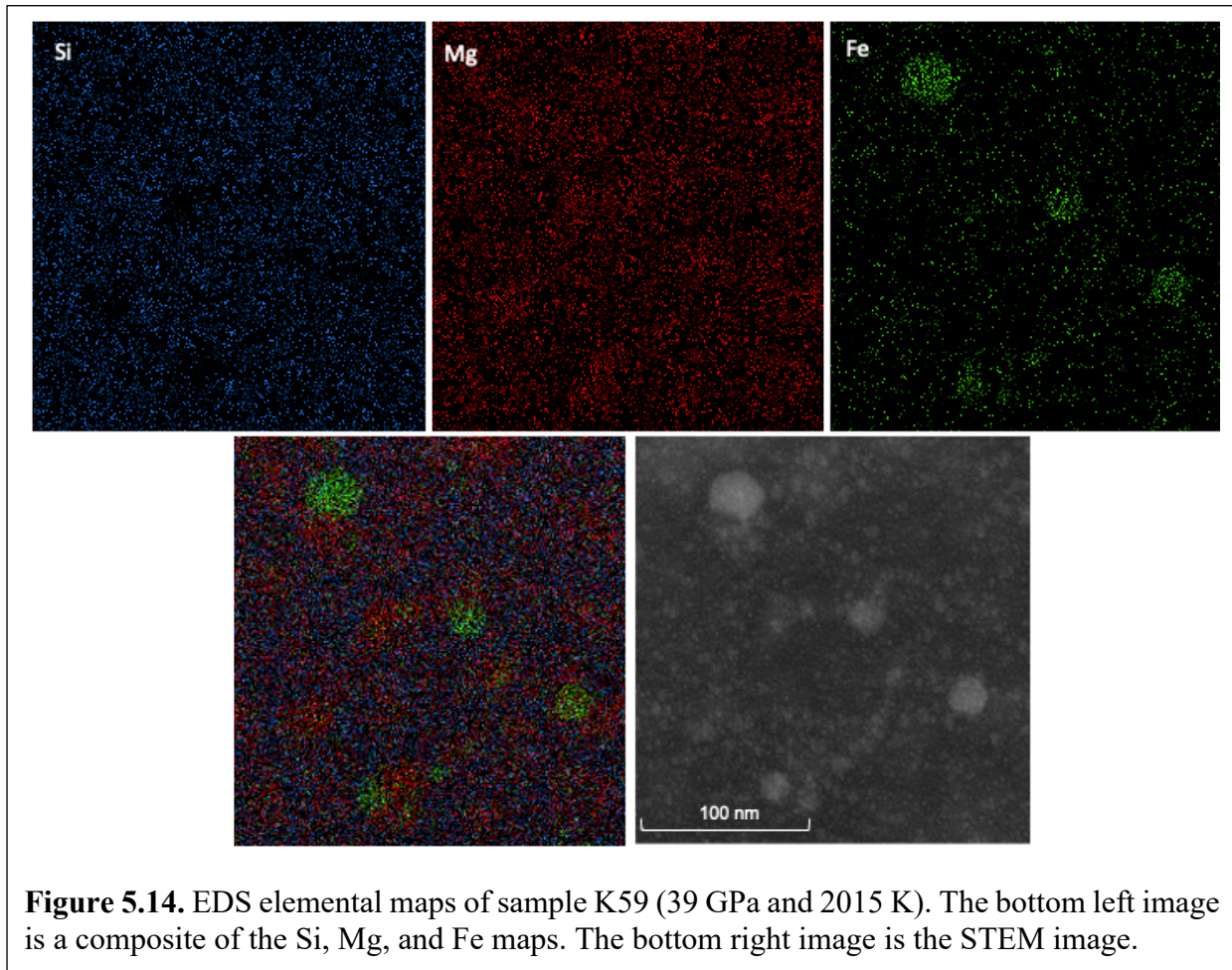


Figure 5.12. STEM images of recovered samples. Pre-heat pressures are given.

5.13 shows images of metallic Fe grains obtained using the TEM and STEM. In both images, the atomic lattice of the grain is visible, demonstrating the crystallinity of the grains. In addition to imaging, EDS measurements were also collected on several of the recovered samples using the STEM. Figure 5.14 shows a set of elemental EDS maps for sample K59, which was recovered from 39 GPa and 2000 K. The Fe map clearly shows Fe enrichment that coincides with the bright grains in the STEM image. Corresponding holes can be seen in the Si and Mg maps, though there is still a signal from Si and Mg in these regions due to the overlap of grains and thickness of the sample. The composite map created by adding the Si, Mg, and Fe maps more clearly shows the distribution of elements between different grains. In the composite map, the metallic Fe grains are green, while Mg-rich ferropericlase grains are red-orange (a mix of Mg and Fe), and the



bridgmanite matrix is blue-purple (a mix of Mg and Si and Fe). If we assume the bridgmanite and ferropericlase compositions given by Lee et al. (2004) (obtained using XRD-derived volumes and cation assignment assuming conservation of cations and charge), where bridgmanite is $\text{Mg}_{0.88}\text{Fe}_{0.06}\text{Al}_{0.12}\text{Si}_{0.94}\text{O}_3$ and ferropericlase is $\text{Mg}_{0.8}\text{Fe}_{0.2}\text{O}$, we expect Mg to be 40% of ferropericlase and 17.6% of bridgmanite, which accounts for the distribution of Mg seen in the map. Another set of elemental EDS maps are provided in Figure 5.15 for sample K76, which was recovered from 72 GPa and 2260 K. Maps are provided for all elements present in the sample: Fe, Mg, Si, O, Al, and Ca. The map was collected over a region with two metallic Fe grains, as confirmed by the Fe EDS map. As with sample K59, there are holes in the Mg and Si maps in the locations of the two metallic Fe grains. There is also a decrease in the number of O counts in those regions, though the counts are still above zero due to grain overlap and the thickness of the sample. Because Al and Ca are present in very low quantities, the counts for both of these elements are quite low, and as a result, the maps do not provide much information. A composite map of Fe, Mg,



and Si emphasizes the metallic Fe grains and highlights the regions of higher Mg content, which correspond to ferropericlasite grains. The accompanying TEM image shows the region around the map (further contextualized in Figure D.10, where the image location corresponds to the green box), which is located near the center of the laser-heated spot. A final demonstration of the fact that the Fe grains are metallic Fe can be provided in the form of EDS line scans. Figure 5.16 shows an EDS line scan across a metallic Fe grain in sample K76. In this line scan, the metallic Fe grain is ~ 30 nm in diameter. In the line scan, the metallic Fe grain is identified by a spike in the amount of Fe, which coincides with a drop in the content of all other elements, including O. The Fe content does not reach 100% because of grain overlap, but these results provide conclusive evidence that

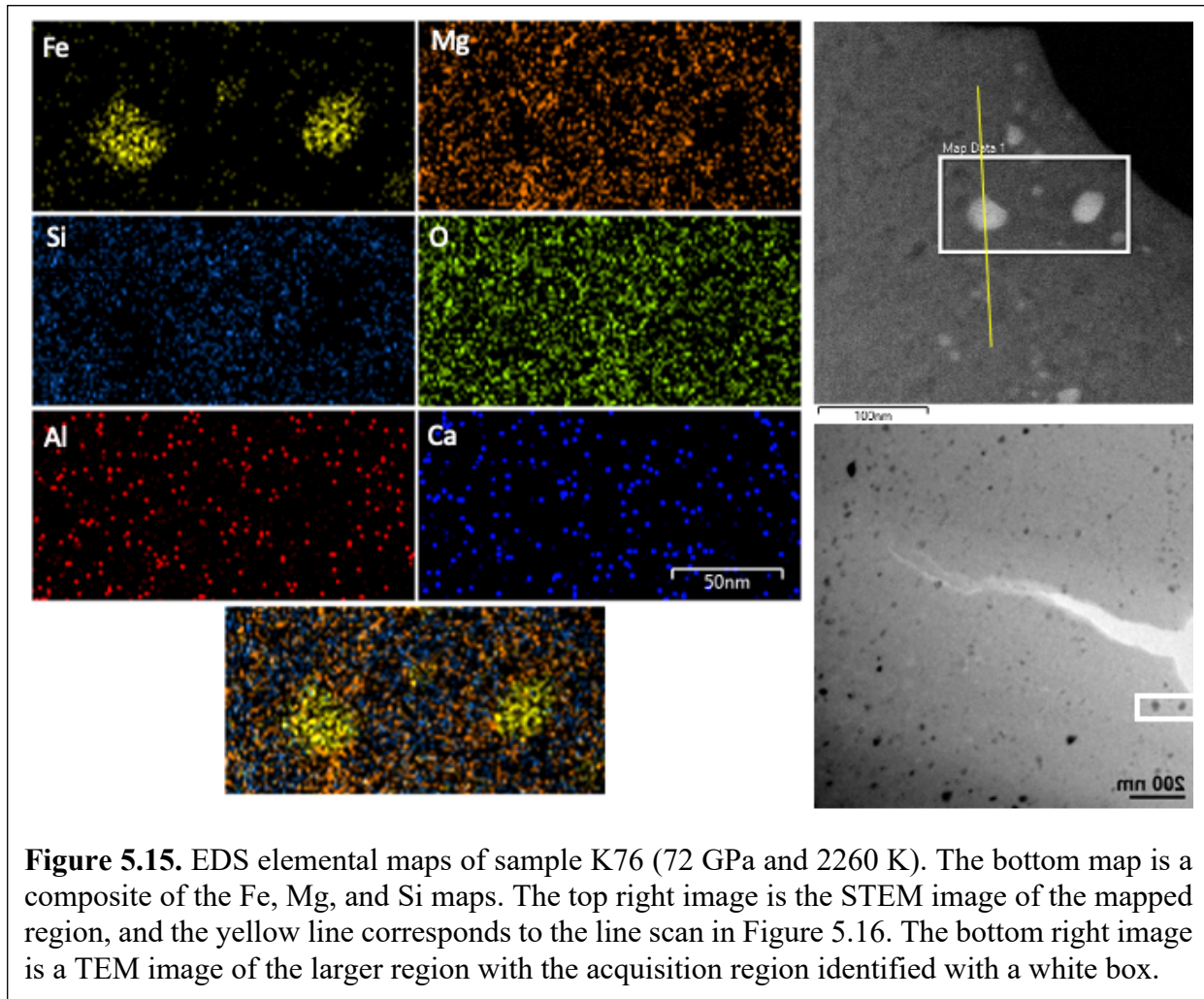


Figure 5.15. EDS elemental maps of sample K76 (72 GPa and 2260 K). The bottom map is a composite of the Fe, Mg, and Si maps. The top right image is the STEM image of the mapped region, and the yellow line corresponds to the line scan in Figure 5.16. The bottom right image is a TEM image of the larger region with the acquisition region identified with a white box.

metallic Fe exists in this sample. Furthermore, the line scan also shows evidence of a ferropericlasite grain just to the right of the metallic Fe grain (which is to the south in the maps in Figure 5.15), distinguished by a spike in Mg content while the Si content remains low. The low detections of Fe outside of the metallic Fe grain are likely due to the fact that Fe is a small fraction of both bridgmanite and ferropericlasite. We also note that the low Ca and Al detections are likely due to the low concentrations of both of these elements. Elemental EDS maps are provided for each recovered sample in Figures D.13-D.21, along with STEM images and EDS line scans. We note that sample K83 (recovered from 94 GPa and 2560 K) was not examined extensively in the SEM

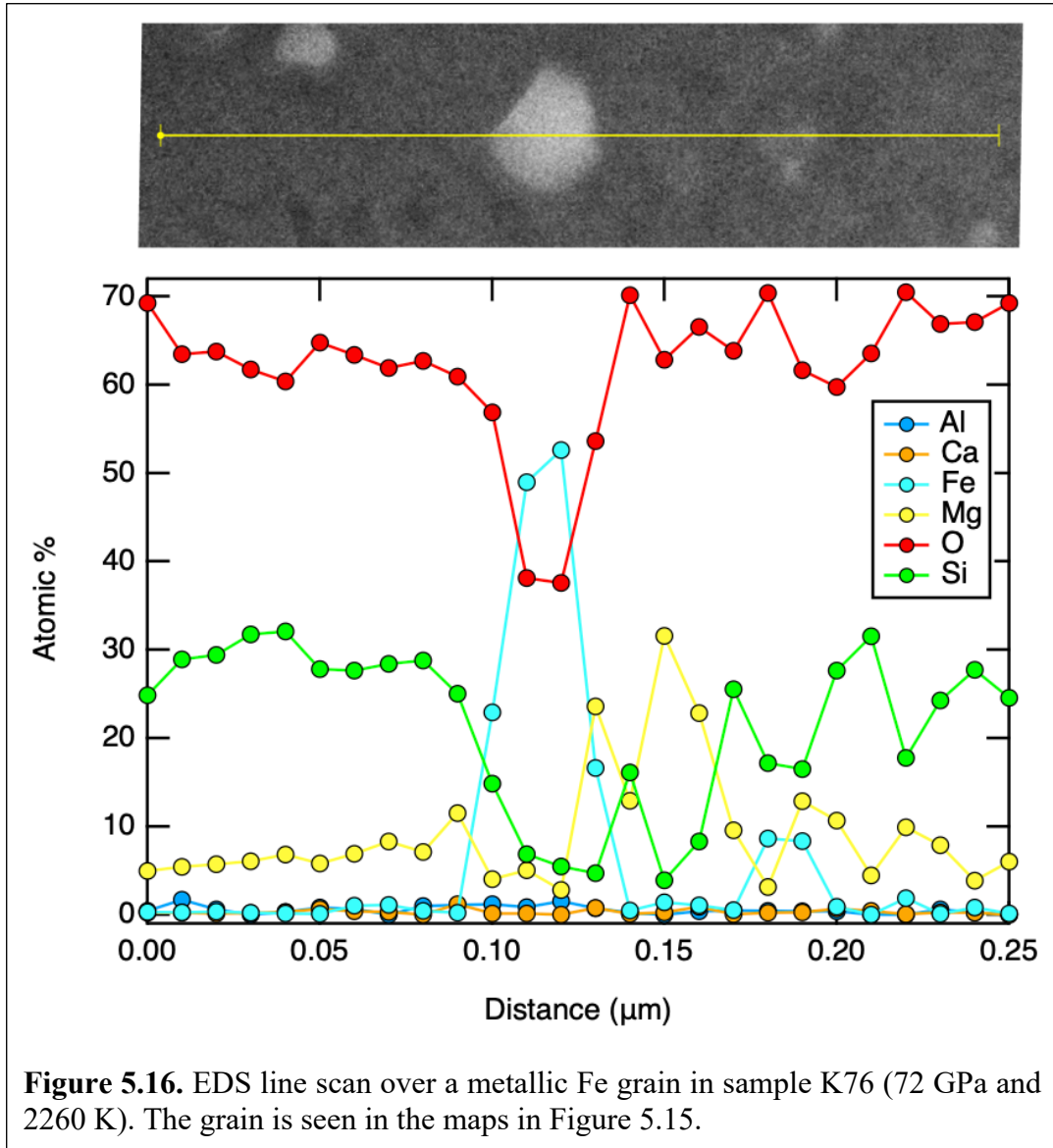


Figure 5.16. EDS line scan over a metallic Fe grain in sample K76 (72 GPa and 2260 K). The grain is seen in the maps in Figure 5.15.

and not imaged with the TEM, so it is the sample least exposed to beam damage, which may explain the appearance of more defined grains of bridgmanite and ferropericlasite in the STEM images (Figure D.16). We provide point analyses and spectra sums for the SEM and STEM EDS measurements in Tables D.2 and D.3. In each recovered sample, we find evidence for disproportionated metallic Fe, confirming the occurrence of the iron disproportionation reaction from 39 GPa to 132 GPa.

5.4 Discussion

5.4.1 *Absence of identifiable davemaoite*

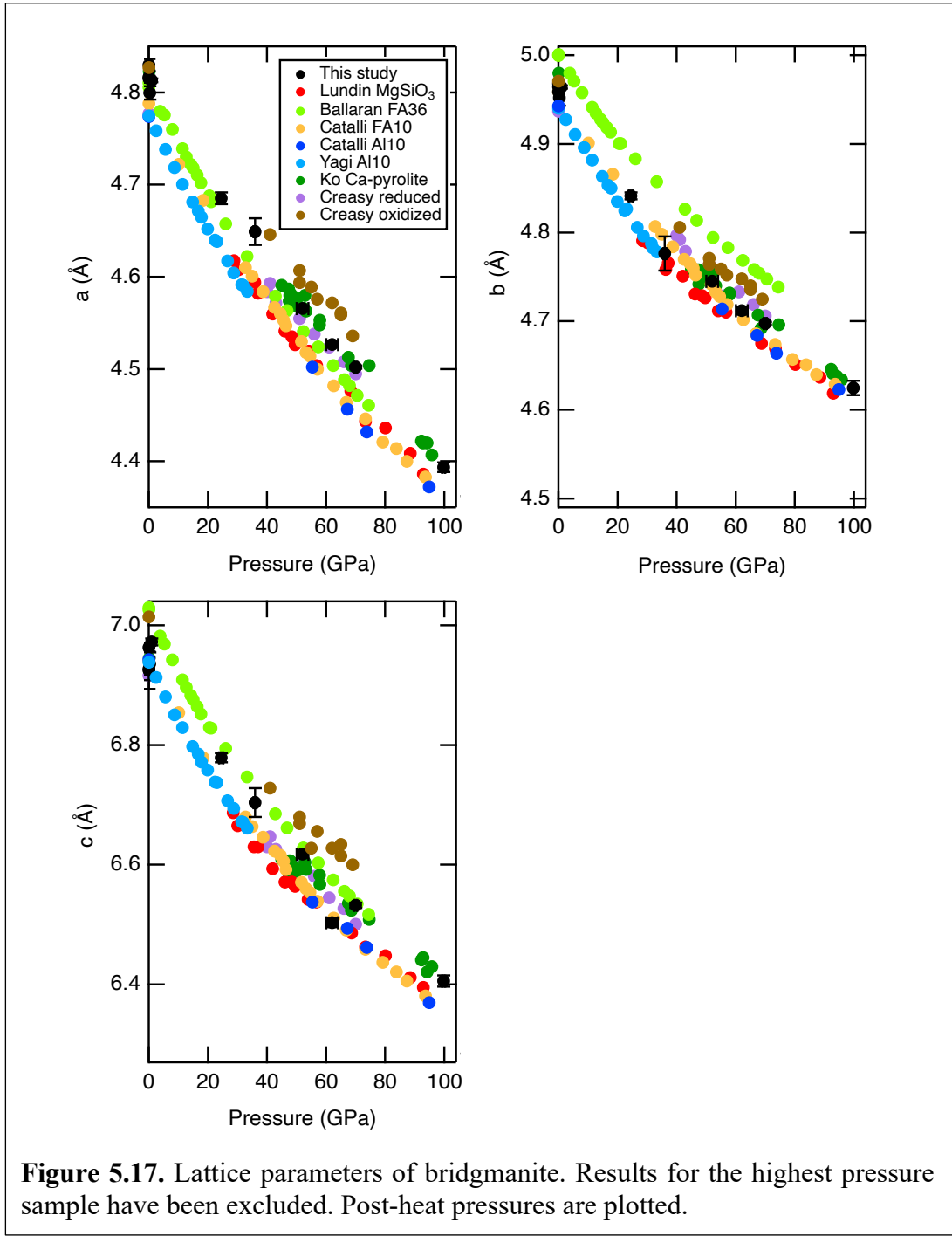
The experimental results provided above indicate that the iron disproportionation reaction occurs in the pyrolitic mantle across the range of lower mantle conditions. We can use the XRD results to understand the compressional behavior of the bridgmanite and ferropericlase that coexists with the disproportionated metallic Fe. First, however, we address the lack of identified davemaoite in the majority of our samples. In a study on a KLB-1 composition, Ono et al. (2005) found that davemaoite and ferropericlase were not detectable in synchrotron XRD patterns in samples at 58 GPa and 2250 K and 35 GPa and 2100 K, which they attribute to a small sample volume, poor laser absorption, and low expected volume of these phases. The authors added gold to the starting material for a higher pressure run at 97 GPa and 2100 K and were able to identify bridgmanite and davemaoite, implying that the addition of gold contributed to stable heating and acquisition of clear XRD patterns. We suggest that it is more likely that the gold took in the Fe in the sample, diminishing the FeAlO₃ content of bridgmanite, making Ca less soluble in bridgmanite. Lee et al. (2004) could not detect davemaoite in their XRD patterns above ~70 GPa, which they attribute to its low abundance and overlap of peaks with bridgmanite. Their heating temperatures are not reported. It has been suggested that the substitution of Fe³⁺ and Al into the bridgmanite structure enhances the solubility of Ca into bridgmanite (Creasy et al., 2020; Ko et al., 2022). Ko et al. (2022) studied a Ca-enriched pyrolite composition and identified single-perovskite and two-perovskite domains. Between 30 GPa and 40 GPa up to 2400 K, both bridgmanite and davemaoite were observed, while between 40 GPa and 110 GPa above 2300 K, only bridgmanite was observed, indicating that at these conditions, there is an increased solubility

of Ca in the bridgmanite structure. This can explain the lack of observation of davemaoite in our samples above 40 GPa and 2300 K. Creasy et al. (2020) studied Al-rich pyroxenite compositions that were reduced ($\text{Fe}^{3+}/\Sigma\text{Fe}\sim 11\%$) and oxidized ($\text{Fe}^{3+}/\Sigma\text{Fe}\sim 55\%$). The authors suggest that a threshold of Al, Fe^{2+} , and Fe^{3+} content must be met before Ca can dissolve into bridgmanite. Creasy et al. (2020) found that the oxidized composition created a single phase bridgmanite that hosted Ca (in addition to all of the Fe and Al in the composition), while the reduced composition created a phase assemblage that included disproportionated metallic Fe and davemaoite in addition to other phases. The reduced sample produced a bridgmanite with 4% FeAlO_3 and 3% FeSiO_3 (which makes a bridgmanite with $\text{Fe}^{3+}/\Sigma\text{Fe}\sim 57\%$), while the oxidized sample produced a bridgmanite with 7% FeAlO_3 , 19% AlAlO_3 , 6% FeSiO_3 , and 18% CaSiO_3 (which keeps the $\text{Fe}^{3+}/\Sigma\text{Fe}\sim 55\%$, meaning that no new Fe^{3+} was produced). It may be that in this composition type and at these conditions, FeAlO_3 has a maximum solubility that was reached in the oxidized sample, and thus no Fe^{2+} disproportionated to produce additional FeAlO_3 or metallic Fe. Given that both samples have similar FeAlO_3 and FeSiO_3 contents, the main differences in the lattice parameters can be attributed to the AlAlO_3 and CaSiO_3 components. It should be noted that the compositions reported in Creasy et al. (2020) are not direct EDS measurements but rather results of Monte Carlo modeling on EMPA measurements that were too coarse to measure individual grains. Additionally, they state that there is no Ca present in the reduced bridgmanite, but we suggest that there is some amount of Ca, given the expansion of the lattice parameters. Given these results, it is possible that the bridgmanite in this study has some Ca in its structure, and this may reduce the amount of davemaoite present, which explains the difficulty in identifying it in XRD patterns. Davemaoite is

also not identifiable in the STEM EDS maps (Figure 5.15), which may be attributed to its low abundance.

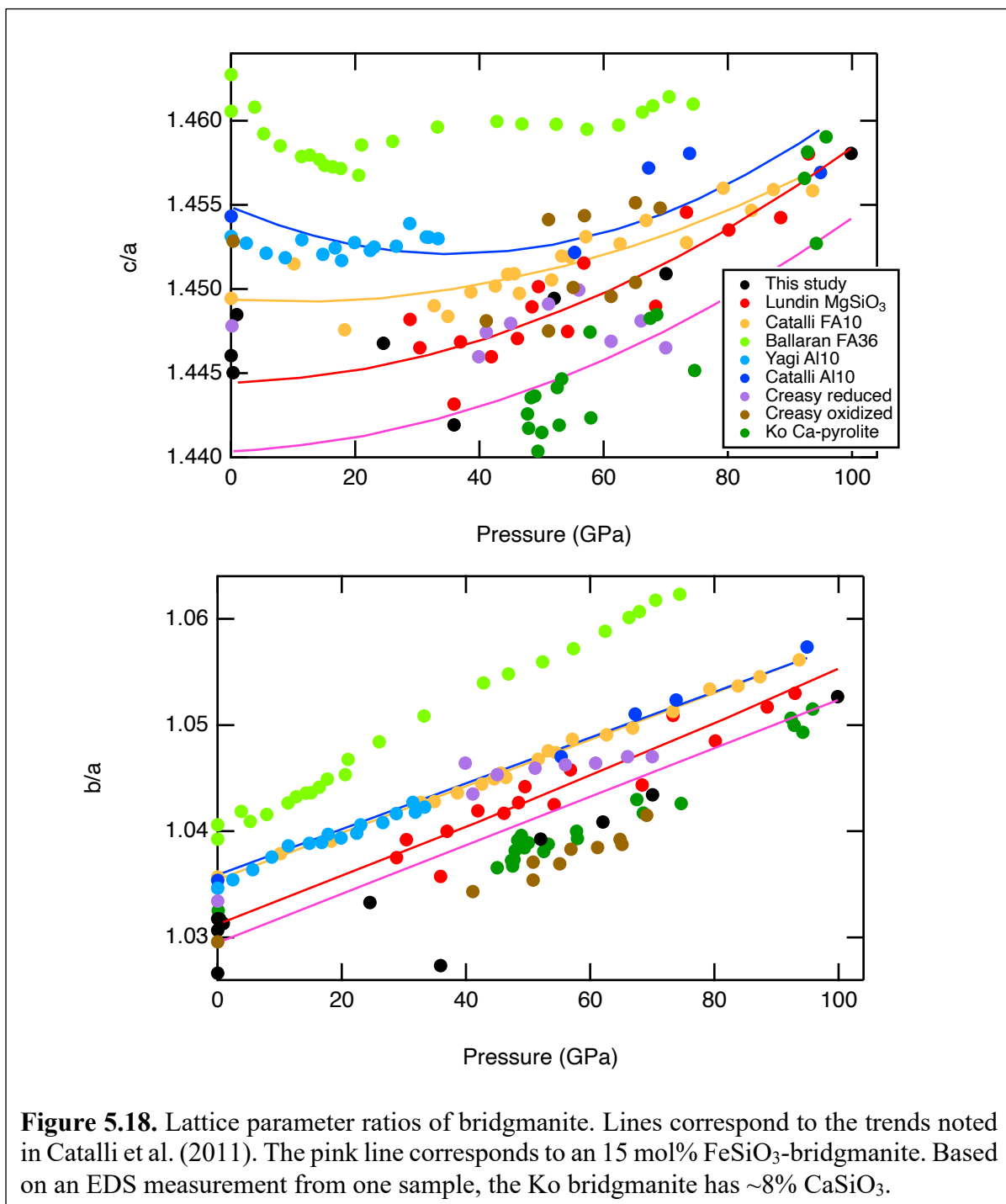
5.4.2 *Compression trends*

In each quenched sample at high pressure, we used the d-spacings from 5 to 16 peaks corresponding to the bridgmanite phase to calculate the a , b , and c lattice parameters of bridgmanite at high pressures. We also calculated the lattice parameters of bridgmanite for five samples that were decompressed to ~ 0 GPa. The resulting lattice parameters are plotted in Figure 5.17 alongside the lattice parameters of pure MgSiO_3 (Lundin et al., 2008), a bridgmanite with the $\text{Mg}_{60}\text{Fe}_{0.03}^{2+}\text{Fe}_{0.38}^{3+}\text{Si}_{0.62}\text{Al}_{0.36}\text{O}_3$ composition (Ballaran et al., 2012, labeled as FA36), a bridgmanite with the $\text{Mg}_{0.88}\text{Fe}_{0.13}\text{Al}_{0.11}\text{Si}_{0.88}\text{O}_3$ composition (Catalli et al., 2011, labeled as FA10), a bridgmanite with the $\text{Mg}_{0.9}\text{Al}_{0.2}\text{Si}_{0.9}\text{O}_3$ composition (Yagi et al., 2004; Catalli et al., 2011), and bridgmanite formed from a Ca-enriched pyrolite composition (Ko et al., 2022). We also include the results of Creasy et al. (2020). Lattice parameters are given in Table D.4. As seen in Figure 5.17, addition of the FeAlO_3 component results in increases in each lattice parameter. Ballaran et al. (2012) found that the c axis of FeAlO_3 -bearing bridgmanite is more compressible than MgSiO_3 -bridgmanite and FeSiO_3 -bridgmanite below 60 GPa, while above 60 GPa, the c axis becomes stiffer and behaves more like the a axis. These results align with the findings of Catalli et al. (2011), who treated the compressibility of FeAlO_3 -bearing bridgmanite below 70 GPa as a regime distinct from that above 70 GPa. Addition of Ca into the bridgmanite structure increases each lattice parameter. The results of Ko et al. (2022) are similar to the results in this study due to the fact that both compositions are pyrolitic. The slight differences between the lattice parameters of Ko et al.



(2022) and this study can be attributed to the extra CaSiO_3 that was added to the composition in the study of Ko et al. (2022). It should be noted that pressures were determined in this study using

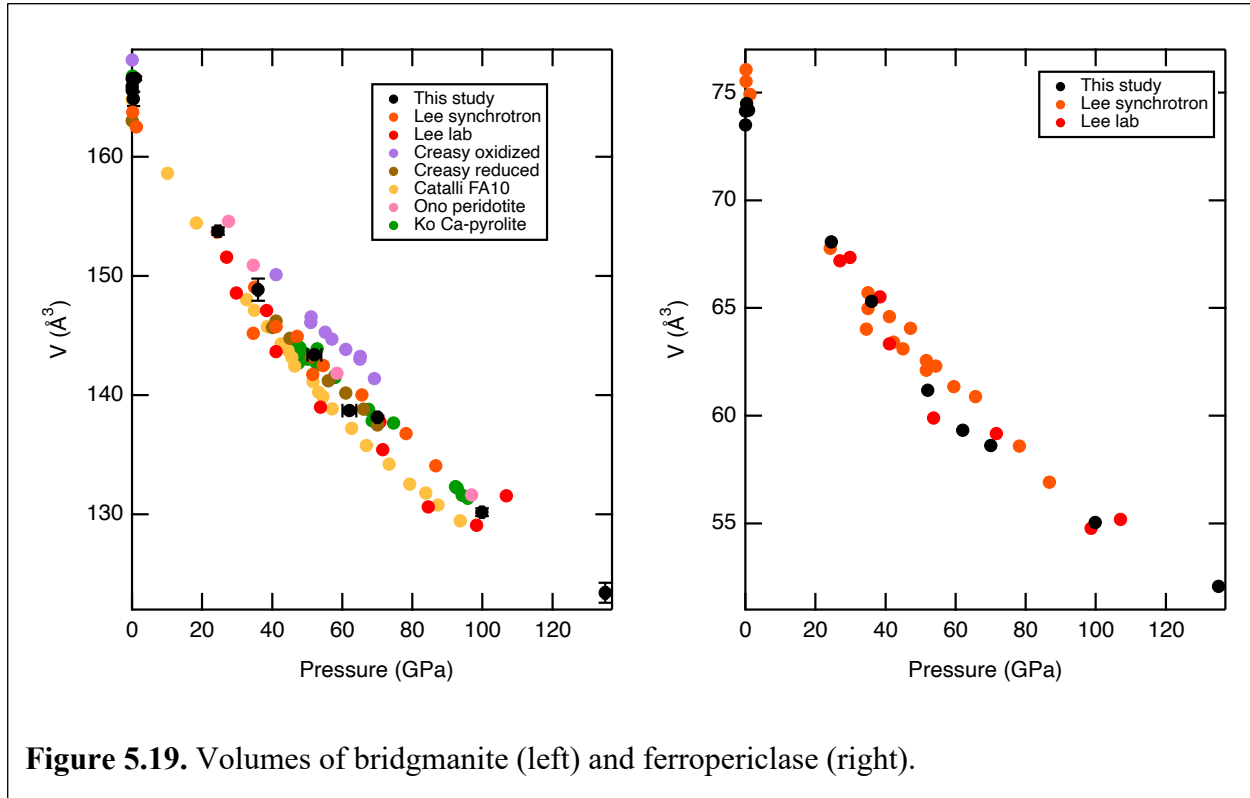
Raman spectroscopy of the diamond culets after quench at high pressure, while other pressure scales were used in the studies included for comparison. Additionally, the composition of bridgmanite likely changes slightly throughout the lower mantle as Fe partitions differently



between bridgmanite and ferropericlase with depth, which can affect the trends seen in the lattice parameters and complicate direct comparisons to fixed composition samples. However, we can determine that based on the observed lattice parameters, the bridgmanite formed in this study clearly has components beyond MgSiO_3 (evidenced by the increase of each lattice parameter above the pure MgSiO_3 endmember), as is expected for bridgmanite formed in a pyrolitic composition (Frost et al., 2004; Lee et al., 2004; Irifune et al., 2010). Based on Figure 5.17, we can estimate that the bridgmanite in this study has contributions from the FeAlO_3 component as well as the CaSiO_3 component.

It is also useful to compare the trends of the lattice parameter ratios to observe how the distortion of the perovskite structure changes with pressure (Figure 5.18). As seen in Figure 5.18, the addition of the FeSiO_3 component decreases both the c/a and b/a ratios (Catalli et al., 2010). Addition of the CaSiO_3 component has the greatest effect on the c axis, which is why the results of Ko et al. (2022) have the lowest c/a ratios. As seen in Figure 5.17, the addition of the FeAlO_3 component acts to increase both the b and c axes more than the a axis, which causes both the c/a and b/a ratios to be largest for the samples with high FeAlO_3 components. The data from this study have a c/a ratio that is scattered about the MgSiO_3 trend and a b/a ratio that is slightly below the MgSiO_3 trend, which can be interpreted as competing influences from the MgSiO_3 component, which composes the majority of pyrolitic bridgmanite, and the FeAlO_3 , FeSiO_3 , and CaSiO_3 components.

Using the lattice parameters of bridgmanite, we can also plot the volume of bridgmanite as a function of pressure (Figure 5.19). We compare the volumes seen in this study to the same studies seen in the lattice parameter comparisons with the addition of the study of Lee et al. (2004). Our



results are consistent with the results from the synchrotron measurements performed by Lee et al. (2004) on a peridotitic composition, which also overlap with the reduced Al-rich pyroxenite of Creasy et al. (2020) and the Ca-rich pyrolite of Ko et al. (2022). We were also able to use the measured lattice parameters of the ferropericlase coexisting with bridgmanite to plot the volume of ferropericlase as a function of pressure (Figure 5.19). Our results are consistent with the results of Lee et al. (2004). The agreement of our results with those of Lee et al. (2004) demonstrates the reproducibility of experiments performed on pyrolitic glass and a natural peridotite.

5.4.3 Disproportionation of Fe throughout the lower mantle

Several studies have suggested that the iron disproportionation reaction may proceed to different degrees as a function of depth (Kobayashi et al., 2005; Shim et al., 2017; Xu et al., 2017; Huang et al., 2021; Tsujino et al., 2023). Xu et al. (2017) developed an ab initio and empirical

fitting-based thermodynamic model to predict the partitioning behavior of Fe between bridgmanite and ferropericlase and used this to predict a decrease in disproportionated metallic Fe with increasing depth in the lower mantle. The authors suggest that Fe^{2+} preferentially partitions into ferropericlase across its spin transition in ferropericlase from 40 GPa to 80 GPa, which depletes bridgmanite of Fe and suppresses the disproportionation reaction. They predict a slight increase in disproportionated metal from 20 GPa (where it accounts for ~4% of all Fe) to 35 GPa (where it accounts for ~5.5% of all Fe), and then a gradual decrease to zero by 100 GPa. Shim et al. (2017) provided experimental results on an aluminous pyroxene composition that suggest a decrease in the $\text{Fe}^{3+}/\Sigma\text{Fe}$ ratio of bridgmanite from 40 GPa to 70 GPa due to a change in the substitution mechanisms in bridgmanite in this pressure range. The authors suggest that the high $\text{Fe}^{3+}/\Sigma\text{Fe}$ ratio of bridgmanite is due to the occurrence of the iron disproportionation reaction, implying that disproportionated metallic Fe can be expected to form throughout the lower mantle outside of the region from 40 GPa to 70 GPa. Huang et al. (2021) predict the formation of 0.7 wt% Fe-Ni alloy at the top of the lower mantle, coexisting with a bridgmanite with an $\text{Fe}^{3+}/\Sigma\text{Fe}$ ratio of 0.50 and a bulk pyrolite $\text{Fe}^{3+}/\Sigma\text{Fe}$ ratio of 0.28. The $\text{Fe}^{3+}/\Sigma\text{Fe}$ ratio of bridgmanite is predicted to increase to 0.65 by 50 GPa, at which point it levels out. The increase in the $\text{Fe}^{3+}/\Sigma\text{Fe}$ ratio of bridgmanite is predicted to increase the amount of disproportionated metallic Fe by 0.003 wt%. Tsujino et al. (2023) observe a decrease in disproportionated metallic Fe in an Al-bearing orthopyroxene from 24.5 GPa to 29 GPa. At 24.5 GPa, the authors determined that there was 12.0 mol% metallic Fe, while at 26.5 GPa, there was 1.4 mol% metallic Fe, and at 29 GPa, there was 0.9 mol% metallic Fe.

By using the TEM images collected on samples recovered from 39 GPa to 132 GPa in this work, we can provide estimates of the amounts of disproportionated metallic Fe produced across lower mantle conditions. For each sample, we used the ImageJ software to analyze regions of TEM

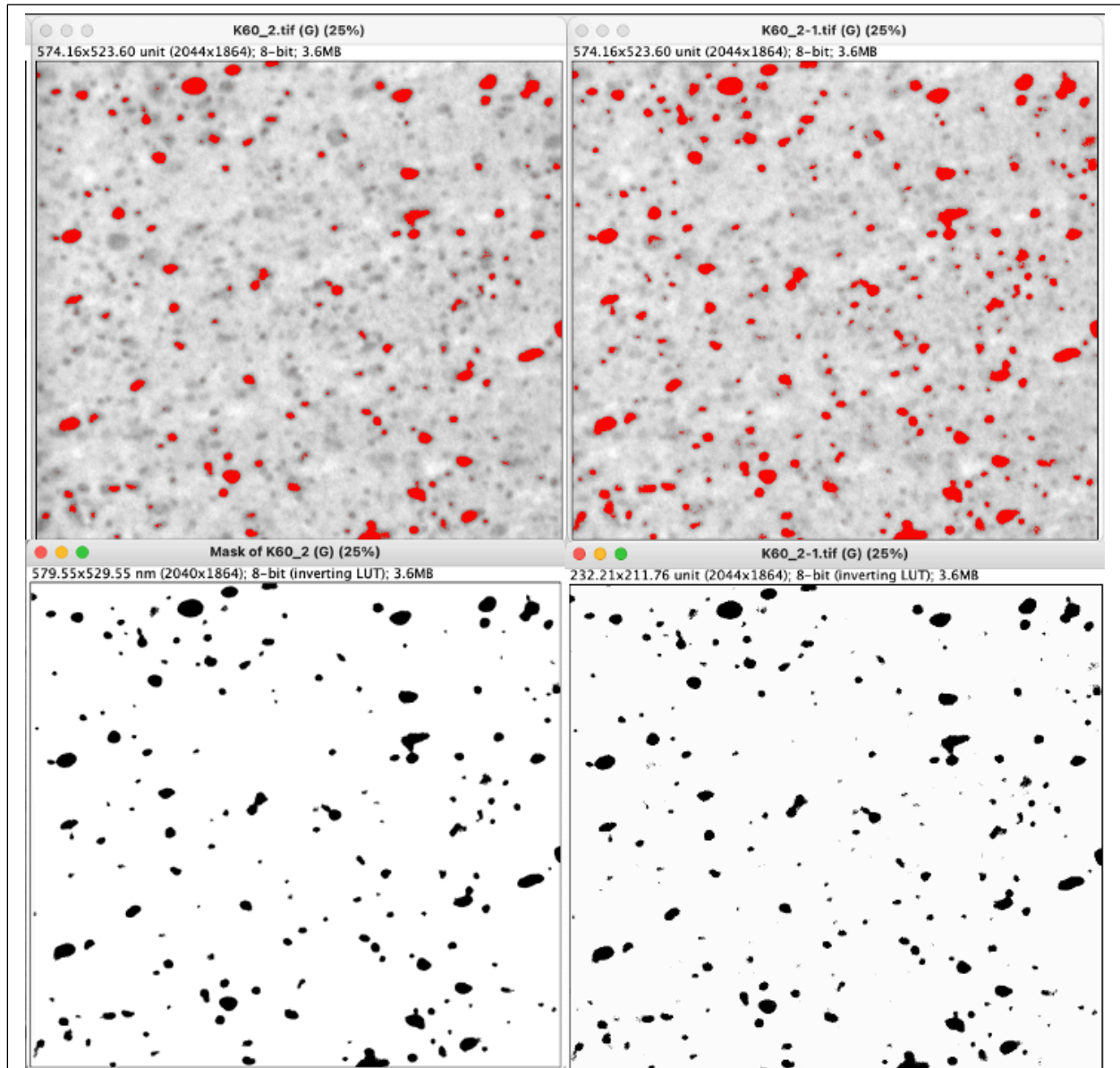
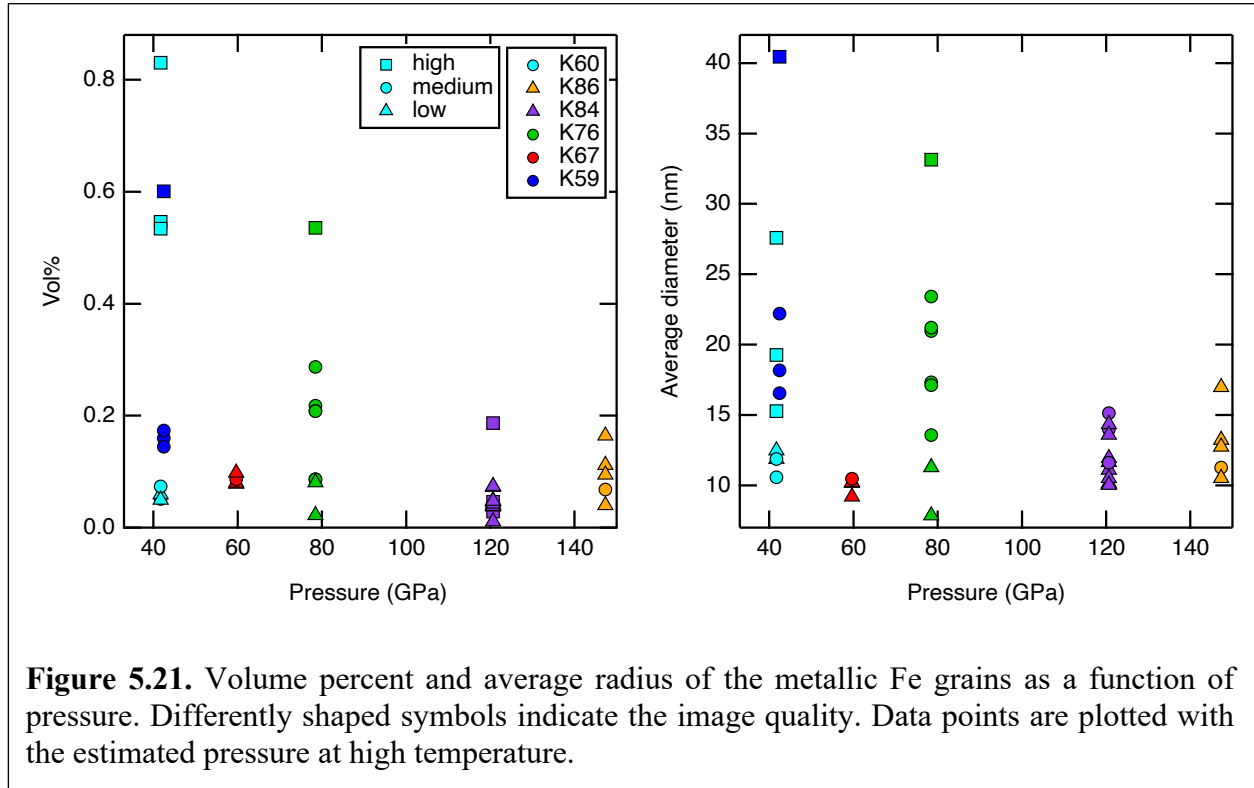


Figure 5.20. Example image analysis for sample K60 (as seen in Figure 5.11). This is what we consider a “high quality” image. Top Left: Minimum metallic Fe grain extent. Top Right: Maximum metallic Fe grain extent. Bottom Left: Extracted metallic Fe grains from the average extent. Bottom right: All grains larger than 5 nm².

images with homogeneous distributions of grains (away from veins of metallic Fe). We used the threshold function to isolate the metallic Fe grains (Figure 5.20). An estimate of the minimum and maximum coverage of metallic Fe grains was produced for each image, and the average of these two results was used for the final quantification of metallic Fe. With the metallic Fe grains extracted, we then retrieved the number of grains larger than 5 nm² and the average grain area. We must consider that the 2-dimensional image shows the entire thickness of the sample. We assume that all samples are 50 nm thick. We use the average area of all of the grains to calculate the total volume of metallic Fe grains present in the 50 nm-thick sample region. The volume fraction of metallic Fe is plotted in Figure 5.20 along with the average radius of the metallic Fe grains in each image. We recognize that this analysis hinges on several assumptions. First, we assume that the metallic Fe grains in each image are only the darkest grains in the image. This excludes metallic Fe grains that may only have small cross sections present in the image. Second, the same procedure is followed for images of varying quality. We have qualitatively categorized the images as high, medium, or low quality and indicated the type in Figure 5.20. Examples of medium and low quality images are given in Figures D.22 and D.23. The “high quality” images appear to yield a larger quantification, likely because the background noise is lower and the contrast between the metallic Fe grains and all other grains is more clear, allowing us to more fully capture each grain. Third, we have assumed that all samples are 50 nm thick, but sample thickness varies between samples and likely within each sample area. We assume that the samples are 50 nm thick given that grains are generally smaller than 20 nm in diameter (on average 10 nm), and we have acquired clear images with a grain density that suggests there are not 10’s of grains overlapping. We note that the volume fraction results depend linearly on the thickness estimate, such that if the thickness is



thicker than the estimate, the volume fraction of Fe metal would be correspondingly lower. Finally, we assumed that the volume of Fe in each image can be described by the average volume of all grains in the image and they are spherical. Despite any bias from these assumptions, the resultant quantification of disproportionated metallic Fe yields important insights into the occurrence of the iron disproportionation reaction across the lower mantle (Figure 5.21). Though there is scatter in the calculated volume fraction within each sample, the volume fraction of disproportionated metallic Fe appears to decrease with increasing pressure. This will be discussed more below. This trend agrees with the general prediction of Xu et al. (2017) and Tsujino et al. (2023). Figure 5.21 also shows that the average size of the metal Fe grains generally decreases with increasing pressure. We note that the reported average grain size is likely an underestimate due to the fact that we include particles in the average that are cross sections of larger grains. We note that the

extremely small size of the grains in these assemblages causes us to enter the regime of nanoparticles, which are small particles that can exhibit different physical and chemical properties than their larger counterparts. Attempts were made to grow larger grains by heating for longer time periods, but these efforts did not yield significant improvements, and the nanoparticle form of the pyrolitic assemblage is the only form we are able to create given the experimental restraints.

Thus far we have only discussed the effect of pressure on the iron disproportionation reaction, but we have several results that allow us to draw conclusions about the effect of temperature. Samples K59 and K60 were both compressed to 39 GPa but heated to different temperatures and for different durations (24 minutes at 2015 K versus 1 hour at 1875 K). As seen in Figure 5.21, this did not have a great effect on the metallic Fe grain size or volume fraction. This lack of observable temperature effect is also seen across the laser-heated spot in each sample. We know that there is a temperature gradient across the laser-heated spot, yet the distribution of metallic Fe does not change considerably across the laser-heated spot.

5.4.4 STEM EDS observations

The STEM EDS maps and line scans provide evidence of iron disproportionation across the range of the lower mantle along the geotherm, clarifying the pressure-temperature space seen in Figure 5.1. An updated version with the results from this study is provided in Figure 5.22. In Figure 5.22, the symbols corresponding to Piet et al. (2016) are for a Ca-free pyrolitic composition as well as an aluminous olivine composition. The authors do not provide the oxidation state of Fe in the Ca-free pyrolitic starting material, and the aluminous olivine has a starting $\text{Fe}^{3+}/\Sigma\text{Fe}\sim 25\%$. Therefore the reason that they do not report any disproportionated metallic Fe could be attributed to the significant Fe^{3+} content in the starting material. Irifune et al. (2010) also studied a pyrolitic

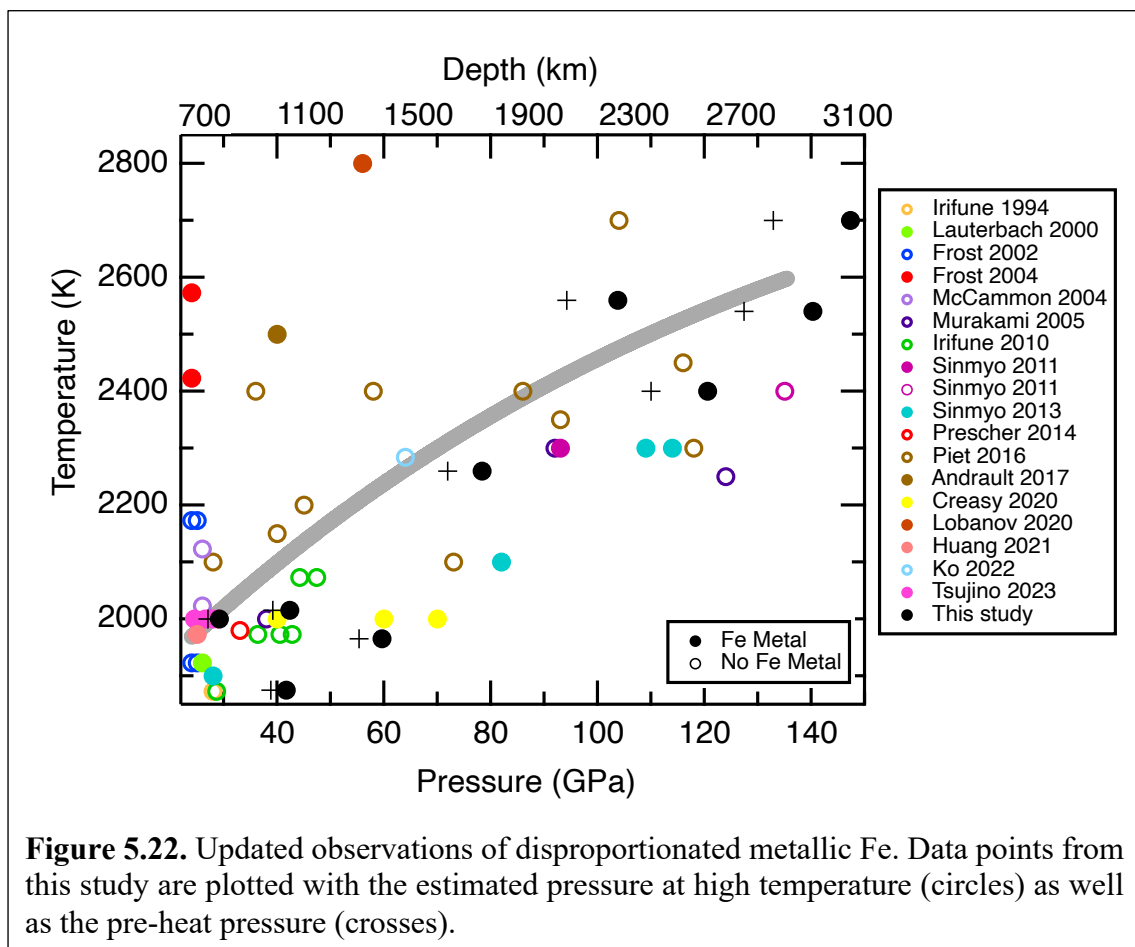


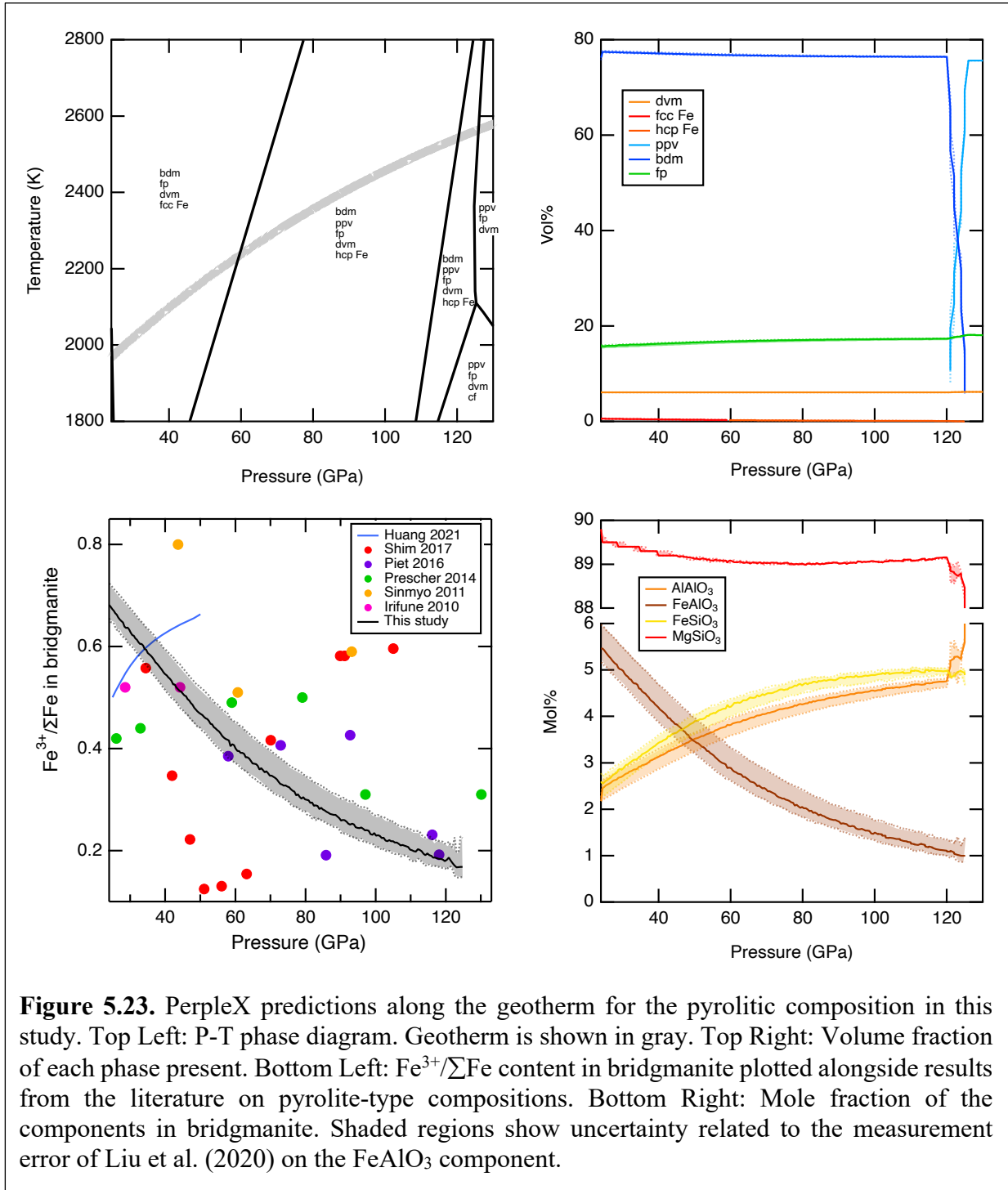
Figure 5.22. Updated observations of disproportionated metallic Fe. Data points from this study are plotted with the estimated pressure at high temperature (circles) as well as the pre-heat pressure (crosses).

composition, and it is likely that they did not observe disproportionated metallic Fe in their recovered samples because they mixed Au into the starting material and because a metal capsule was not used in their multianvil experiments, which may have allowed the sample to be exposed to oxidizing agents. The oxidation state of the Fe in the Ca-rich pyrolite of the Ko et al. (2022) study was not provided, so again high Fe^{3+} content may explain why disproportionated metal was not seen in that study. Generally, when metallic Fe was not observed in experiments in the literature, we conclude that it can be attributed to the starting oxidation state of Fe in the samples, poor image quality, mixing of a laser (and Fe) absorber, or oxidation during a multianvil experiment.

We note that the STEM EDS maps and line scans reveal that metallic Fe is often found adjacent to ferropericlasite grains, which is most clearly seen in the maps in Figures 5.14 (39 GPa and 2015 K), 5.15 (72 GPa and 2260 K), and D.17 (94 GPa and 2560 K) and the line scans in Figures 5.16 (72 GPa and 2260 K) and D.16 (94 GPa and 2560 K).

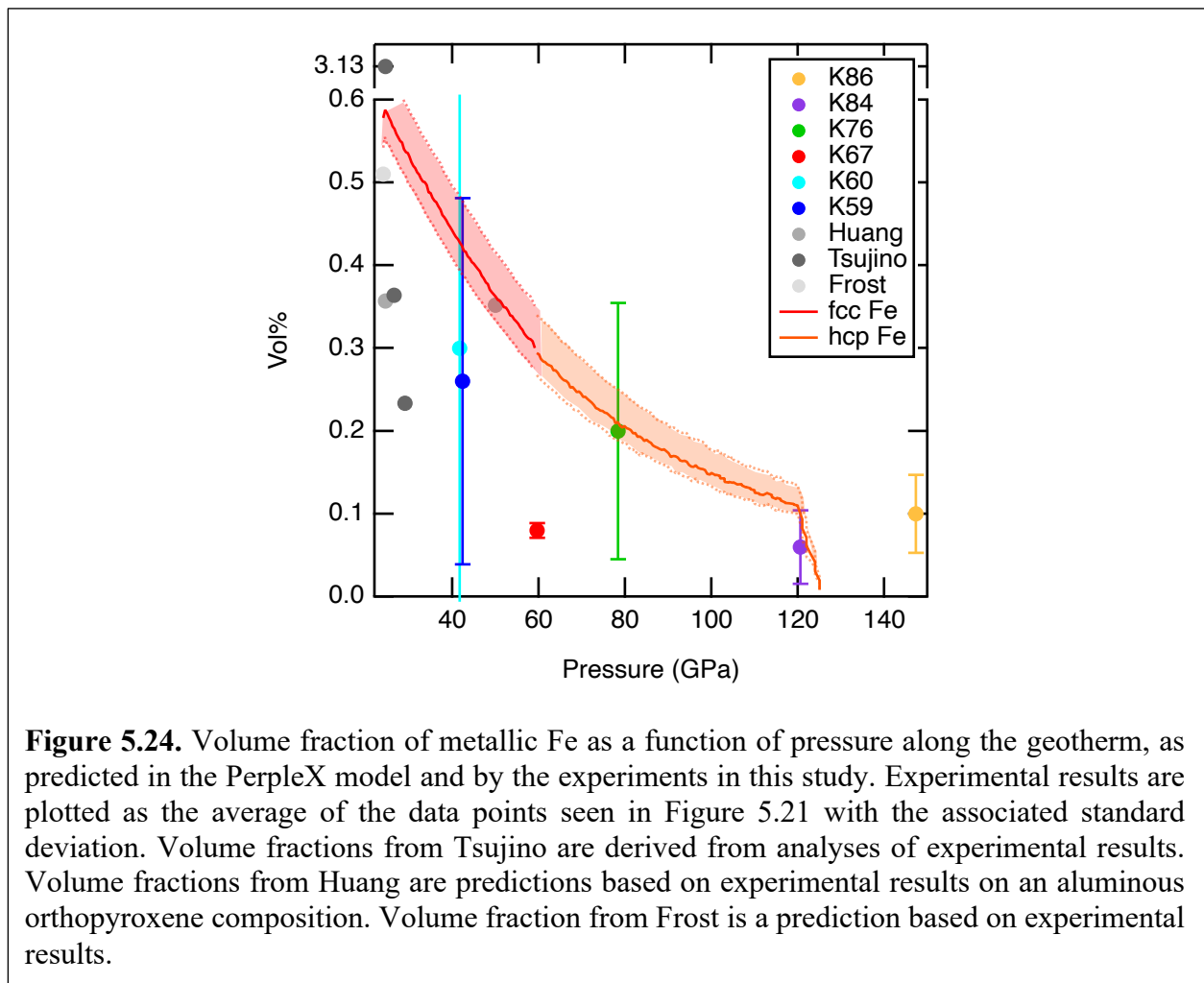
5.4.5 PerpleX modelling of disproportionation

The PerpleX thermodynamic calculation package (Connolly, 2009) can be used with the thermodynamic database provided by Stixrude & Lithgow-Bertelloni (2022) (with the modifications described in Chapter 3) to predict the phase assemblage of a pyrolite composition across the pressure and temperature range of the lower mantle, and the results match well with our observations from the XRD electron microscopy results (Figure 5.23). Bridgmanite makes up on average ~75 vol% of the assemblage, with ferropericlasite ~17 vol%, davemaoite ~6 vol%, and metallic Fe ~0.5 vol%. The model predicts that along the geotherm (Katsura, 2022), bridgmanite will have an FeAlO_3 component that is ~5.4 mol% at the top of the lower mantle, and this component will steadily decrease throughout the lower mantle to ~1 mol% at the base of the lower mantle (before the transition to post-perovskite). If all of the Fe^{3+} is in the FeAlO_3 component and the only other Fe is in the FeSiO_3 component, the $\text{Fe}^{3+}/\Sigma\text{Fe}$ content is ~0.67 at the top of the lower mantle and decreases to ~0.016 at the base of the lower mantle. This $\text{Fe}^{3+}/\Sigma\text{Fe}$ prediction is plotted alongside results from the literature on pyrolite-type compositions. There are clearly conflicting results on the expected trend of the $\text{Fe}^{3+}/\Sigma\text{Fe}$ content of bridgmanite throughout the lower mantle, but our calculation aligns with the trend of decreasing metallic Fe that is suggested by our



experimental results. As a result of the incorporation of the FeAlO_3 component into bridgmanite, the model further predicts that fcc Fe and then hcp Fe will exist throughout the lower mantle

(Figures 5.23 and 5.24). At the top of the lower mantle, we expect ~0.58 vol% fcc Fe, while at the base of the lower mantle, we expect ~0.007 vol% hcp Fe. Post-perovskite becomes stable at the base of the lower mantle and dominates the phase assemblage, and because the database does not contain an FeAlO₃ component of post-perovskite, the disproportionation reaction does not occur and no metallic Fe is predicted. This explains the sharp decrease in modeled Fe metal content above 120 GPa in Figure 5.24. The PerpleX calculation provides a slightly larger estimate than what we have determined from the experiments in this study, as seen in Figure 5.24. This is either a result of a systematic underestimation of the volume fraction from the experiments (due to an



overestimation of sample thickness) or an overestimation of the FeAlO_3 content in the bridgmanite in the model (assuming all Fe^{3+} in the bridgmanite is a result of disproportionation that also creates metallic Fe).

5.4.6 Implications

Though the amount of disproportionated metallic Fe is predicted to be quite small throughout the lower mantle, its presence is of great importance for the consideration of the geochemical evolution of the mantle and behavior of siderophile and volatile elements in the lower mantle. It has been suggested that ‘self-oxidation’ of the mantle through the disproportionation reaction can help to explain the necessary increase in the mantle oxidation state during the first billion years of Earth history (Galimov, 2005; Wood et al., 2006). Metallic Fe in the lower mantle can act as a host for volatile elements such as C, S, and H, as well as for siderophile elements, which include geochemical tracers such as the Pt group elements (Pt, Pd, Rh, Ru, Os, Ir) and isotopic tracers such as Re, Os, Pt, and W. Because Pt group elements are so highly siderophile, any amount of metallic Fe would act as a host for these elements.

In particular, the pressure dependence of iron disproportionation and the resultant decrease in metallic Fe with increasing depth in the lower mantle bears further consideration. The implications can be considered with two connected approaches: considering the effects of a decreasing $\text{Fe}^{3+}/\Sigma\text{Fe}$ ratio in bridgmanite and considering the effects of a decreasing quantity of metallic Fe with depth. Fu et al. (2023) demonstrated that an Fe₁₀-Al₁₄ bridgmanite has sound speeds v_s and v_p that are 2.6-3.5% and 3.1-4.7% lower than those of pure MgSiO_3 bridgmanite. Thus, a decreasing Fe^{3+} content of bridgmanite throughout the mantle would result in a slight increase in sound speeds with depth. We will explore how the decreasing proportion of metallic

Fe in the lower mantle can affect the volatile element C. Carbon in the lower mantle can be found in the form of carbonates, carbides, or diamond. Metallic Fe in the lower mantle can react with subducted carbonates to form carbides (such as Fe_3C at lower pressures or Fe_7C_3 at higher pressures), or C can dissolve into metallic Fe (Stagno et al., 2011). At the high pressure and temperature conditions of the lower mantle, C is extremely soluble in Ni-Fe alloys (~2 wt% C), metallic Fe-rich liquids (~6 wt% C), and carbides (Day et al., 2023). If, as suggested by the PerpleX prediction, the volume fraction of metallic Fe drops by a factor of 5 from the top of the lower mantle to the base of the lower mantle, the concentration of C in an Fe alloy or carbide would increase by a factor of 5 (Figure 5.25). If C saturates in the Fe alloy or carbide, diamond may also become stable. We can use the PerpleX estimates of the weight percent of metallic Fe at the top and bottom of the lower mantle along with the fraction of C/Fe in Fe_7C_3 carbide to estimate what mass of C would be required to saturate all of the available Fe metal to form the carbide phase. If we take the PerpleX prediction of ~1.1 wt% metallic Fe at the top of the lower mantle (25 GPa), this would require 1032 ppm C to use all of the available Fe metal to create the Fe_7C_3 phase. If we take the PerpleX prediction of ~0.2 wt% metallic Fe near the base of the lower mantle (120 GPa) to be metallic Fe, this would require 212 ppm C to use all of the available Fe metal to create the Fe_7C_3 phase. Estimates of primordial carbon contained in the mantle range from 30-1000 ppm (Dasgupta & Hirschmann, 2010). If we imagine a scenario in which the mantle C content is in the middle of this range at 500 ppm, we might expect both the Fe_7C_3 phase and metallic Fe to exist at the top of the lower mantle. At base of the lower mantle, we might expect both Fe_7C_3 phase and diamond to exist. Stagno et al. (2011) suggest that carbonate (in the form of magnesite MgCO_3)

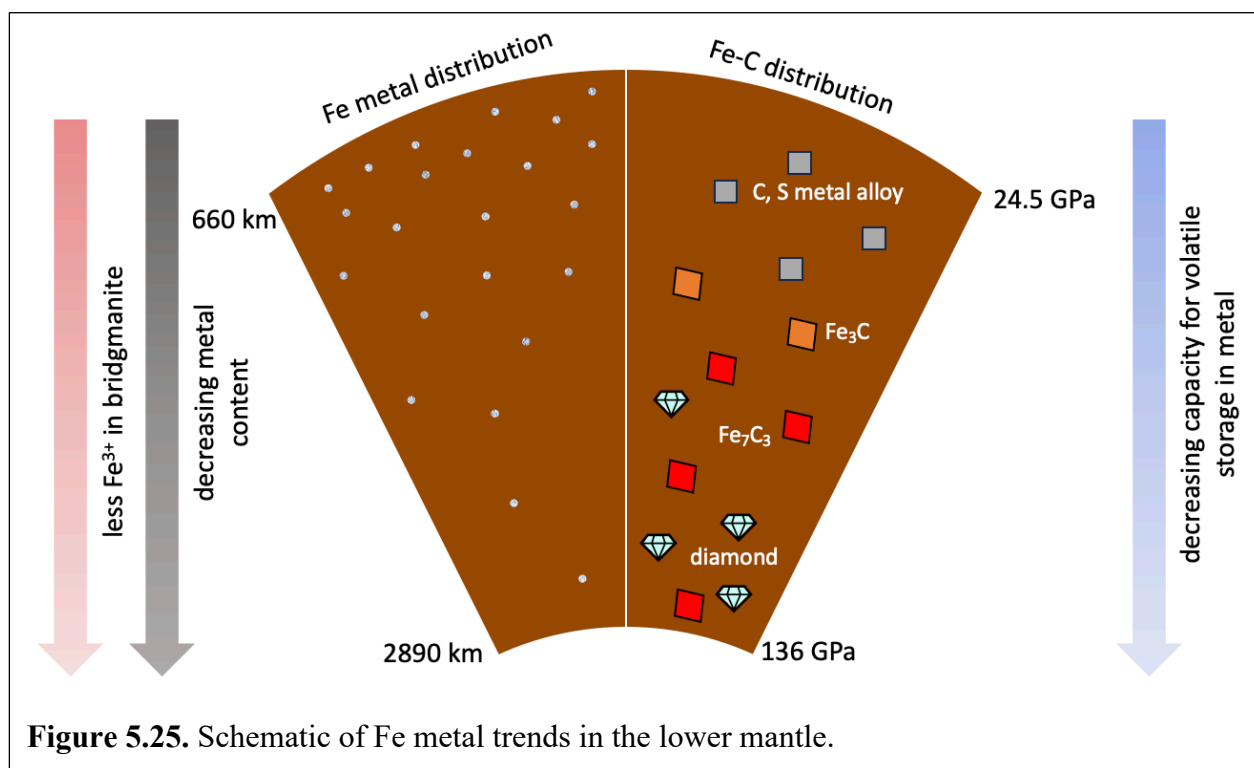


Figure 5.25. Schematic of Fe metal trends in the lower mantle.

may be stable at the base of the mantle, where it could coexist with Fe-rich carbides. This scenario also aligns with the predictions in this study, as the decrease in metallic Fe, which acts as a host for C throughout the lower mantle, could force C at the base of the mantle to saturate in the metallic Fe and form a separate carbonate phase. We have discussed only carbon here, but sulfur would also take up some of the metallic Fe, removing some of the capacity for volatile storage in the Fe metal or carbide phases.

5.5 Conclusion

We have demonstrated that the iron disproportionation reaction occurs across the entire range of the lower mantle by using SEM, TEM, and STEM analyses on pyrolitic compositions recovered from high pressure and temperature experiments. The major phases were confirmed to be bridgmanite and ferropericlase by *in-situ* synchrotron XRD, while *ex-situ* microscopy analyses

confirmed the existence of disproportionated metallic Fe. Analysis of the TEM images of the recovered samples revealed that the volume proportion of disproportionated metallic Fe decreases across the lower mantle, and thermodynamic modeling using the PerpleX software confirmed this trend. Decreasing metallic Fe content with depth in the lower mantle has implications for the storage and cycling of important volatile elements such as C.

6 CONCLUSIONS

This thesis describes the occurrence of the iron disproportionation reaction across the pressure and temperature range of Earth's lower mantle. While the occurrence of the iron disproportionation reaction has been proposed to occur in the lower mantle by Frost et al. (2004), there have been no targeted experimental explorations of the occurrence of the reaction across the pressure and temperature range of the lower mantle. This thesis is centered on experimentally detecting disproportionated Fe metal across a range of pressure and temperature conditions and confirming the experimental results with thermodynamic modelling.

Issues in understanding the conditions in which iron disproportionation occurs at high pressures and temperatures stem from inconsistencies in experimental conditions and analytical techniques used in studies in the literature. In Chapter 2, I detailed the experimental techniques that were determined to be essential for the detection of disproportionated Fe metal in DAC experiments. I found that the use of SEM, TEM, and STEM analyses was necessary for the detection of disproportionated metallic Fe.

To robustly demonstrate the occurrence of iron disproportionation across a range of pressure and temperature conditions, I employed the thermodynamic modelling software PerpleX to supplement experimental techniques. In Chapter 3, I detailed the modifications to the Stixrude & Lithgow-Bertelloni (2022) thermodynamic database of lower mantle mineral phases that were necessary to model the iron disproportionation reaction. I added the following phases to the database: fcc Fe, hcp Fe, hematite, and the FeAlO₃ endmember of bridgmanite. With the addition of these phases, I was able to use PerpleX to make predictions of iron disproportionation at lower mantle conditions. I demonstrated that these modifications enabled predictions of phase

assemblages and phase compositions that explain results seen in the literature. I provided predictions of iron disproportionation across the pyrope-almandine join at high pressures, demonstrating that the disproportionated metallic Fe was not identified in the XRD study of Dorfman et al. (2012). I also provided predictions of iron disproportionation in an Al-rich olivine composition studied in Shim et al. (2017) and an Al-rich pyroxenite studied in Creasy et al. (2020).

In Chapter 4, I detailed how disproportionated metallic Fe was detected in high pressure and temperature phase assemblages created from a garnet starting material. To explore the occurrence of the iron disproportionation reaction from 25 to 65 GPa, a natural almandine-pyrope-grossular garnet was studied with *in-situ* X-ray diffraction in the laser-heated diamond anvil cell and with *ex-situ* scanning electron microscopy techniques. Upon heating the natural almandine-pyrope-grossular garnet up to 3000 K up to 65 GPa, the formation of a phase assemblage consisting of bridgmanite, stishovite, and davemaoite was confirmed by X-ray diffraction, but because of the low abundance of Fe metal and small grain size, X-ray diffraction was determined not to be effective to detect the disproportionation reaction. Examination of the samples recovered between 39-64 GPa by scanning electron microscopy analysis revealed the presence of nm-scale disproportionated iron metal grains as an additional product of this reaction that was not detectable in the X-ray diffraction patterns. Volume compression data of bridgmanite synthesized in the experiments were fit to the Birch-Murnaghan equation of state and compared to similar compositions. Bridgmanite was found to decompress to the LiNbO₃-type structure, indicating a high FeAlO₃ content, in accordance with the occurrence of a disproportionation reaction. The experimental results were confirmed with the use of PerpleX thermodynamic modelling. With the PerpleX calculations, we predicted a bridgmanite FeAlO₃ component of 39 mol% at 52 GPa and

2000 K, which aligned with the estimation of FeAlO₃ content based on volume calculations from XRD results (32 mol%). We also used PerpleX to predict the phase diagram of pure almandine and demonstrated that the modification of the Stixrude & Lithgow-Bertelloni (2022) database significantly altered the high pressure and temperature phase assemblage predictions.

In Chapter 5, I detailed how disproportionated metallic Fe was detected in high pressure and temperature phase assemblages created from a pyrolitic starting material. Pyrolite glass was compressed and heated in a LHDAC from 27 to 132 GPa and 1875 to 3000 K. Synchrotron XRD confirmed the formation of bridgmanite and ferropericlase at high pressures and temperatures, while davemaoite could not conclusively be detected in most samples, which we attributed to its low abundance or potential dissolution into bridgmanite, as suggested by Ko et al. (2022). We used the bridgmanite and ferropericlase peaks in the XRD patterns to determine the lattice parameters of these phases from 0 to 100 GPa and compared the compression behavior to similar compositions. We found that the lattice parameter trends aligned with similar results in the literature (Lee et al., 2004; Ko et al., 2022). Seven samples were recovered from high pressure and temperature conditions and analyzed with TEM and/or STEM techniques. We identified grains of bridgmanite, ferropericlase, and metallic Fe in samples recovered from 39 to 132 GPa. Though grains were on the scale of 10s to 100s of nm, we were able to confirm that metallic Fe exists in the phase assemblages through the use of EDS mapping and line scans. We used the TEM images of the recovered samples to estimate the volume fraction of disproportionated metallic Fe formed throughout the lower mantle, and we found that the amount of disproportionated Fe decreases from ~0.3 vol% at 40 GPa to ~0.06 vol% at the base of the lower mantle. We confirmed this trend with PerpleX modelling, with which we predicted ~0.55 vol% metallic Fe at 30 GPa and ~0.1 vol%

metallic Fe at the base of the lower mantle. We explored the implications of a decreasing amount of disproportionated metallic Fe with depth in the lower mantle and predicted how it might impact the distribution of C by stabilizing different C-bearing phases with depth.

Through the work presented in this thesis, I have demonstrated that the disproportionation reaction operates across the range of lower mantle pressure and temperature conditions. In the future, this work could be extended with further recovery experiments to confirm the observed trend of decreasing metallic Fe content in the lower mantle with more finely spaced pressure points. Geochemical and geodynamical modeling could then be performed to explore the implications of decreasing metallic Fe with depth in the lower mantle. Additionally, with further refinement of sample recovery and thin section cutting with the FIB, it may be possible to create thin sections that will allow EDS measurements without grain overlap, which would yield essential information on the compositions of bridgmanite and ferropericlase coexisting with disproportionated metallic Fe and further elucidate the mechanisms driving a decrease in disproportionation throughout the mantle. Specifically, further work could be done to clarify the effects of the Fe³⁺ spin state and its consequences on the physical properties of bridgmanite.

APPENDIX A SUPPLEMENTAL MATERIAL FOR CHAPTER 2

Figure A.1. Lab and synchrotron Mössbauer results on glass beads.

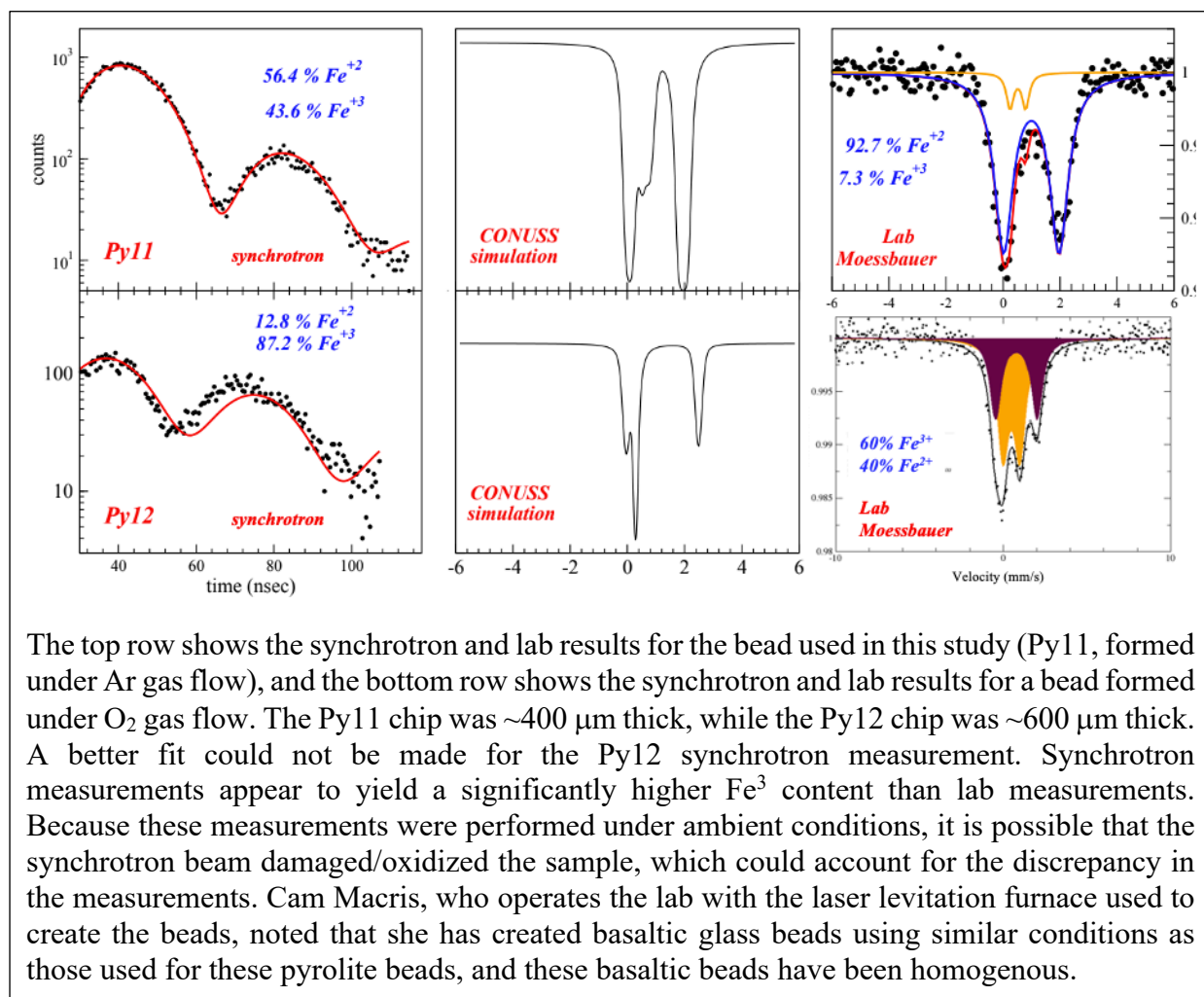


Figure A.2. Additional lab Mössbauer results on glass beads.

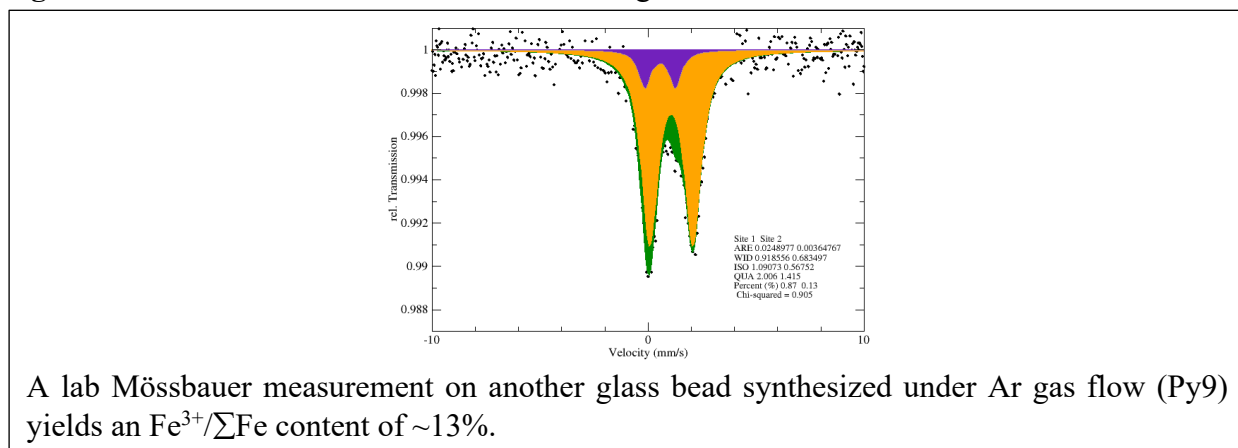


Figure A.3. Example of a sample with C contamination.

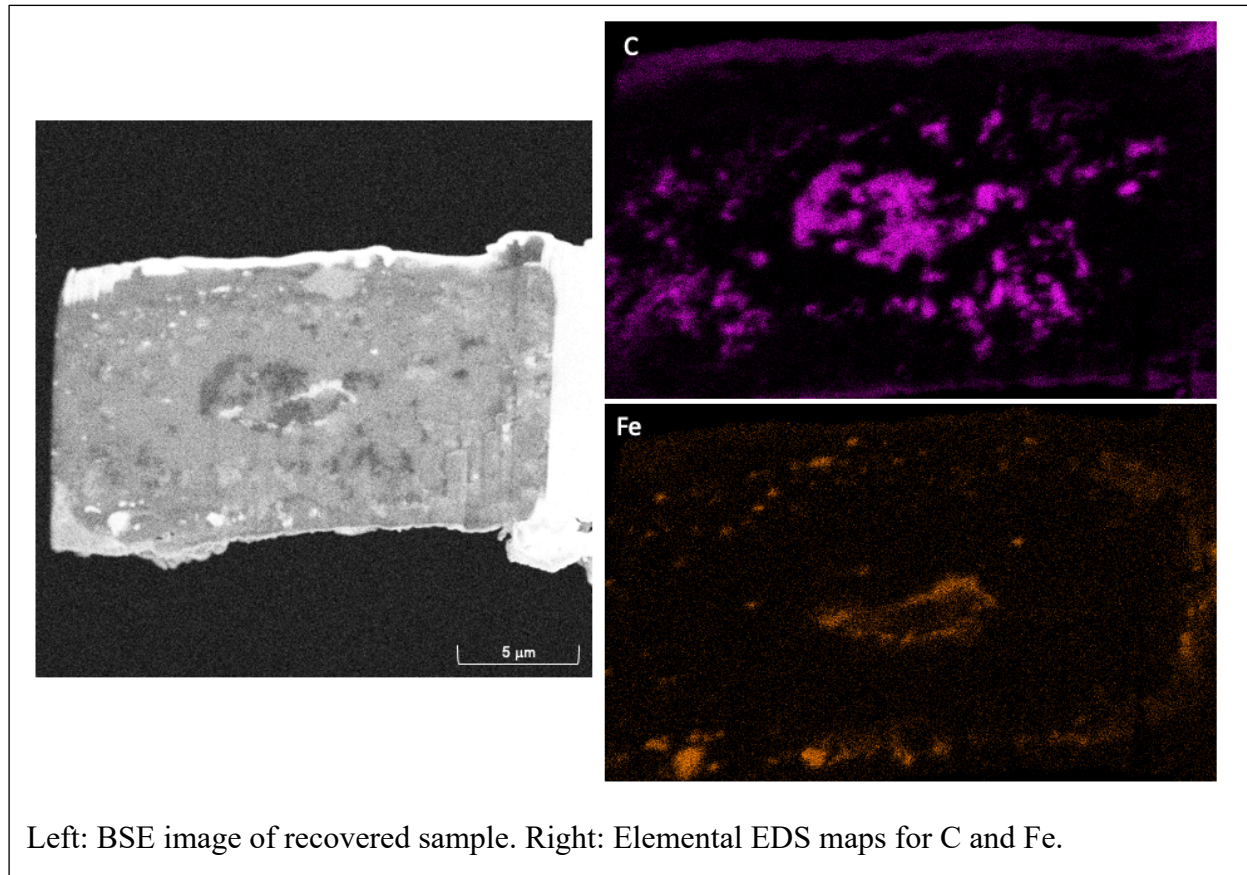
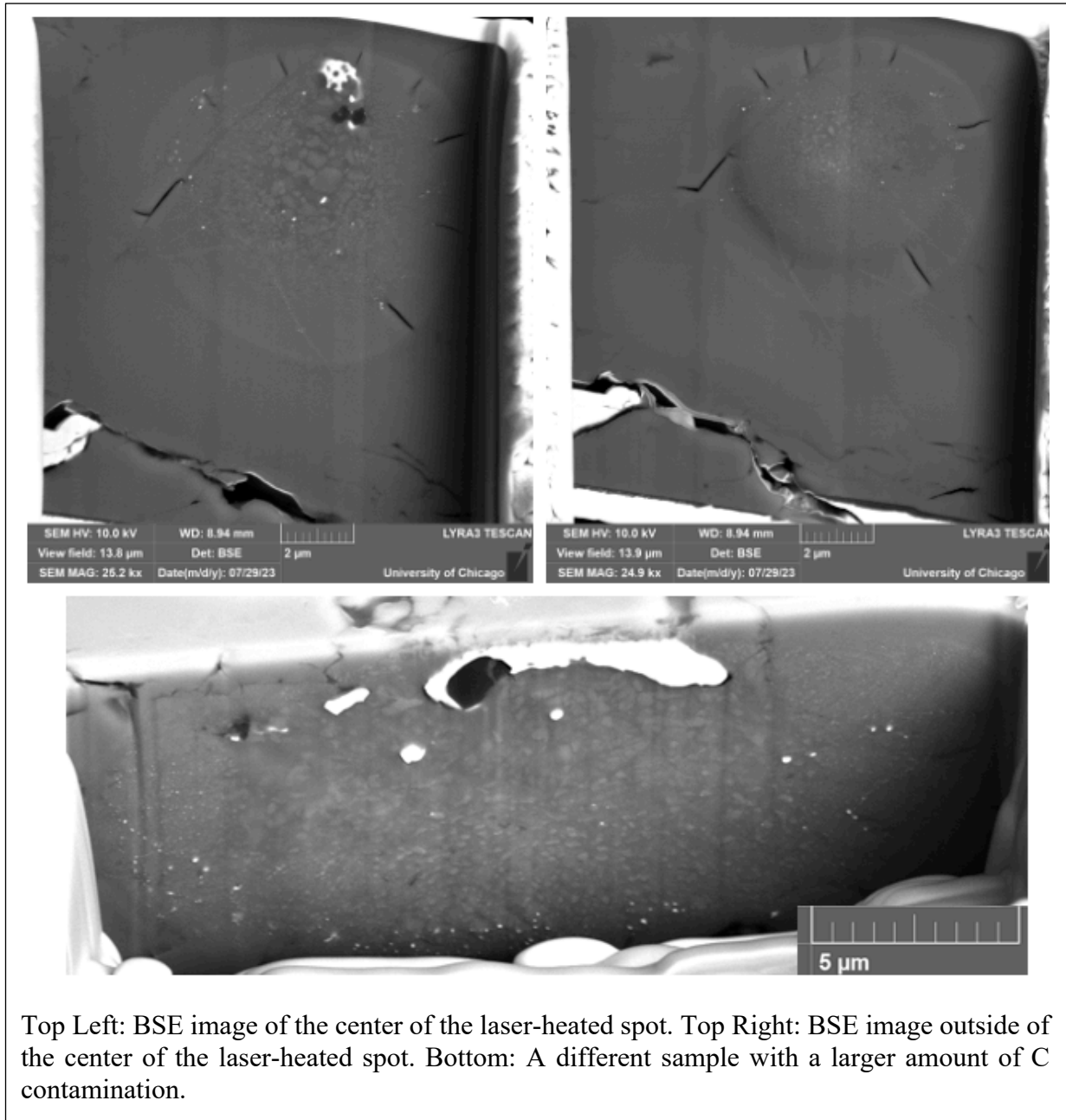
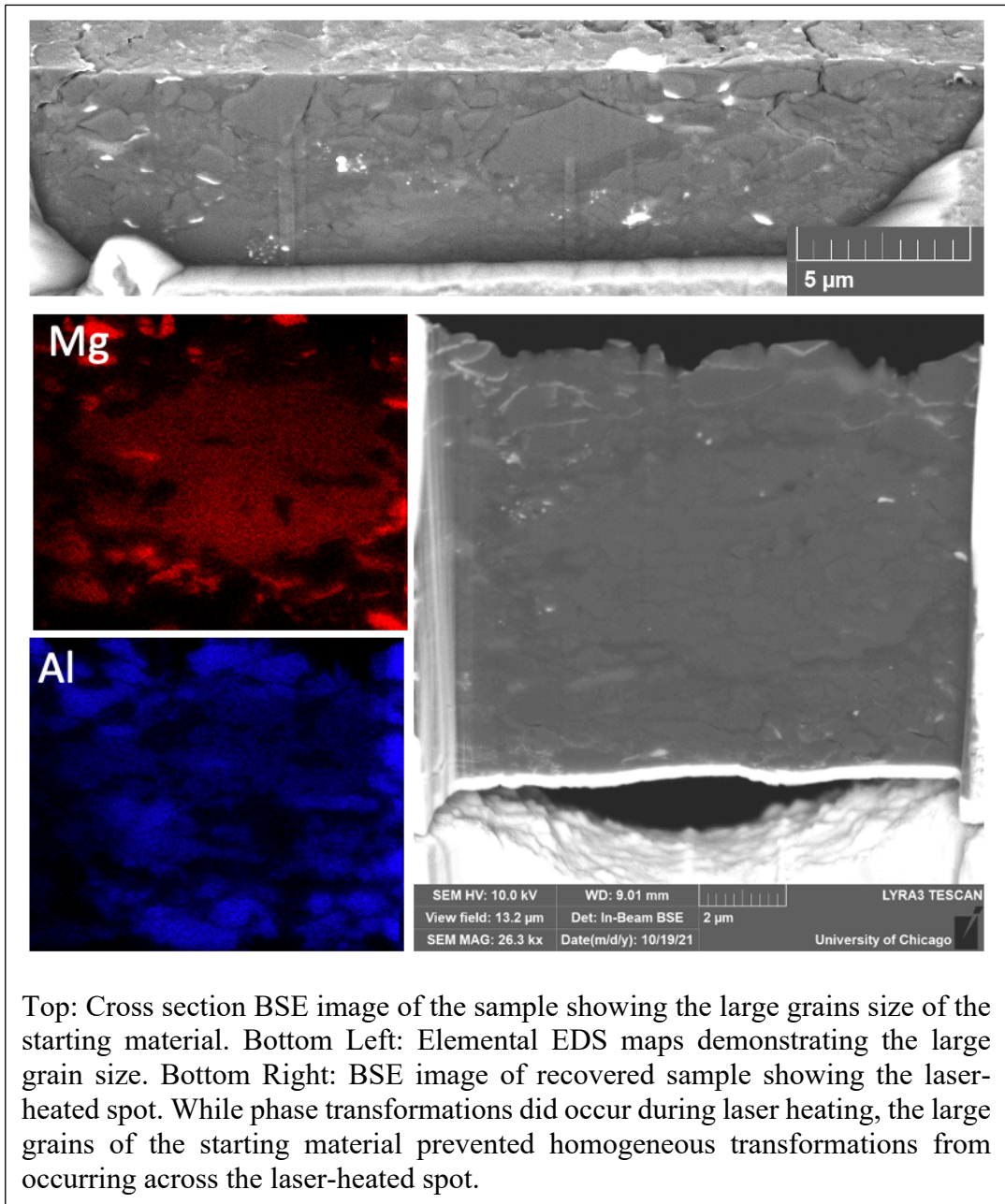


Figure A.4. Example of a pyrolite glass sample with C contamination.



Top Left: BSE image of the center of the laser-heated spot. Top Right: BSE image outside of the center of the laser-heated spot. Bottom: A different sample with a larger amount of C contamination.

Figure A.5. Example of a recovered powdered pyrolite sample that did not achieve phase equilibrium.



Top: Cross section BSE image of the sample showing the large grains size of the starting material. Bottom Left: Elemental EDS maps demonstrating the large grain size. Bottom Right: BSE image of recovered sample showing the laser-heated spot. While phase transformations did occur during laser heating, the large grains of the starting material prevented homogeneous transformations from occurring across the laser-heated spot.

Figure A.6. Example of a recovered powdered peridotite sample that did not achieve phase equilibrium.

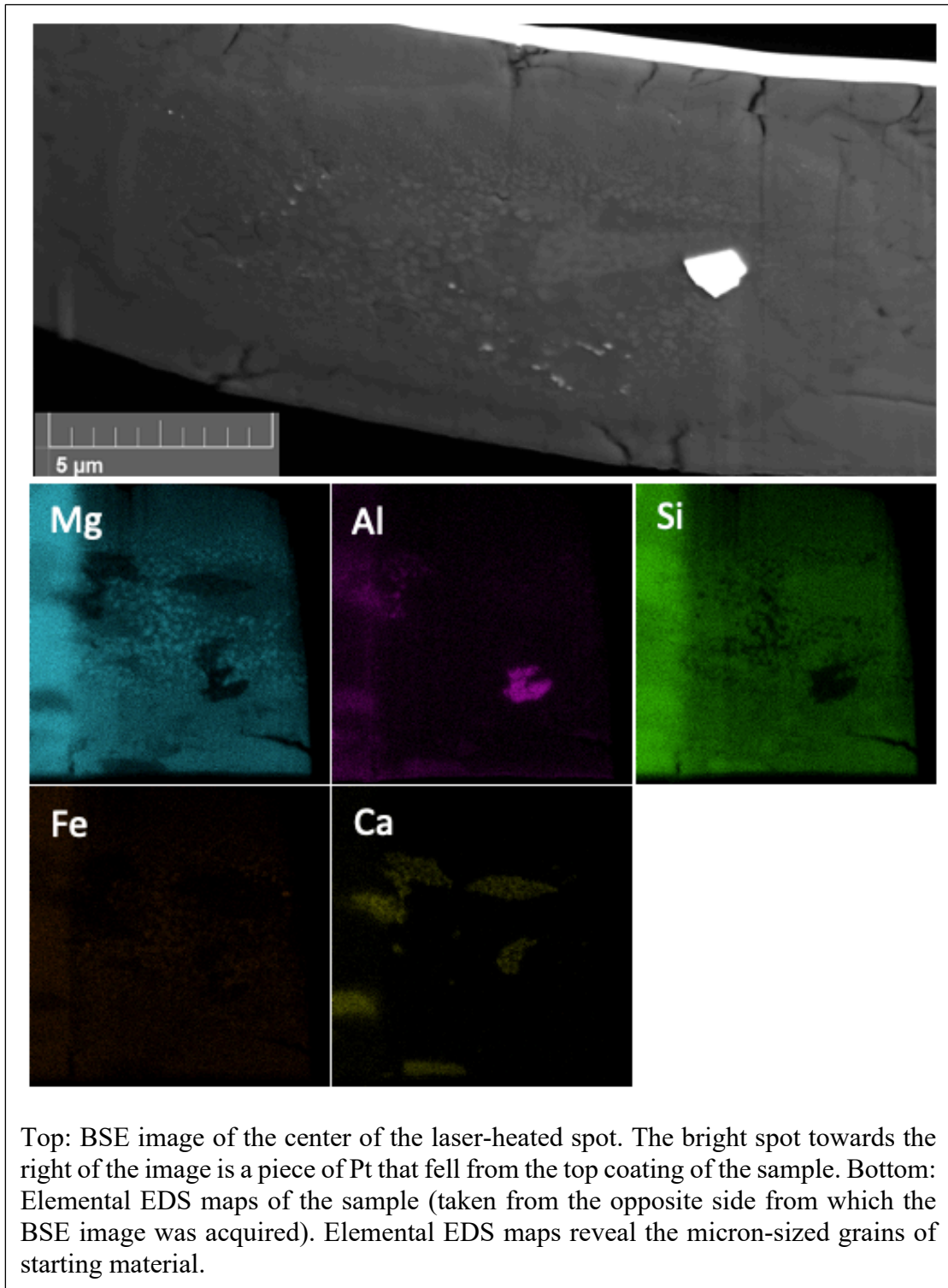


Figure A.7. Compressed garnet and pyrolite glass samples prior to laser heating.

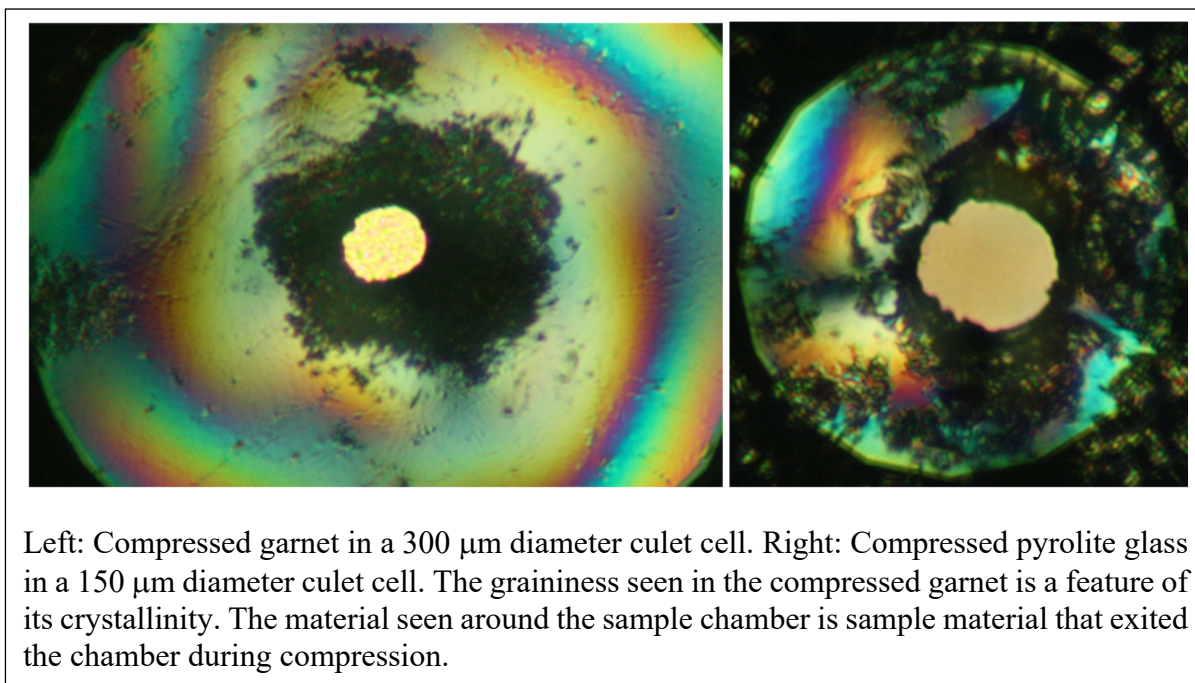


Figure A.8. Recovered sample in a gasket.

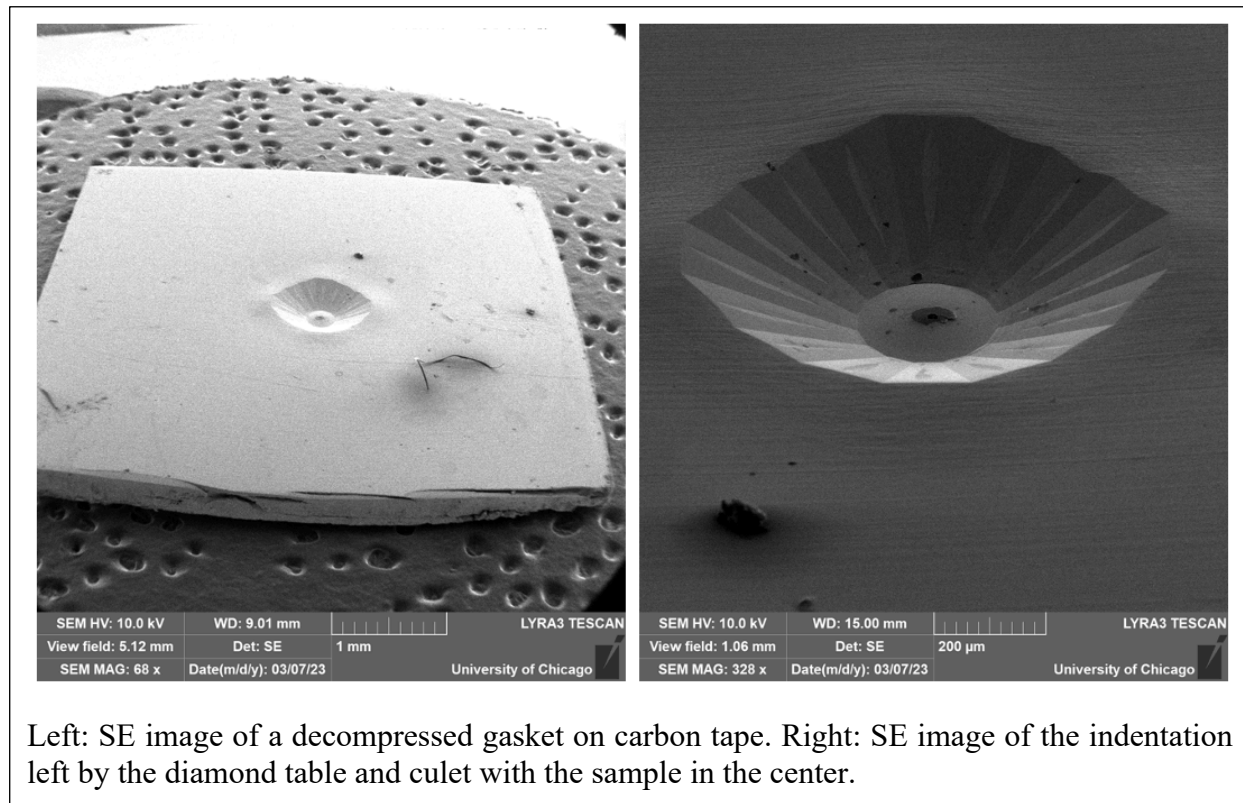


Figure A.9. Bending of a sample attached to a TEM post.

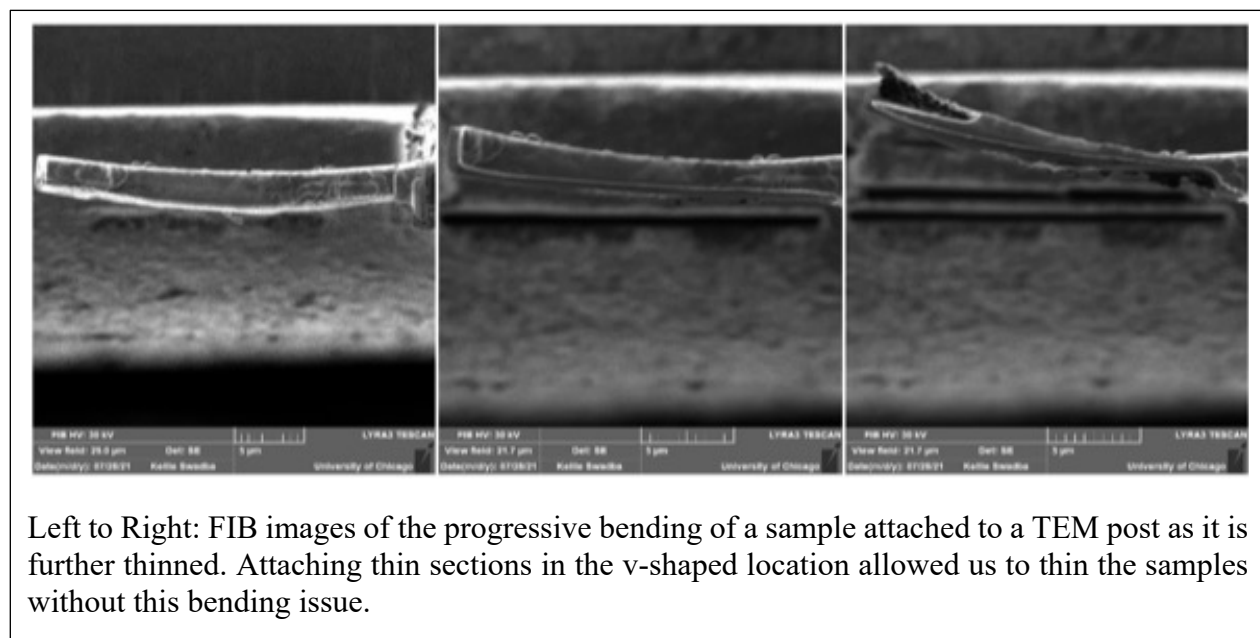


Figure A.10. Example of Ga deposition.

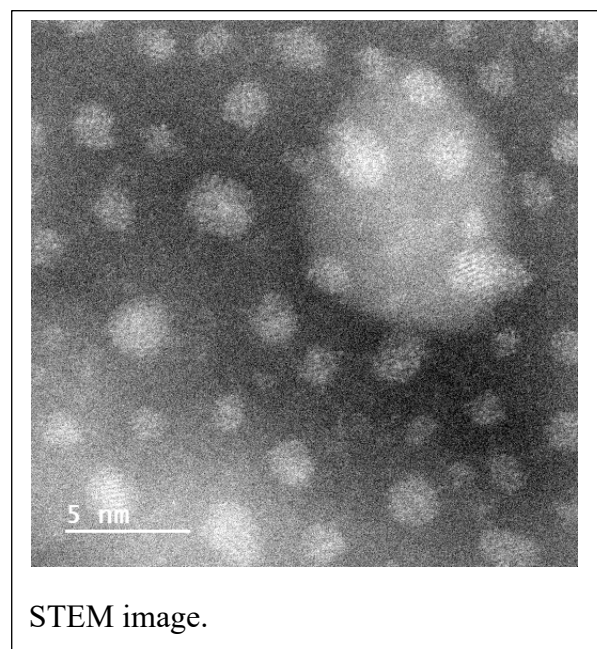


Figure A.11. Example of a thinned sample viewed in the SEM.

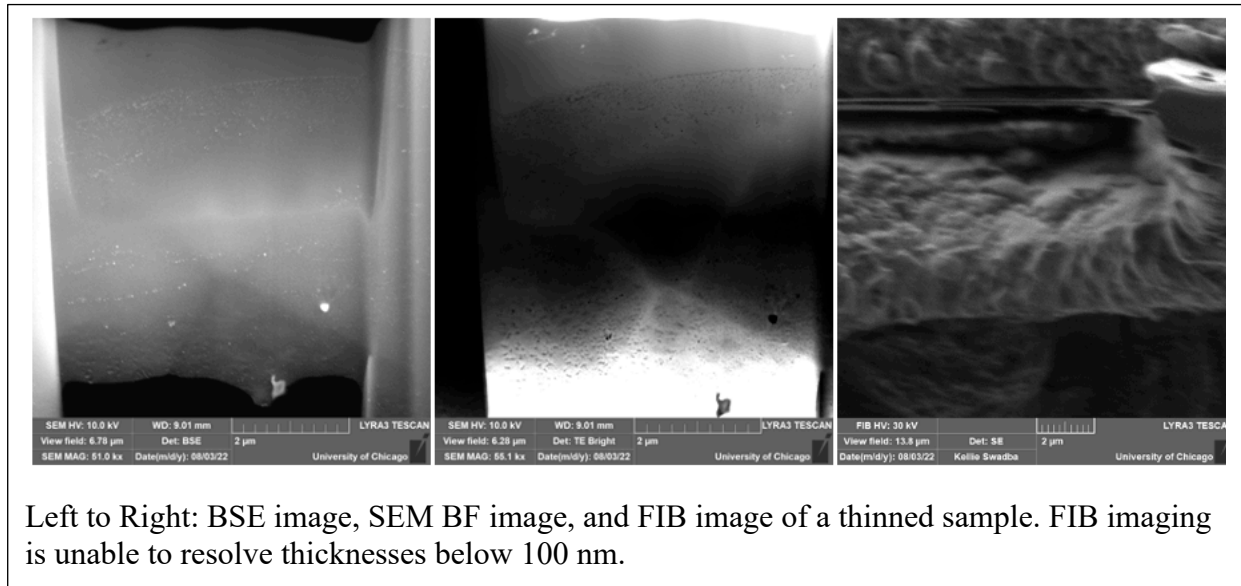


Figure A.12. Example of an unevenly thinned sample.

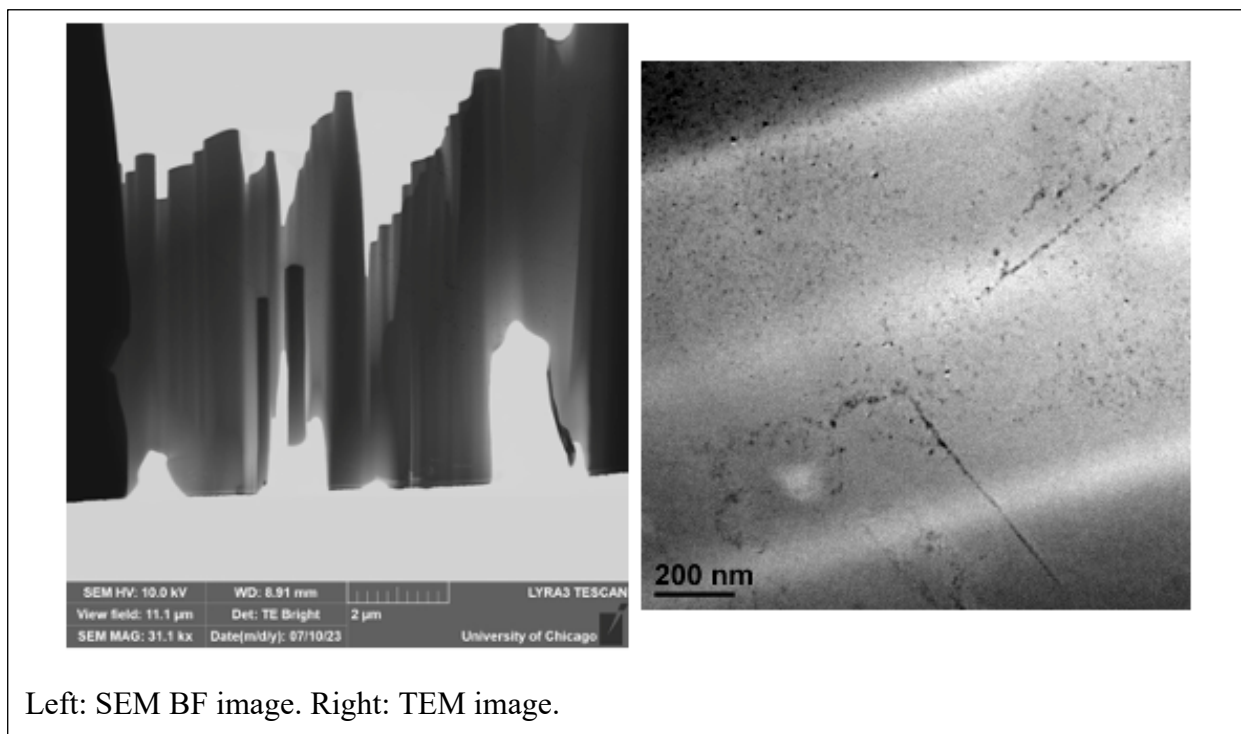


Figure A.13. Example of underfocusing in the TEM.

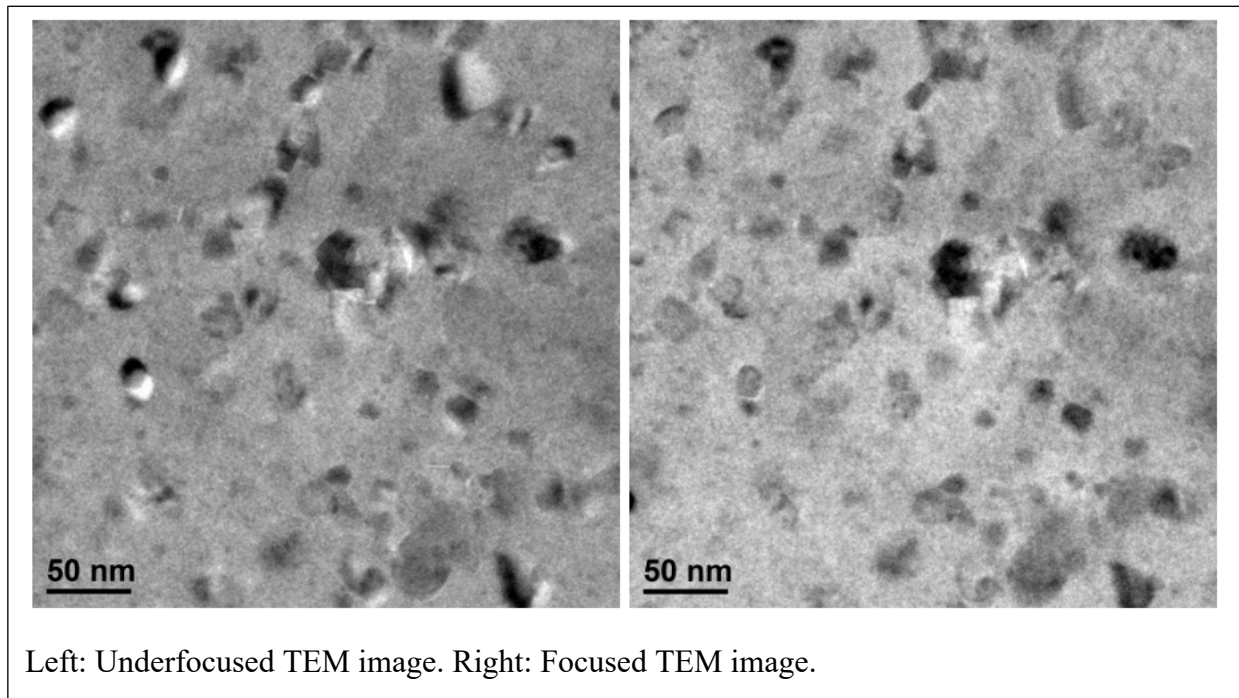


Figure A.14. Example of grain overlap.

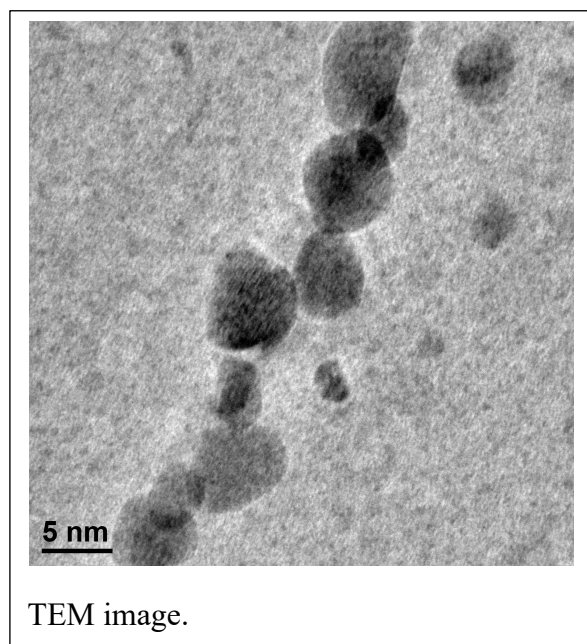


Figure A.15. Examples of electron diffraction images.

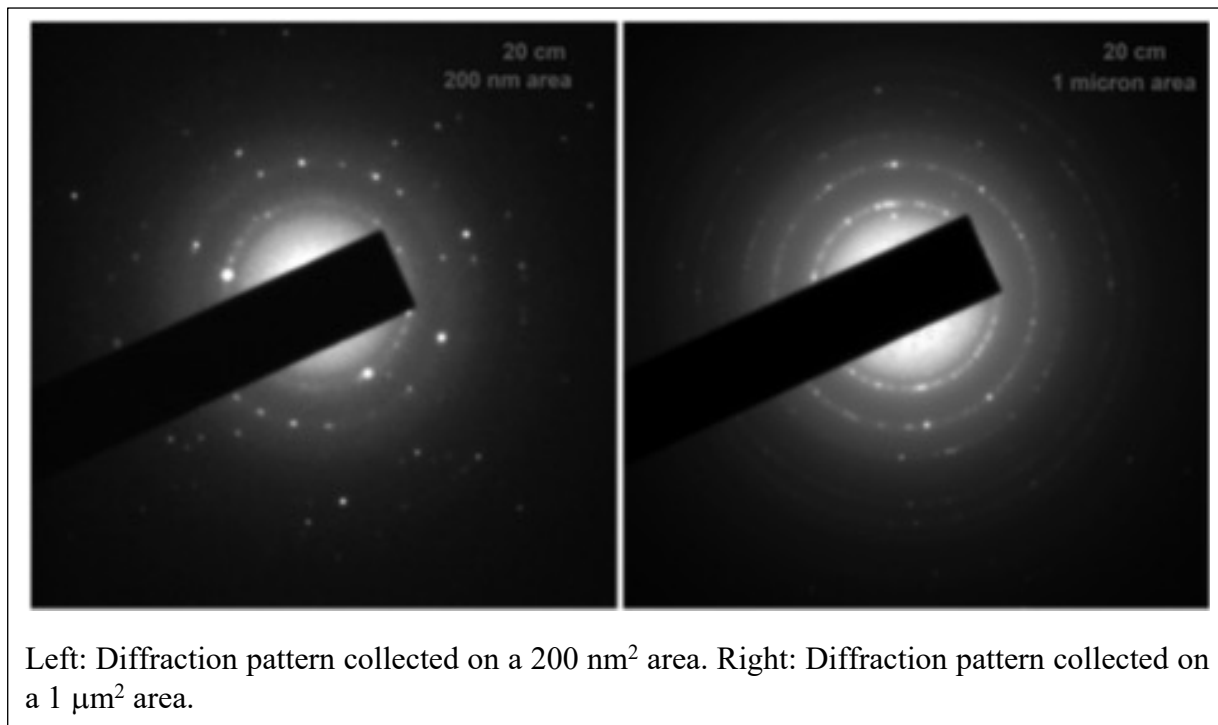


Figure A.16. Examples of visible contamination on samples after STEM EDS measurements.

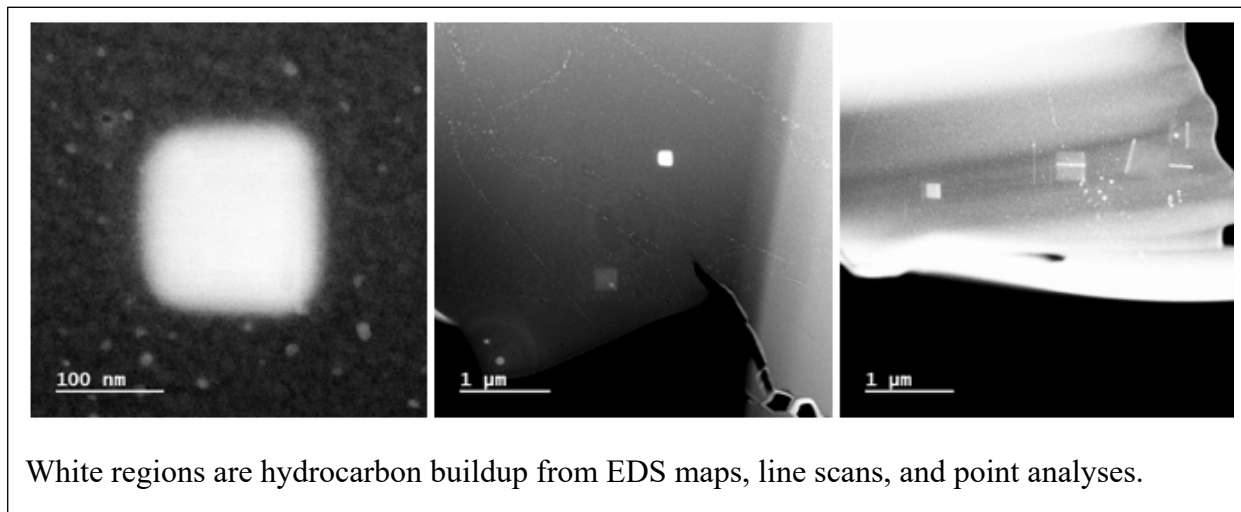
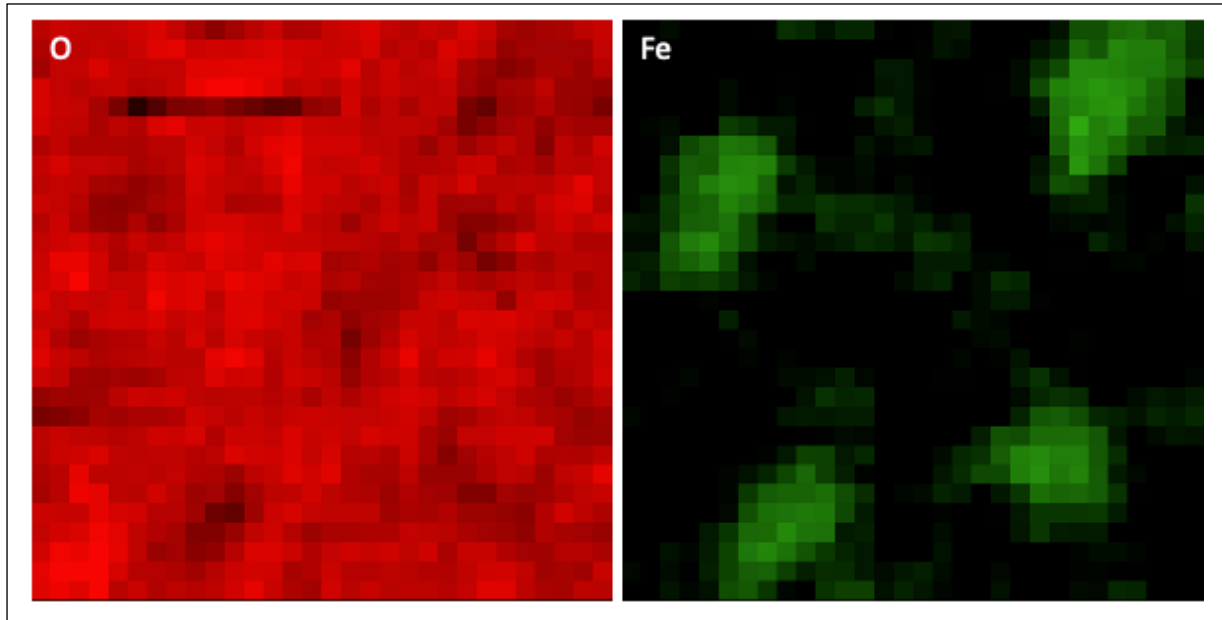


Figure A.17. EELS collection on a pyrolite glass sample.



APPENDIX B SUPPLEMENTAL MATERIAL FOR CHAPTER 3

Figure B.1. Sample problem definition file.

```

stx21ver_updatedtran.dat      thermodynamic data file ← name of thermodynamic data file
print      | no_print suppresses print output
plot       | obsolete 6.8.4+
stx21_solution_model.dat      | solution model file, blank = none ← name of solution model file
fealo3_test_stx21
perplex_option.dat           | Perple_X option file ← name of option file
  5 calculation type: 0- composition, 1- Schreinemakers, 3- Mixed, 4- swash, 5- gridded min, 7- 1d
fract, 8- gwash, 9- 2d fract, 10- 7 w/file input, 11- 9 w/file input, 12- 0d infiltration ↑
  0 unused place holder, post 06
  0 number component transformations
  7 number of components in the data base
  0 component amounts, 0 - molar, 1 weight ← components are entered as molar amounts
  0 unused place holder, post 06                               to define composition
  0 unused place holder, post 06
  0 unused place holder, post 05
  0 ifug EoS for saturated phase
  2 gridded minimization dimension (1 or 2)
  0 special dependencies: 0 - P and T independent, 1 - P(T), 2 - T(P)
  0.00000  0.00000  0.00000  0.00000  0.00000  Geothermal gradient polynomial
  coeffs.

begin thermodynamic component list
MGO  2  1.00000  0.00000  0.00000  molar amount
SI02 2  1.00000  0.00000  0.00000  molar amount
FE   2  0.00000  1.00000  0.00000  molar amount
AL2O3 2  0.00000  0.50000  0.00000  molar amount
O2   2  0.00000  0.75000  0.00000  molar amount
end thermodynamic component list

begin saturated component list
end saturated component list

begin saturated phase component list
end saturated phase component list

begin independent potential/fugacity/activity list
end independent potential list

begin excluded phase list
end excluded phase list

begin solution phase list
Pv ← solid solution phases that should be included in the calculation
Aki
end solution phase list

270000. ← 2300.00 ← min and max of variables involved in calculation
270000. 1800.00 0.00000 0.00000 0.00000 max p, t, xco2, u1, u2
0.00000 0.00000 0.00000 0.00000 0.00000 min p, t, xco2, u1, u2
06 unused place holder post

2 1 4 5 3 indices of 1st & 2nd independent & sectioning variables

```

Table B.1. Thermodynamic parameters from the literature.

PerpleX symbol	Parameter	Stx11 MgSiO ₃	Stx21 MgSiO ₃	Stx11 FeSiO ₃	Stx21 FeSiO ₃	Stx11 AlAlO ₃	Stx21 AlAlO ₃	Kurnosov FeAlO ₃	HP02 EOS2 Hem	HP11 EOS8 Hem
G0	Helmholtz energy									
S0	$F_0 = G_0$ [$\frac{J}{mol}$]	-1368283	-1362442.8	-1040920	-1002662.5	-1533878	-1517728.6	n/a	-743740.7	-851658.3
V0	Negative number of atoms pfu	-5	-5	-5	-5	-5	-5	n/a	-5	-5
	Negative volume									
c1	V_0 [$\frac{J}{bar}$]	-2.4445	-2.4445	-2.5485	-2.5321	-2.4944	-2.4944	-2.69	-3.0274	-3.027
c2	Isothermal bulk modulus K_0 [bar]	2505264	2505469	2721152	2705825.5	2582000	2424000	2200000	1996000	2230000
	Pressure derivative of isothermal bulk modulus K'_0	4.14	4.13499	4.14	4.01	4.14	4.1	1.3	4	4.04
c3	Debye temperature θ [K]	905.9412	880.01895	870.8122	746.56455	886.4601	858.26509	886	n/a	551.6762
c4	Gruneisen thermal parameter γ	1.56508	1.54222	1.56508	1.54222	1.56508	1.54222	1.57	n/a	n/a
c5	Mie-Gruneisen exponent q	1.10945	0.84088	1.1095	0.84088	1.10945	0.84088	1.1	n/a	n/a

Stx11 and Stx21 refer to Stixrude & Lithgow-Bertelloni (2011) and (2021), respectively. Kurnosov refers to Kurnosov et al. (2017), and these parameters are taken from the paper and are not found in any PerpleX database. HP02 and HP11 refer to Holland & Powell (1998) and (2011), respectively. Liu et al. (2020) also provide estimates of V_0 and K_0 for MgSiO₃, FeSiO₃, AlAlO₃, and FeAlO₃ based on experimental results. In that order they give V_0 of 2.444, 2.538, 2.584, and 2.794 J/bar and K_0 of 2560000, 2590000, 2550000, and 1970000 bar.

Figure B.2. Demonstration of removal of Landau transitions in stx21ver.dat database.

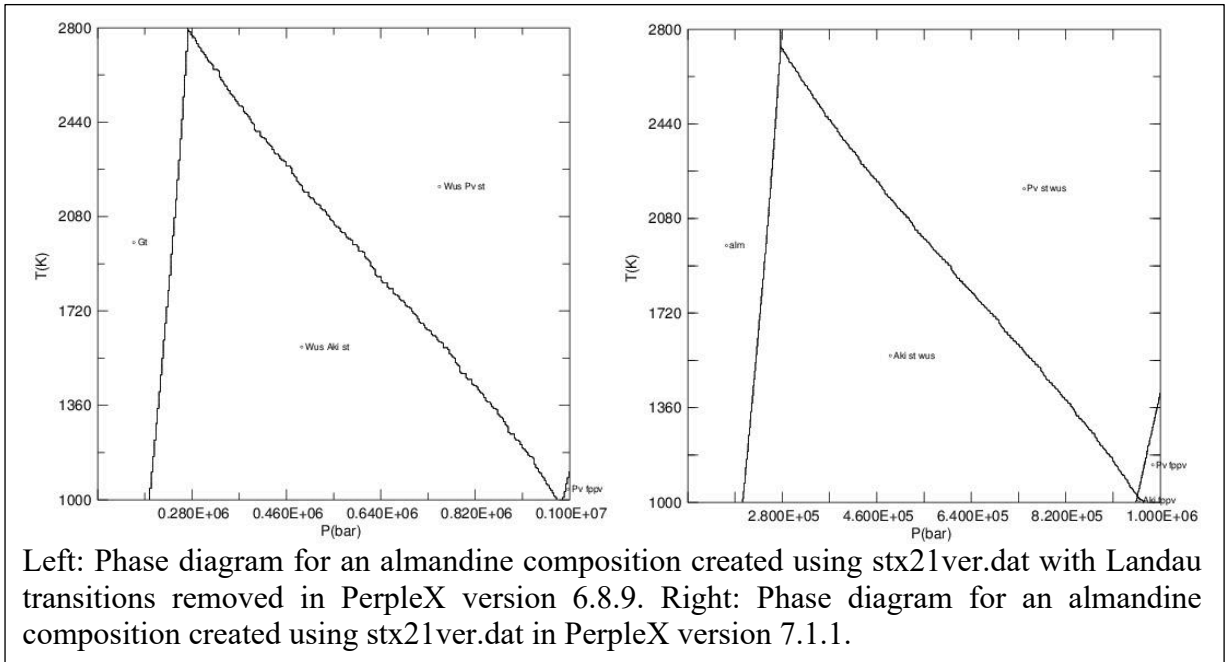


Figure B.2. Phase boundary generated by special Komabayashi & Fei (2010) EOS in PerpleX.

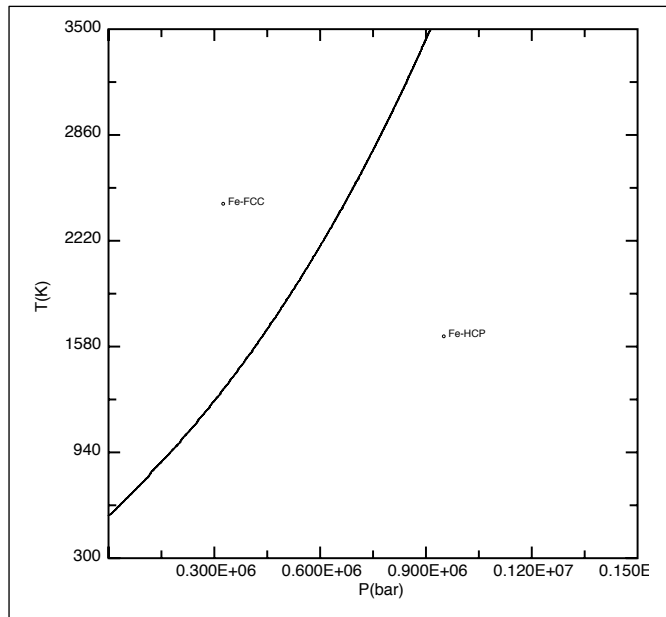


Figure B.3. Fits of fcc Fe and hcp Fe isotherms to the Stixrude & Lithgow-Bertelloni (2005) equation of state.

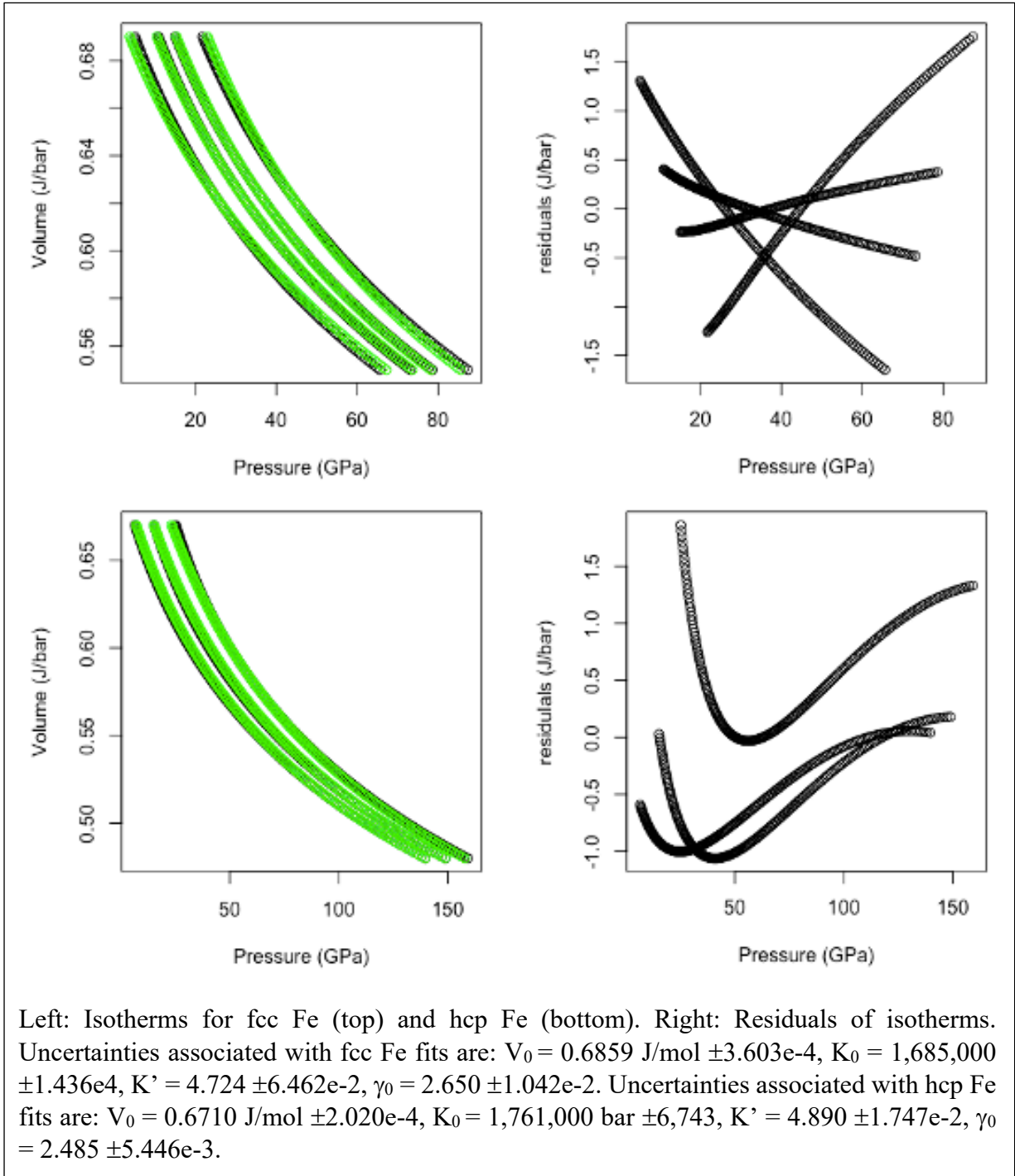


Figure B.4. P-T plot of FeO bulk composition.

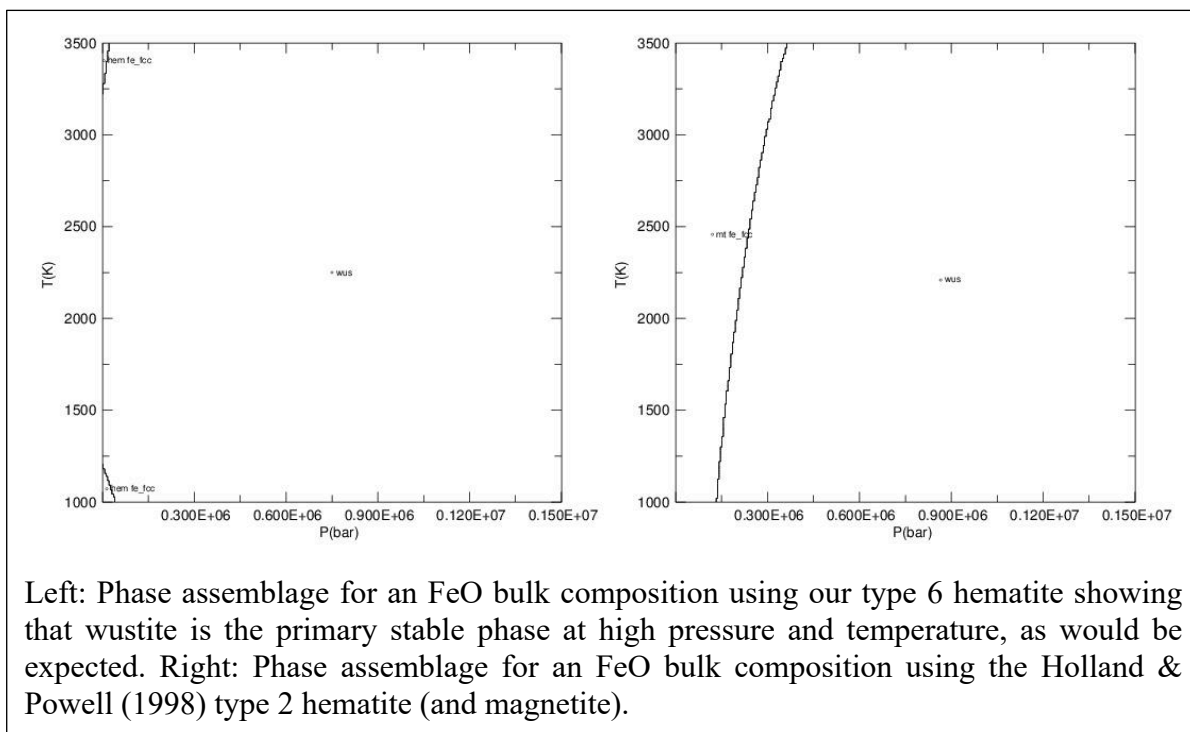
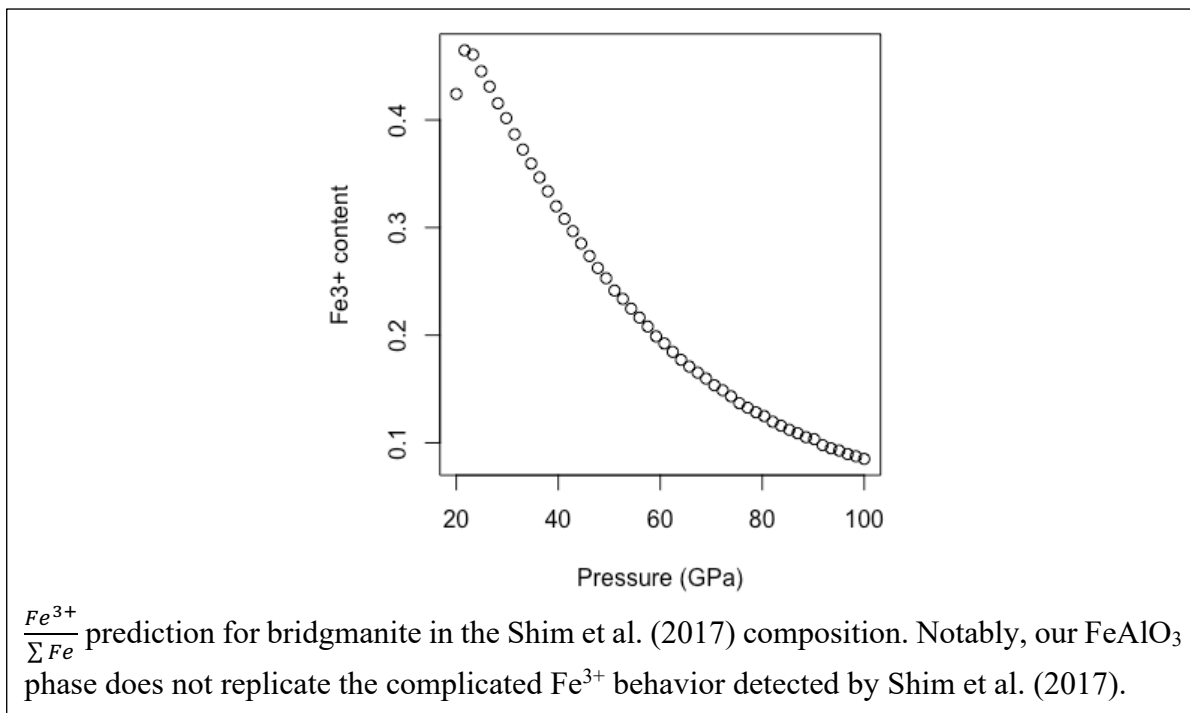


Figure B.5. Fe^{3+} prediction for the Shim et al. (2017) study.



APPENDIX C SUPPLEMENTAL MATERIAL FOR CHAPTER 4

Table C.1. WDS measurements on the natural almandine-pyrope-grossular garnet.

Element	Atomic %
Mg	5.03
Al	9.87
Si	15
Ca	1.85
Mn	0.28
Fe	7.97
O	59.98

Figure C.1. XRD patterns collected at 42 keV on samples with no Ir foils.

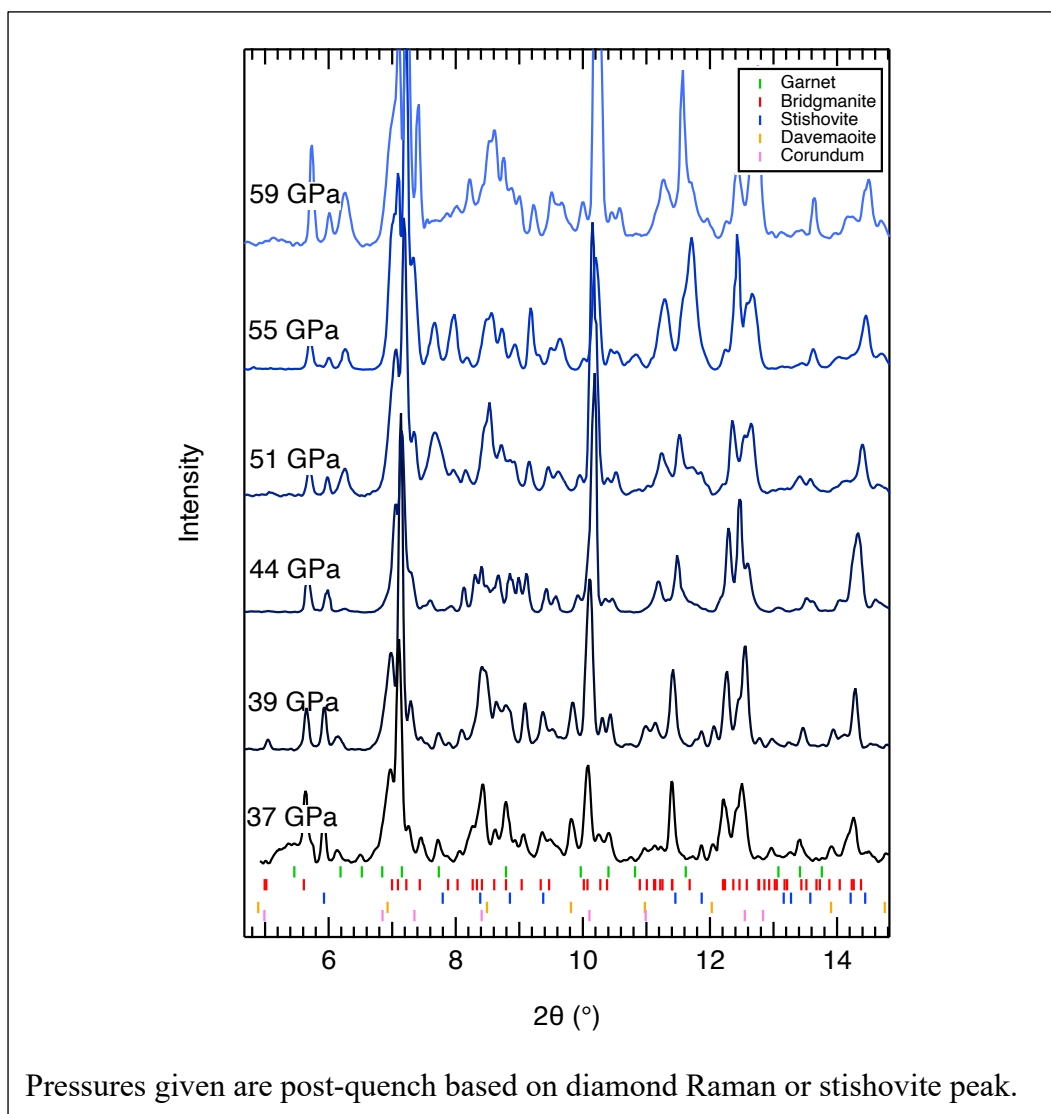


Figure C.2. Example XRD pattern from the K11 thin section XRD map in which the stishovite and LiNbO_3 phases are present.

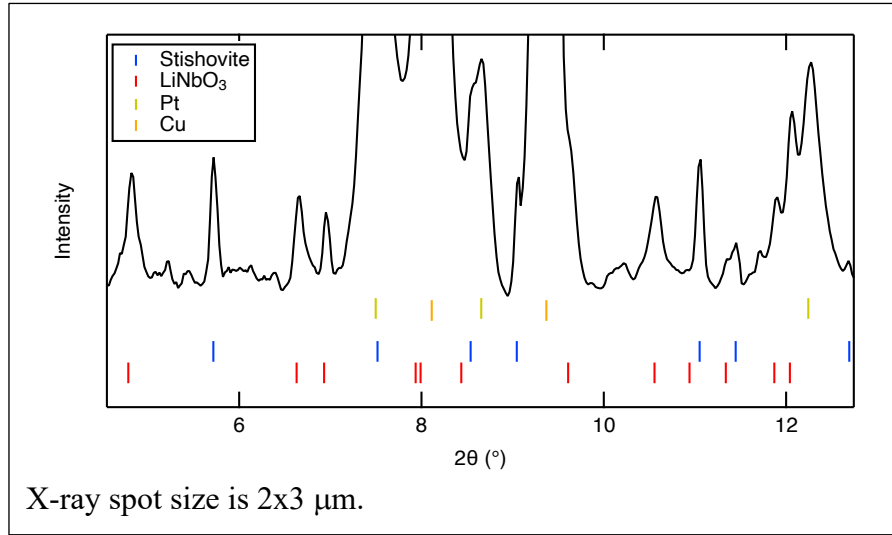


Figure C.3. EDS maps collected at 5 kV on a portion of the laser-heated spot in sample K54 (indicated with dashed box in Figure 4.6).

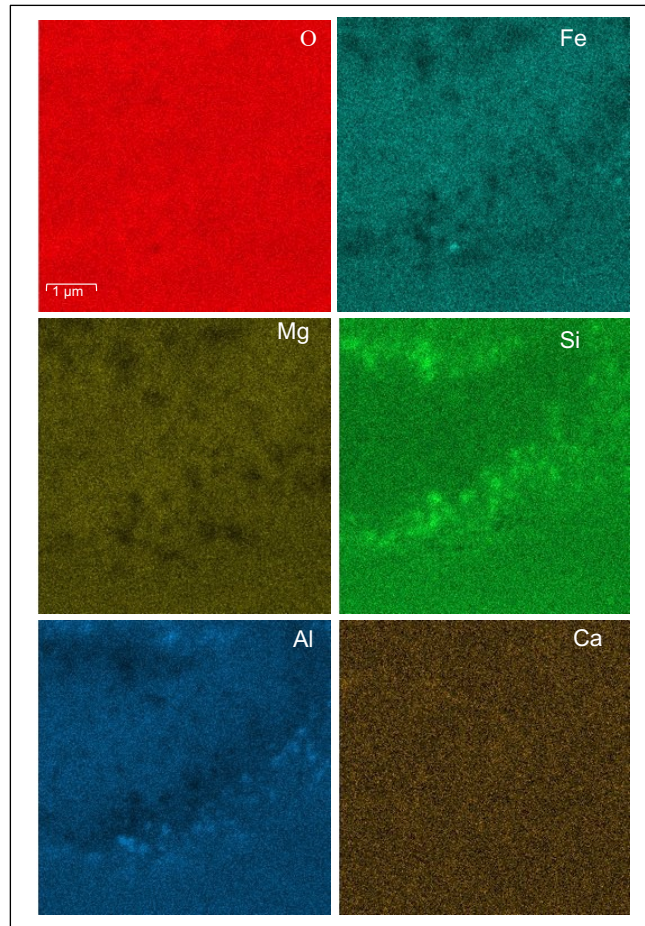
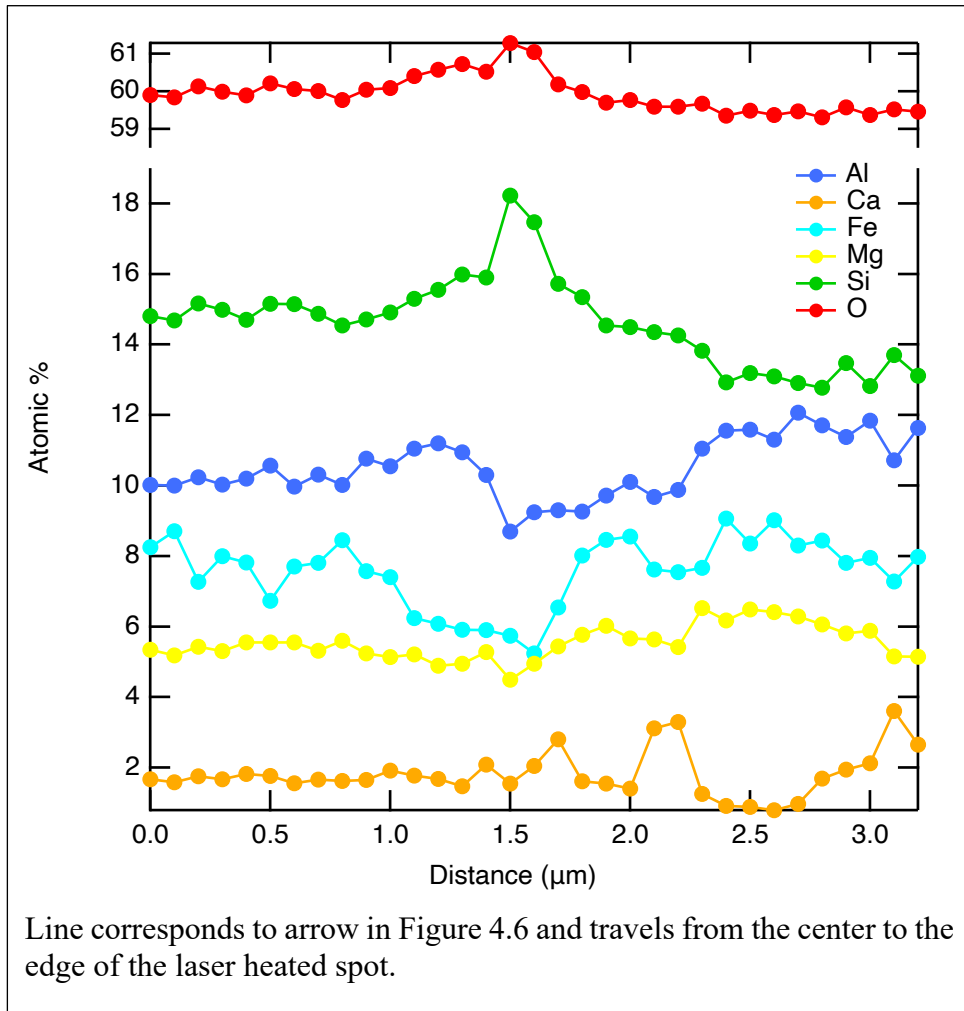


Figure C.4. Line scan collected across the laser-heated spot in K54 at 5 keV.



APPENDIX D SUPPLEMENTAL MATERIAL FOR CHAPTER 5

Table D.1. Detailed review of SEM/TEM observations of disproportionated metallic Fe (corresponding to Figure 5.1). MA: multianvil apparatus, uk: unknown, nm: no mention.

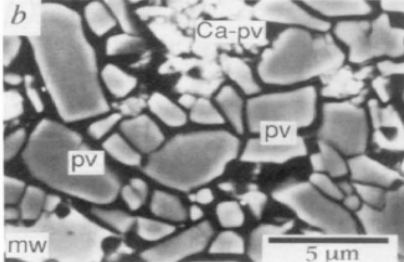
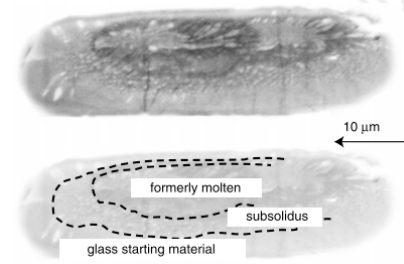
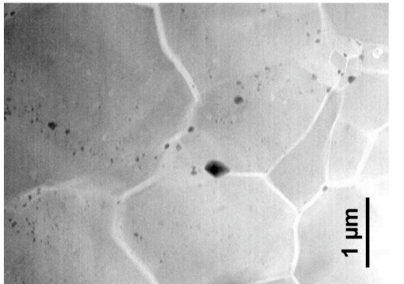
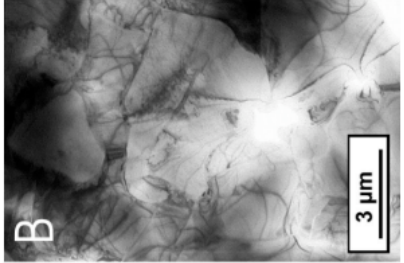
First Author	Year	Composition	P	T	Pressure device	Fe metal?	Details
Irifune	1994	Wt %: SiO ₂ : 45.2 TiO ₂ : 0.3 Al ₂ O ₃ : 3.9 Cr ₂ O ₃ : 0.5 FeO: 8.1 MgO: 37.5 NiO: 0.3 CaO: 3.8 Na ₂ O: 0.3	23 24 25 27 28	1773 1773 1773 1773 1873	MA (Pt capsule)	No (nm)	SEM Poor quality BSE image (28 GPa, 1873 K) 
Kesson	1998	Pyrolite (no specific comp given)	70 135	uk uk	DAC	uk uk	SEM Poor quality BSE image (70 GPa, melted) 
Lauterbach	2000	Al-bearing opx + 2 wt% SiO ₂	26	1923 - 2023	MA (Fe or Re capsule)	Yes	TEM 
Frost	2002	Al ₂ O ₃ -bearing pyroxenes + mw	24 24 25 25	1923 2173 1923 2173	MA (Re capsule)	No No No No	TEM State lack of metallic Fe in TEM image (but only provide one image) 

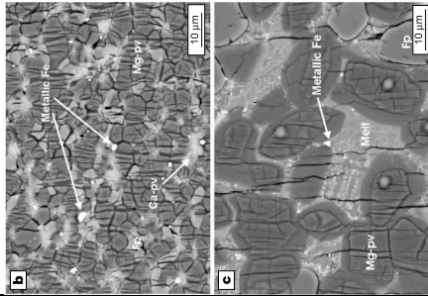
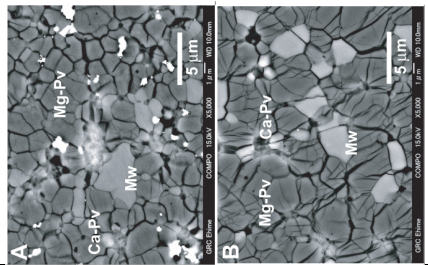
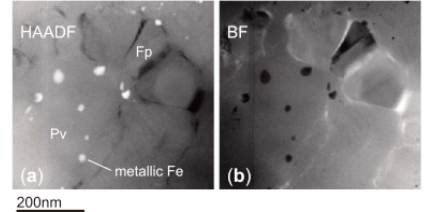
Table D.1 continued							
Frost	2004	Synthetic peridotite (no specific comp given)	24 24	2423 2573	MA (graphite capsule)	Yes Yes	SEM Subsolidus and supersolidus observations in 
McCammon	2004	Peridotite Wt%: SiO2: 44.5 TiO2: 0.16 Al2O3: 3.59 Cr2O3: 0.5 FeO: 8.10 MgO: 39.2 NiO: 0.25 CaO: 3.44 Na2O: 0.3	26 26	2023 2123	MA (Fe or Re capsule)	No No	TEM Positively identify metallic Fe in one non-peridotite sample (which was aluminous) No images provided
Murakami	2005	Peridotite gel (KLB-1)	38 92 124	2000 2300 2250	DAC (gold film, NaCl)	No No No (nm)	TEM Recovered several samples TEM but no images provided
Irifune	2010	Wt %: SiO2: 45.2 TiO2: 0.3 Al2O3: 3.9 Cr2O3: 0.5 FeO: 8.1 MgO: 37.5 NiO: 0.3 CaO: 3.8 Na2O: 0.3	28.7 36.4 40.5 42.8 44.2 47.4	1873 1973 1973 1973 2073 2073	MA (no metal capsule)	No No No No No No	SEM, TEM Only give BSE images for two samples (28.7 and 44.2), and state that no metallic Fe was found (bright spots are Au) 
Sinmyo	2011	Synthetic KLB-1 peridotite	93 135	2300 2400	DAC (gold film, SiO2 glass)	Yes No	TEM Show increase of Fe3+ in bgm from starting material, and state no metallic Fe with ppv 

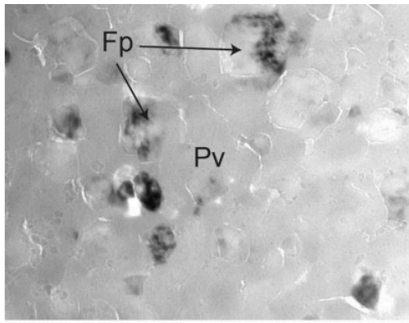
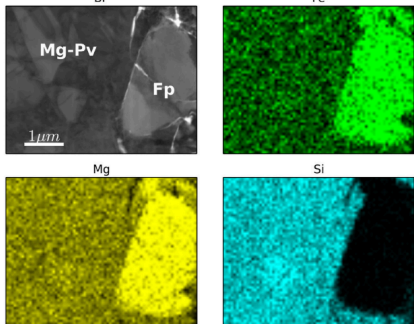
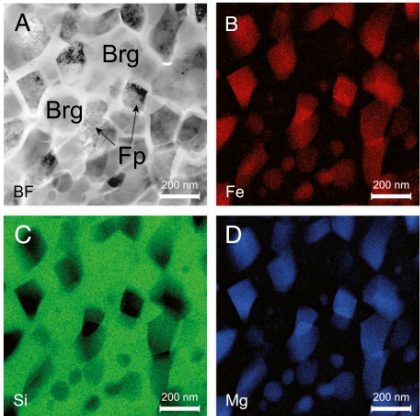
Table D.1 continued							
Sinmyo	2013	Pyrolite gel (used in Sinmyo 2011)	28 82 109 114	1900 2100 2300 2300	DAC (gold film, SiO ₂ glass)	Yes Yes Yes Yes	TEM State that trace amounts of metallic Fe grains were observed 
Prescher	2014	Pyrolite Wt% SiO ₂ : 44.95 TiO ₂ : 0.71 Al ₂ O ₃ : 3.53 FeO: 9.33 MgO: 37.3 CaO: 3.06 Na ₂ O: 0.57 K ₂ O: 0.13 Cr ₂ O ₃ : 0.43	33 40 59 79 97 130	1980 2120 2190 2300 2450 2500	MA (Re capsule) and DAC (Neon)	No No No No No No (nm)	STEM Powders turned into glass and then re-ground and then compressed in a multianvil press at 25 GPa and 1650C for 8 hrs then crushed and then loaded 
Piet	2016	Ca-free py Wt % oxides: Mg: 37.7 Fe: 8.2 Si: 48.8 Al: 5.2 Also had Al-rich ol: San carlos ol + Al ₂ O ₃	py 40 93 116 Oliv 28 36 45 58 73 86 104 118	2150 2350 2450 2100 2400 2200 2400 2100 2400 2700 2300	DAC	No No No No No No No No No No No	TEM (ol + Al ₂ O ₃ 58 GPa, 2400 K) 

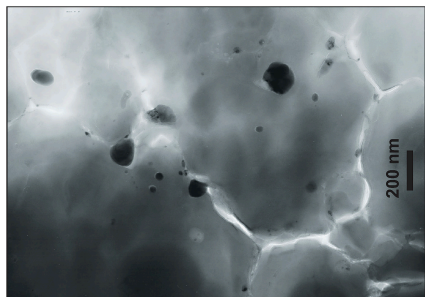
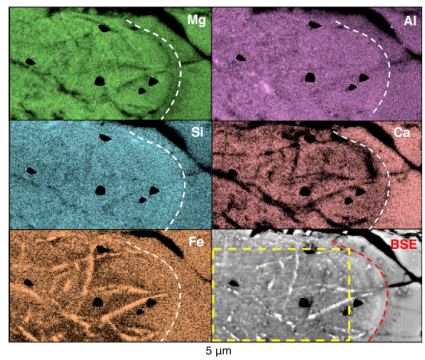
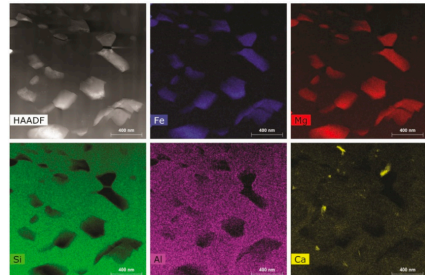
Table D.1 continued							
Andrault	2017	Al-rich pyroxene	40	2500	DAC	Yes	TEM 
Creasy	2020	oxidized and reduced Al-rich pyroxenite glass red Mol% MgO: 27.3 SiO ₂ : 41.8 Al ₂ O ₃ : 13.1 CaO: 10.3 FeO: 7.12 Fe ₂ O ₃ : 0.44	40 60 70	2000 2000 2000	DAC (Neon)	Yes Yes Yes	SEM Glass samples were powdered and then prepared with stepped anvils Images and temperatures not provided for 60 and 70 GPa, but metallic Fe is assumed based on XRD 
Lobanov	2020	Pyrolite (used Fe ₂ O ₃)	56	2800	DAC	Yes (stated in text)	STE 
Huang	2021	Al-px + fp + Ir	25	1973	MA (Pt-Au capsule)	Yes	SEM Ir was added to the mix but an Fe-Ir alloy was listed in the table

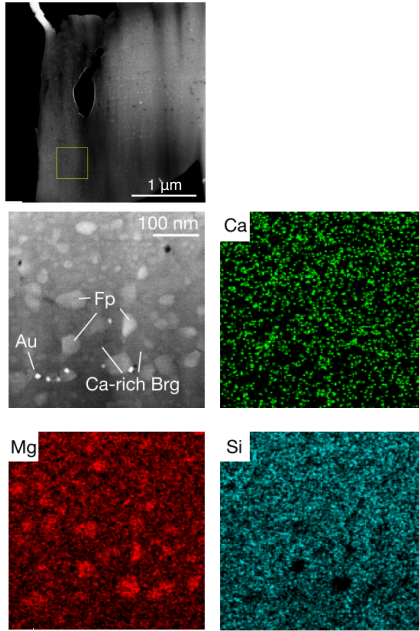
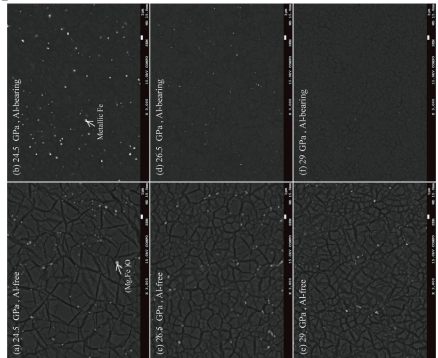
Table D.1 continued							
Ko	2022	Ca-rich pyrolite glass (pyrolite glass + CaSiO ₃) + Au powder	64	2284	DAC (Ne, Ar, or NaCl)	No	STEM 
Tsujino	2023	Al-px (Mg _{0.9} Fe _{0.1}) SiO ₃ + 5wt% Al ₂ O ₃	24.5 26.5 28 29	2000 2000 2000 2000	MA (Au capsule)	Yes Yes Yes Yes	SEM Hot-pressed in Mo capsule in Kawai-type multianvil press at 3 GPa before high pressure 

Figure D.1. Images of the pyrolite powder pellet and synthesized pyrolite glass bead.

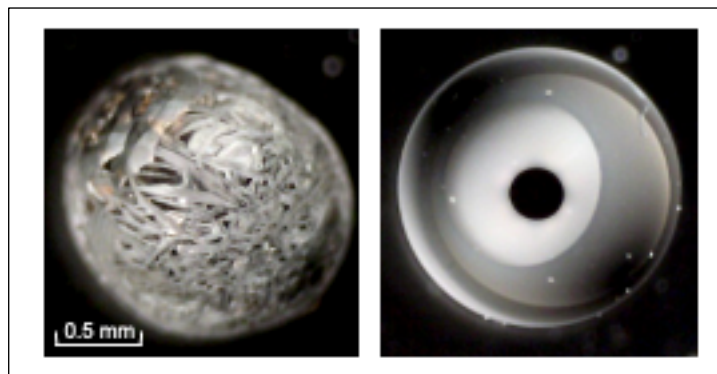


Figure D.2. XRD patterns of decompressed samples.

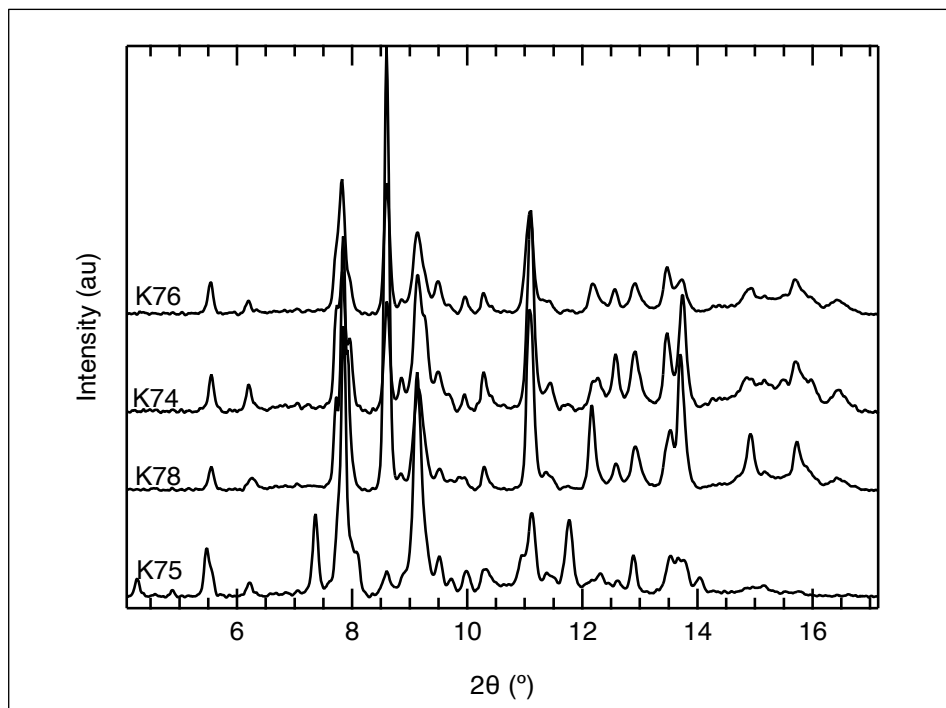


Figure D.3. mXRD pattern of K59 (recovered thin section).

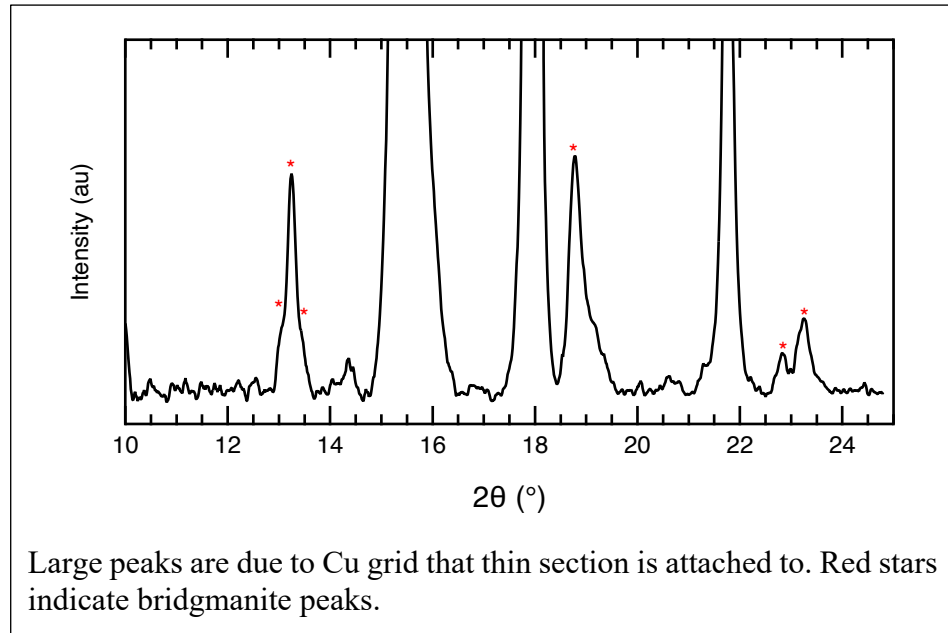


Figure D.4. EDS map of sample K59 (as seen in Figure 5.6).

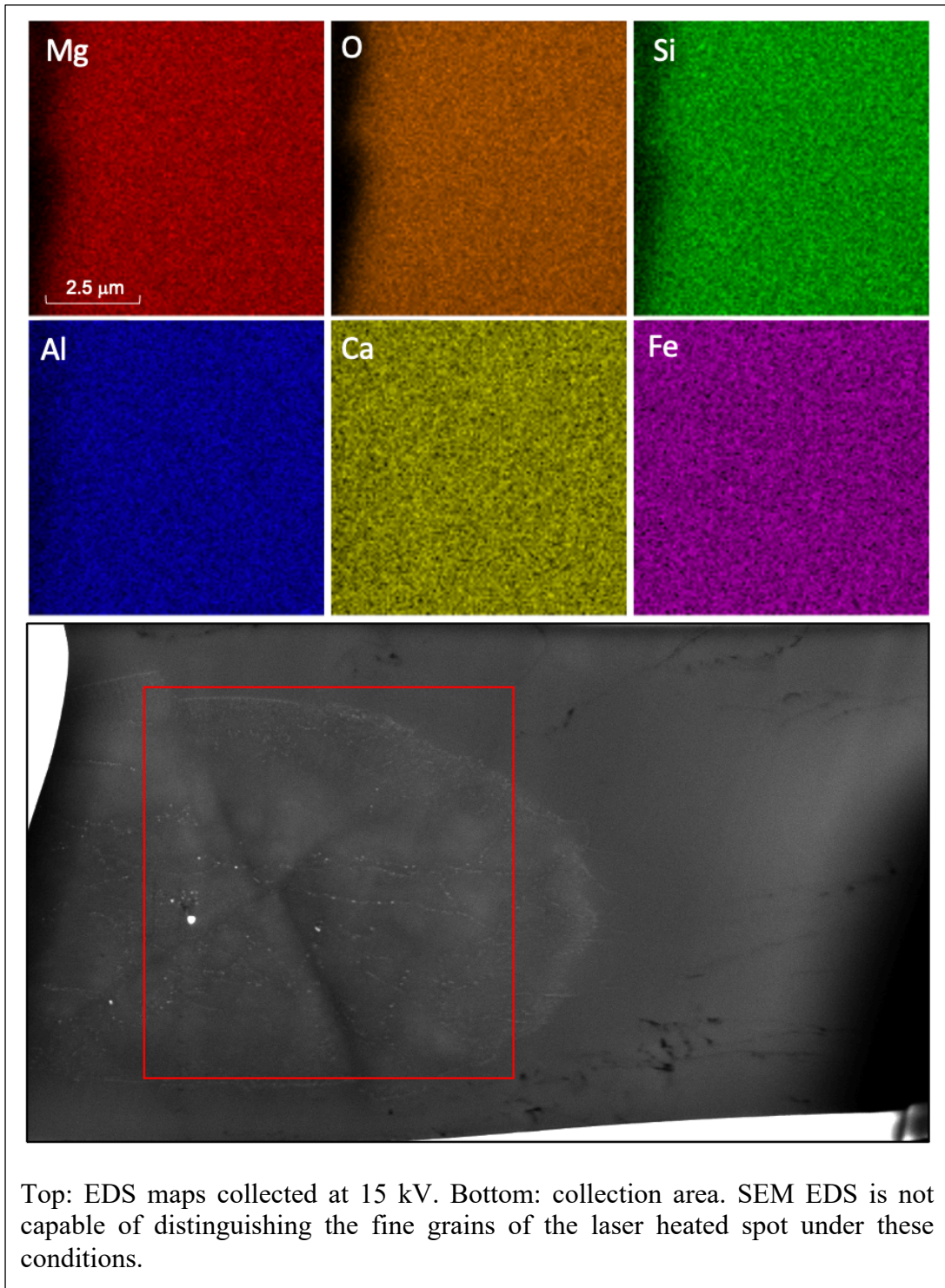


Figure D.5. SEM EDS line scan across sample K60.

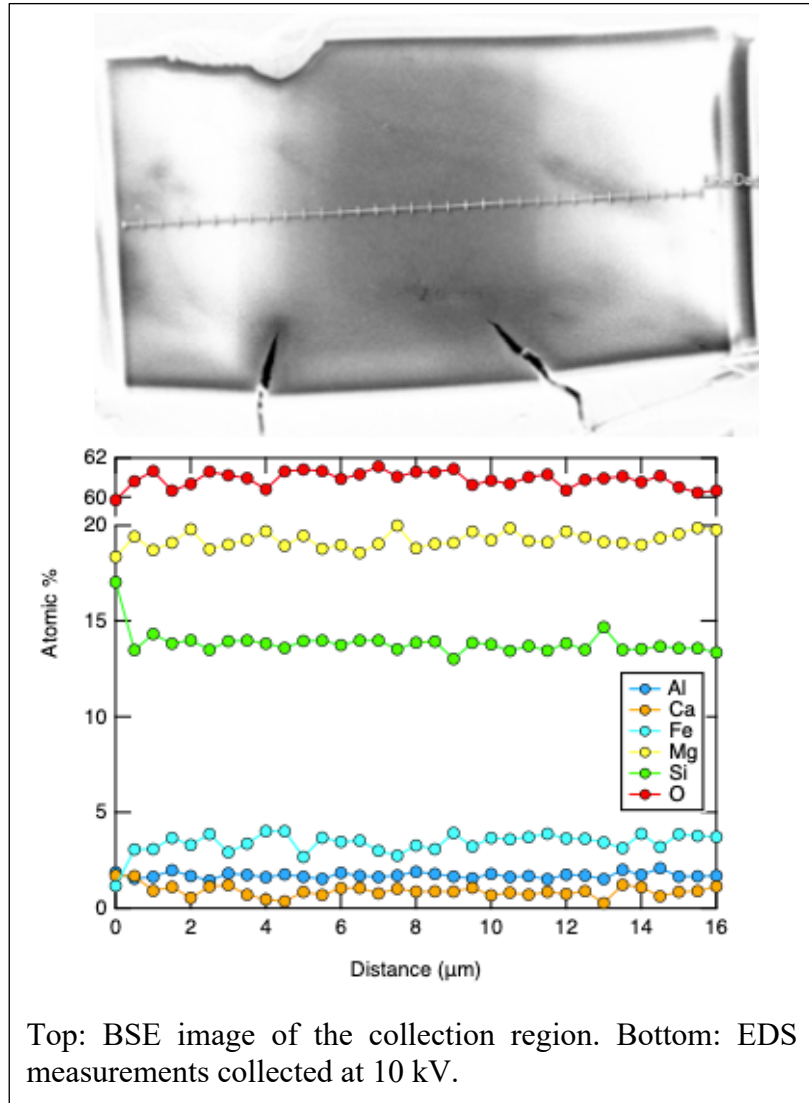


Figure D.6. TEM images of recovered samples at higher magnification than Figure 5.10.

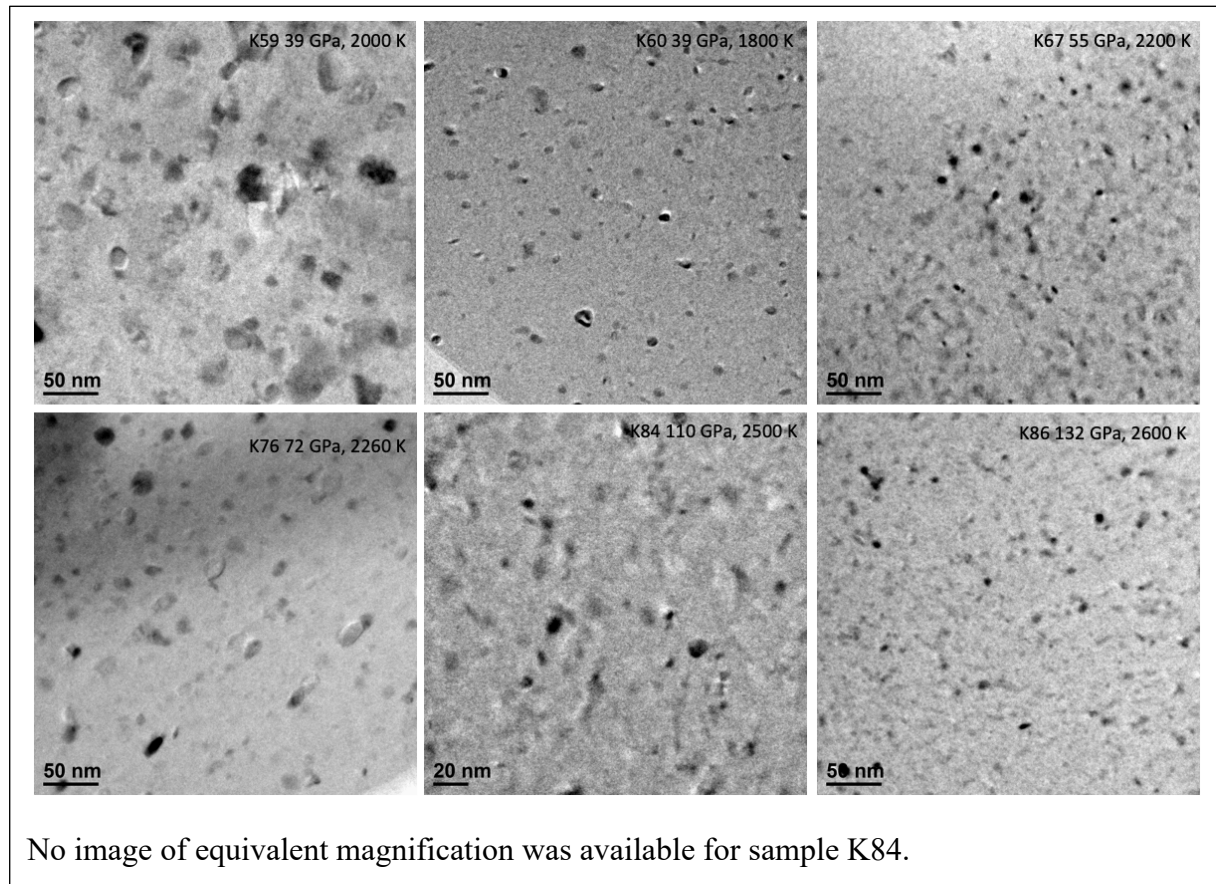
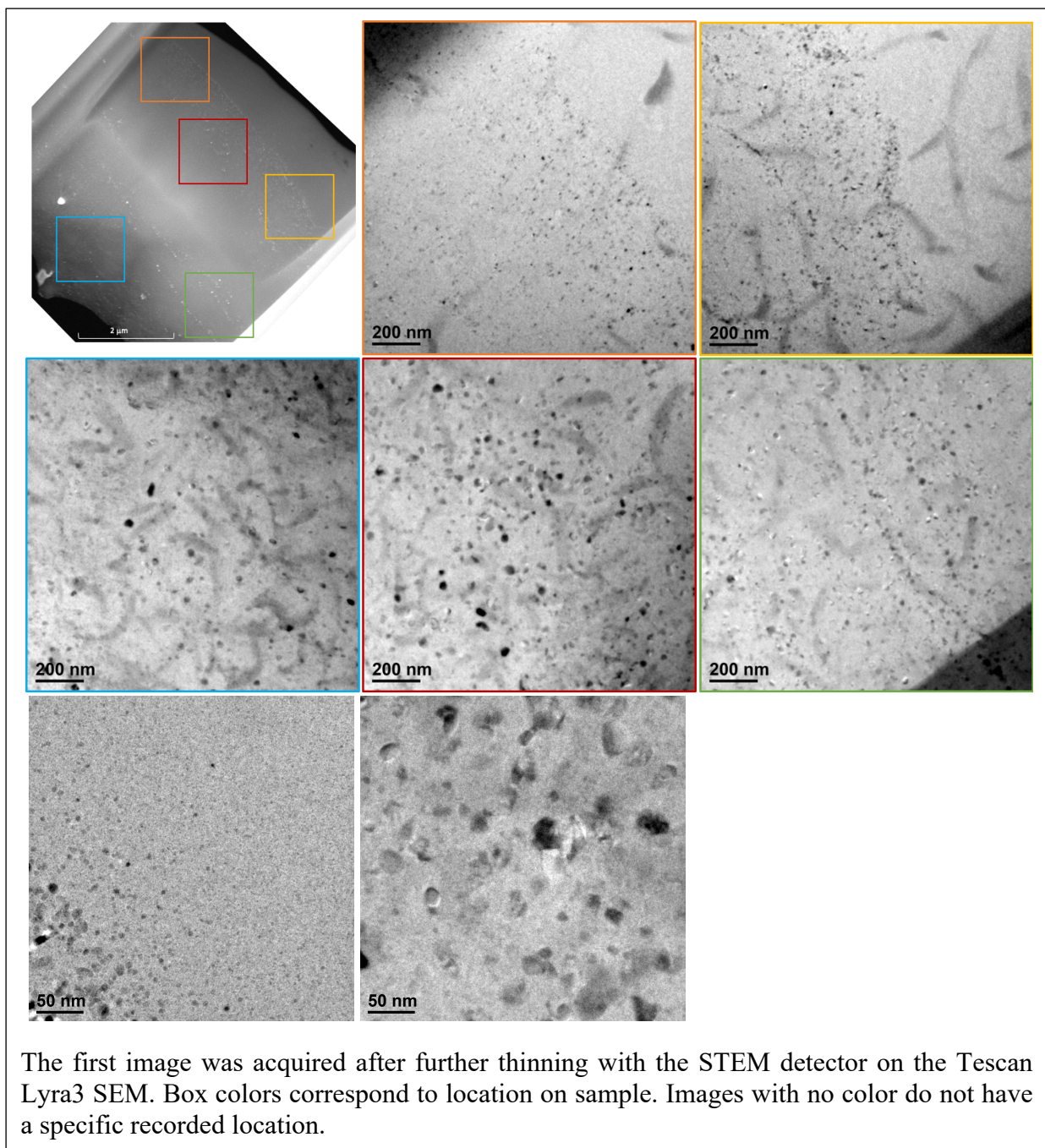
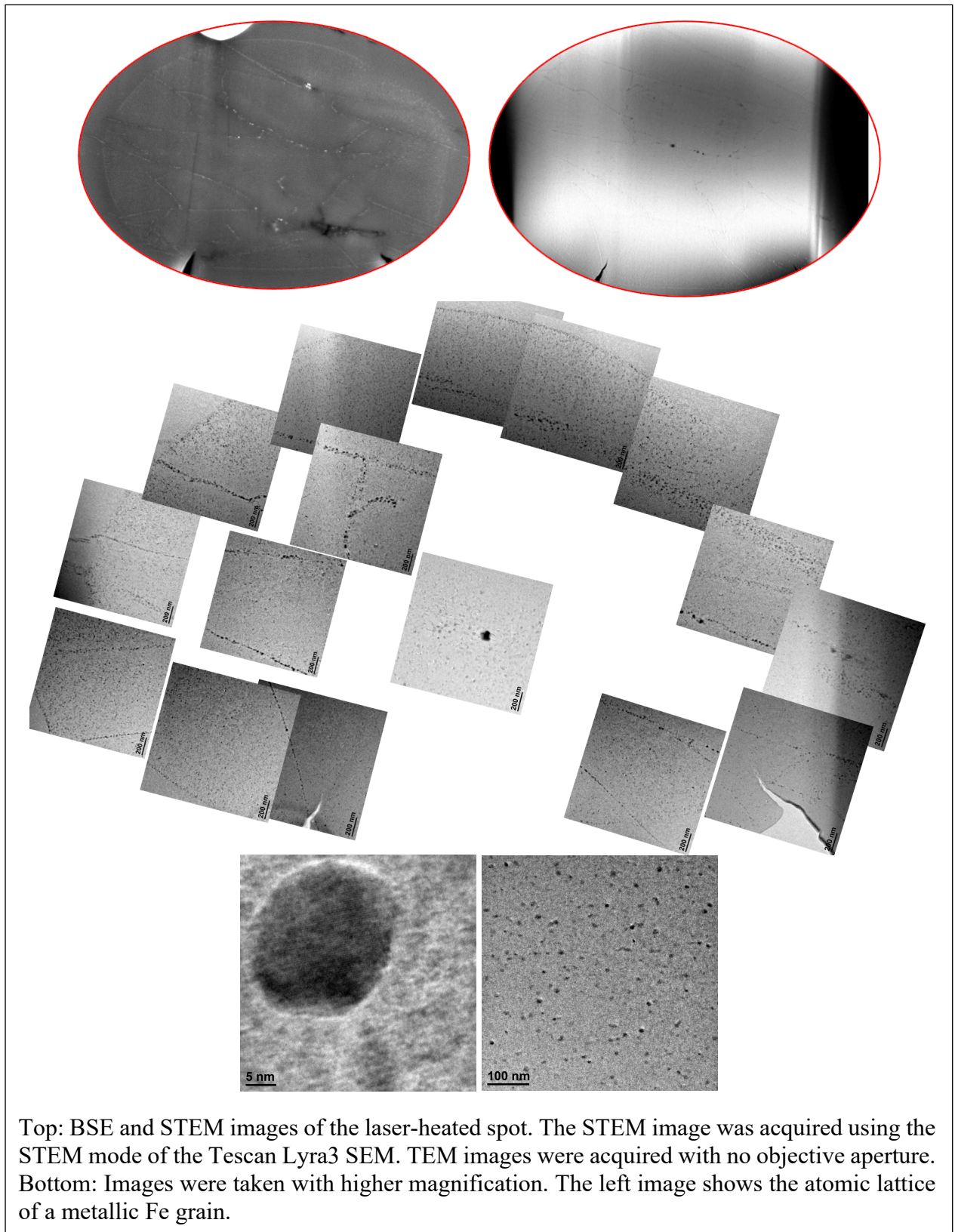


Figure D.7. TEM images for sample K59.



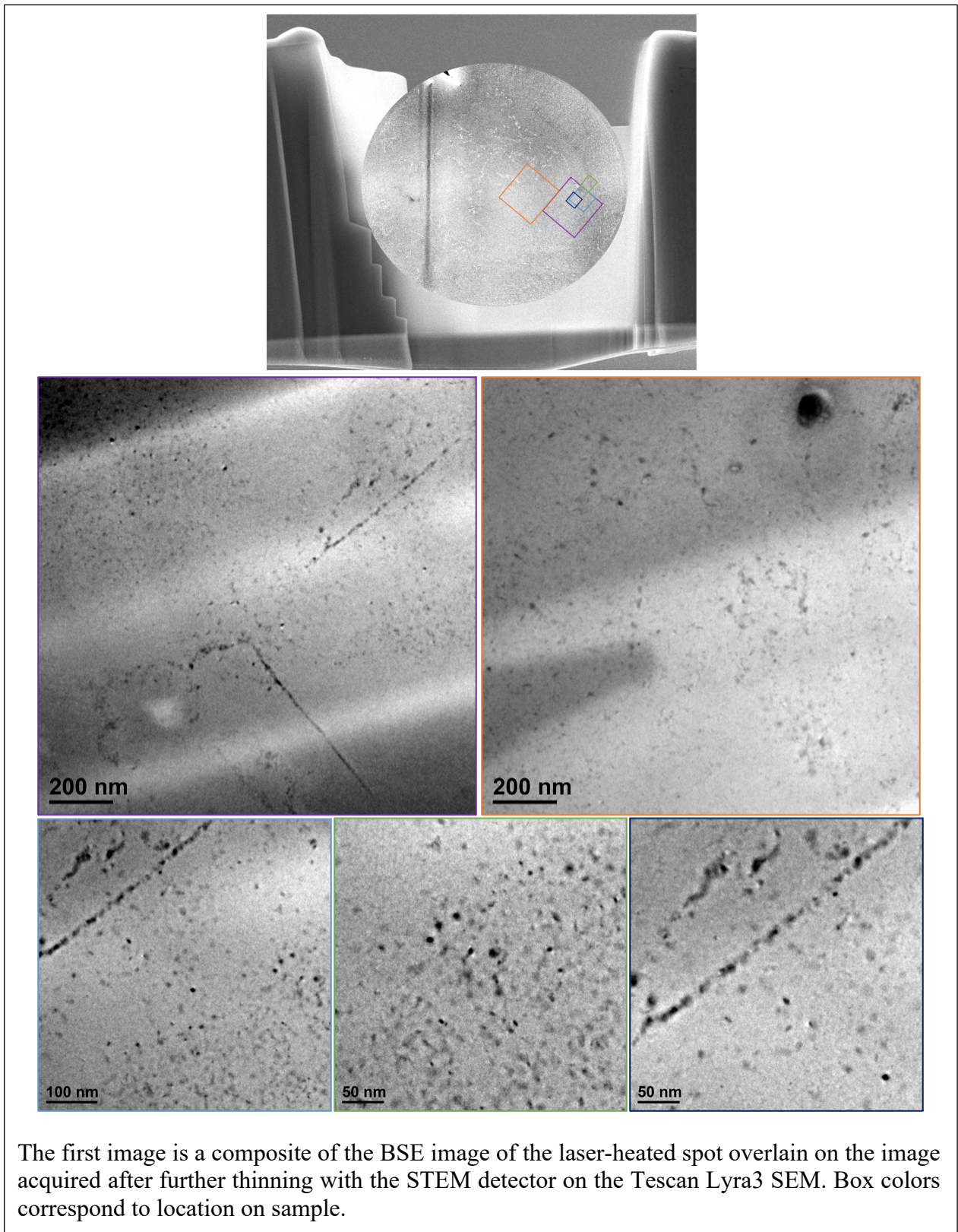
The first image was acquired after further thinning with the STEM detector on the Tescan Lyra3 SEM. Box colors correspond to location on sample. Images with no color do not have a specific recorded location.

Figure D.8. TEM images for sample K60.



Top: BSE and STEM images of the laser-heated spot. The STEM image was acquired using the STEM mode of the Tescan Lyra3 SEM. TEM images were acquired with no objective aperture. Bottom: Images were taken with higher magnification. The left image shows the atomic lattice of a metallic Fe grain.

Figure D.9. TEM images for sample K67.



The first image is a composite of the BSE image of the laser-heated spot overlain on the image acquired after further thinning with the STEM detector on the Tescan Lyra3 SEM. Box colors correspond to location on sample.

Figure D.10. TEM images for sample K76.

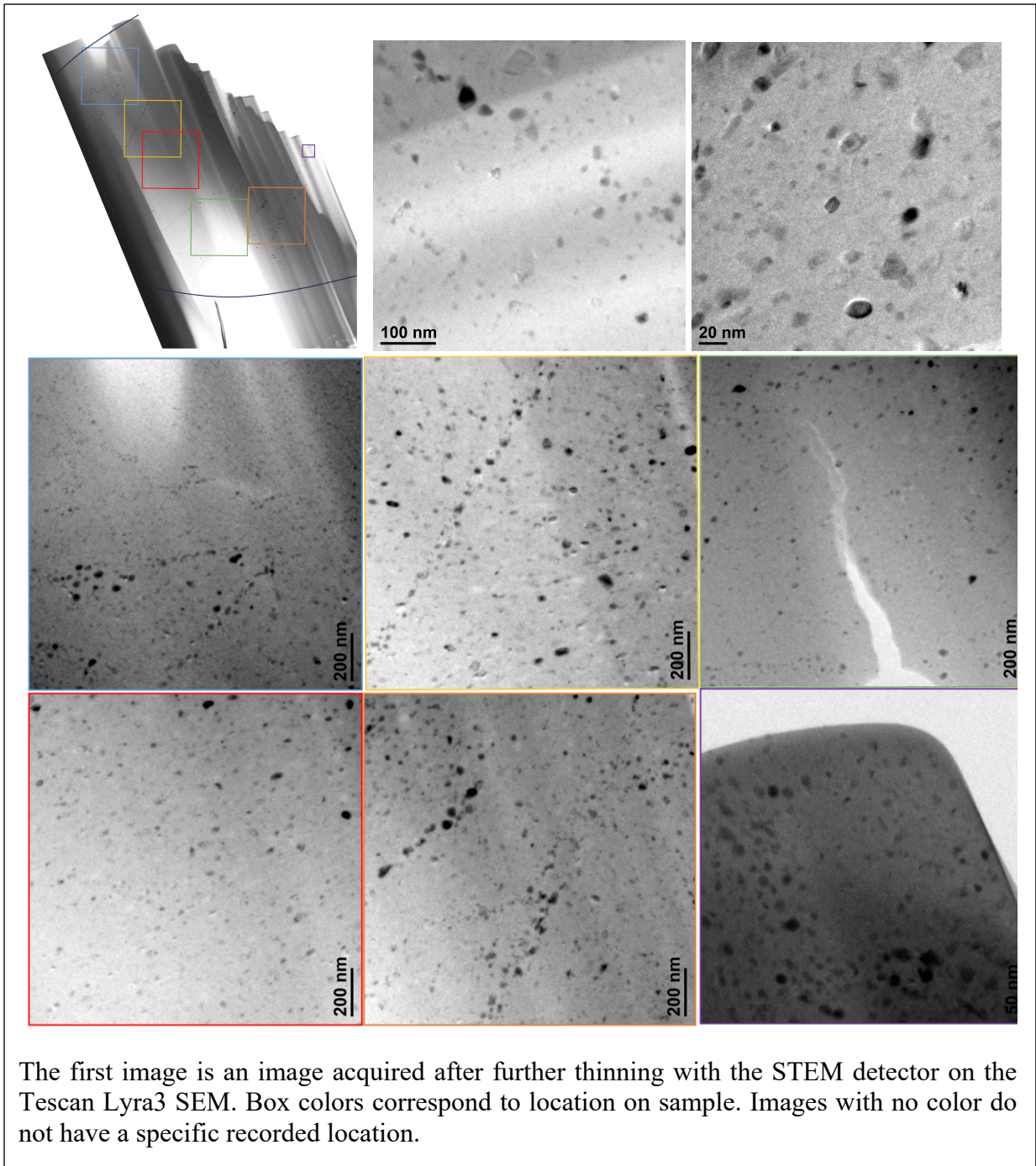


Figure D.11. TEM images for sample K84.

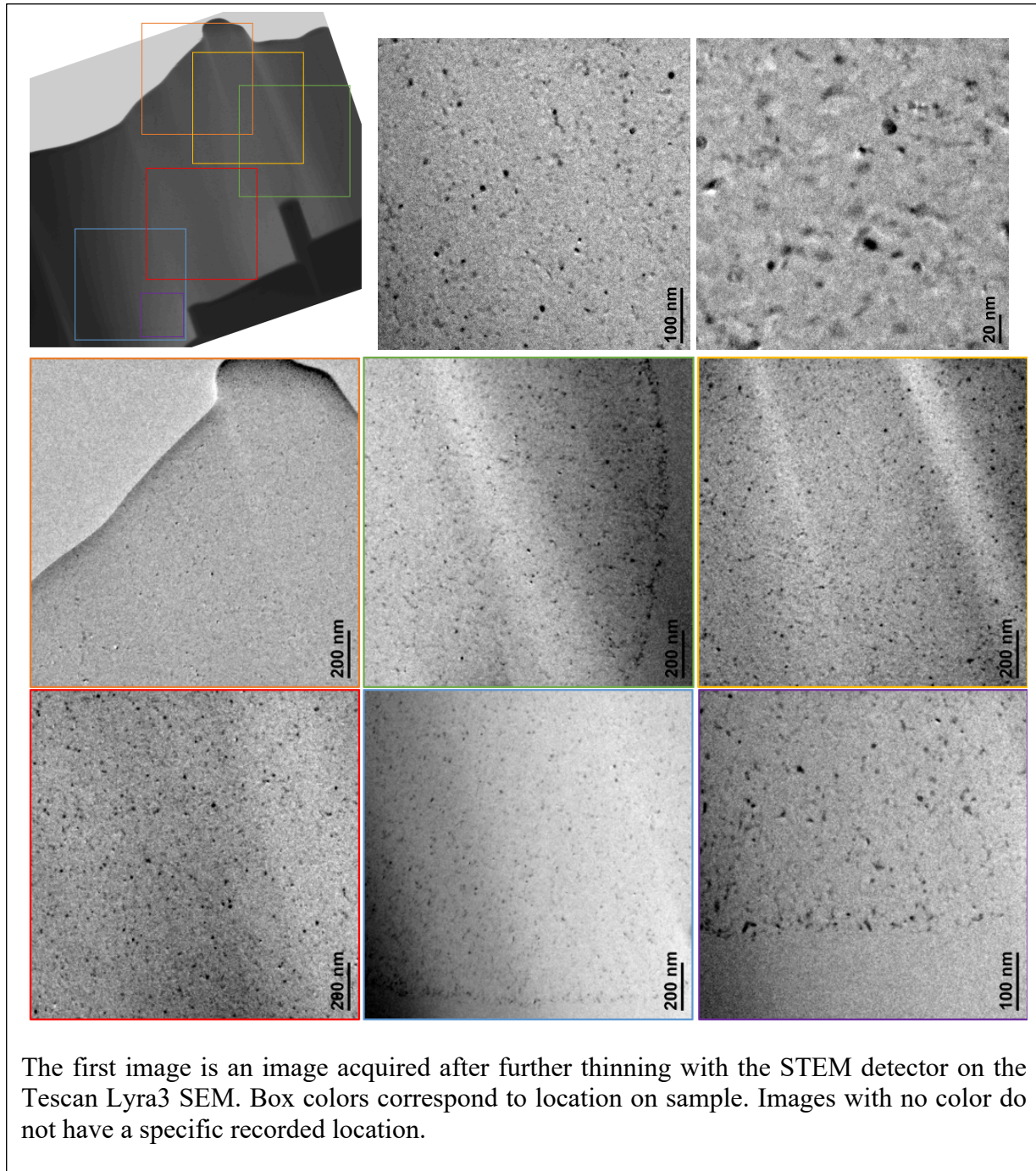


Figure D.12. TEM images for sample K86.

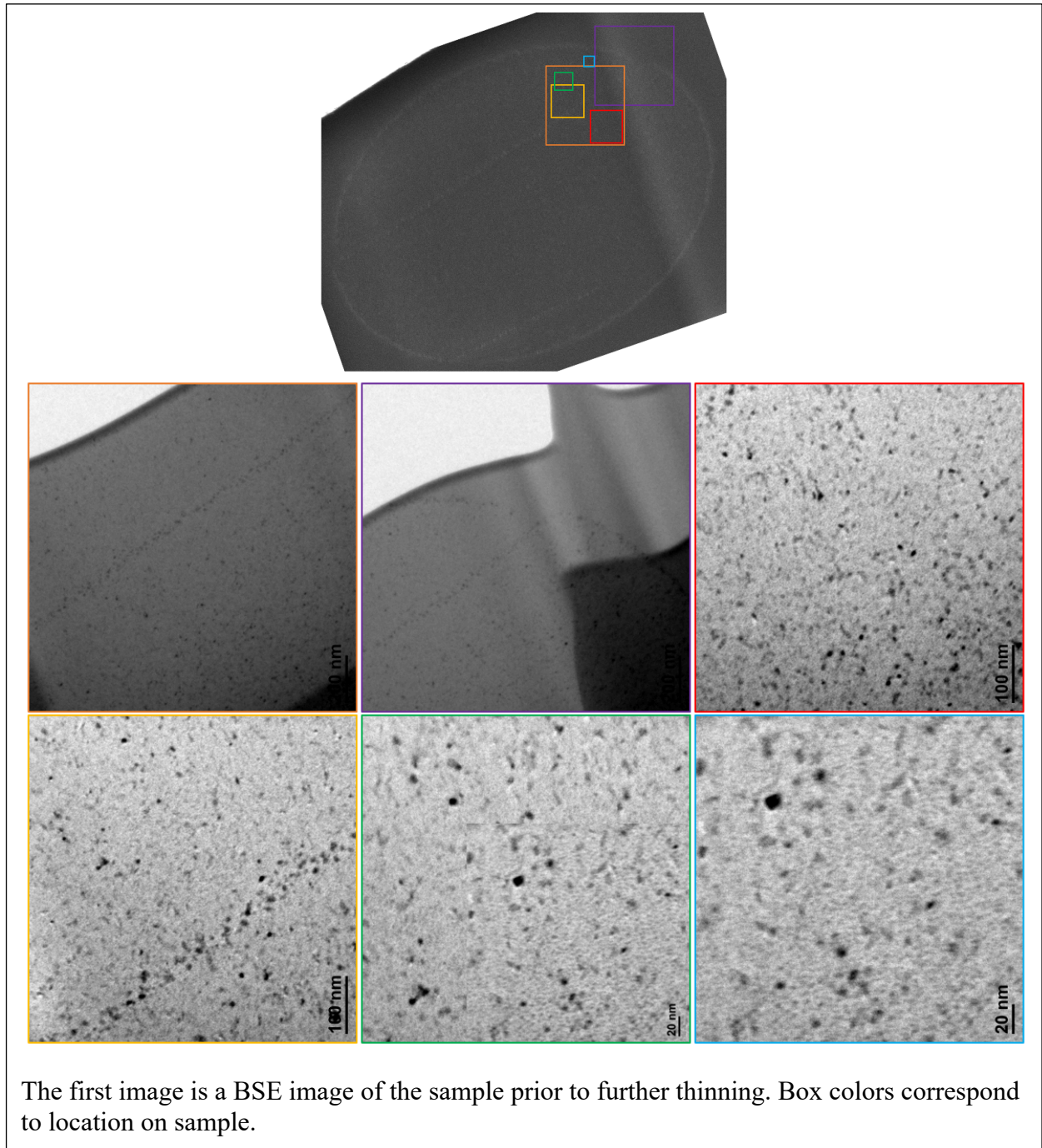
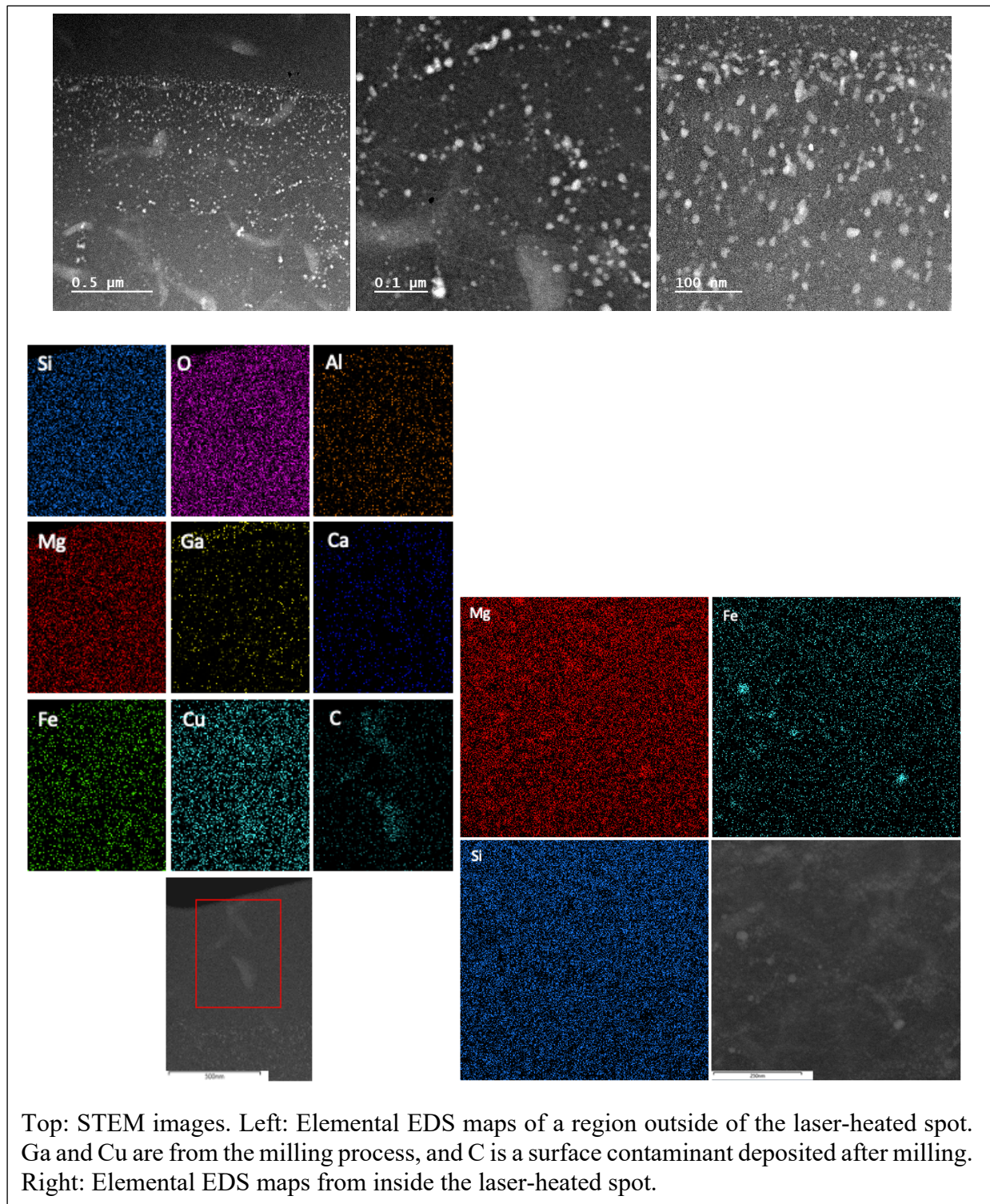


Figure D.13. STEM images and EDS maps for sample K59.



Top: STEM images. Left: Elemental EDS maps of a region outside of the laser-heated spot. Ga and Cu are from the milling process, and C is a surface contaminant deposited after milling. Right: Elemental EDS maps from inside the laser-heated spot.

Figure D.14. STEM images and elemental EDS maps for sample K60.

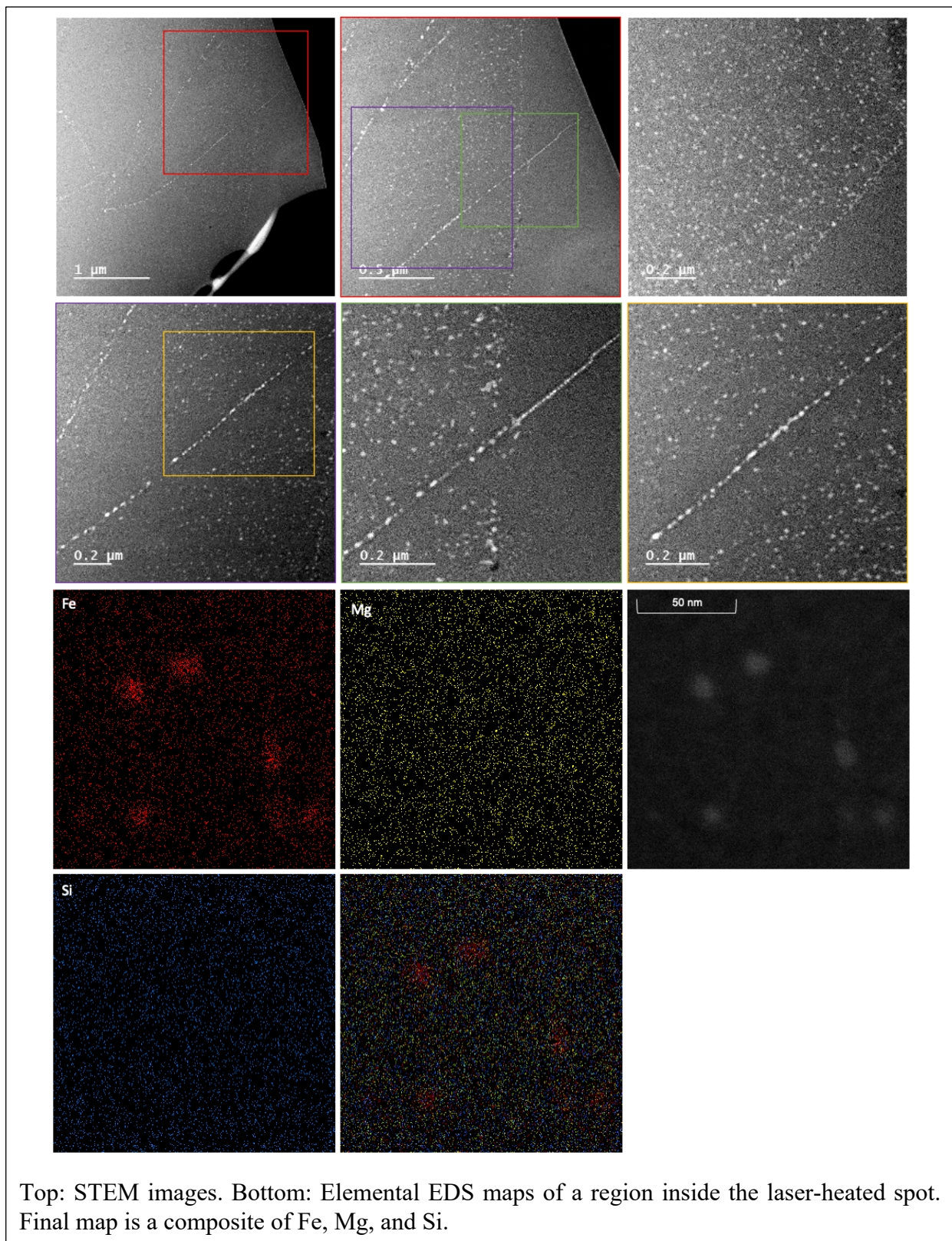


Figure D.15. Elemental EDS maps for sample K76.

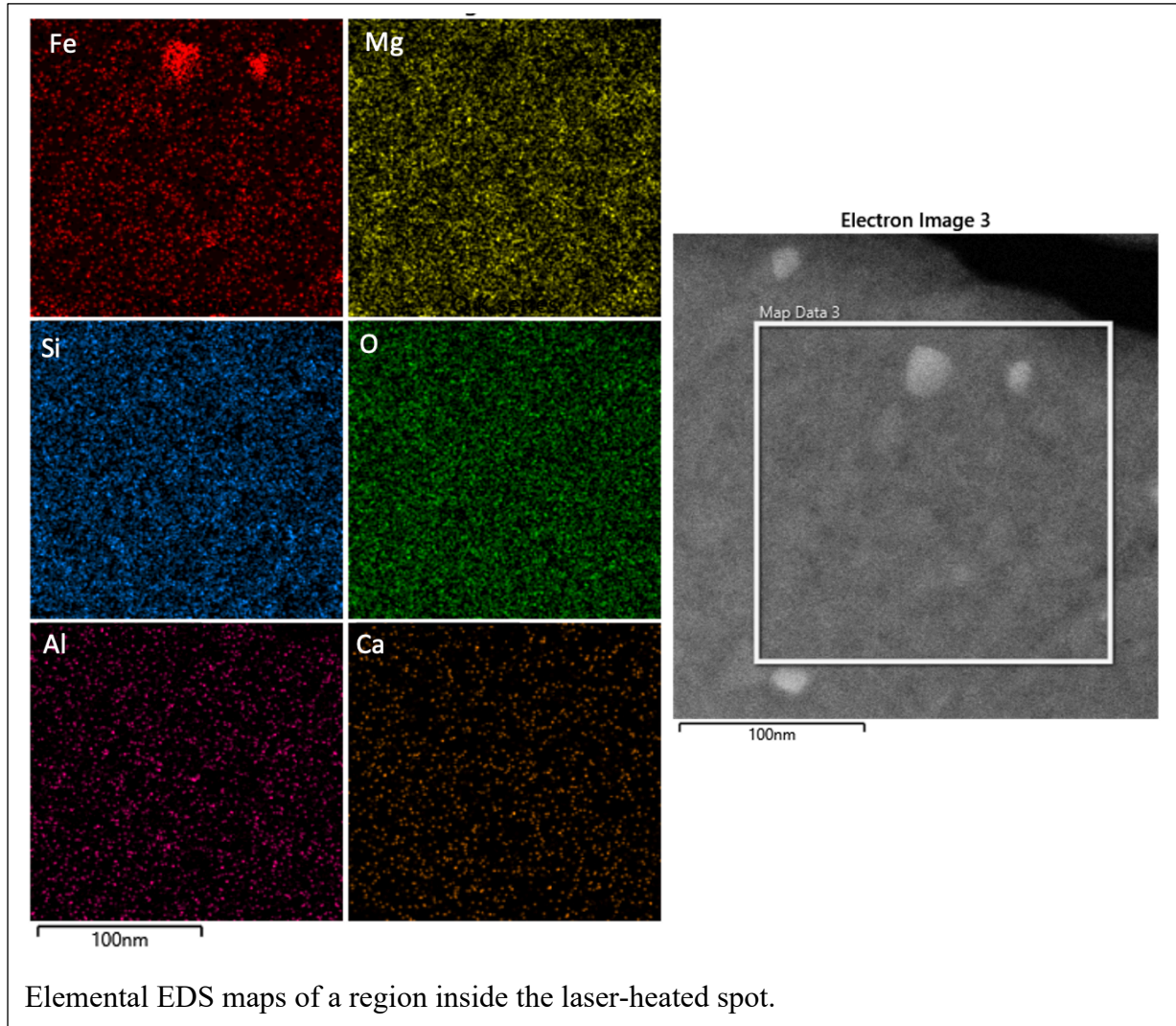
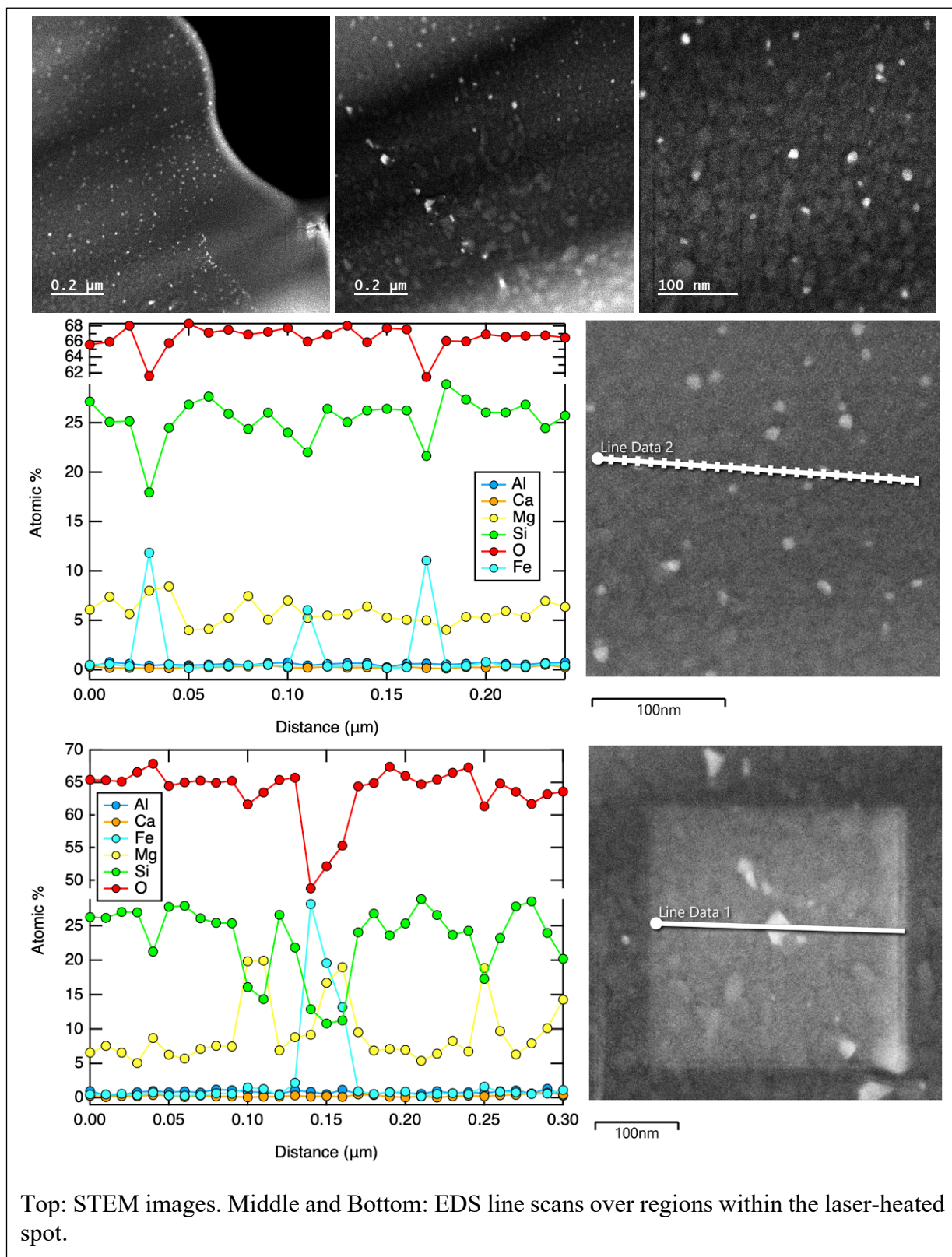


Figure D.16. STEM images and EDS line scans for sample K83.



Top: STEM images. Middle and Bottom: EDS line scans over regions within the laser-heated spot.

Figure D.17. Elemental EDS maps for sample K83.

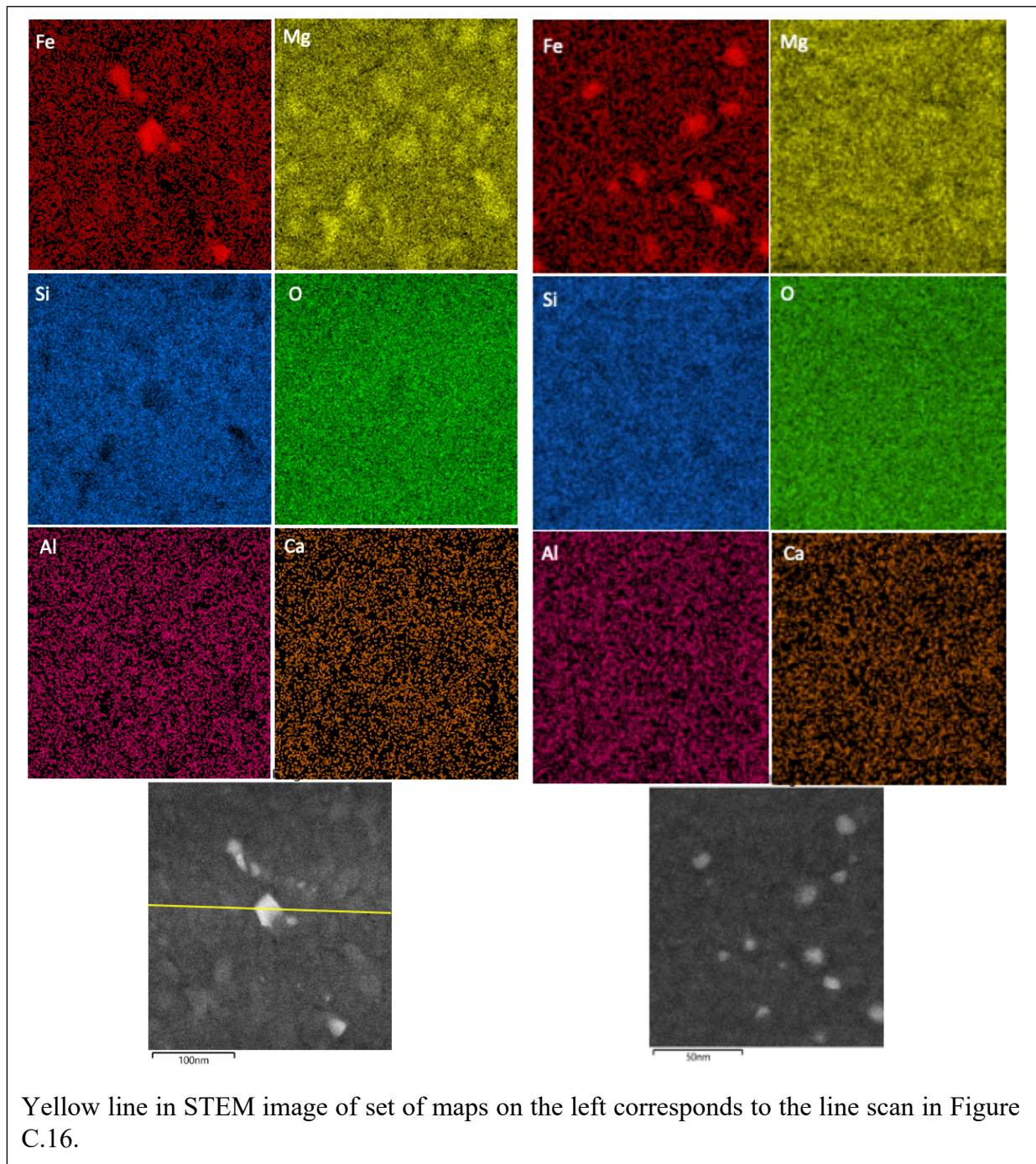


Figure D.18. STEM images and EDS line scans for sample K84.

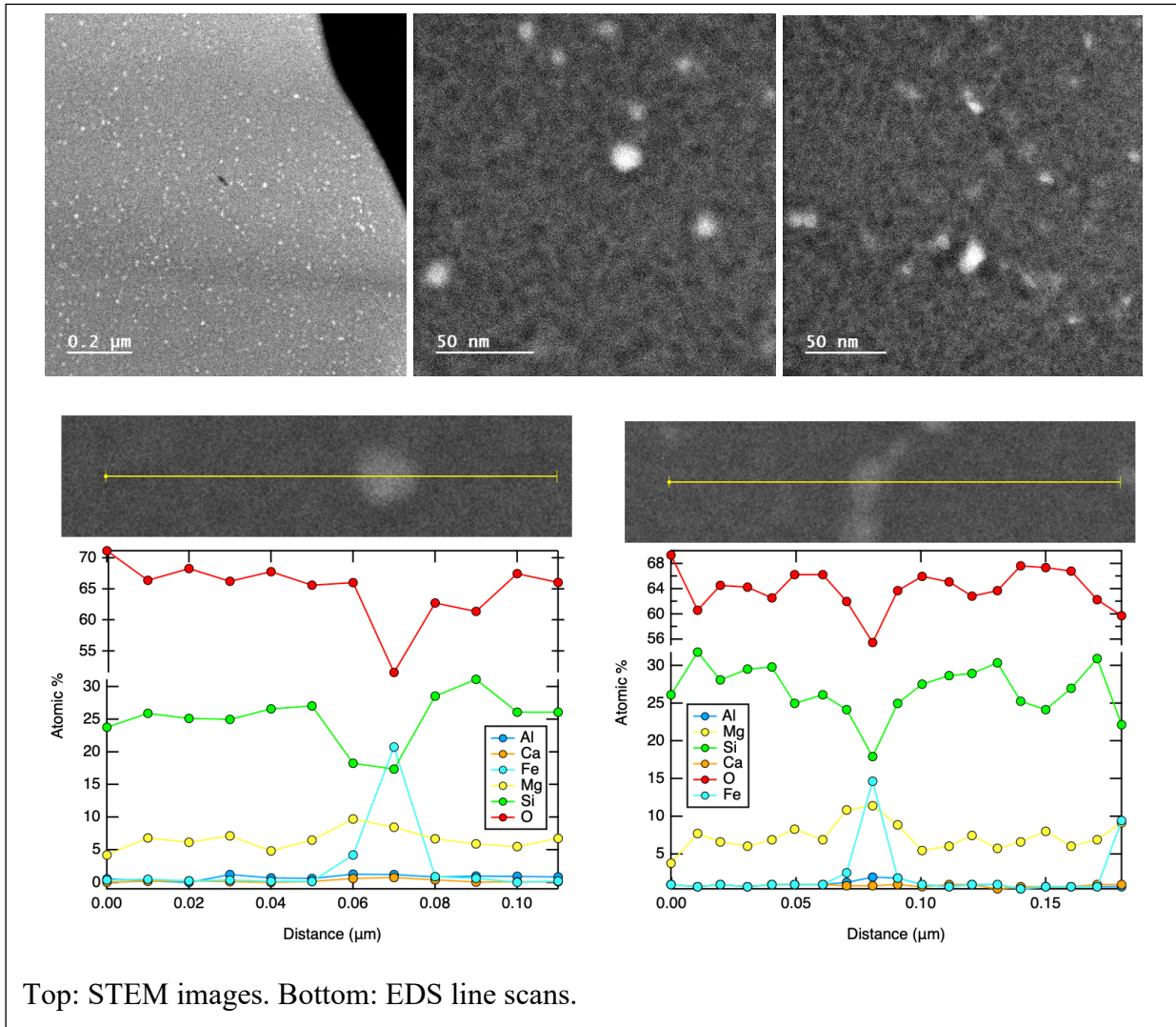


Figure D.19. Elemental EDS maps for sample K84.

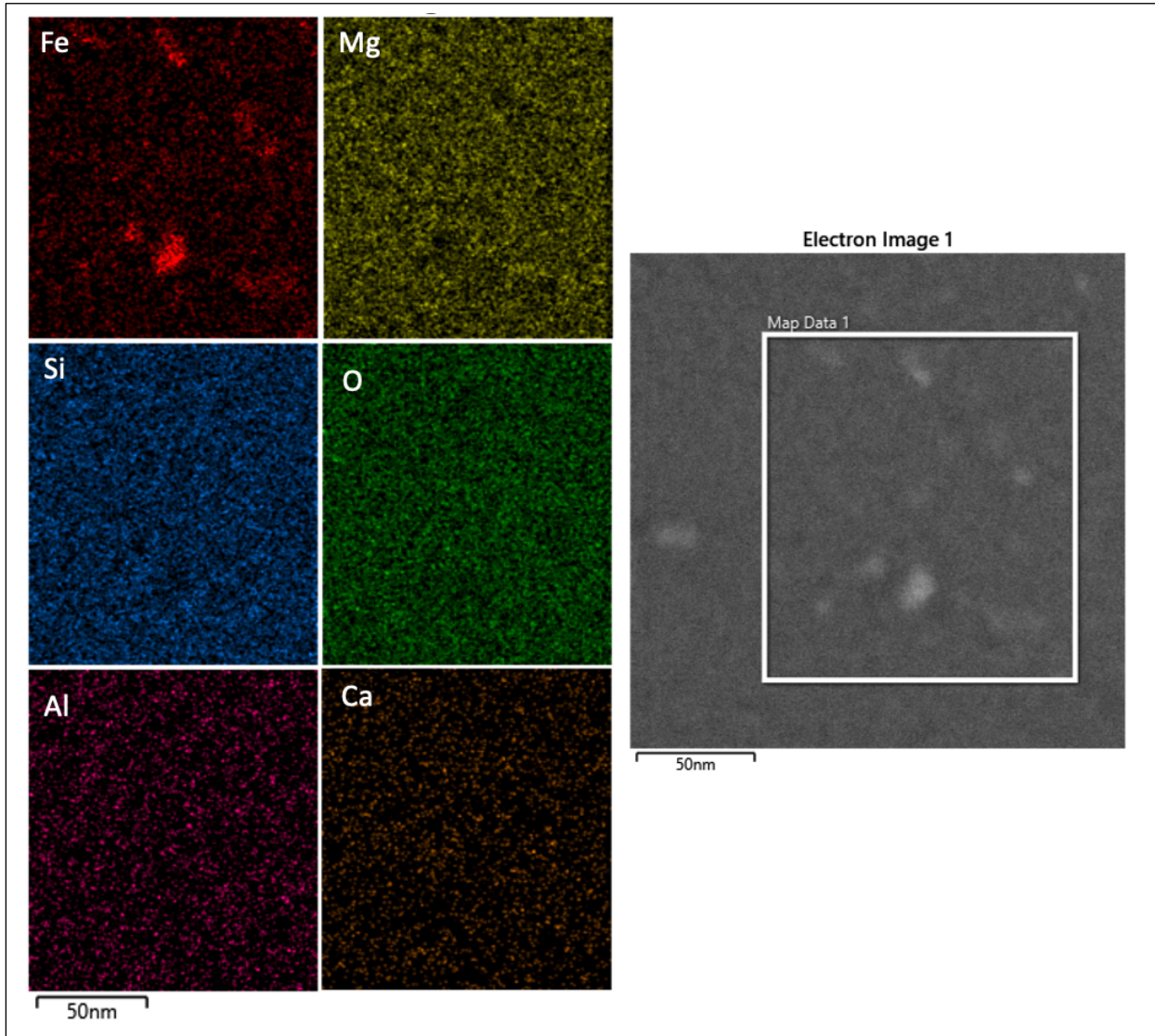


Figure D.20. STEM image and EDS line scans for sample K86.

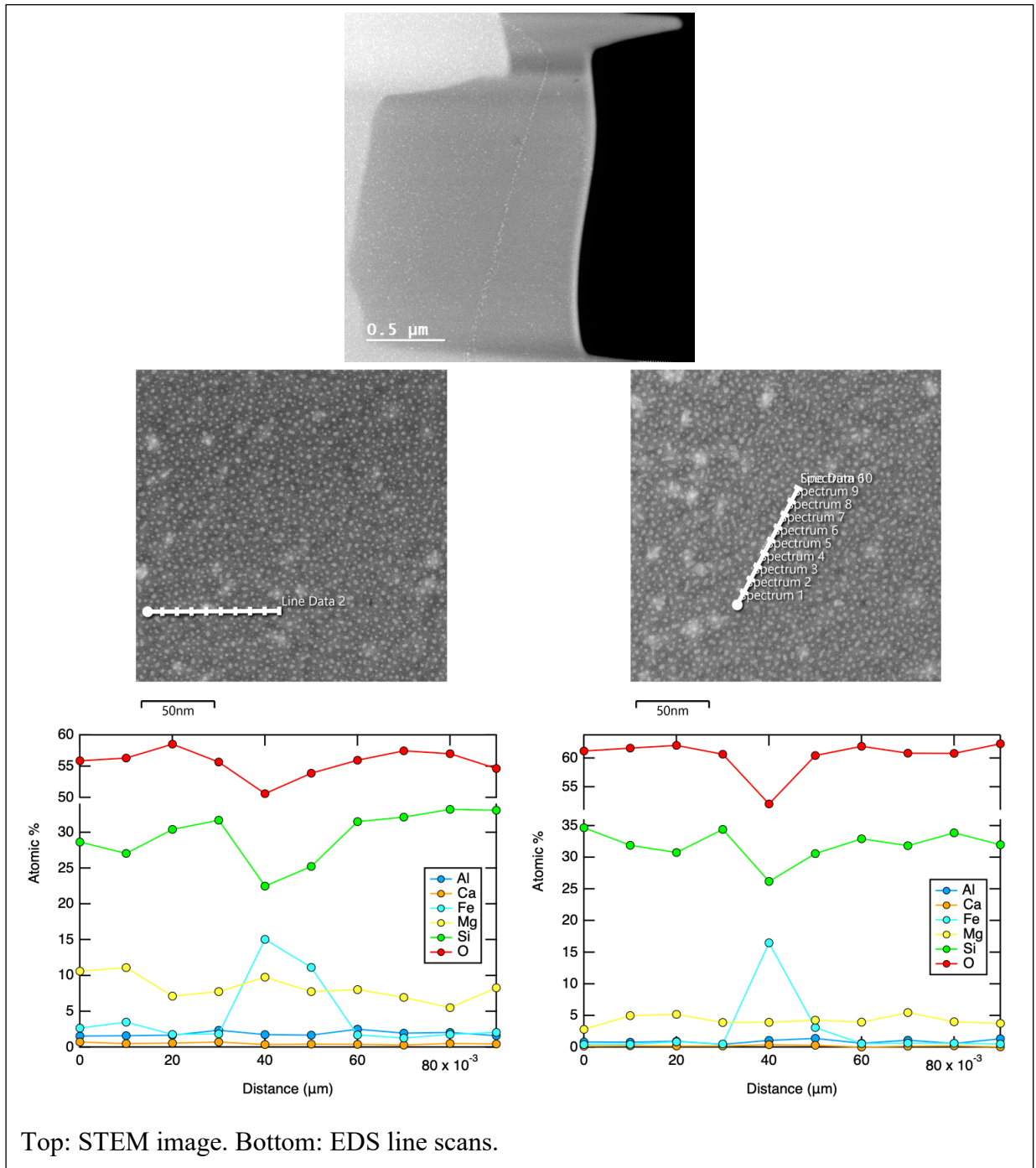


Figure D.21. Elemental EDS maps of sample K86.

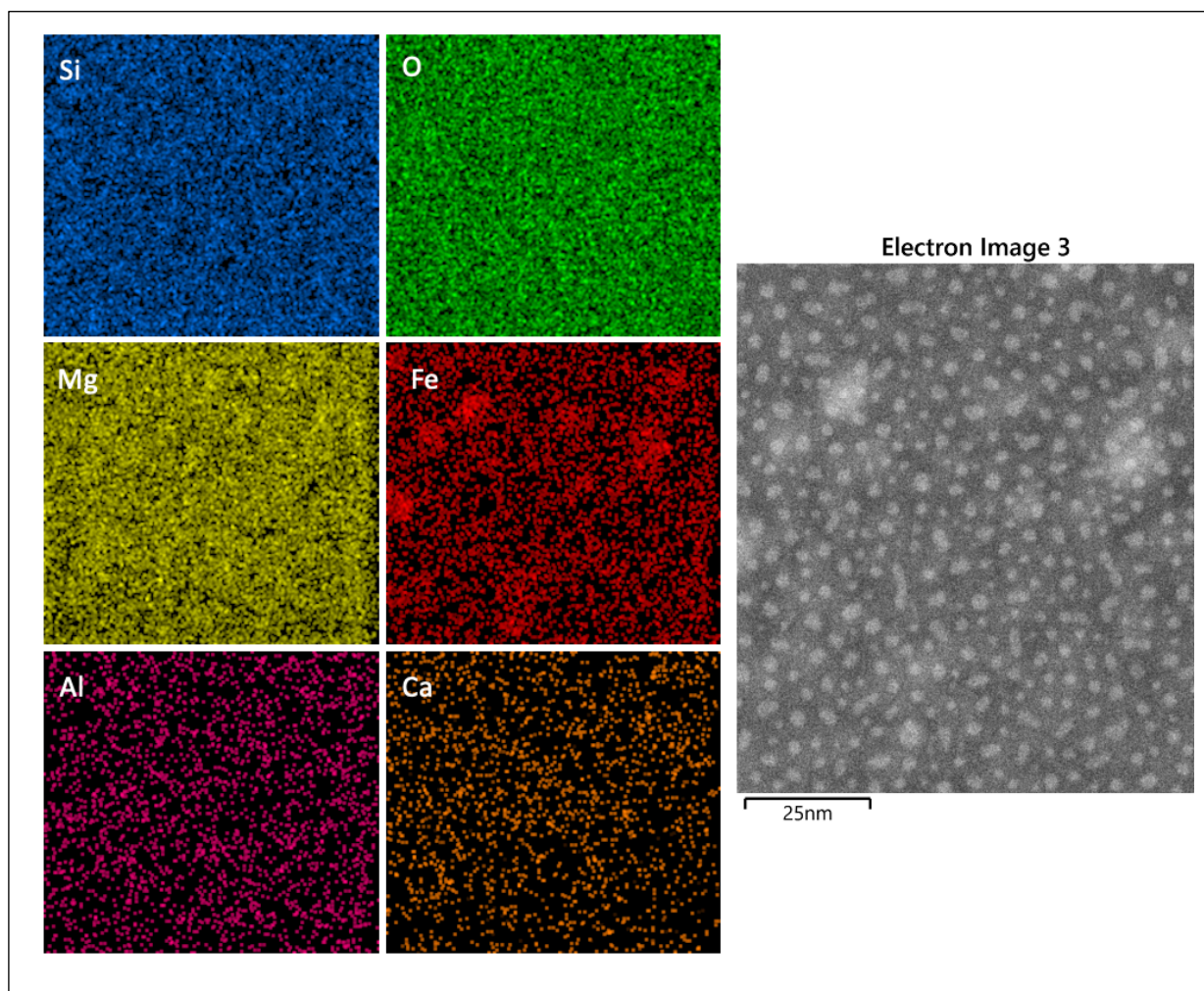


Table D.2. SEM EDS measurements on recovered samples.

Spectrum Label	O	Mg	Al	Si	Ca	Fe		collection current
K59								
Line2 sum	58.39	21.37	1.89	15.67	0.90	1.78		15 kV
Line5 sum (-highFe)	60.90	19.10	1.64	13.96	0.95	3.46		7 kV
Line6 sum (-highFe)	61.24	18.88	1.65	13.73	0.84	3.66		10 kV
K60								
Spectrum 4	58.22	21.2	2.03	15.42	0.94	1.86	0.33	15 kV
Line4 sum	60.91	19.22	1.72	13.84	0.91	3.40		10 kV
K83								
Spectrum 12	58.79	19.76	3.69	12.93	0.54	4.29		10 kV
Spectrum 14	58.28	19.47	3.62	13.08	0.51	5.04		10 kV
K84								
Spectrum	56.27	20.37	3.61	14.88	1.05	3.83		10 kV

Table D.3. STEM EDS measurements on recovered samples

Spectrum Label	O	Mg	Al	Si	Ca	Fe
K76						
Spectrum 2	80.1	6.75		13.15		
Spectrum 5	76.13	6.19		15.84		1.84
Spectrum 6	74.01	3.98		21.62		0.39
Spectrum 4	73.94	3.42		22.1		0.54
Spectrum 3	69.87	4.94		25.19		
Spectrum 1		7.23		6.58		86.19
K83						
Spectrum 4	70.76	3.65	0.64	24.59	0.14	0.23
Spectrum 12	70.19	6.13	0.7	22.1	0.42	0.47
Spectrum 13	69.85	3.31	0.43	25.99	0.18	0.24
Spectrum 3	69.64	4.47		25.54		0.35
Spectrum 16	69.61	3.84	0.55	25.66	0.18	0.16
Spectrum 15	68.86	4.45	0.43	25.8	0.2	0.26
Spectrum 11	68.18	5.01	0.59	25.12	0.31	0.79
Spectrum 7	67.73	13.04	0.63	16.76	0.21	1.63
Spectrum 2	66.96	14.17	0.53	16.65	0.24	1.46
Spectrum 14	64	16.2	0.72	17.08	0.34	1.66
Spectrum 1	62.27	24.92	0.59	10.11	0.2	1.91
Spectrum 6	61.03	19.71	1.61	15.38	0.73	1.54
Spectrum 10	59.82	3.76	0.7	19.77	0.2	15.74
Spectrum 5	56.08	27.36	0.5	1.81		14.26
Spectrum 9	55.58	8.97	0.92	16.27	0.45	17.83
Spectrum 23	47.34	23.7	2.83	20.16	1.71	4.26
Spectrum 22	46.43	21.13	2.73	23.77	2	3.94
Spectrum 20	42.99	43.35		7.29		6.37
Spectrum 21	42.14	16.27		16.33		25.26
Spectrum 19	41.55	43.13		8.83		6.49
Spectrum 17	38.68	31.04		10.98		19.31
Spectrum 18	30.43	19.67		11.27	1.08	37.55
K83 Map Sum Spectrum						
K83_1	60.29	20.32	1.72	15.04	0.85	1.78
K83_2	60.87	19.81	1.77	15.01	0.82	1.73
K86_1	53.79	21.28	2.16	18.13	1.16	3.48
K86_2	54.81	20.48	2.14	17.97	1.11	3.49
K86_3	44.65	20.49	3.09	23.67	1.56	6.54

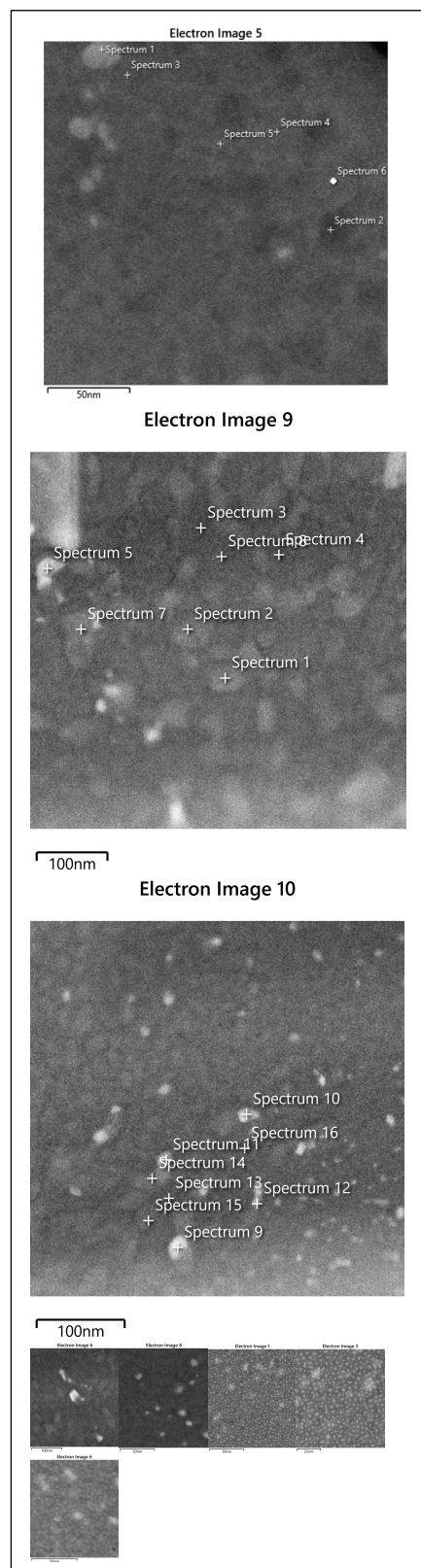


Table D.4. Lattice parameters and volumes for this study.

P (GPa)	a (Å)	b (Å)	c (Å)	V (Å ³)
24.5	4.685	4.842	6.779	153.780
35.9	4.649	4.776	6.704	148.867
52	4.566	4.745	6.618	143.393
62	4.527	4.712	6.504	138.725
70	4.502	4.698	6.532	138.164
99.8	4.394	4.625	6.406	130.172
135	4.362	4.502	6.285	123.433
0.3	4.800	4.952	6.936	164.865
0	4.830	4.959	6.927	165.921
0	4.817	4.964	6.925	165.589
0.9	4.813	4.964	6.972	166.595
0	4.815	4.968	6.963	166.573

Figure D.22. Example of image analysis on a “medium quality” image.

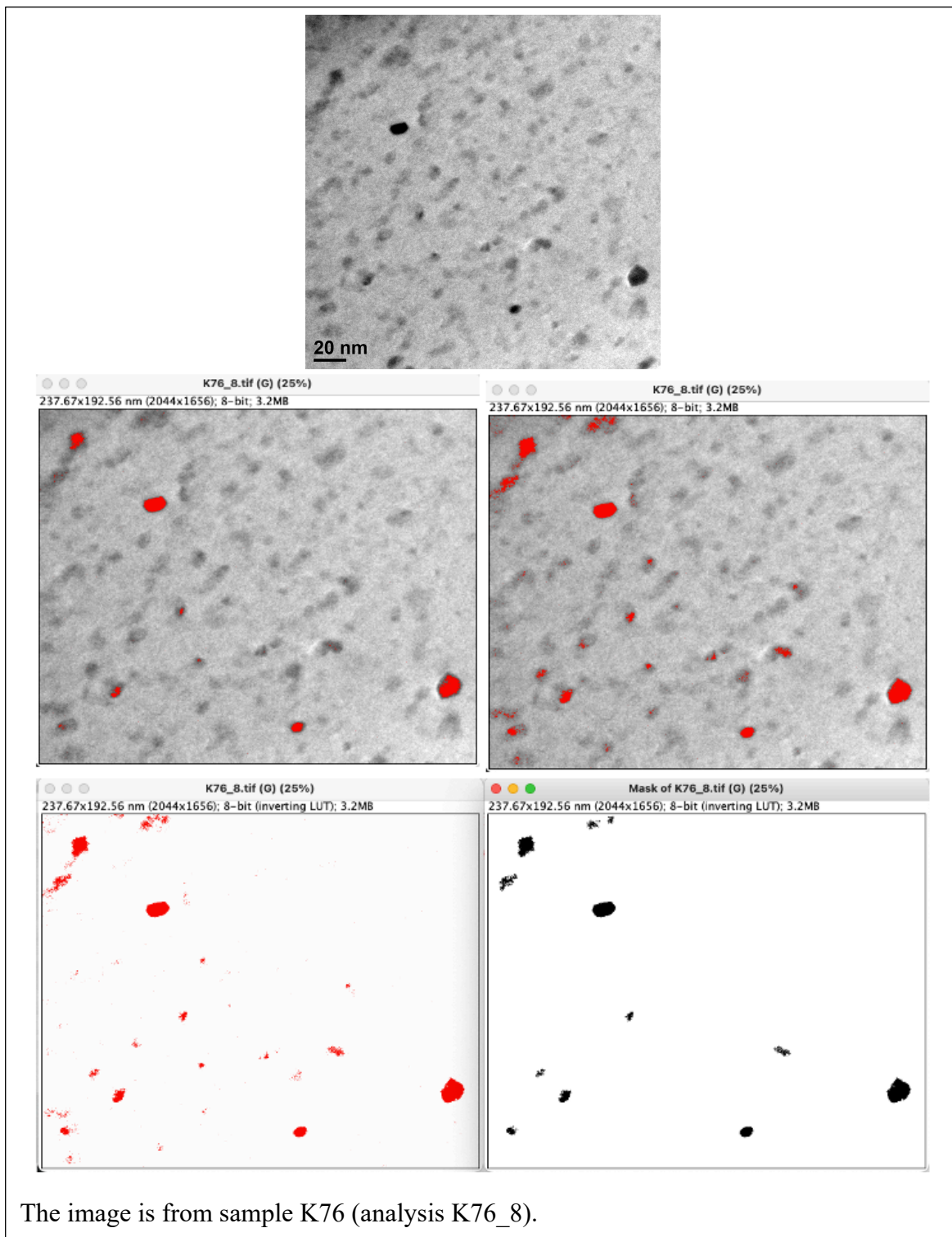
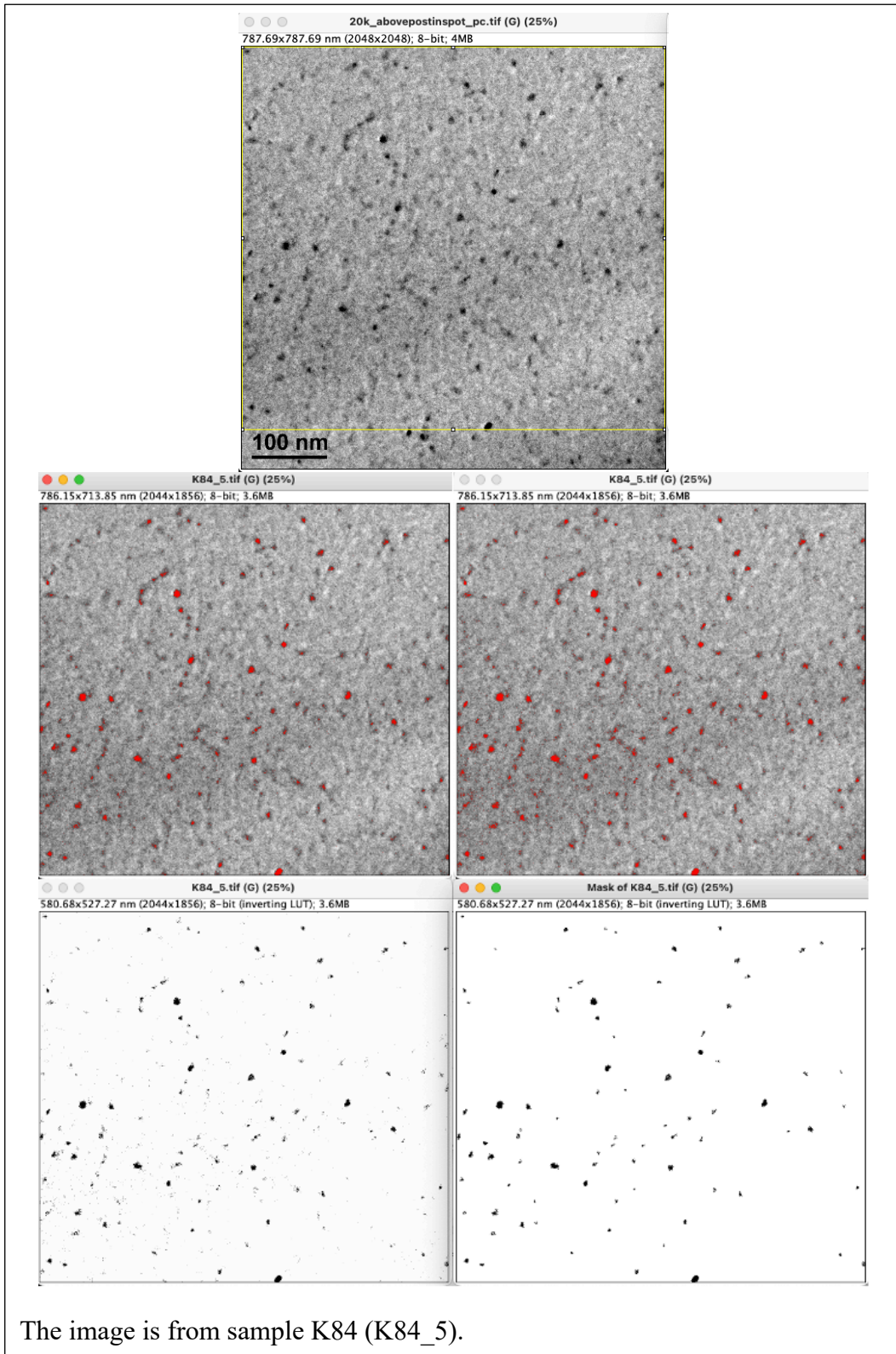


Figure D.23. Example of image analysis on a “low quality” image.



REFERENCES

- Akahama, Y., & Kawamura, H. (2004). High-pressure Raman spectroscopy of diamond anvils to 250 GPa: Method for pressure determination in the multimegabar pressure range. *Journal of Applied Physics*, 96(7), 3748–3751. <https://doi.org/10.1063/1.1778482>
- Akaogi, M., Ohmura, N., & Suzuki, T. (1998). High-pressure dissociation of Fe₃Al₂Si₃O₁₂ garnet: Phase boundary determined by phase equilibrium experiments and calorimetry. *Physics of the Earth and Planetary Interiors*, 106(1–2), 103–113. [https://doi.org/10.1016/S0031-9201\(97\)00084-8](https://doi.org/10.1016/S0031-9201(97)00084-8)
- Andrault, D., Muñoz, M., Pesce, G., Cerantola, V., Chumakov, A., Kantor, I., Pascarelli, S., Rüffer, R., & Hennet, L. (2017). Large oxygen excess in the primitive mantle could be the source of the Great Oxygenation Event. *Geochemical Perspectives Letters*, 6(2017), 5–10. <https://doi.org/10.7185/geochemlet.1801>
- Armstrong, L. S., Walter, M. J., Tuff, J. R., Lord, O. T., Lennie, A. R., Kleppe, A. K., & Clark, S. M. (2012). Perovskite Phase Relations in the System CaO–MgO–TiO₂–SiO₂ and Implications for Deep Mantle Lithologies, *Journal of Petrology*, 53(3), 611–635. <https://doi.org/10.1093/petrology/egr073>
- Badro, J. (2014). Spin transitions in mantle minerals. *Annual Review of Earth and Planetary Sciences*, 42, 231–248. <https://doi.org/10.1146/annurev-earth-042711-105304>
- Ballaran, T. B., Kurnosov, A., Glazyrin, K., Frost, D. J., Merlini, M., Hanfland, M., & Caracas, R. (2012). Effect of chemistry on the compressibility of silicate perovskite in the lower mantle. *Earth and Planetary Science Letters*, 333–334, 181–190. <https://doi.org/10.1016/j.epsl.2012.03.029>
- Bindi, L., Shim, S. H., Sharp, T. G., & Xie, X. (2020). Evidence for the charge disproportionation of iron in extraterrestrial bridgmanite. *Science Advances*, 6(2), 1–7. <https://doi.org/10.1126/sciadv.aay7893>
- Blanchard, I., Rubie, D. C., Jennings, E. S., Franchi, I. A., Zhao, X., Petitgirard, S., Miyajima, N., Jacobson, S. A., & Morbidelli, A. (2022). The metal–silicate partitioning of carbon during Earth’s accretion and its distribution in the early solar system. *Earth and Planetary Science Letters*, 580, 117374. <https://doi.org/10.1016/j.epsl.2022.117374>
- Brodholt, J. P. (2000). Pressure-induced changes in the compression mechanism of aluminous perovskite in the Earth’s mantle. *Nature*, 407(6804), 620–622. <https://doi.org/10.1038/35036565>

- Campbell, A. J. (2008). Measurement of temperature distributions across laser heated samples by multispectral imaging radiometry. *Review of Scientific Instruments*, 79(1). <https://doi.org/10.1063/1.2827513>
- Caracas, R. (2010). Spin and structural transitions in AlFeO₃ and FeAlO₃ perovskite and post-perovskite. *Physics of the Earth and Planetary Interiors*, 182(1–2), 10–17. <https://doi.org/10.1016/j.pepi.2010.06.001>
- Catalli, K., Shim, S. H., Dera, P., Prakapenka, V. B., Zhao, J., Sturhahn, W., Chow, P., Xiao, Y., Cynn, H., & Evans, W. J. (2011). Effects of the Fe³⁺ spin transition on the properties of aluminous perovskite—New insights for lower-mantle seismic heterogeneities. *Earth and Planetary Science Letters*, 310(3–4), 293–302. <https://doi.org/10.1016/j.epsl.2011.08.018>
- Cerenius, Y., & Dubrovinsky, L. (2000). Compressibility measurements on iridium. *Journal of Alloys and Compounds*, 306(1–2), 26–29. [https://doi.org/10.1016/S0925-8388\(00\)00767-2](https://doi.org/10.1016/S0925-8388(00)00767-2)
- Chidester, B. A., Rahman, Z., Righer, K., & Campbell, A. J. (2017). Metal-silicate partitioning of U: Implications for the heat budget of the core and evidence for reduced U in the mantle. *Geochimica et Cosmochimica Acta*, 199, 1-12. <https://doi.org/10.1016/j.gca.2016.11.035>
- Connolly, J. A. D. (2005). Computation of phase equilibria by linear programming: A tool for geodynamic modeling and its application to subduction zone decarbonation. *Earth and Planetary Science Letters*, 236(1–2), 524–541. <https://doi.org/10.1016/j.epsl.2005.04.033>
- Connolly, J. A. D. (2009). The geodynamic equation of state: What and how. *Geochemistry, Geophysics, Geosystems*, 10(10). [Software] <https://www.perplex.ethz.ch/> <https://doi.org/10.1029/2009GC002540>
- Conrad, P. G., Shen, G., Mao, H. K., Fei, Y., & Hemley, R. J. (1996). Stability of garnets in the system MgSiO₃–FeSiO₃–Al₂O₃ at high pressure. In *US–Japan Seminar High Pressure-Temperature Research: Properties of Earth and Planetary Materials* (Vol. 73).
- Creasy, N., Girard, J., Eckert, J. O., & Lee, K. K. M. (2020). The Role of Redox on Bridgmanite Crystal Chemistry and Calcium Speciation in the Lower Mantle. *Journal of Geophysical Research: Solid Earth*, 125(10), 1–17. <https://doi.org/10.1029/2020JB020783>
- Dasgupta, R., and Hirschmann, M.M. (2010), The deep carbon cycle and melting in Earth's interior. *Earth and Planetary Science Letters*, 298(1-2), 1-13.
- Day, M. C., Pamato, M. G., Novella, D., & Nestola, F. (2023). Imperfections in natural diamond: the key to understanding diamond genesis and the mantle. *Rivista Del Nuovo Cimento*, 46(7), 381–471. <https://doi.org/10.1007/s40766-023-00045-6>

- Dewaele, A. S., Loubeyre, P., Occelli, F., Mezouar, M., Dorogokupets, P. I., & Torrent, M. (2006). *Quasihydrostatic Equation of State of Iron above 2 Mbar*. <https://doi.org/10.1103/PhysRevLett.97.215504>
- Dorfman, S. M., Shieh, S. R., Meng, Y., Prakapenka, V. B., & Duffy, T. S. (2012). Synthesis and equation of state of perovskites in the (Mg, Fe)₃Al₂Si₃O₁₂ system to 177GPa. *Earth and Planetary Science Letters*, 357–358, 194–202. <https://doi.org/10.1016/j.epsl.2012.09.024>
- Dorfman, S. M., Potapkin, V., Lv, M., Greenberg, E., Kuppenko, I., Chumakov, A. I., Bi, W., Alp, E. E., Liu, J., Magrez, A., Dutton, S. E., Cava, R. J., Mccammon, C. A., & Gillet, P. (2020). Effects of composition and pressure on electronic states of iron in bridgmanite. *American Mineralogist*, 105(7), 1030–1039. <https://doi.org/10.2138/am-2020-7309>
- Fei, Y., Virgo, D., Mysen, B. O., Wang, Y., & Mao, H.-K. (1994). Temperature-dependent electron delocalization in (Mg,Fe)SiO₃ perovskite. *American Mineralogist*, 79, 826–837.
- Fiquet, G., Auzende, A., Siebert, J., & Corgne, A. (2010). Melting of Peridotite to 140 Gigapascals. *Science*, September. <https://doi.org/10.1126/science.1192448>
- Fischer, R. A., Nakajima, Y., Campbell, A. J., Frost, D. J., Harries, D., Langenhorst, F. et al. (2015). High pressure metal-silicate partitioning of Ni, Co, V, Cr, Si, and O. *Geochimica et Cosmochimica Acta*, 167, 177-194. <https://doi.org/10.1016/j.gca.2015.06.026>
- Frost, D. J., & Langenhorst, F. (2002). The effect of Al₂O₃ on Fe-Mg partitioning between magnesiowustite and magnesian silicate perovskite. *Earth and Planetary Science Letters*, 199, 227–241. [https://doi.org/10.1016/S0012-821X\(02\)00558-7](https://doi.org/10.1016/S0012-821X(02)00558-7)
- Frost, D. J., Liebske, C., Langenhorst, F., McCammon, C. A., Tronnes, R. G., & Rubie, D. C. (2004). Experimental evidence for the existence of iron-rich metal in the Earth's lower mantle. *Nature*, 428, 409–412. <https://doi.org/10.1029/2003JC000964>
- Frost, D. J., & McCammon, C. A. (2008). The Redox State of earth's mantle. *Annual Review of Earth and Planetary Sciences*, 36, 389–420. <https://doi.org/10.1146/annurev.earth.36.031207.124322>
- Fu, S., Zhang, Y., Okuchi, T., Lin, J. (2023). Single-crystal elasticity of (Al,Fe)-bearing bridgmanite up to 82 GPa. *American Mineralogist*, 108(4), 719–730. <https://doi-org.proxy.uchicago.edu/10.2138/am-2022-8435>
- Fujino, K., Sasaki, Y., Komori, T., Ogawa, H., Miyajima, N., Sata, N., & Yagi, T. (2004). Approach to the mineralogy of the lower mantle by a combined method of a laser-heated diamond anvil cell experiment and analytical electron microscopy. *Physics of the Earth and Planetary Interiors*, 143(1–2), 215–221. <https://doi.org/10.1016/j.pepi.2003.11.013>

- Funamori, N., Yagi, T., Miyajima, N., & Fujino, K. (1997). Transformation in Garnet from Orthorhombic Perovskite to LiNbO₃ Phase on Release of Pressure. *American Association for the Advancement of Science*, 275(5299), 513–515.
- Galimov, E. M. (2005). Redox evolution of the Earth caused by a multi-stage formation of its core. *Earth and Planetary Science Letters*, 233(3–4), 263–276. <https://doi.org/10.1016/j.epsl.2005.01.026>
- Heinz, D.L. & Jeanloz, R. (1987). Temperature Measurements in the Laser-Heated Diamond Cell. In *High-Pressure Research in Mineral Physics: A Volume in Honor of Syun-iti Akimoto* (eds M.H. Manghnani and Y. Syono). <https://doi.org/10.1029/GM039p0113>
- Holland, T. J. B., & Powell, R. (1998). An internally consistent thermodynamic data set for phases of petrological interest. *Journal of Metamorphic Geology*, 16(3), 309–343. <https://doi.org/10.1111/j.1525-1314.1998.00140.x>
- Holland, T.J.B. and Powell, R. (2011). An improved and extended internally consistent thermodynamic dataset for phases of petrological interest, involving a new equation of state for solids. *Journal of Metamorphic Geology*, 29: 333–383. <https://doi.org/10.1111/j.1525-1314.2010.00923.x>
- Horiuchi, H., Ito, E., & Weidner, D. J. (1987). Perovskite-type MgSiO₃: Single-crystal X-ray diffraction study. In *American Mineralogist* (Vol. 72).
- Hu, Q., Kim, D. Y., Yang, W., Yang, L., Meng, Y., Zhang, L., & Mao, H. K. (2016). FeO₂ and FeOOH under deep lower-mantle conditions and Earth's oxygen-hydrogen cycles. *Nature*, 534(7606), 241–244. <https://doi.org/10.1038/nature18018>
- Huang, R., Boffa Ballaran, T., McCammon, C. A., Miyajima, N., & Frost, D. J. (2021). The Effect of Fe-Al Substitution on the Crystal Structure of MgSiO₃ Bridgmanite. *Journal of Geophysical Research: Solid Earth*, 126(9). <https://doi.org/10.1029/2021JB021936>
- Hummer, D. R., & Fei, Y. (2012). Synthesis and crystal chemistry of Fe³⁺-bearing (Mg,Fe³⁺)(Si,Fe³⁺)O₃ perovskite. *American Mineralogist*, 97(11–12), 1915–1921. <https://doi.org/10.2138/am.2012.4144>
- Irifune, T. (1994). Absence of an aluminous phase in the upper part of the Earth's lower mantle. *Nature*, 370(6485), 131–133. <https://doi.org/10.1038/370131a0>
- Irifune, T., Koizumi, T., & Ando, J. I. (1996). An experimental study of the garnet-perovskite transformation in the system MgSiO₃-Mg₃Al₂Si₃O₁₂. *Physics of the Earth and Planetary Interiors*, 96(2-3 SPEC. ISS.), 147–157. [https://doi.org/10.1016/0031-9201\(96\)03147-0](https://doi.org/10.1016/0031-9201(96)03147-0)

- Irfune, T., Shinmei, T., McCammon, C. A., Miyajima, N., Rubie, D. C., & Frost, D. J. (2010). Iron partitioning and density changes of pyrolite in Earth's lower mantle. *Science*, 327(5962), 193–195. <https://doi.org/10.1126/science.1181443>
- Ito, E., Kubo, A., Katsura, T., Akaogi, M., & Fujita, T. (1998). High-pressure transformation of pyrope (Mg₃Al₂Si₃O₁₂) in a sintered diamond cubic anvil assembly. *Geophysical Research Letters*, 25(6), 821–824.
- Katsura, T. (2022). A Revised Adiabatic Temperature Profile for the Mantle. *Journal of Geophysical Research: Solid Earth*, 127(2), 1–11. <https://doi.org/10.1029/2021JB023562>
- Kesson, S. E., Fitz Gerald, J. D., & Shelley, J. M. G. (1994). Mineral chemistry and density of subducted basaltic crust at lower-mantle pressures. *Nature*, 372(6508), 767–769. <https://doi.org/10.1038/372767a0>
- Kesson, S. E., Fitz Gerald, J. D., Shelley, J. M. G., & Withers, R. L. (1995). Phase relations, structure and crystal chemistry of some aluminous silicate perovskites. *Earth and Planetary Science Letters*, 134(1–2), 187–201. [https://doi.org/10.1016/0012-821X\(95\)00112-P](https://doi.org/10.1016/0012-821X(95)00112-P)
- Kesson, S. E., Fitz Gerald, J. D., & Shelley, J. M. (1998). Mineralogy and dynamics of a pyrolite lower mantle. *Nature*, 393, 252–255. <https://doi.org/10.1038/246170a0>
- Knight, D. S., & White, W. B. (1989). Characterization of diamond films by Raman spectroscopy. *Journal of Materials Research*, 4(2), 385–393.
- Knittle, E., & Jeanloz, R. (1987). Synthesis and equation of state of (Mg,Fe)SiO₃ perovskite to over 100 gigapascals. *Science*, 235(4789), 668–670. <https://doi.org/10.1126/science.235.4789.668>
- Ko, B., Greenberg, E., Prakapenka, V., Alp, E. E., Bi, W., Meng, Y., Zhang, D., & Shim, S. H. (2022). Calcium dissolution in bridgmanite in the Earth's deep mantle. *Nature*, 611(7934), 88–92. <https://doi.org/10.1038/s41586-022-05237-4>
- Kobayashi, Y., Kondo, T., Ohtani, E., Hirao, N., Miyajima, N., Yagi, T., Nagase, T., & Kikegawa, T. (2005). Fe-Mg partitioning between (Mg, Fe)SiO₃ post-perovskite, perovskite, and magnesiowüstite in the Earth's lower mantle. *Geophysical Research Letters*, 32(19), 1–4. <https://doi.org/10.1029/2005GL023257>
- Komabayashi, T., Fei, Y., Meng, Y., & Prakapenka, V. (2009). In-situ X-ray diffraction measurements of the γ - ϵ transition boundary of iron in an internally-heated diamond anvil cell. *Earth and Planetary Science Letters*, 282(1–4), 252–257. <https://doi.org/10.1016/j.epsl.2009.03.025>

- Kudoh, Y., Prewitt, C. T., Finger, L. W., Darovskikh, A., & Ito, E. (1990). Effect of iron on the crystal structure of (Mg,Fe)SiO₃ perovskite. *Geophysical Research Letters*, *17*(10), 1481–1484. <https://doi.org/10.1029/GL017i010p01481>
- Kurnosov, A., Marquardt, H., Frost, D. J., Boffa Ballaran, T., & Ziberna, L. (2017). Evidence for a Fe³⁺-rich pyrolitic lower mantle from (Al,Fe)-bearing bridgmanite elasticity data. *Nature*, *543*(7646), 543–546. <https://doi.org/10.1038/nature21390>
- Lauterbach, S., McCammon, C. A., Van Aken, P., Langenhorst, F., & Seifert, F. (2000). Mossbauer and ELNES spectroscopy of (Mg,Fe)(Si,Al)O₃ perovskite: A highly oxidised component of the lower mantle. *Contributions to Mineralogy and Petrology*, *138*(1), 17–26. <https://doi.org/10.1007/PL00007658>
- Lee, K. K. M., O'Neill, B., Panero, W. R., Shim, S. H., Benedetti, L. R., & Jeanloz, R. (2004). Equations of state of the high-pressure phases of a natural peridotite and implications for the Earth's lower mantle. *Earth and Planetary Science Letters*, *223*(3–4), 381–393. <https://doi.org/10.1016/j.epsl.2004.04.033>
- Lee, K. K. M., O'Neill, B., & Jeanloz, R. (2004). Limits to resolution in composition and density in ultra high-pressure experiments on natural mantle-rock samples. *Physics of the Earth and Planetary Interiors*, *143*(1–2), 241–253. <https://doi.org/10.1016/j.pepi.2003.06.002>
- Li, J., Fei, Y., Mao, H. K., Hirose, K., & Shieh, S. R. (2001). Sulfur in the Earth's inner core. *Earth and Planetary Science Letters*, *193*(3–4), 509–514. [https://doi.org/10.1016/S0012-821X\(01\)00521-0](https://doi.org/10.1016/S0012-821X(01)00521-0)
- Li, Z.-X. A., & Lee, C.-T. A. (2004). The constancy of upper mantle fO₂ through time inferred from V/Sc ratios in basalts. *Earth and Planetary Science Letters*, *228*(3–4), 483–493. <https://doi.org/10.1016/j.epsl.2004.10.006>
- Liu, L. G. (1976). Orthorhombic perovskite phases observed in olivine, pyroxene and garnet at high pressures and temperatures. *Physics of the Earth and Planetary Interiors*, *11*(4), 289–298. [https://doi.org/10.1016/0031-9201\(76\)90016-9](https://doi.org/10.1016/0031-9201(76)90016-9)
- Liu, L. G. (1989). Silicate perovskites: A review. In *Surveys in Geophysics* (Vol. 10, Issue 1, pp. 63–81). Kluwer Academic Publishers. <https://doi.org/10.1007/BF01901665>
- Liu, Z., Nishi, M., Ishii, T., Fei, H., Miyajima, N., Ballaran, T. B., et al. (2017). Phase relations in the system MgSiO₃-Al₂O₃ up to 2300 K at lower mantle pressures. *Journal of Geophysical Research: Solid Earth*, *122*, 7775–7788. <https://doi.org/10.1002/2017JB014579>
- Liu, Z., McCammon, C., Wang, B., Dubrovinsky, L., Ishii, T., Bondar, D., et al. (2020). Stability and Solubility of the FeAlO₃ Component in Bridgmanite at Uppermost Lower Mantle

- Conditions. *Journal of Geophysical Research: Solid Earth*, 125(2). <https://doi.org/10.1029/2019JB018447>
- Lobanov, S. S., Holtgrewe, N., Ito, G., Badro, J., Piet, H., Nabiei, F., Lin, J. F., Bayarjargal, L., Wirth, R., Schreiber, A., & Goncharov, A. F. (2020). Blocked radiative heat transport in the hot pyrolitic lower mantle. *Earth and Planetary Science Letters*, 537. <https://doi.org/10.1016/j.epsl.2020.116176>
- Lundin, S., Catalli, K., Santillán, J., Shim, S. H., Prakapenka, V. B., Kunz, M., & Meng, Y. (2008). Effect of Fe on the equation of state of mantle silicate perovskite over 1 Mbar. *Physics of the Earth and Planetary Interiors*, 168, 97-102. <https://doi.org/10.1016/j.pepi.2008.05.002>
- Mao, H. K., Shen, G., & Hemley, R. J. (1997). Multivariable dependence of Fe-Mg partitioning in the lower mantle. *Science*, 278(5346), 2098–2100. <https://doi.org/10.1126/science.278.5346.2098>
- McCammon, C. A., Rubie, D. C., Ross, C. R., Seifert, F., & O'Neill, H. S. C. (1992). Mossbauer spectra of $57\text{Fe}_{0.05}\text{Mg}_{0.95}\text{SiO}_3$ perovskite at 80 and 298 K. *American Mineralogist*, 77(7–8), 894–897.
- McCammon, C. (1997). Perovskite as a possible sink for ferric iron in the lower mantle. *Nature*, 387(6634), 694–696. <https://doi.org/10.1038/42685>
- McCammon, C. A. (1998). The crystal chemistry of ferric iron in $\text{Fe}_{0.05}\text{Mg}_{0.95}\text{SiO}_3$ perovskite as determined by Mössbauer spectroscopy in the temperature range 80-293 K. *Physics and Chemistry of Minerals*, 25(4), 292–300. <https://doi.org/10.1007/s002690050117>
- McCammon, C. A., Lauterbach, S., Seifert, F., Langenhorst, F., & van Aken, P. A. (2004). Iron oxidation state in lower mantle mineral assemblages I. Empirical relations derived from high-pressure experiments. *Earth and Planetary Science Letters*, 222(2), 435–449. <https://doi.org/10.1016/j.epsl.2004.03.018>
- McDonough, W. F., & Sun, S. s. (1995). The composition of the Earth. *Chemical Geology*, 120(3–4), 223–253. [https://doi.org/10.1016/0009-2541\(94\)00140-4](https://doi.org/10.1016/0009-2541(94)00140-4)
- Murakami, M., Hirose, K., Sata, N., & Ohishi, Y. (2005). Post-perovskite phase transition and mineral chemistry in the pyrolitic lowermost mantle. *Geophysical Research Letters*, 32(3), 1–4. <https://doi.org/10.1029/2004GL021956>
- Myhill, R. (2018). The elastic solid solution model for minerals at high pressures and temperatures. *Contributions to Mineralogy and Petrology*, 172(2). <https://doi.org/10.1007/s00410-017-1436-z>

- Myhill, B. (2018, May 17). Re: Holland and Powell 2011 database as implemented in Perple_X [Discussion post]. Perple_X discussion forum <https://groups.io/g/PerpleX/topic/64122762#1514>
- Nagai, T., Hamane, D., Sujatha Devi, P., Miyajima, N., Yagi, T., Yamanaka, T., & Fujino, K. (2005). *A New Polymorph of FeAlO₃ at High Pressure*. <https://doi.org/10.1021/jp054409s>
- Nishio-Hamane, D., Nagai, T., Fujino, K., Seto, Y., & Takafuji, N. (2005). Fe³⁺ and Al solubilities in MgSiO₃ perovskite: Implication of the Fe³⁺+AlO₃ substitution in MgSiO₃ perovskite at the lower mantle condition. *Geophysical Research Letters*, 32(16), 1–4. <https://doi.org/10.1029/2005GL023529>
- Nzogang, B. C., Bouquerel, J., Cordier, P., Mussi, A., Girard, J., & Karato, S. (2018). Characterization by Scanning Precession Electron Diffraction of an Aggregate of Bridgmanite and Ferropervicite Deformed at HP-HT. *Geochemistry, Geophysics, Geosystems*, 19(3), 582–594. <https://doi.org/10.1002/2017GC007244>
- O'Neill, B., & Jeanloz, R. (1990). Experimental petrology of the lower mantle: a natural peridotite taken to 54 GPa. *Geophysical Research Letters*, 17(10), 1477–1480. <https://doi.org/10.1029/GL017i010p01477>
- O'Neill, Bridget F. & Raymond Jeanloz. MgSiO₃-FeSiO₃-Al₂O₃ in the Earth's lower mantle: Perovskite and garnet at 1200 km depth. *Journal of Geophysical Research* 99 (1994), 19901-19915. <https://doi.org/10.1029/94JB01752>
- Ohira, I., Ohtani, E., Sakai, T., Miyahara, M., Hirao, N., Ohishi, Y., & Nishijima, M. (2014). Stability of a hydrous δ -phase, AlOOH-MgSiO₂(OH)₂, and a mechanism for water transport into the base of lower mantle. *Earth and Planetary Science Letters*, 401, 12–17. <https://doi.org/10.1016/j.epsl.2014.05.059>
- Ono, S., Ohishi, Y., Isshiki, M., & Watanuki, T. (2005). In situ X-ray observations of phase assemblages in peridotite and basalt compositions at lower mantle conditions: Implications for density of subducted oceanic plate. *Journal of Geophysical Research: Solid Earth*, 110(B2), 1–11. <https://doi.org/10.1029/2004JB003196>
- Pack, A., Kremer, K., Albrecht, N., Simon, K., & Kronz, A. (2010). Description of an aerodynamic levitation apparatus with applications in Earth sciences. *Geochemical Transactions*, 11, 1–16. <https://doi.org/10.1186/1467-4866-11-4>
- Palme, H., & O'Neill, H. (2013). Cosmochemical Estimates of Mantle Composition. In *Treatise on Geochemistry: Second Edition* (2nd ed., Vol. 3). Elsevier Ltd. <https://doi.org/10.1016/B978-0-08-095975-7.00201-1>

- Piet, H., Badro, J., Nabiei, F., Dennenwaldt, T., Shim, S. H., Cantoni, M., Hébert, C., & Gillet, P. (2016). Spin and valence dependence of iron partitioning in Earth's deep mantle. *Proceedings of the National Academy of Sciences of the United States of America*, *113*(40), 11127–11130. <https://doi.org/10.1073/pnas.1605290113>
- Piet, H., Leinenweber, K. D., Tappan, J., Greenberg, E., Prakapenka, V. B., Buseck, P. R., & Sang-Heon, S. (2020). Dehydration of δ -AIOOH in earth's deep lower mantle. *Minerals*, *10*(4), 1–16. <https://doi.org/10.3390/min10040384>
- Prakapenka, V. B., Kubo, A., Kuznetsov, A., Laskin, A., Shkurikhin, O., Dera, P., et al. (2008). Advanced flat top laser heating system for high pressure research at GSECARS: Application to the melting behavior of germanium. *High Pressure Research*, *28*(3), 225–235. <https://doi.org/10.1080/08957950802050718>
- Prescher, C., Langenhorst, F., Dubrovinsky, L. S., Prakapenka, V. B., & Miyajima, N. (2014). The effect of Fe spin crossovers on its partitioning behavior and oxidation state in a pyrolitic Earth's lower mantle system. *Earth and Planetary Science Letters*, *399*, 86–91. <https://doi.org/10.1016/j.epsl.2014.05.011>
- Prescher, C., & Prakapenka, V. B. (2015). DIOPTAS: A program for reduction of two-dimensional X-ray diffraction data and data exploration. *High Pressure Research*, *35*(3), 223–230. <https://doi.org/10.1080/08957959.2015.1059835>
- Richmond, N. C., & Brodholt, J. P. (1998). Calculated role of aluminum in the incorporation of ferric iron into magnesium silicate perovskite. *American Mineralogist*, *83*(9–10), 947–951. <https://doi.org/10.2138/am-1998-9-1003>
- Ricolleau, A., Fiquet, G., Addad, A., Menguy, N., Vanni, C., Perrillat, J. P., Daniel, I., Cardon, H., & Guignot, N. (2008). Analytical transmission electron microscopy study of a natural MORB sample assemblage transformed at high pressure and high temperature. *American Mineralogist*, *93*(1), 144–153. <https://doi.org/10.2138/am.2008.2532>
- Ringwood, A. E. (1975). Composition and Petrology of the Earth's Mantle. *MacGraw-Hill*, 618.
- Rohrbach, A., & Schmidt, M. W. (2011). Redox freezing and melting in the Earth's deep mantle resulting from carbon-iron redox coupling. *Nature*, *472*(7342), 209–214. <https://doi.org/10.1038/nature09899>
- Ross, M., Mao, H.K., Bell, P.M., Xu, J.A. (1986). The Equation of State of Dense Argon; A Comparison of Shock and Static Studies. In: Gupta, Y.M. (eds) Shock Waves in Condensed Matter. Springer, Boston, MA. https://doi.org/10.1007/978-1-4613-2207-8_14
- Ryabchikov, I. D., & Kaminsky, F. V. (2014). Physicochemical parameters of the material of mantle plumes: Evidence from the thermodynamic analysis of mineral inclusions in

- sublithospheric diamond. *Geochemistry International*, 52(11), 903–911. <https://doi.org/10.1134/S001670291411007X>
- Shieh, S. R., Dorfman, S. M., Kubo, A., Prakapenka, V. B., & Duffy, T. S. (2011). Synthesis and equation of state of post-perovskites in the (Mg,Fe)₃Al₂Si₃O₁₂ system. *Earth and Planetary Science Letters*, 312(3–4), 422–428. <https://doi.org/10.1016/j.epsl.2011.09.054>
- Shim, S. H., Duffy, T. S., & Shen, G. (2000). The equation of state of CaSiO₃ perovskite to 108 GPa at 300 K. *Physics of the Earth and Planetary Interiors*, 120, 327–338. [https://doi.org/10.1016/S0031-9201\(00\)00154-0](https://doi.org/10.1016/S0031-9201(00)00154-0)
- Shim, S. H., Grocholski, B., Ye, Y., Alp, E. E., Xu, S., Morgan, D., Meng, Y., & Prakapenka, V. B. (2017). Stability of ferrous-iron-rich bridgmanite under reducing midmantle conditions. *Proceedings of the National Academy of Sciences of the United States of America*, 114(25), 6468–6473. <https://doi.org/10.1073/pnas.1614036114>
- Sinmyo, R., Hirose, K., Muto, S., Ohishi, Y., & Yasuhara, A. (2011). The valence state and partitioning of iron in the Earth's lowermost mantle. *Journal of Geophysical Research: Solid Earth*, 116(7), 1–9. <https://doi.org/10.1029/2010JB008179>
- Sinmyo, R., & Hirose, K. (2013). *Iron partitioning in pyrolitic lower mantle*. <https://doi.org/10.1007/s00269-012-0551-7>
- Sinmyo, R., Bykova, E., McCammon, C., Kuppenko, I., Potapkin, V., & Dubrovinsky, L. (2013). Crystal chemistry of Fe³⁺-bearing (Mg, Fe)SiO₃ perovskite: a single-crystal X-ray diffraction study. *Physics and Chemistry of Minerals* 41:6, 41(6), 409–417. <https://doi.org/10.1007/S00269-013-0639-8>
- Skinner, B. J. (1966). Thermal expansion. In *Handbook of Physical Constants* (editor S. Clark), Section 6, 75–96.
- Smith, E. M. & Kopylova, M. G. 2014. Implications of metallic iron for diamonds and nitrogen in the sublithospheric mantle. *Canadian Journal of Earth Sciences*. 51(5): 510–516. <https://doi.org/10.1139/cjes-2013-0218>
- Smith, E. M., Shirey, S. B., Nestola, F., Bullock, E. S., Wang, J., Richardson, S. H., & Wang, W. (2016). Large gem diamonds from metallic liquid in Earth's deep mantle. *Science*, 354(6318), 1403–1406.
- Stagno, V., Tange, Y., Miyajima, N., McCammon, C. A., Irifune, T., & Frost, D. J. (2011). The stability of magnesite in the transition zone and the lower mantle as function of oxygen

- fugacity. *Geophysical Research Letters*, 38(19), 1–5.
<https://doi.org/10.1029/2011GL049560>
- Stixrude, L., & Lithgow-Bertelloni, C. (2005). Thermodynamics of mantle minerals - I. Physical properties. *Geophysical Journal International*, 162(2), 610–632.
<https://doi.org/10.1111/j.1365-246X.2005.02642.x>
- Stixrude, L., & Lithgow-Bertelloni, C. (2011). Thermodynamics of mantle minerals - II. Phase equilibria. *Geophysical Journal International*, 184(3), 1180–1213.
<https://doi.org/10.1111/j.1365-246X.2010.04890.x>
- Stixrude, L., Lithgow-Bertelloni, C. (2022) Thermal expansivity, heat capacity and bulk modulus of the mantle. *Geophysical Journal International*, 228(2), 1119–1149.
<https://doi.org/10.1093/gji/ggab394>
- Swadba, K. E., Davis, A. H., Zurkowski, C. C., Chariton, S., Prakapenka, V. B., and Campbell, A.J. (2023). Disproportionation of iron in almandine-pyrope-grossular garnet from 25 to 65 GPa. *Geochemistry, Geophysics, Geosystems*. 24, e2023GC011081.
- Tateno, S., Hirose, K., & Ohishi, Y. (2014). Melting experiments on peridotite to lowermost mantle conditions. *Journal of Geophysical Research: Solid Earth*, 4684–4694.
<https://doi.org/10.1002/2013JB010616>.Received
- Terasaki, H., Ohtani, E., Sakai, T., Kamada, S., Asanuma, H., Shibazaki, Y., Hirao, N., Sata, N., Ohishi, Y., Sakamaki, T., Suzuki, A., & Funakoshi, K. ichi. (2012). Stability of Fe-Ni hydride after the reaction between Fe-Ni alloy and hydrous phase (δ -AlOOH) up to 1.2Mbar: Possibility of H contribution to the core density deficit. *Physics of the Earth and Planetary Interiors*, 194–195, 18–24. <https://doi.org/10.1016/j.pepi.2012.01.002>
- Tsujino, N., Nishihara, Y., Nakajima, Y., Takahashi, E., Funakoshi, K. ichi, & Higo, Y. (2013). Equation of state of γ -Fe: Reference density for planetary cores. *Earth and Planetary Science Letters*, 375, 244–253. <https://doi.org/10.1016/J.EPSL.2013.05.040>
- Tsujino, N., Girard, J., Bi, W., Alp, E. E., & Karato, S. (2023). Formation of metallic Fe in bridgmanite under shallow lower mantle conditions. *Physics of the Earth and Planetary Interiors*, 337(June 2022), 107010. <https://doi.org/10.1016/j.pepi.2023.107010>
- Vanpeteghem, C. B., Angel, R. J., Ross, N. L., Jacobsen, S. D., Dobson, D. P., Litasov, K. D., & Ohtani, E. (2006). Al, Fe substitution in the MgSiO₃ perovskite structure: A single-crystal X-ray diffraction study. *Physics of the Earth and Planetary Interiors*, 155(1–2), 96–103.
<https://doi.org/10.1016/j.pepi.2005.10.003>
- Walter, M. J., Kubo, A., Yoshino, T., Brodholt, J., Koga, K. T., & Ohishi, Y. (2004). Phase relations and equation-of-state of aluminous Mg-silicate perovskite and implications for

- Earth's lower mantle. *Earth and Planetary Science Letters*, 222(2), 501–516. <https://doi.org/10.1016/j.epsl.2004.03.014>
- Wang, X., Tsuchiya, T., & Hase, A. (2015). Computational support for a pyrolitic lower mantle containing ferric iron. *Nature Geoscience*, 8(7), 556–559. <https://doi.org/10.1038/ngeo2458>
- Wicks, J. K., & Duffy, T. S. (2015). Crystal Structures of Minerals in the Lower Mantle. *Deep Earth: Physics and Chemistry of the Lower Mantle and Core*, 69–87. <https://doi.org/10.1002/9781118992487.ch6>
- Wood, B. J. (2000). Phase transformations and partitioning relations in peridotite under lower mantle conditions. *Earth and Planetary Science Letters*, 174(3–4), 341–354. [https://doi.org/10.1016/S0012-821X\(99\)00273-3](https://doi.org/10.1016/S0012-821X(99)00273-3)
- Wood, B. J., Walter, M. J., & Wade, J. (2006). Accretion of the Earth and segregation of its core. *Nature*, 441(7095), 825–833. <https://doi.org/10.1038/nature04763>
- Xu, S., Lin, J. F., & Morgan, D. (2017). Iron partitioning between ferropericlase and bridgmanite in the Earth's lower mantle. *Journal of Geophysical Research: Solid Earth*, 122(2), 1074–1087. <https://doi.org/10.1002/2016JB013543>
- Yagi, T., Okabe, K., Nishiyama, N., Kubo, A., & Kikegawa, T. (2004). Complicated effects of aluminum on the compressibility of silicate perovskite. *Physics of the Earth and Planetary Interiors*, 143(1–2), 81–91. <https://doi.org/10.1016/j.pepi.2003.07.020>
- Zhang, F., & Oganov, A. R. (2006). Valence state and spin transitions of iron in Earth's mantle silicates. *Earth and Planetary Science Letters*, 249(3–4), 436–443. <https://doi.org/10.1016/j.epsl.2006.07.023>
- Zhu, F., Liu, J., Lai, X., Xiao, Y., Prakapenka, V., Bi, W., Alp, E. E., Dera, P., Chen, B., & Li, J. (2020). Synthesis, Elasticity, and Spin State of an Intermediate MgSiO₃-FeAlO₃ Bridgmanite: Implications for Iron in Earth's Lower Mantle. *Journal of Geophysical Research: Solid Earth*, 125(7), 1–11. <https://doi.org/10.1029/2020JB019964>